



Delft University of Technology

**How can something empty be so full
Virus-like particles as next generation vaccines**

Kuijpers, L.C.

DOI

[10.4233/uuid:d0c09760-c716-4e8f-8574-29ef0fc84977](https://doi.org/10.4233/uuid:d0c09760-c716-4e8f-8574-29ef0fc84977)

Publication date

2023

Document Version

Final published version

Citation (APA)

Kuijpers, L. C. (2023). *How can something empty be so full: Virus-like particles as next generation vaccines*. [Dissertation (TU Delft), Delft University of Technology]. <https://doi.org/10.4233/uuid:d0c09760-c716-4e8f-8574-29ef0fc84977>

Important note

To cite this publication, please use the final published version (if applicable). Please check the document version above.

Copyright

Other than for strictly personal use, it is not permitted to download, forward or distribute the text or part of it, without the consent of the author(s) and/or copyright holder(s), unless the work is under an open content license such as Creative Commons.

Takedown policy

Please contact us and provide details if you believe this document breaches copyrights. We will remove access to the work immediately and investigate your claim.

**How can something empty be so full:
Virus-like particles as next generation
vaccines**

Louis Christiaan KUIJPERS

How can something empty be so full: Virus-like particles as next generation vaccines

Dissertation

for the purpose of obtaining the degree of doctor
at Delft University of Technology
by the authority of Rector Magnificus prof. dr. ir. T.H.J.J. van der Hagen
chair of the Board of Doctorates
to be defended publicly on
Wednesday 27 September 2023 at 15:00 o'clock

by

Louis Christiaan KUIJPERS

Master of Science in Life Science & Technology,
Delft University of Technology, The Netherlands
born in Voorburg, The Netherlands

This dissertation has been approved by the promotor.

Composition of the doctoral committee:

Rector Magnificus	chairperson
Prof. dr. N. H. Dekker	Delft University of Technology, <i>promotor</i>
Dr. A. Jakobi	Delft University of Technology, <i>copromotor</i>

Independent members:

Prof. dr. ir. S.J.J. Brouns	Delft University of Technology
Prof. dr. ir. S.J.T. van Noort	Leiden University
Prof. dr. M.M. van Oers	Wageningen University & Research
Dr. D.H.M. Meijer	Delft University of Technology
Prof. dr. C. Joo	Delft University of Technology, <i>reserve member</i>

Other member:

Dr. L.A. van der Pol	Intravacc B.V.
----------------------	----------------



Keywords: virus-like particles, BEVS, vaccine, HFMD, EV71, CVA6, RdRp

Printed by: Gildeprint

Cover: Louis Kuijpers – CVA6 VLPs on EM grid with broken carbon layer

Copyright © 2023 by L.C. Kuijpers

Casimir PhD series: 2023-15

ISBN: 978-90-8593-563-6

An electronic copy of this dissertation is available at <https://repository.tudelft.nl/>.

Contents

1	Introduction	1
1.1	Viruses	2
1.2	Enteroviruses	3
1.3	Preventive measures against viruses	5
1.4	Virus-like particles	10
1.5	Baculoviruses	12
1.6	Biophysical techniques	13
1.7	Thesis outline & research questions	17
1.8	References	18
2	Automated cell counting for Trypan blue-stained cell cultures using machine learning	29
2.1	Introduction	30
2.2	Results & Discussion	32
2.3	Conclusion	38
2.4	Supplemental information	38
2.5	Materials & methods	39
2.6	References	41
3	Optimization of enterovirus-like particle yield during production and purification	45
3.1	Introduction	46
3.2	Results	49
3.3	Discussion	61
3.4	Materials & methods	63
3.5	References	66

4	Beyond the RNA: Alternative mechanisms for the stability and maturation of enterovirus-like particles	69
4.1	Introduction	70
4.2	Results	72
4.3	Discussion	80
4.4	Materials & methods	84
4.5	Supplemental information	89
4.6	References	90
5	Characterizing single-molecule dynamics of viral RNA-dependent RNA polymerases with multiplexed magnetic tweezers	97
5.1	Introduction	98
5.2	Preparation of the RNA construct	98
5.3	Key resources table	102
5.4	Materials & methods	105
5.5	Step-by-step method details	106
5.6	Quantification and statistical analysis	115
5.7	Expected outcomes	117
5.8	Limitations	118
5.9	Troubleshooting	119
5.10	References	121
6	Induced intra- and intermolecular template switching as therapeutic mechanism against RNA viruses	123
6.1	Introduction	124
6.2	Results	125
6.3	Discussion	135
6.4	Materials & methods	141
6.5	Quantification and statistical analysis	149
6.6	Supplemental information	152
6.7	References	156

7	Concluding remarks	163
7.1	Translating the protocol for multivalent vaccine purposes	164
7.2	Cell culture maintenance	164
7.3	Virus detection	166
7.4	Stabilization studies	167
7.5	Biophysics developments	167
7.6	Final remarks	171
7.6	References	172
	Summary	177
	Samenvatting	181
	Acknowledgements	185
	Curriculum Vitae	189
	List of publications	191

1

Introduction

Viruses, as illustrated by the coronavirus pandemic, pose a significant risk to public health. The most effective approach for containing and eventually eradicating circulating viruses is vaccination. The eradication of smallpox in 1980, following large immunization programs, was the first major success in counteracting a virus of which the earliest descriptions date back to ancient Egypt, India and China¹. However, the virus is believed to date back to the time of the first settlements in northeastern Africa, 10,000 B.C.². To date, smallpox is the only human infective virus that has been declared fully eradicated³. However, the prevention of viral infection started far earlier, during the development of a process called variolation, the predecessor of vaccination.

The first records of counteractive measures against viruses date back to 1022 A.D., when a Buddhist monk living in a southern province of China wrote a book entitled 'the correct treatment of smallpox'. The book described the technique of variolation, which involved the deliberate inoculation with smallpox to generate immunity to the disease. According to historical records, the original method of variolation involved grinding up smallpox scabs and blowing the resulting powder directly into the nose of healthy individuals. This method was based on the observation that people who recovered from smallpox were immune to future infections. Over time, the technique was modified, and scabs were rubbed into small scratches made on the skin. This method was considered less risky than the nasal method, which could cause severe side effects. It needs to be noted that the term "variolation" refers specifically to the inoculation with smallpox (*Variola*) and should not be used to describe other virus-infection preventive measures. Despite initial resistance, variolation became a common approach against smallpox infection in Europe in the second half of the 18th century. However, this practice was replaced by the discovery of vaccination by dr. Edward Jenner. While working as an apprentice, Jenner received a notion from a dairy maid who claimed that she could not contract smallpox anymore because she had contracted cowpox, a much less severe and non-lethal virus that could be contracted from infected animals. Many dairy maids who were exposed to cowpox were found to be immune to smallpox, even during endemic periods through the 18th and 19th

centuries. Despite initial skepticism and opposition from the scientific communities in England and Germany, Jenner's experiments with cowpox inoculation eventually led to the development of the first smallpox vaccine, which was the first successful vaccine for any disease.

Jenner's discovery of the smallpox vaccine was a turning point in the history of infectious diseases. In his papers and books, Jenner coined the term "variole vaccinae" ("smallpox of the cow") and this is where the term vaccination originated. Despite the increased efficacy and safety of his vaccination over variolation, Jenner faced opposition from many high-society physicians and was branded by some as a charlatan. However, with the help of other physicians who viewed his research more favorably, Jenner continued to vaccinate people with cowpox with great success. His work, supported by increased statistics, was accepted on the European mainland relatively quickly, but took decades to convince Britain^{1,2,4,5}. Eventually, vaccination replaced variolation as the main protective measure against smallpox, and variolation became prohibited in Britain in 1840. Following major vaccination campaigns by the World Health Organization (WHO) in the 19th and 20th centuries, smallpox was declared eradicated in 1980. The technique developed by Jenner is fundamentally analogous to conventional vaccines developed throughout the 20th century and is now most commonly known as live (attenuated) vaccines⁶. Jenner's work laid the foundation for the development of vaccines against other infectious diseases, leading to the prevention of many different types of illnesses and saving countless lives.

1.1 Viruses

Viruses are the most abundant type of biological entity on earth, with an estimated 10^{31} active virions are present, equating to tens of millions of different types of viruses^{7,8}. Despite this vast number, only 5,000 types have been studied and described in detail^{9,10}. The origins of the study of viruses can be traced back to the late 1800s when a Russian botanist named Dmitri Ivanovsky observed that the sap of diseased tobacco plants, even after being filtered, remained capable of infecting new crops¹¹. While Ivanovsky initially believed that the infectious material was toxin secreted by bacteria, it was later discovered by the Dutch microbiologist Martinus Beijerinck that this infective material was a new form of infectious agent, which he opted "virus"¹². He was the first to observe that viruses could only sustain and multiply in dividing cells, a characteristic that sets them apart from other forms of life and has led to viruses being categorized as "organisms at the edge of life"^{13,14}.

In the extracellular environment, viruses exist as discrete particles called virions. These virions are composed of three basic components: the nucleocapsid, the genetic material (either RNA or DNA), and in some cases an outer envelope composed of lipids that surrounds the capsid. The classification system for viruses that is still in use today is

primarily based on the type of genome they possess (i.e., DNA, RNA, single strand (ss), double strand (ds), positive (+) or negative (-) sense), as well as the method they use for replication. In opposition to the conventional central dogma, many viruses use RNA, instead of DNA, as genetic information carrier¹⁵. RNA viruses are subdivided further based on the polarity of the RNA, either sense (positive (+)) or antisense (negative (-)). RNA is considered sense when its sequence can be directly translated to a protein, meaning that the viral RNA serves as messenger RNA (mRNA) in a eukaryotic cell. Some well-known (+)sense RNA viruses include SARS-CoV-2 and poliovirus. The (+)ssRNA viruses are classified into three orders: *Nidovirales*, *Tymovirales*, and *Picornavirales*. The *Picornavirales* (pico for small, rna for RNA, virales for viruses) contains families of viruses with specific characteristics, such as the ability to translate their genome RNA into a polyprotein, which is then in turn cut into mature viral proteins by one or several virus-encoded proteases. These viruses also contain a small protein, VPg (viral genome-linked protein), covalently attached to the 5' end, and store the genomic RNA in non-enveloped, icosahedral virion particles with a diameter of ~30 nm¹⁶. One of these families is the *Picornaviridae* comprising non-enveloped viruses that use vertebrates, including humans, as a natural host. One step further down in viral taxonomy yields our genus of interest: *Enterovirus*.

1.2 Enteroviruses

Enteroviruses, belonging to the *Enterovirus* genus within the *Picornaviridae* family, are transmitted through the fecal-oral route and can cause a range of symptoms upon infection, from mild respiratory illness to acute flaccid paralysis¹⁷. The *Enterovirus* genus includes various viruses, including poliovirus, enterovirus A71 (EV71), coxsackievirus A6 (CVA6), and coxsackievirus A16 (CVA16), among others. Although poliovirus is the most prevalent member, several viruses in this genus, particularly EV71, CVA6, and CVA16, are the primary cause of hand, foot, and mouth disease (HFMD). HFMD manifests a distinct set of symptoms, such as vesicles and lesions on the hands, feet, mouth, and buttocks. In most instances, the lesions resolve within a few weeks without scarring; however, in some cases, especially those caused by EV71, the disease can spread to the central nervous system, leading to severe complications like aseptic meningitis or encephalitis. Furthermore, prolonged infection can cause a cytokine storm that can exacerbate the damage to the heart and lungs. Children are most vulnerable to the severe symptoms due to their lack of immunity¹⁸. The major outbreaks of HFMD in Asia have made it one of the major public health concerns for the region^{19,20}. Apart from an inactivated EV71 vaccine, which does not confer cross-reactive immunity, protection against HFMD-causing viruses remains absent²¹. This is especially worrisome since enterovirus strains co-circulate, rendering the monovalent vaccination against EV71 insufficient to protect against HFMD.

Originally, the viruses of the *Enterovirus* genus were classified into four groups: polioviruses, coxsackievirus A viruses, coxsackie B viruses, and echoviruses. Upon discovery of new enterovirus strains, it was found that there was significant biological overlap between the different groups. To classify these viruses, genotyping of the VP1 capsid region was used. Furthermore, these newly discovered viruses were also given names using a system of consecutive numbers, such as EV-D68, EV-B69, EV-D70, EV-A71²². All members of this genus have a positive sense RNA genome of ~7.5 kbp (kilobase pairs), meaning that the RNA can be translated directly as mRNA. The genome consists of a 5' untranslated region (5' UTR), a single open reading frame, and a polyadenylated 3' UTR. For translation initiation of the polyprotein, an internal ribosomal entry site (IRES) is located in the 5' UTR²³. The open reading frame encodes a 260 kDa polyprotein that comprises three regions P1, P2, and P3^{23,24} (**Figure 1.1A**). P1 consists of the structural proteins, responsible for the capsid constructions. Post-translation, the polyprotein is modified by the host cell through addition of myristic acid, a process called myristylation. This modification makes the polyprotein a target for Hsp90, a chaperone protein of the host cell. After processing by the chaperone, P1 is stepwise cleaved into protein precursors, some of which exhibit specific functionalities like proteolytic activity, and finally into the 11 mature viral proteins²⁵.

The capsids of enteroviruses are composed of four viral proteins, namely VP1-VP4. Upon separation of the P1 region from the polyprotein and subsequent cleavage of the region using the 3CD precursor protein, protomers comprising VP0 (precursor VP2 and VP4), VP1, and VP3 will self-oligomerize into a pentamer (**Figure 1.1B**). Further self-assembly of twelve pentamers results in the formation of a the higher-order structure, known as the empty capsid or procapsid²⁶. In the last stage of viral maturation, VP0 is autocatalytically cleaved in the mature VP2 and VP4 proteins, yielding the infectious particle (virions)²⁷. Investigation of the *Enterovirus* viral capsid indicates that VP1-VP3 are situated on the outside of the capsid, whereas VP4 is located on the inside, in proximity to the RNA²⁸⁻³⁰. P2 and P3 harbor non-structural proteins, but apart from the previously mentioned 3CD protein are beyond the scope of this thesis.

The high mutation rate of enteroviruses within the *Enterovirus* genus can be attributed to the error-prone RNA-dependent RNA polymerase (RdRp or 3D protein). This is due to both misincorporation during replication and recombination events. The RdRp has a high transcription velocity and lacks a proof-reading mechanism, causing a high mutation rate of approximately 10^{-4} mutation per base per replication cycle³¹⁻³³. Because of this high mutation rate, the RdRp has been a target of interest for antiviral therapies³⁴. Post-infection, viral replication can be counteracted by increasing the mutation load on the viral genome (lethal mutagenesis). Additionally, through recombination more quasispecies arise, which can have significant alterations in pathogenicity³⁵. This evolution of recombinant enteroviruses may therefore potentially lead to new phenotypes or changes in severity of naturally occurring enterovirus-

associated diseases³⁶. Recombination is conceptualized through template-switching, in which the elongating RdRp switches from a donor to an acceptor template^{37,38}. The recombination rate of many enteroviruses was determined at 10^{-1} recombination events per replication, rendering recombination a key determinant of viral fitness and virulence³⁹⁻⁴².

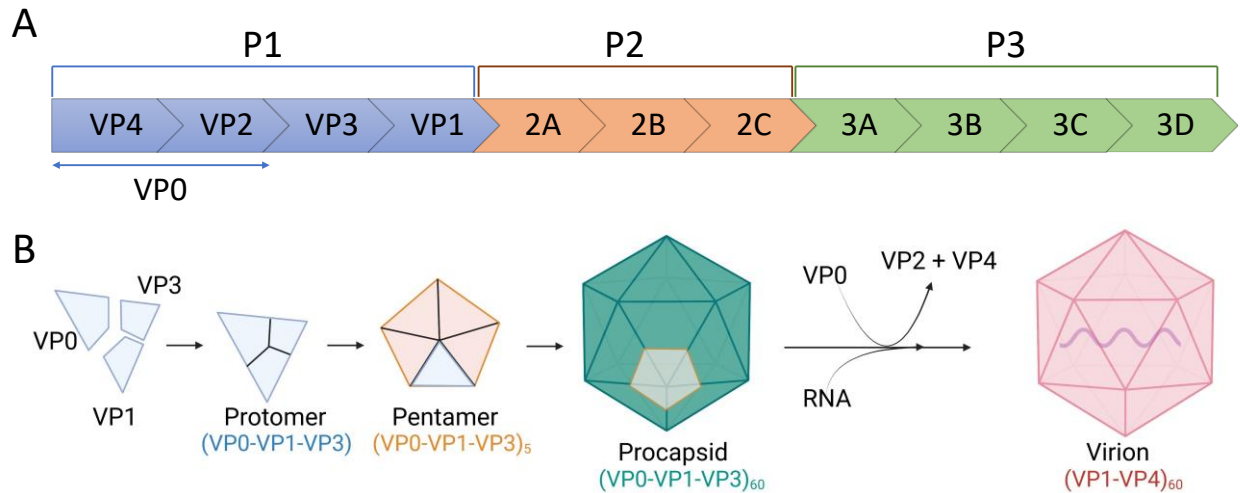


Figure 1.1. Enterovirus genome and morphogenesis.

(A) Enterovirus genome and its subsequent proteolytic cleavage into 11 mature proteins. P1 encodes the capsid proteins, P2 and P3 the non-structural, replication-associated proteins. (B) Enterovirus morphogenesis is a complex process involving self-assembly of viral proteins. Viral proteins VP0, VP1, and VP3, assemble into a protomer, and five protomers make up a pentamer. Twelve pentamers then assemble to form a procapsid (empty capsid). The final stage of viral maturation involves RNA-guided proteolytic cleavage of VP0 into VP2 and VP4, resulting in the formation of infectious virions. It needs to be noted that this model includes the hypothesis that the RNA enters the capsid in the last stage of viral maturation.

Since both recombination and the mutation rate are dictated by the RdRp, it is the dominant source of viral evolution. However, the mutations at the basis of viral evolution can also be deleterious, indicating the need for a precise balancing of the two. Despite significant efforts in the field, the underlying molecular mechanism of viral RNA transcription remains poorly understood.

1.3 Preventive measures against viruses

It is difficult to predict which virus will cause the next pandemic. Influenza has long been considered a likely candidate, with the potential for zoonotic transmission from birds or pigs⁴³. This is due in part to the observation that the rate of endemic outbreaks of influenza among animals has been increasing and that the influenza virus continues to circulate in many populations. Additionally, approximately 60% of the approximately 400 identified infectious diseases are zoonotic^{44,45}. In 2003, the SARS coronavirus outbreak in Asia prompted increased attention to viruses belonging to the *Coronaviridae* family as potential pandemic agents. As a result of increased preparedness efforts, authorities were able to act swiftly to contain the outbreak,

resulting in only 21% of the reported total number of cases and 11% of deaths worldwide occurring in the region, despite its population representing one-fifth of the world's population⁴⁶. Although these statistics indicated a relatively positive outcome, it highlighted the challenges in containing virus outbreaks, even with preparation for future pandemics. While predicting the specific virus that will cause the next pandemic is challenging, pandemics are not uncommon in human history. In fact, there have been several pandemics throughout history that were even more severe than COVID-19.

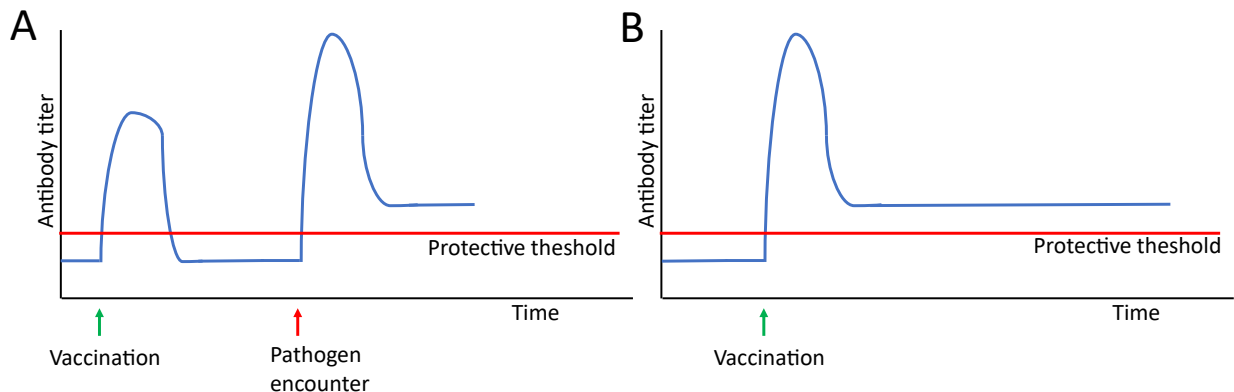


Figure 1.2. Immune memory in vaccine induced protection. Immune response is triggered by vaccine administration.

(A) The memory response (originating from the memory B cell) promoted production of T-cells (B) Vaccination provides protection by maintaining lifelong protective antibody levels.

Prophylactic vaccination is currently the most successful approach for preventing viral infections and epidemics. The principle of vaccination relies on the fact that initial recognition of a pathogen by the immune system is slow. Vaccines introduce weakened or inactivated parts of a pathogen (antigen) into the body, triggering an immune response. When the body is subsequently infected by the same pathogen, the immune system recognizes it and responds much faster, thus clearing the pathogen and protecting the patient from the disease. This immune memory response can be re-activated upon 2nd exposure to the pathogen (**Figure 1.2A**), or it can result in a long-lasting high antibody titer following vaccination (**Figure 1.2B**). An example of the former scenario is *Hepatitis B virus* (HBV). The vaccinated subject will still be protected against viral infection, despite the drop in antibody titers below the protective threshold. The incubation period of HBV ranges from 6 weeks to 6 months, providing the immune system with sufficient time to eliminate the virus. Generally, the first encounter with the pathogen following vaccination results in a faster and more robust immune response (**Figure 1.2A**)⁴⁷. An example of a vaccine that can induce decades-long antibody titer levels is the human papilloma virus vaccine⁴⁸. The rate of decreasing antibody levels depends on various factors, such as the age of the vaccine recipient, the antigen, and the number of booster doses administered. Despite the advantages of vaccination, there is a major downside to immune memory known as

original antigenic sin (Figure 1.3). This phenomenon occurs when a host is infected by a pathogen closely related to a previous one, and the immune system assumes that the two viruses are identical due to the highly similar or identical recessive antigen. However, another antigen on the virus particle has become dominant, and the immune system does not recognize it as a new pathogen. In turn the antibody response will be tailored towards the old (and now recessive) antigen and not the new dominant one. As a result, the immune response is much lower and possibly ineffective, exposing the patient to significant risks. Viruses such as SARS-CoV-2, influenza, and human immunodeficiency virus (HIV) use this phenomenon to evade immune responses^{49–52}.

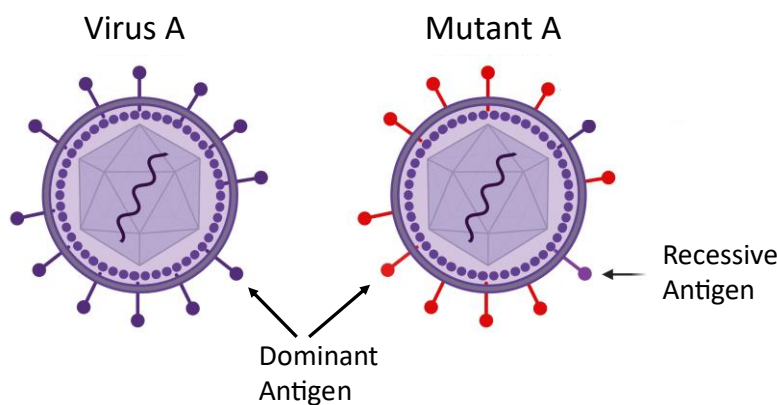


Figure 1.3. Original antigenic sin.

When a person is infected with virus A for the first time, their immune system produces antibodies against the dominant antigen (purple). If the person is infected with mutant A, which has a new dominant antigen (red) and maintains the original one as recessive antigen (purple), the immune system will still produce the former antibodies against the old (and now recessive) antigen. This can result in an ineffective antibody response and weak immunity against the new dominant antigen.

Conventional vaccines are classified into two main groups: the live attenuated vaccines, invented by Dr. Jenner, and the inactivated vaccines (Figure 1.4). Production of the latter, inactivated vaccines, involves the isolation of the active virions, followed by a process of inactivation that renders the particles incapable of infecting cells⁵³. This process typically involves crosslinking of the viral receptors using aldehydes such as formalin, as described in Salk's original paper on the poliovirus vaccine^{54,55}. For enteroviruses, heat inactivation can also be used. The principle underlying this method is the viral protein alteration yielding a structurally different particle. This heat-inactivated particle is unable to recognize, nor bind host cells, thus inhibiting replication of the virus. At temperatures above 60 °C, the viral genomic RNA also denatures, providing an additional safeguard for inactivated vaccines^{56,57}. Other forms of inactivation include, but are not limited to: use of solvents (destruction of the envelope), detergents (denaturation of proteins and other macromolecules), mild surfactants (breaking lipid-lipid and protein-lipid interactions), oxidizing agents (causing radical-mediated genomic damage), and UV radiation (inducing crosslinking between pyrimidines)^{53,58–62}. Unfortunately, inactivation of virus can be time-consuming procedure, with general WHO procedures ranging from 2-6 weeks for formalin inactivation^{53,63}. Consequently, the production process for inactivated vaccines is relatively expensive.

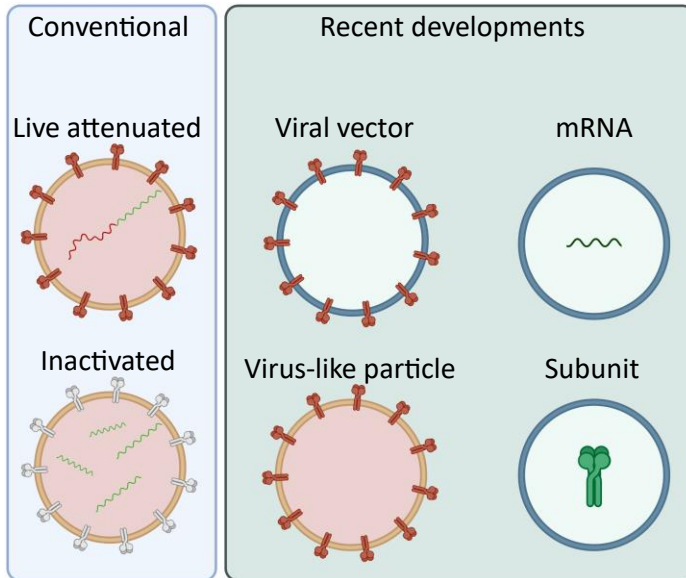


Figure 1.4. Overview of types of vaccines.

Conventional vaccines are either attenuated, reducing the reproducibility rate of the virus through genomic alteration (green RNA), or inactivated, thus preventing them from infecting cells. The newer types of vaccines comprise of viral vectors and mRNA vaccines both exemplified by the success of COVID-19 vaccines. Additionally, some protein vaccines are being investigated or in clinical trials using just a subunit of the virus particle. The last described category is the virus-like particles which resemble the native virions but lack the infectious and replicating RNA/DNA.

The conventional alternative to inactivated vaccines was the live attenuated vaccines. These vaccines confer protection by inoculating with a live virus that has been weakened through genetic alteration, or by inoculation with another virus that offers cross-protective immunity. The latter scenario is exemplified by the cow- and smallpox scenarios described above and is therefore not classified by some as an attenuated vaccine. In the former scenario is the more classical way of approaching live attenuated vaccines, in which a subject is inoculated with a small amount of the (weakened) virus, to stimulate an immune response. Classic examples of live attenuated vaccines include smallpox, measles, poliovirus, yellow fever, rotavirus, and mumps. The poliovirus vaccine based on this type of vaccination was developed by Albert Sabin in the 1950s and has been in use since the 1960s^{64,65}. Unfortunately, viruses, particularly enteroviruses, can mutate rapidly (described in section 1.2). This means that poliovirus can revert to an active form of the virus through a process called reversion, giving rise to disease^{66,67}. This is known as circulating vaccine-derived poliovirus (cVDPV)⁶⁸. The possibility of reversion, alongside the concern of possible integration of the viral DNA in the host cell's DNA, are among the limiting factors of live attenuated vaccines. Despite these downsides, live attenuated vaccines are more likely to cause lifelong protection, as was exemplified with yellow fever⁶⁹. Furthermore, because of the reduced production process time, the production cost of this vaccine is approximately five times lower than its inactivated counterpart, and it can be administered orally⁷⁰.

The recent SARS-CoV-2 (COVID-19) pandemic has led to the emergence of two new classes of vaccines: viral vector and mRNA vaccines (**Figure 1.4**). Viral vector vaccines were already in development prior to the pandemic and were first approved for human use against flaviviruses and ebolavirus in 2010 and 2015, respectively⁷¹. The approach uses a replication-defective, nonenveloped virus, conventionally adenovirus vectors, as a delivery system for the genetic instructions underlying a specific antigen,

in the case of COVID-19 the spike (S) glycoprotein (or just S protein or “spike protein”). The genetic information undergoes transcription in the nucleus of the host cell, leading to the formation of mRNA. Subsequently, this mRNA is transported to the cytoplasm, where it is translated into the spike protein. The spike protein is then presented by the cell to the immune system, initiating a cascade of events that leads to immunity to the disease⁷². This method is much safer than using live attenuated vaccines since it eliminates the use of an infective disease-causing agent. However, vector-associated phenomena have been identified as a concern. Many individuals have been infected with adenoviruses at some point in their life and have memory cells against the virus. Following high dose second infection (the vaccination), the patient may develop an immune response to the vector instead of the antigen presented by the vector. As a result, the pathogen is cleared from the body before immunity to the antigen is achieved. Moreover, repeated vaccinations using the same vector may face similar obstacles⁷³.

In contrast to viral vector vaccines, mRNA vaccines utilize synthetic mRNA that encodes an antigen (e.g., the spike protein for SARS-CoV-2) for immunization (**Figure 1.4**). *In vitro* translation of mRNA has been achieved in the late 1960s, and over the past two decades, it has primarily been researched for cancer therapeutic^{74,75}. However, it was not until the COVID-19 pandemic that mRNA technology gained widespread appeal. Once inside the host cell, the mRNA is taken up and used by the cell to produce the viral protein. The mRNA vaccines mimic a conventional viral infection, but contain a shorter RNA fragment, that only codes for the spike protein. A main advantage of mRNA vaccines is their safety, resulting from the absence of viral agents in the vaccine production process and the lack of reversion possibilities in a host. Additionally, the process is less time-consuming, since there is no need to produce large quantities of viruses. Unfortunately, a limitation of mRNA vaccines is the amount of RNA that can be included; for COVID-19, only the coding sequence for the spike protein was necessary to elicit an immune response. If multiple proteins are required, this could pose a challenge. Moreover, mRNA (and RNA in general) is relatively unstable and requires storage and transportation on dry ice to ensure its efficacy during the vaccination process⁷⁶.

It is crucial to address the side effects of vaccinations. Side effects such as fever, headache, fatigue, and pain at the injection site are not uncommon following vaccination, as the immune response triggered by the vaccine takes a toll on the body’s physiology⁷⁷. Fever is a natural response of the body to combat bacterial or viral infections by elevating the body temperature⁷⁸. Vaccination side effects are investigated for each vaccine independently and monitored for years after first administration in phase IV clinical trials for new vaccine market entries^{79,80}. However, a false notion still circulates among a portion of the population, particularly in anti-vax groups, that vaccines cause autism. It is important to state that this argument is baseless. It was mainly based on the discredited work of dr. Andrew Wakefield, who

claimed that the measles, mumps, and rubella (MMR) vaccine caused autism in 8 out of 12 children in his study^{81,82}. However, it was later found that Wakefield's study was unethical, and his results were falsified. The sample size was exceptionally small, the children were selected by Wakefield himself, and the study was partially funded by lawyers who were suing vaccine manufacturers⁸³. Numerous scientific studies have since refuted any connection between MMR and autism. Nevertheless, Wakefield's ideas have created widespread public hesitancy towards vaccination, leading to a spike in 2008 and a drop in vaccination coverage⁸⁴⁻⁸⁹. While vaccination coverage has since rebounded, the false claims made by Wakefield have had long-lasting and damaging effects.

Most vaccine development efforts have primarily focused on protecting individuals from infection. However, an essential aspect of eradicating a virus is the concept of herd immunity. There are various reasons why some individuals in a population may not receive vaccines, such as religious or personal beliefs or being immunodeficient. Nonetheless, if a sufficient proportion of the population is vaccinated, those who are unvaccinated can still be protected. This protection is obtained by decreasing the chances of person-to-person transmission of the pathogen since the vaccinated individuals are less likely to become infected, and thus less likely to spread the virus. The percentage of the population that needs to be vaccinated to achieve herd immunity is pathogen-dependent, ranging from 95%, for highly transmissible pathogens such as measles, to 80% for less transmissible pathogens like poliovirus^{90,91}. As a trade-off, herd immunity decreases the likelihood of natural boosting of vaccinated individuals, thus possibly causing waning of antibody titers in individuals.

1.4 Virus-like particles

Virus-like particles (VLPs) are multimeric nanoparticle self-assemblies that derive from one or more viral structures. By design, VLPs are hypothesized to be void of genetic material, rendering them non-replicative and non-infective. Despite the lack of genetic material, their surface structure resembles the immune-inducing patterns from the native virus, enabling them to be recognized by the immune system^{92,93}. This feature can be exploited for vaccine purposes. VLPs can bridge problems encountered with previously mentioned types of vaccines. Recognition of many viruses, including many enteroviruses, by the adaptive immune system does not depend on a single protein. To ensure proper recognition, an arrangement of VP2 and VP3 has to be detected⁹⁴. In turn this means (partial) viral capsid assembly is vital, which would be exceedingly complex to mimic using mRNA, subunit, or vector vaccine technology.

The safety and efficacy of VLP-based vaccines have been established. The first VLP vaccine against *Hepatitis B virus* dates back to 1986. The current market has several VLP vaccines available, with the HPV VLP vaccines (e.g., Gardasil and Cervarix) being the

most prominent having a dominant market share. Additionally, several VLP vaccines against other viruses are currently in clinical trials. Moreover, the HPV VLP vaccine is currently the standard of care for HPV-induced cervical cancer prevention^{48,95}.

Empty capsid structures like the artificially created VLPs are not a novel phenomenon *in vivo*. EV71 for example, produces a decoy effect using these *in vivo* produced empty capsids. The more loosely associated capsids, usually empty, more readily bind antibodies, and therefore allow the tightly associated capsids, which usually contain viral RNA, to circulate more freely⁹⁶. Evidence suggests that this behavior is similar to the C-antigen and D-antigen of poliovirus, where the rarer, more tightly packed D-antigen contains infectious RNA, while the more abundant, more loosely packed C-antigen is usually empty⁹⁷⁻¹⁰⁰.

Due to the necessity of Hsp90 and highly regulated post-translational modifications to form EV71 VLPs in the correct native configuration (see section 1.2), a eukaryotic expression system is required for their production. The baculovirus expression vector system (BEVS) has been shown to be suitable for *Enterovirus* VLP production and was selected for our application^{29,101-106}. However, there are major differences between the *Enterovirus* VLPs and the virions. It is hypothesized that the VLPs do not have any RNA in the particles, which has implications for particle stability, structure, and viral maturation. The RNA itself can be a stabilizer for the particles. Additionally, the final step in the virion maturation process, the cleaving of VP0 into VP2 and VP4, is hypothesized to be regulated by the RNA, thus should not occur making the VLPs distinctively different from their native counterpart. Recent studies exhibited that the VLPs have more resemblance with the procapsids than the mature virion (**Figure 1.1B**), which could possibly be detrimental for the immunogenicity^{107,108}. Fortunately, preclinical animal studies on *Enterovirus* VLPs indicated protective immune responses for VLPs^{95,103,104,109-114}. In this work we will investigate the differences in stability between VLPs and virions, and investigate the origin of possible differences.

Virus-like particles are highly diverse regarding structure and functionality. They can have repeats of a single or multiple viral proteins, be enveloped, be antigen presenting, or packaging nucleic acid or proteins¹¹⁵⁻¹¹⁹. Detailed and informative reviews have been written, describing additional functionalities and enhanced characteristics with time^{92,93,120-123}.

1.5 Baculoviruses

It sounds counterintuitive, but using a virus to exclude another virus in the production process to increase safety can be an advantageous approach. The baculovirus expression vector system, which exploits *Baculoviridae* (baculovirus or BacV) to produce viruses or (viral) proteins, has a narrow host range. Although they can enter mammalian cells, they are not pathogenic to humans, nor can they replicate in these types of cells¹²⁴. For proliferation, they are restricted to infecting invertebrate species, specifically *Lepidoptera Hymenoptera* and *Diptera* orders. Therefore, these viruses can be used and stored with minimal containment procedures. Because BacV infects only higher-order organisms (insect cells), post-translational modifications, required for correct folding of a significant number of proteins, can be performed. Baculoviruses are rod-shaped (250-300 nm in length), enveloped, DNA viruses. In nature, they occur either as occlusion-derived or budded viruses. The former is present in a protein matrix, polyhedrin, mostly designed to protect the virus from the environment of the insect gut, where the first infection occurs. The latter is responsible for spreading infection from cell to cell within the same organism¹²⁵. Baculoviruses have a double-stranded, circular genome of 80-180 kbp, depending on the species¹²⁶. Furthermore, the genome contains 100-200 open reading frames (ORFs), which differentiate significantly. Only 38 ORFs are conserved throughout all baculoviruses; the polyhedrin gene is one of them.

To ensure high expression of the protein of interest, the coding sequence for the polyhedrin protein is replaced by that of the target protein, while the polyhedrin promoter is remained in place¹²⁷. Once the baculovirus has infected the insect cell, the genome is uncoated in the nucleus of the host cell, where it is transcribed by the host's polymerase. Viral proteins, including a DNA polymerase, are synthesized, and assemble progeny genomes. Baculovirus infection is considered late stage when viral DNA synthesis by the viral polymerase has begun, alongside the transcription of structural proteins. Viral particle assembly can occur in both the nucleus or the cytoplasm of the infected cell and is dependent on the nuclear envelope's integrity. In the last stage of the baculovirus cycle, the mature virions are encapsulated in a new polyhedrin matrix, and the occlusion-derived virus are released after cell death¹²⁵.

In addition to safety, there are many advantages to using the BEVS. First, there are manufacturing advantages i) easy to scale-up, thus lower cost, ii) the possibility to build multi-purpose facilities that produce more than one product using this technology. Secondly, the use of recombinant technologies, employed in the BEVS, allows for flexible product design and an opportunity to fast adaptation of the vector if required. In turn, this will allow fast response to endemic outbreaks or even pandemics. Lastly, regulatory advantages: a single cell line is required for multiple products, and products produced using the BEVS have already been licensed worldwide, setting precedence for the future products¹²⁸.

1.6 Biophysical techniques

The biophysical characterization of the VLPs, virions, and RdRp, was performed using multiple techniques. Since the technical background of these techniques is considerable, a synopsis is presented here.

1.6.1 Atomic force microscopy

Atomic force microscopy (AFM) is a type of microscopy that can achieve resolution in the order of fractions of a nanometer, surpassing the optical diffraction limit by more than 1,000 times. AFM operates by physically examining the surface using a mechanical probe (cantilever containing a sharp tip), enabling the collection of information about the surface topography. Precise scanning is facilitated by piezoelectric elements that enable accurate and precise movements upon electronic command¹²⁹. AFM has three major abilities: force measurements, topographic imaging, and manipulation. Firstly, AFM is commonly employed for force measurements, as they can precisely measure the forces between the sample and probe while varying their distance. Secondly, AFM can be utilized for high-resolution imaging of a sample's 3D surface topography by monitoring the probe's response to the forces exerted by the sample (**Figure 1.5A**). This is accomplished by raster scanning the sample's position relative to the tip and recording the height of the probe, which corresponds to a consistent probe-sample interaction (**Figure 1.5B**). Lastly, AFM is exploited to manipulate and alter the properties of a sample in a controlled manner by utilizing the forces that can be asserted by the tip on the sample (**Figure 1.5A**). In this work, we used the latter two techniques to image and manipulate virus-like particles^{130,131}.

The use of AFM over other microscopy techniques such as electron microscopy (EM) offers several advantages: i) AFM provides high-resolution 3D images instead of 2D projections or images, ii) no sample treatment, thus minimizing the risk of sample damage or alteration, iii) measurements can be performed in a liquid environment, important for studying biological processes, iv) following dynamics of biological samples in over time.

While AFM has many advantages, it also has its limitations, including: i) spatial dimensions. The scanning area is typically in the order of hundreds of micrometers and a maximum height of the sample of ~20 μm , both significantly lower than other forms of microscopy, ii) the AFM scans can take minutes. Although high-speed AFMs have been developed, they cannot match the (near) real-time measurements of an EM, iii) imaging artifacts can originate from tip of the instrument. Contamination of the tip with proteins in solution is not uncommon and difficult to avoid^{130,132}.

In this thesis, we employ AFM to manipulate particles and determine their mechanical properties by applying forces up to 5 nN using the cantilever. Our primary objective is to discern mechanical differences “empty” VLPs and the RNA-filled virions, and

potentially identify the underlying source of these distinctions. Furthermore, we examined discrepancies in virus origins within the same genus.

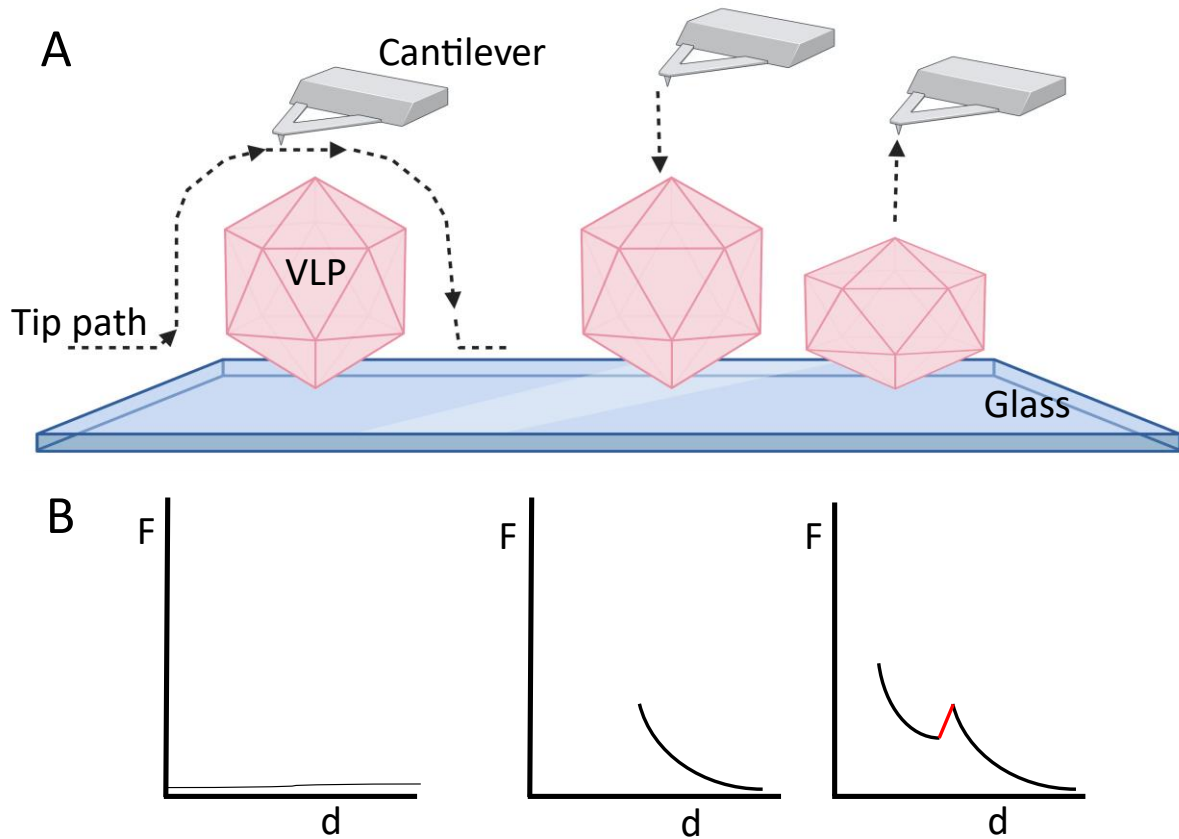


Figure 1.5. Schematic representation of AFM imaging and manipulation.

Dotted lines represent the cantilever's movement. (A) During the imaging experiments, the force is maintained at a constant value and the cantilever will start scanning a surface. When it encounters a structure the force increases, and the cantilever adjusts accordingly. The same process occurs in reverse as the cantilever moves away from the structure. During the nanoindentation, the cantilever approaches the particle whose location was previously determined and starts applying force, until a set threshold is reached. (B) Force curves corresponding to the scenarios presented above. During imaging (left) the force remains constant. During the nanoindentation the force will increase, up until the particle breaks (red line), and will continue to increase thereafter until the set threshold is reached.

1.6.2 Electron microscopy

Electron microscopy is regarded as one of the most powerful imaging techniques. It involves the use of a beam of electrons as a source of illumination instead of photons, as in light microscopy. The advantage of using electrons over photons originates from the shorter wavelength of the former. The shorter wavelength allows for much higher resolution, as light microscopy is limited by the wavelength of light. State-of-the-art EMs have reached magnifications up to 10,000,000 times with a resolution of 50 pm, which is significantly better than the 2,000 times magnification and 200 nm resolution

for light microscopes¹³³. EMs use magnetic fields in a similar fashion to light microscopes use lenses. There are several modes of operation in electron microscopy, including transmission electron microscopy (TEM), scanning electron microscopy (SEM), and scanning transmission electron microscopy (STEM). In TEM, a high voltage electron beam is transmitted through a thin sample, producing a 2D image (Figure 1.6). In SEM, the sample is scanned with a focused electron beam, and the scattered electrons are detected to form a 3D image. In STEM, a focused electron beam is scanned over a thin sample, and the transmitted electrons are detected to form a high-resolution image (Figure 1.6).

There are various sample preparation techniques for EM imaging, each with its own advantages and drawbacks. In this study, we employed two methods: negative stain and cryofixation (cryo-EM). The former uses an electron-opaque solution (e.g., uranyl acetate) to blot the sample on the grids and fix them for imaging. The use of negative staining is employed extensively as it allows for rapid, albeit crude, morphological identification of microorganisms. Cryo-EM is often used to preserve the native characteristics of biological samples by rapidly freezing the sample, thus keeping it in its soluble state^{134,135}.

The electron microscope offers unparalleled resolution; however, this technique has limitations too. The requirement for the samples to be measured in vacuum can lead to the creation of artifacts or negatively impact the sample. Moreover, sample preparation, particularly for biological samples or when employing cryo-EM, can be a time-consuming process.

Here, we employed TEM to firstly identify the presence of VLPs and the purity of samples, using negative staining as a means of direct observation (in contrast to indirect observations such as western blot). Secondly, we used cryo-EM to reconstitute the VLP structure and compare them to the virion structures to identify differences and potentially uncover the origin of stabilizing structure features.

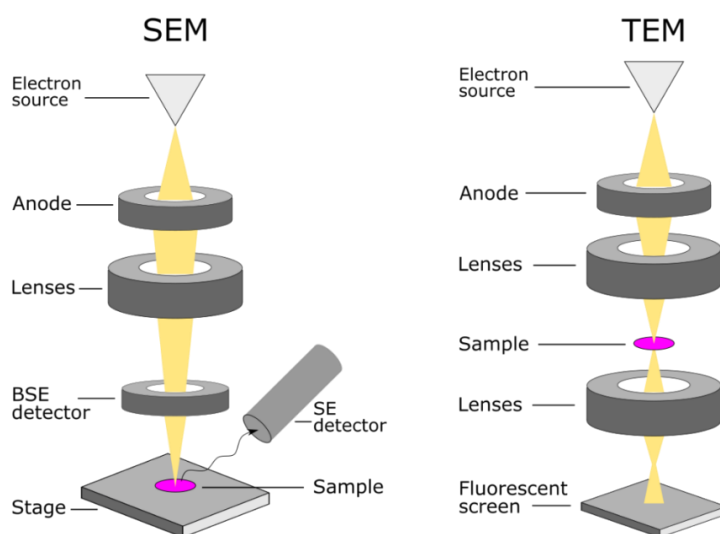


Figure 1.6. Schematic representation of scanning electron microscopy versus transmission electron microscopy. Image obtained from REF¹⁴⁰.

(Left) SEM, the sample is scanned with a focused electron beam, and the scattered electrons are detected to form a 3D image. BSE: back-scattered electron. SE: secondary electron. (Right) TEM, a high voltage electron beam is transmitted through a thin sample, producing a 2D image.

1.6.3 Magnetic tweezers

Despite their apparent simplicity in comparison to AFM and EM, magnetic tweezers (MT) provide a powerful tool within the single-molecule field. MT allows for quantitative analysis of force-dependent mechanisms of biological processes¹³⁶. Additionally, the MT provide a high spatial resolution, enabling the discovery of biomolecules' molecular mechanisms¹³⁷. A typical MT set-up consists of a flow cell, magnetic pair, light emitting diode (LED), camera, objective, piezo, and analysis software (Figure 1.7). The light travels through a gap in the magnets to the flow cell mounted below, where it will encounter the magnetic beads. The light is reflected and incidents with the incoming light, creating a diffraction pattern. The diffraction pattern is observed by the camera and matched to a constructed calibration profile (lookup-table or LUT), yielding the absolute z-position¹³⁸. To ensure shifts in z-position of beads originating from thermal and mechanical noise are corrected for, surface-attached reference bead positions are subtracted from all tracked magnetic bead positions¹³⁹. Real-time tracking of up to 350 tethers in a single experiment enables the analysis of the mechanical properties of biomolecules and facilitates the discovery of underlying molecular mechanisms.

Due to the aforementioned benefits, we employed the MT technique for the real-time tracking of hundreds of RNA replication events by the RNA-dependent RNA polymerase (RdRp). This enabled us not only to identify the polymerase-specific pausing, but also to evaluate the efficacy of polymerase-targeted antivirals. The MT provides a large number of statistics, enabling quick screening, while maintaining a high spatial resolution.

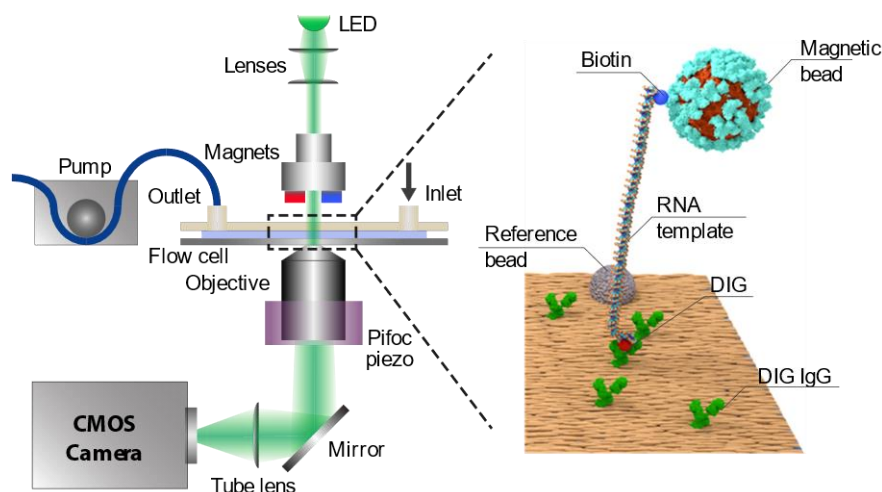


Figure 1.7. Schematic of the MT and flow cell configuration for MT assay

(Left) General overview of the MT setup: light originating from an LED travels through the gap between the magnets, illuminates the flow cell, and is captured by the objective. The images are reflected to and recorded by a CMOS camera and analyzed with custom-written software to determine the x, y and z positions of the magnetic beads in real time¹³⁸. The outlet of the flow cell holder is connected to a suction pump. (Right) Experimental representation of tethering the RNA to a flow cell to investigate RNA-binding protein dynamics.

1.7 Thesis outline & research questions

Chapter 2 introduces a machine learning (ML) model, that was trained, validated, and tested for the classification of live and dead insect cells using the dye exclusion method. It presents a faster, cheaper, and bias-free alternative to manual and automated cell counting. We tested two insect cell lines with cell densities ranging from 5 to over 300 cells/field of view. We also investigated the versatility of the model by applying it to a distinct eukaryotic cell line, HEK cells.

Chapter 3 describes the optimization of production and purification of virus-like particles (VLPs). Through application of Design of Experiments, the interplay of culturing conditions, such as multiplicity of infection, infection period, and the cell density at the time of infection were optimized to maximize VLP production (upstream processing or USP). Additionally, a purification process (downstream processing or DSP) was developed to ensure a high purity of the final samples. The protocols presented in this chapter demonstrate the interdisciplinary nature of the work in this research, lending biochemical techniques for virology research with a final application in biophysics.

The VLPs produced using the optimized protocols described in Chapter 3, were subjected to biophysical characterization in **Chapter 4**. Here, we present multiple biophysical techniques such as transmission electron microscopy and atomic force microscopy, to elucidate the origins of the reduced VLP stability in comparison to native virions. This chapter is an exemplification of the collaborative work in this thesis, bringing multiple groups, people from distinctive backgrounds, and biophysical techniques together to solve some of the questions related to VLPs.

In **Chapter 5** a detailed protocol is presented for simultaneously probing the RNA synthesis dynamics of hundreds of single polymerases with magnetic tweezers (MT). The protocol describes the process from preparation of the RNA constructs to analysis, quantification, and statistical analysis of the MT measurements of RNA synthesis kinetics. Here the step-by-step process is detailed for measurements resulting in the characterization of single-molecule dynamics presented in the subsequent chapter.

Chapter 6 describes the power of magnetic tweezers (MT) for the mechanistic characterization of the viral RNA-dependent RNA polymerase (RdRp). Each viral polymerase has its own mechanistic properties in the form of pause dynamics and probabilities, which can be deciphered using MT. Moreover, the results presented in this chapter indicate that the use of antivirals targeting the template switching of the RdRp is a viable approach with broad-spectrum appeal. Antivirals, in opposition to the prophylactic approaches (e.g., vaccination), come into play post infection and are therefore a logical successor of the previous work mentioned in Chapter 1-5. Here, we demonstrated that magnetic tweezers could scan promising candidates and indicate the most propitious one.

Lastly, **Chapter 7** summarizes the main conclusions of this work. It ties the different chapters together and presents some concluding remarks. Additionally, it presents an outlook into the future of VLPs and possible advances of the BEVS. Moreover, it presents the hurdles to overcome and opportunities for investigation or exploitation of both technologies to realize their full potential.

1.8 References

1. Behbehani AM. The smallpox story: Life and death of an old disease. *Microbiol Rev.* 1983;47(4):455-509. doi:10.1128/membr.47.4.455-509.1983
2. Riedel S. Edward Jenner and the History of Smallpox and Vaccination. *Baylor Univ Med Cent Proc.* 2005;18(1):21-25. doi:10.1080/08998280.2005.11928028
3. *Plotkin's Vaccines.*; 2018. doi:10.1016/c2013-0-18914-3
4. Stern AM, Markel H. The History Of Vaccines And Immunization: Familiar Patterns, New Challenges. *Health Aff.* 2005;24(3):611-621. doi:10.1377/hlthaff.24.3.611
5. Greenwood B. The contribution of vaccination to global health: Past, present and future. *Philos Trans R Soc B Biol Sci.* 2014;369(1645). doi:10.1098/rstb.2013.0433
6. Plotkin S. History of vaccination. *Proc Natl Acad Sci U S A.* 2014;111(34):12283-12287. doi:10.1073/pnas.1400472111
7. Breitbart M, Rohwer F. Here a virus, there a virus, everywhere the same virus? *Trends Microbiol.* 2005;13(6):278-284. doi:10.1016/j.tim.2005.04.003
8. Edwards, R.A. Rogwer F. Viral metagenomics. *Nat Rev Microbiol.* 2005;3.
9. Mushegian AR. Are there 10³¹ virus particles on earth, or more, or fewer? *J Bacteriol.* 2020;202(9):18-22. doi:10.1128/JB.00052-20
10. Hendrix RW, Smith MCM, Burns RN, Ford ME, Hatfull GF. Evolutionary relationships among diverse bacteriophages and prophages: All the world's a phage. *Proc Natl Acad Sci U S A.* 1999;96(5):2192-2197. doi:10.1073/pnas.96.5.2192
11. Iwanowski U. Über die Mosaikkrankheit der Tabakspflanze Author. *Verlag Eugen Ulmer.* 1903;13(1):1-41. <https://www.jstor.org/stable/43221892>
12. Beijerinck M. Ueber ein Contagium vivum fluidum als Ursaehe der Fleckenkrankheit der Tabaksblätter. *Verh der K Akad van Wet te Amsterdam.* 1898;6(5):3-21. <http://www.dwc.knaw.nl/DL/publications/PU00011860.pdf>
13. Rybicki EP. The classification of organisms at the edge of life, or problems with virus systematics. *S Afr J Sci.* 1990;86:182-186.
14. Baltimore D. Expression of animal virus genomes. *Bacteriol Rev.* 1971;35(3):235-241.
15. Crick FH. On protein synthesis. In: *Symposia of the Society for Experimental Biology.* Vol 12. ; 1958:138-163. doi:10.1038/227561a0

16. King AMQ, Adams MJ, Carsten EB, Lefkowitz EJ. *Virus Taxonomy: Classification and Nomenclature of Viruses. Ninth Report of the International Committee on Taxonomy of Viruses.*; 2012. doi:10.1007/s13398-014-0173-7.2
17. Tesini B. Overview of Enterovirus Infections. Merck. Published 2021. Accessed February 20, 2023. <https://www.merckmanuals.com/professional/infectious-diseases/enteroviruses/overview-of-enterovirus-infections>
18. Ventarola D, Bordone L, Silverberg N. Update on hand-foot-and-mouth disease. *Clin Dermatol.* 2015;33(3):340-346. doi:10.1016/j.clindermatol.2014.12.011
19. Anh NT, Nhu LNT, Van HMT, et al. Emerging coxsackievirus A6 causing hand, foot and mouth disease, Vietnam. *Emerg Infect Dis.* 2018;24(4):654-662. doi:10.3201/eid2404.171298
20. Liu H, Zhang M, Feng C, et al. Characterization of Coxsackievirus A6 Strains Isolated From Children With Hand, Foot, and Mouth Disease. *Front Cell Infect Microbiol.* 2021;11(August):1-11. doi:10.3389/fcimb.2021.700191
21. Aswathyraj S, Arunkumar G, Alidjinou EK, Hober D. Hand, foot and mouth disease (HFMD): emerging epidemiology and the need for a vaccine strategy. *Med Microbiol Immunol.* 2016;205(5):397-407. doi:10.1007/s00430-016-0465-y
22. Oberste MS, Maher K, Kilpatrick DR, Pallansch MA. Molecular Evolution of the Human Enteroviruses: Correlation of Serotype with VP1 Sequence and Application to Picornavirus Classification. *J Virol.* 1999;73(3):1941-1948. doi:10.1128/jvi.73.3.1941-1948.1999
23. Pelletier J, Sonenberg N. Internal initiation of translation of eukaryotic mRNA directed by a sequence derived from poliovirus RNA. *Nature.* 1988;334(6180):320-325. doi:10.1038/334320a0
24. Wang J, Fan T, Yao X, et al. Crystal Structures of Enterovirus 71 3C Protease Complexed with Rupintrivir Reveal the Roles of Catalytically Important Residues. *J Virol.* 2011;85(19):10021-10030. doi:10.1128/JVI.05107-11
25. Jiang P, Liu Y, Ma HC, Paul A V., Wimmer E. Picornavirus Morphogenesis. *Microbiol Mol Biol Rev.* Published online 2014. doi:10.1128/MMBR.00012-14
26. Ansardi DC, Porter DC, Morrow CD. Coinfection with recombinant vaccinia viruses expressing *Poliovirus* P1 and P3 proteins results in polyprotein processing and formation of empty capsid structures. *J Virol.* 1991;65(4):2088-2092. <http://www.pubmedcentral.nih.gov/articlerender.fcgi?artid=240068&tool=pmcentrez&rendertype=abstract>
27. Hindiyeh M, Li QH, Basavappa R, Hogle JM, Chow M. Poliovirus mutants at histidine 195 of VP2 do not cleave VP0 into VP2 and VP4. *J Virol.* 1999;73(11):9072-9079.
28. Muckelbauer JK, Kremer M, Minor I, et al. The structure of coxsackievirus B3 at 3.5 Å resolution. *Structure.* 1995;3(7):653-667. doi:10.1016/S0969-2126(01)00201-5

29. Gong M, Zhu H, Zhou J, et al. Cryo-Electron Microscopy Study of Insect Cell-Expressed Enterovirus 71 and Coxsackievirus A16 Virus-Like Particles Provides a Structural Basis for Vaccine Development. *J Virol.* 2014;88(11):6444-6452. doi:10.1128/jvi.00200-14
30. Ren J, Wang X, Zhu L, et al. Structures of Coxsackievirus A16 Capsids with Native Antigenicity: Implications for Particle Expansion, Receptor Binding, and Immunogenicity. *J Virol.* Published online 2015. doi:10.1128/JVI.01102-15
31. Li L, He Y, Yang H, et al. Genetic characteristics of human enterovirus 71 and coxsackievirus A16 circulating from 1999 to 2004 in Shenzhen, People's Republic of China. *J Clin Microbiol.* 2005;43(8):3835-3839. doi:10.1128/JCM.43.8.3835-3839.2005
32. Jiang H, Weng L, Zhang N, et al. Biochemical characterization of enterovirus 71 3D RNA polymerase. *Biochim Biophys Acta - Gene Regul Mech.* 2011;1809(3):211-219. doi:10.1016/j.bbagr.2011.01.001
33. Steinhauer DA, Domingo E, Holland JJ. Lack of evidence for proofreading mechanisms associated with an RNA virus polymerase. *Gene.* 1992;122(2):281-288. doi:10.1016/0378-1119(92)90216-C
34. Tsai CH, Lee PY, Stollar V, Li ML. Antiviral Therapy Targeting Viral Polymerase. *Curr Pharm Des.* 2006;12(11). doi:10.2174/138161206776361156
35. Harvala H, Kalimo H, Bergelson J, Stanway G, Hyypiä T. Tissue tropism of recombinant coxsackieviruses in an adult mouse model. *J Gen Virol.* 2005;86(7):1897-1907. doi:10.1099/vir.0.80603-0
36. Simmonds P, Welch J. Frequency and dynamics of recombination within different species of human enteroviruses. *J Virol.* 2006;80(1):483-493. doi:10.1128/JVI.80.1.483-493.2006
37. Kirkegaard K, Baltimore D. The mechanism of RNA recombination in poliovirus. *Cell.* 1986;47(3):433-443. doi:10.1016/0092-8674(86)90600-8
38. Arnold JJ, Cameron CE. Poliovirus RNA-dependent RNA polymerase (3D(pol)) is sufficient for template switching in vitro. *J Biol Chem.* 1999;274(5):2706-2716. doi:10.1074/jbc.274.5.2706
39. Runckel C, Westesson O, Andino R, DeRisi JL. Identification and Manipulation of the Molecular Determinants Influencing Poliovirus Recombination. *PLoS Pathog.* 2013;9(2). doi:10.1371/journal.ppat.1003164
40. Brown B a, Oberste MS, Alexander JP, Kennett ML, Pallansch M a. Molecular epidemiology and evolution of enterovirus 71 strains isolated from 1970 to 1998. *J Virol.* 1999;73(12):9969-9975. doi:10.1007/s11434-007-0215-z
41. Martín J, Dunn G, Hull R, Patel V, Minor PD. Evolution of the Sabin strain of type 3 poliovirus in an immunodeficient patient during the entire 637-day period of virus excretion. *J Virol.* 2000;74(7):3001-3010. doi:10.1128/JVI.74.7.3001-3010.2000
42. Takeda, N. Tanimura, M Miyamura K. Molecular evolution of the major capsid protein

- VP1 of enterovirus 70. *J Virol.* 1994;68(2):854-862.
43. Morse SS, Mazet JAK, Woolhouse M, et al. Prediction and prevention of the next pandemic zoonosis. *Lancet.* 2012;380(9857):1956-1965. doi:10.1016/S0140-6736(12)61684-5
 44. Karesh WB, Dobson A, Lloyd-Smith JO, et al. Ecology of zoonoses: Natural and unnatural histories. *Lancet.* 2012;380(9857):1936-1945. doi:10.1016/S0140-6736(12)61678-X
 45. Lycett SJ, Duchatel F, Digard P. A brief history of bird flu. *Philos Trans R Soc B Biol Sci.* 2019;374(1775):0-3. doi:10.1098/rstb.2018.0257
 46. Babu GR, Khetrupal S, John DA, Deepa R, Narayan KMV. Pandemic preparedness and response to COVID-19 in South Asian countries. *Int J Infect Dis.* 2021;104:169-174. doi:10.1016/j.ijid.2020.12.048
 47. Henry B, Baclic O. Summary of the NACI Update on the Recommended Use of Hepatitis B Vaccine. *Canada Commun Dis Rep.* 2017;43(5):104-106. doi:10.14745/ccdr.v43i05a04
 48. Deleré Y, Wichmann O, Klug SJ, et al. The efficacy and duration of vaccine protection against human papillomavirus. *Dtsch Arztebl Int.* 2014;111(35-36). doi:10.3238/arztebl.2014.0584
 49. Focosi D, Genoni A, Lucenteforte E, et al. Previous humoral immunity to the endemic seasonal alphacoronaviruses NL63 and 229E is associated with worse clinical outcome in COVID-19 and suggests original antigenic sin. *Life.* 2021;11(4). doi:10.3390/life11040298
 50. Pollard AJ, Bijker EM. A guide to vaccinology: from basic principles to new developments. *Nat Rev Immunol.* 2021;21(2):83-100. doi:10.1038/s41577-020-00479-7
 51. Singh RAK, Rodgers JR, Barry MA. The Role of T Cell Antagonism and Original Antigenic Sin in Genetic Immunization. *J Immunol.* 2002;169(12):6779-6786. doi:10.4049/jimmunol.169.12.6779
 52. Kim JH, Skountzou I, Compans R, Jacob J. Original Antigenic Sin Responses to Influenza Viruses. *J Immunol.* 2009;183(5):3294-3301. doi:10.4049/jimmunol.0900398
 53. Elveborg S, Monteil VM, Mirazimi A. Methods of Inactivation of Highly Pathogenic Viruses for Molecular, Serology or Vaccine Development Purposes. *Pathogens.* 2022;11(2):1-25. doi:10.3390/pathogens11020271
 54. Salk JE. Considerations in the preparation and use of poliomyelitis virus vaccine. *J Am Med Assoc.* 1955;158(14). doi:10.1001/jama.1955.02960140001001
 55. Martín J, Crossland G, Wood DJ, Minor PD. Characterization of formaldehyde-inactivated poliovirus preparations made from live-attenuated strains. *J Gen Virol.* 2003;84(7):1781-1788. doi:10.1099/vir.0.19088-0
 56. Mitchell SW, McCormick JB. Physicochemical inactivation of Lassa, Ebola, and Marburg viruses and effect on clinical laboratory analyses. *J Clin Microbiol.* 1984;20(3):486-489.

- doi:10.1128/jcm.20.3.486-489.1984
57. Woodroffe GM. The heat inactivation of vaccinia virus. *Virology*. 1960;10(3):379-382. doi:10.1016/0042-6822(60)90031-3
 58. Amanna IJ, Raué HP, Slifka MK. Development of a new hydrogen peroxide-based vaccine platform. *Nat Med*. 2012;18(6). doi:10.1038/nm.2763
 59. Roberts PL. Virus inactivation by solvent/detergent treatment using Triton X-100 in a high purity factor VIII. *Biologicals*. 2008;36(5). doi:10.1016/j.biologicals.2008.06.002
 60. Kraus AA, Priemer C, Heider H, Krüger DH, Ulrich R. Inactivation of hantaan virus-containing samples for subsequent investigations outside biosafety level 3 facilities. *Intervirology*. 2005;48(4). doi:10.1159/000084603
 61. Johnson M. Detergents: Triton X-100, Tween-20, and More. *Mater Methods*. 2013;3. doi:10.13070/mm.en.3.163
 62. Lawrence RM, Zook JD, Hogue BG. Full inactivation of alphaviruses in single particle and crystallized forms. *J Virol Methods*. 2016;236. doi:10.1016/j.jviromet.2016.07.020
 63. PAHO. General Procedures for Inactivation of Potentially Infectious Samples With Ebola. Published online 2014:1-6.
 64. Minor PD. Live attenuated vaccines: Historical successes and current challenges. *Virology*. 2015;479-480:379-392. doi:10.1016/j.virol.2015.03.032
 65. Sabin AB. Pathogenesis of Poliomyelitis Reappraisal in the Light of New Data. *Science (80-)*. 1956;123(3209). doi:10.1126/science.123.3209.1151
 66. Burns CC, Diop OM, Sutter RW, Kew OM. Vaccine-derived polioviruses. *J Infect Dis*. 2014;210(Suppl 1):S283-S293. doi:10.1093/infdis/jiu295
 67. Alleman MM, Jorba J, Greene SA, et al. Update on Vaccine-Derived Poliovirus Outbreaks — Worldwide, July 2019–February 2020. *MMWR Morb Mortal Wkly Rep*. 2020;69(16):489-495. doi:10.15585/mmwr.mm6916a1
 68. Minor P. Vaccine-derived poliovirus (VDPV): Impact on poliomyelitis eradication. *Vaccine*. 2009;27(20):2649-2652. doi:10.1016/j.vaccine.2009.02.071
 69. Report WHO. Vaccines and vaccination against yellow fever: WHO Position Paper, June 2013-Recommendations. *Vaccine*. 2015;33(1):76-77. doi:10.1016/j.vaccine.2014.05.040
 70. Initiative GPE. IPV. Accessed February 15, 2023. <https://polioeradication.org/polio-today/polio-prevention/the-vaccines/ipv/#:~:text=IPV is over five times,sterile injection equipment and procedures.>
 71. McCann N, O'Connor D, Lambe T, Pollard AJ. Viral vector vaccines. *Curr Opin Immunol*. 2022;77(Figure 1):102210. doi:10.1016/j.coi.2022.102210
 72. García-Montero C, Fraile-Martínez O, Bravo C, et al. An updated review of sars-cov-2 vaccines and the importance of effective vaccination programs in pandemic times.

- Vaccines*. 2021;9(5). doi:10.3390/vaccines9050433
73. Kremer EJ. Pros and Cons of Adenovirus-Based SARS-CoV-2 Vaccines. *Mol Ther*. 2020;28(11):2303-2304. doi:10.1016/j.ymthe.2020.10.002
 74. Lockard RE, Lingrel JB. The synthesis of mouse hemoglobin chains in a rabbit reticulocyte cell-free system programmed with mouse reticulocyte 9S RNA. *Biochem Biophys Res Commun*. 1969;37(2). doi:10.1016/0006-291X(69)90720-7
 75. Beck JD, Reidenbach D, Salomon N, et al. mRNA therapeutics in cancer immunotherapy. *Mol Cancer*. 2021;20(1). doi:10.1186/s12943-021-01348-0
 76. Nguyen KV. Problems associated with antiviral drugs and vaccines development for COVID-19: approach to intervention using expression vectors via GPI anchor. *Nucleosides, Nucleotides and Nucleic Acids*. 2021;40(6):665-706. doi:10.1080/15257770.2021.1914851
 77. CDC. Possible Side Effects After Getting a COVID-19 Vaccine. Published 2022. Accessed February 20, 2023. <https://www.cdc.gov/coronavirus/2019-ncov/vaccines/expect/after.html>
 78. Mackowiak PA. Concepts of fever. *Arch Intern Med*. 1998;158(17):1870-1881. doi:10.1001/archinte.158.17.1870
 79. FDA. The Drug Development Process. Published 2018. Accessed February 20, 2023. <https://www.fda.gov/patients/learn-about-drug-and-device-approvals/drug-development-process>
 80. Riad A, Hocková B, Kantorová L, et al. Side effects of mRNA-based COVID-19 vaccine: Nationwide phase IV study among healthcare workers in Slovakia. *Pharmaceuticals*. 2021;14(9):1-24. doi:10.3390/ph14090873
 81. Wakefield AJ, Murch SH, Anthony A, et al. Retracted: Ileal-lymphoid-nodular hyperplasia, non-specific colitis, and pervasive developmental disorder in children. *Lancet*. 1998;351(9103):637-641. doi:10.1016/S0140-6736(97)11096-0
 82. Editors T. Retraction-Ileal-lymphoid-nodular hyperplasia, non-specific colitis, and pervasive developmental disorder in children. *Lancet*. 2010;375(9713):445. doi:10.1016/S0140-6736(10)60175-4
 83. Eggertson L. Lancet retracts 12-year-old article linking autism to MMR vaccines. *CMAJ*. 2010;182(4):199-200. doi:10.1503/cmaj.109-3179
 84. DeStefano F, Shimabukuro TT. The MMR Vaccine and Autism. *Annu Rev Virol*. 2019;6:585-600. doi:10.1146/annurev-virology-092818-015515
 85. Taylor LE, Swerdfeger AL, Eslick GD. Vaccines are not associated with autism: An evidence-based meta-analysis of case-control and cohort studies. *Vaccine*. 2014;32(29):3623-3629. doi:10.1016/j.vaccine.2014.04.085
 86. England TN. Number 19 Vaccination and Autism. 2010;347(19):1477-1482.

87. *Immunization Safety Review.*; 2001. doi:10.17226/10101
88. *Immunization Safety Review.*; 2004. doi:10.17226/10997
89. Stratton K, Ford A, Rusch E, Clayton EW. *Adverse Effects of Vaccines: Evidence and Causality.*; 2012. doi:10.17226/13164
90. Plans-Rubió P. Are the objectives proposed by the who for routine measles vaccination coverage and population measles immunity sufficient to achieve measles elimination from europe? *Vaccines.* 2020;8(2). doi:10.3390/vaccines8020218
91. Lai YA, Chen X, Kunasekaran M, Rahman B, MacIntyre CR. Global epidemiology of vaccine-derived poliovirus 2016–2021: A descriptive analysis and retrospective case-control study. *eClinicalMedicine.* 2022;50:101508. doi:10.1016/j.eclinm.2022.101508
92. Qian C, Liu X, Xu Q, et al. Recent progress on the versatility of virus-like particles. *Vaccines.* 2020;8(1):1-14. doi:10.3390/vaccines8010139
93. Tariq H, Batool S, Asif S, Ali M, Abbasi BH. Virus-Like Particles: Revolutionary Platforms for Developing Vaccines Against Emerging Infectious Diseases. *Front Microbiol.* 2022;12(January). doi:10.3389/fmicb.2021.790121
94. Tan S, Tan X, Sun X, et al. VP2 Dominated CD4+ T Cell Responses against Enterovirus 71 and Cross-Reactivity against Coxsackievirus A16 and Polioviruses in a Healthy Population. *J Immunol.* 2013;191(4):1637-1647. doi:10.4049/jimmunol.1301439
95. Schiller J, Lowy D. Explanations for the high potency of HPV prophylactic vaccines. *Vaccine.* 2018.
96. Shingler KL, Cifuentes JO, Ashley RE, Hafenstein S, Makhov AM, Conway JF. The Enterovirus 71 Procapsid Binds Neutralizing Antibodies and Rescues Virus Infection In Vitro. *J Virol.* Published online 2014. doi:10.1128/jvi.03098-14
97. Adeyemi OO, Nicol C, Stonehouse NJ, Rowlands DJ. Increasing Type 1 Poliovirus Capsid Stability by Thermal Selection. *J Virol.* Published online 2016. doi:10.1128/jvi.01586-16
98. Jore JPM, Veldhuisen G, Pouwels PH, Boeye LA, Vrijzen R, Rombaut B. Formation of subviral particles by in vitro translation of subgenomic poliovirus RNAs. *J Gen Virol.* Published online 1991. doi:10.1099/0022-1317-72-11-2721
99. J. P. M. JORE, G. VELDHUISEN, M. KOTTENHAGEN, P. H. POUWELS, A. FORIERS BRombaut, BOEYE AA. Formation of Poliomyelitis Subviral Particles in the Yeast *Saccharomyces cerevisiae.* *Yeast.* 1994;10:907-922.
100. Rombaut B, Jore JPM. Immunogenic, non-infectious polio subviral particles synthesized in *Saccharomyces cerevisiae.* *J Gen Virol.* Published online 1997. doi:10.1099/0022-1317-78-8-1829
101. Chung Y chi, Huang J huang, Lai C wei, et al. Expression, purification and characterization of enterovirus-71 virus-like particles. 2006;12(6):921-927.

102. Chung CY, Chen CY, Lin SY, et al. Enterovirus 71 virus-like particle vaccine: Improved production conditions for enhanced yield. *Vaccine*. 2010;28(43):6951-6957. doi:10.1016/j.vaccine.2010.08.052
103. Zhang W, Dai W, Zhang C, et al. A virus-like particle-based tetravalent vaccine for hand, foot, and mouth disease elicits broad and balanced protective immunity article. *Emerg Microbes Infect*. 2018;7(1). doi:10.1038/s41426-018-0094-1
104. Kim, HJ Son, HS Lee, SW Yoon, Y Hyeon, JY Gyung, TC Lee JYJ. Efficient expression of enterovirus 71 based on virus-like particles vaccine. *PLoS One*. 2019;14(3). doi:10.1371/journal.pone.0210477
105. Koho T, Koivunen MRL, Oikarinen S, et al. Coxsackievirus B3 VLPs purified by ion exchange chromatography elicit strong immune responses in mice. *Antiviral Res*. Published online 2014. doi:10.1016/j.antiviral.2014.01.013
106. Shih-Yeh Lin a , Li-Yu Sung a , Chia-Tsui Yeh b , c , Cheng-Ping Yu b , d , Jyh-Yuan Yang e YCH. Production and purification of virus-like particles of different enterovirus subtypes as vaccines. *J Taiwan Inst Chem Eng*. 2018;82:1-9.
107. Xu Y, Ma S, Huang Y, et al. Virus-like particle vaccines for poliovirus types 1, 2, and 3 with enhanced thermostability expressed in insect cells. *Vaccine*. Published online 2019. doi:10.1016/j.vaccine.2019.03.031
108. Xu L, Zheng Q, Li S, et al. Atomic structures of Coxsackievirus A6 and its complex with a neutralizing antibody. *Nat Commun*. 2017;8(1):1-12. doi:10.1038/s41467-017-00477-9
109. Lin SY, Sung LY, Yeh CT, Yu CP, Yang JY, Hu YC. Production and purification of virus-like particles of different enterovirus subtypes as vaccines. *J Taiwan Inst Chem Eng*. 2018;82:1-9. doi:10.1016/j.jtice.2017.10.020
110. Wang X, Xiao X, Zhao M, et al. EV71 virus-like particles produced by co-expression of capsid proteins in yeast cells elicit humoral protective response against EV71 lethal challenge Microbiology. *BMC Res Notes*. 2016;9(1):1-9. doi:10.1186/s13104-015-1780-x
111. Lin YL, Yu CI, Hu YC, et al. Enterovirus type 71 neutralizing antibodies in the serum of macaque monkeys immunized with EV71 virus-like particles. *Vaccine*. 2012;30(7):1305-1312. doi:10.1016/j.vaccine.2011.12.081
112. Dai W, Zhang C, Zhang X, et al. A virus-like particle vaccine confers protection against enterovirus D68 lethal challenge in mice. *Vaccine*. 2018;36(5):653-659. doi:10.1016/j.vaccine.2017.12.057
113. Zhou Y, Zhang C, Liu Q, Gong S, Geng L, Huang Z. A virus-like particle vaccine protects mice against coxsackievirus A10 lethal infection. *Antiviral Res*. 2018;152(February):124-130. doi:10.1016/j.antiviral.2018.02.016
114. Zhang N, Zheng T, Chen Y, et al. Coxsackievirus B5 virus-like particle vaccine exhibits greater immunogenicity and immunoprotection than its inactivated counterpart in mice. *Vaccine*. 2021;39(39):5699-5705. doi:10.1016/j.vaccine.2021.07.095

115. Whitacre DC, Lee BO, Milich DR. Use of hepadnavirus core proteins as vaccine platforms. *Expert Rev Vaccines*. 2009;8(11). doi:10.1586/erv.09.121
116. Porta C, Kotecha A, Burman A, et al. Rational Engineering of Recombinant Picornavirus Capsids to Produce Safe, Protective Vaccine Antigen. *PLoS Pathog*. 2013;9(3). doi:10.1371/journal.ppat.1003255
117. Pushko P, Pearce MB, Ahmad A, et al. Influenza virus-like particle can accommodate multiple subtypes of hemagglutinin and protect from multiple influenza types and subtypes. *Vaccine*. 2011;29(35). doi:10.1016/j.vaccine.2011.06.068
118. Kato S, Kobayashi K, Inoue KI, et al. A lentiviral strategy for highly efficient retrograde gene transfer by pseudotyping with fusion envelope glycoprotein. *Hum Gene Ther*. 2011;22(2). doi:10.1089/hum.2009.179
119. Kawano M, Matsui M, Handa H. SV40 virus-like particles as an effective delivery system and its application to a vaccine carrier. *Expert Rev Vaccines*. 2013;12(2). doi:10.1586/erv.12.149
120. Lua LHL, Connors NK, Sainsbury F, Chuan YP, Wibowo N, Middelberg APJ. Bioengineering virus-like particles as vaccines. *Biotechnol Bioeng*. Published online 2014. doi:10.1002/bit.25159
121. Kushnir N, Streatfield SJ, Yusibov V. Virus-like particles as a highly efficient vaccine platform: Diversity of targets and production systems and advances in clinical development. *Vaccine*. Published online 2012. doi:10.1016/j.vaccine.2012.10.083
122. Mona O. Mohsena, Lisha Zha, Gustavo Cabral-Mirandaa MFB. Major findings and recent advances in virus-like particle (VLP)-based vaccines. *Semin Immunol*. 2017;34:123-132.
123. Fuenmayor J, Gòdia F, Cervera L. Production of virus-like particles for vaccines. *N Biotechnol*. Published online 2017. doi:10.1016/j.nbt.2017.07.010
124. Hofmann C, Sandig V, Jennings G, Rudolph M, Schlag P, Strauss M. Efficient gene transfer into human hepatocytes by baculovirus vectors. *Proc Natl Acad Sci U S A*. 1995;92(22):10099-10103. doi:10.1073/pnas.92.22.10099
125. Harrison RL, Herniou EA, Jehle JA, et al. ICTV virus taxonomy profile: Baculoviridae. *J Gen Virol*. 2018;99(9):1185-1186. doi:10.1099/jgv.0.001107
126. van Oers M, Vlak J. Baculovirus Genomics. *Curr Drug Targets*. 2007;8(10). doi:10.2174/138945007782151333
127. van Oers MM. Opportunities and challenges for the baculovirus expression system. *J Invertebr Pathol*. 2011;107(SUPPL.):S3-S15. doi:10.1016/j.jip.2011.05.001
128. Felberbaum RS. The baculovirus expression vector system: A commercial manufacturing platform for viral vaccines and gene therapy vectors. *Biotechnol J*. 2015;10(5):702-714. doi:10.1002/biot.201400438
129. Ohnesorge F, Binnig G. True atomic resolution by atomic force microscopy through

- repulsive and attractive forces. *Science* (80-). 1993;260(5113):1451-1456. doi:10.1126/science.260.5113.1451
130. *Encyclopedia of Biophysics.*; 2013. doi:10.1007/978-3-642-16712-6
131. Roos WH. How to perform a nanoindentation experiment on a virus. *Methods Mol Biol.* 2011;783. doi:10.1007/978-1-61779-282-3_14
132. Ando T. High-speed atomic force microscopy. *Curr Opin Chem Biol.* 2019;51:105-112. doi:10.1016/j.cbpa.2019.05.010
133. Erni R, Rossell MD, Kisielowski C, Dahmen U. Atomic-resolution imaging with a sub-50-pm electron probe. *Phys Rev Lett.* 2009;102(9):1-4. doi:10.1103/PhysRevLett.102.096101
134. Dubochet J, McDowell AW. VITRIFICATION OF PURE WATER FOR ELECTRON MICROSCOPY. *J Microsc.* 1981;124(3). doi:10.1111/j.1365-2818.1981.tb02483.x
135. Adrian M, Dubochet J, Lepault J, McDowell AW. Cryo-electron microscopy of viruses. *Nature.* 1984;308(5954):32-36. doi:10.1038/308032a0
136. Neuman KC, Nagy A. Single-molecule force spectroscopy: optical tweezers, magnetic tweezers and atomic force microscopy. *Nat Methods.* 2008;5(6):491-505. doi:10.1038/nmeth.1218
137. Dulin D, Cui TJ, Cnossen J, Docter MW, Lipfert J, Dekker NH. High Spatiotemporal-Resolution Magnetic Tweezers: Calibration and Applications for DNA Dynamics. *Biophys J.* 2015;109(10):2113-2125. doi:10.1016/j.bpj.2015.10.018
138. Cnossen JP, Dulin D, Dekker NH. An optimized software framework for real-time, high-throughput tracking of spherical beads. *Rev Sci Instrum.* 2014;85(10). doi:10.1063/1.4898178
139. Vilfan ID, Lipfert J, Koster DA, Lemay SG, Dekker NH. Magnetic Tweezers for Single-Molecule Experiments. In: *Handbook of Single-Molecule Biophysics.* ; 2009:371-395. doi:10.1007/978-0-387-76497-9_13
140. AnaPath. Electron microscopy. Accessed February 22, 2023. <https://anapath.ch/electron-microscopy-2/>

2

Automated cell counting for Trypan blue-stained cell cultures using machine learning

*Cell counting is a vital practice in the maintenance and manipulation of cell cultures. It is a crucial aspect of assessing cell viability and determining proliferation rates, which are integral to maintaining the health and functionality of a culture. Additionally, it is critical for establishing the time of infection in bioreactors and monitoring cell culture response to targeted infection over time. However, when cell counting is performed manually, the time involved can become substantial, particularly when multiple cultures need to be handled in parallel. Automated cell counters, which enable significant time reduction, are commercially available but remain relatively expensive. Here, we present a machine learning (ML) model based on YOLOv4 that is able to perform cell counts with a high accuracy (>95%) for Trypan blue-stained insect cells. Images of two distinctly different cell lines, *Trichoplusia ni* (High Five™; Hi5 cells) and *Spodoptera frugiperda* (Sf9), were used for training, validation, and testing of the model. The ML model yielded F1 scores of 0.97 and 0.96 for alive and dead cells, respectively, which represents a substantially improved performance over that of other cell counters. Furthermore, the ML model is versatile, as an F1 score of 0.96 was also obtained on images of Trypan blue-stained human embryonic kidney (HEK) cells that the model had not been trained on. Our implementation of the ML model comes with a straightforward user interface and can image in batches, which makes it highly suitable for the evaluation of multiple parallel cultures (e.g. in Design of Experiments). Overall, this approach for accurate classification of cells provides a fast, bias-free alternative to manual counting.*

2.1 Introduction

Protein expression is traditionally performed using bacterial cells (most prominently *E.coli*) or their eukaryotic counterpart, yeast cells¹⁻³. Among the advantages presented by these expression platforms are their ease-of-use, fast growth, high yields, relative simplicity of required safety measures, extensive knowledge base, feasible induction of expression, and wealth of commercially available tools for handling and analysis^{1,4}. Unfortunately, protein expression via these organisms also comes with limitations, including the number of proteins that can be expressed simultaneously, the variance in the expression levels of the individual proteins that derives from different promoters, the lack of secretion of larger proteins resulting in increased purification efforts as cell disruption is required, potential species-specific differences in RNA splicing, and a lack of (or dissimilarity in) post-translational modifications⁵. The latter two limitations can be problematic when yielding proteins that vary from their native counterparts, which in turn can be detrimental for our understanding of the intricate biological systems in higher-order organisms.

For these reasons, many research groups consider the alternative baculovirus expression vector system (BEVS) for protein purification. In this system, the baculovirus infects the higher-order eukaryotic insect cells and transform them into expression platforms for its viral proteins. This viral protein expression can be exploited by inserting into the baculovirus backbone the coding sequences for proteins of interest⁶. Once the insect cells are infected, these proteins of interest are produced in high concentrations⁷. Amongst others, the advantages of this expression platform include the ease of culturing insect cells in a broader range of conditions than animal cells, the expression of multiple proteins (>20 proteins) on the same baculovirus vector under the same promoter, the narrow host range of baculovirus limiting the biological restriction levels, the cGMP classification, and the post-translational modifications (PTMs) closely mimicking human ones⁸. Additionally, the BEVS can leave the activity of proteins and - in most cases - immunogenicity (for virus) intact^{9,10}.

Rather than attempting to mimic PTMs using the BEVS, a human cell line such as human embryonic kidney (HEK) cells can be employed for the production of recombinant proteins such as antibodies, growth factors, and viral vectors. At present, for the production of these complex biomolecules Chinese hamster ovary (CHO) cells have become the standard expression system¹¹. However, due to the HEK cell line's high transfectivity, rapid growth rate, and ability to grow serum-free, as well as its capability to perform human-like PTMs accurately, it presents itself as a promising alternative to CHO cells for specific biopharmaceutical products^{12,13}.

To maximize the protein expression using the BEVS or HEK cells, maintaining the cell culture in a viable state is critical¹⁴. Conventional determination of alive and intact dead cell concentrations is performed using a hemocytometer (e.g. Bürker-Türk counting chamber)¹⁵. The chamber consists of nine squared wells, each with a set

volume, and is placed under a brightfield microscope (Figure 2.1). Dividing the total cell count by the total volume of the counted large squares yields the cell density. To enhance the accuracy of counting, dye exclusion methods are used to assess whether a cell is alive or dead: because dead cells lose membrane integrity, dye can traverse the membrane, staining dead cells in a distinctive color¹⁶. The most commonly used dye for insect cells is Trypan blue¹⁷. The major advantage of this conventional approach is the direct observation of the cell culture by the operator, which enables the rapid detection of problems such as contamination or aggregation of cells. However, manual cell counting is time-consuming, especially when a multiple counts are performed on the same culture for increased accuracy. Additionally, because this technique relies on human interpretation, operator-to-operator variance is not uncommon. Lastly, the reproducibility of manual cell counts can be low, especially if high cell density cultures are used¹⁸.

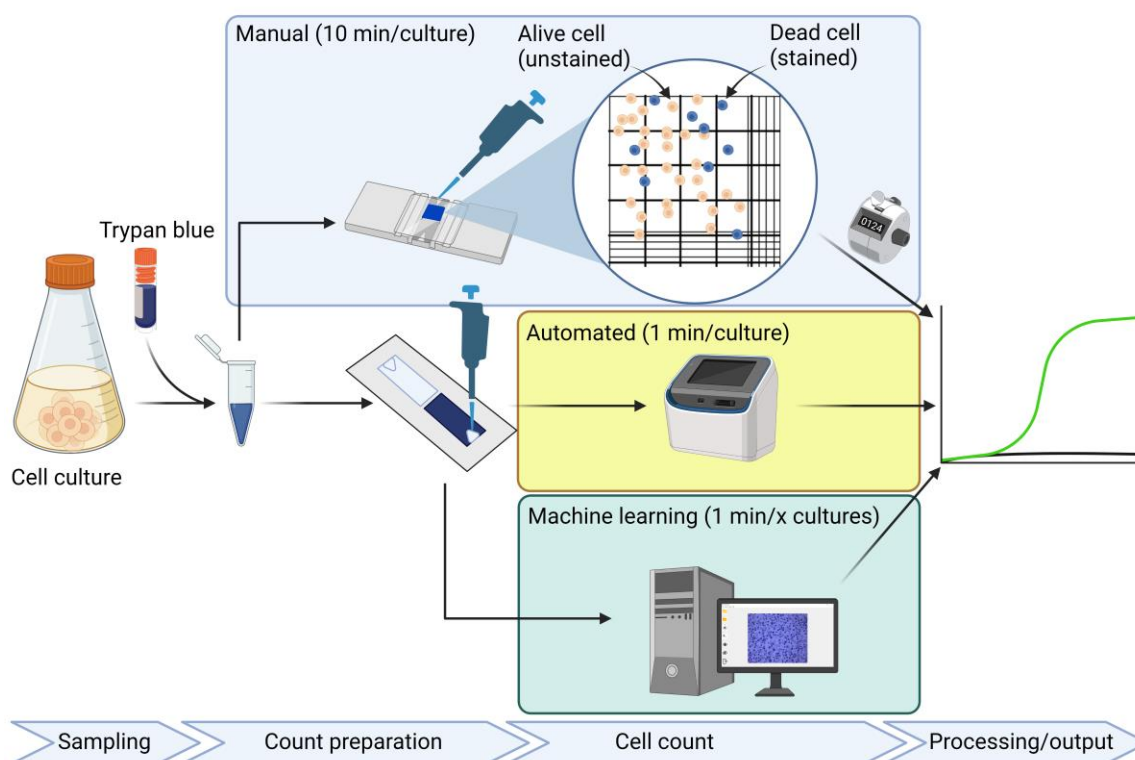


Figure 2.1. Overview of the most commonly used techniques for cell counting.

In cell counting, one exploits the difference in membrane integrity between alive (membrane intact, no staining of the cell interior; thus cell observed as white) and dead cells (membrane damaged, allowing Trypan blue to traverse the membrane; thus cell observed as blue). Tracking alive cell density over time then allows one to establish the growth curve of the cell culture. Conventional cell counting (depicted in light blue box) using a counting chamber represents a time-consuming protocol susceptible to significant operator-to-operator variance. Automated cell counters (depicted in yellow box) significantly reduce the operation time, at the expense of a loss of direct observation of the cell culture by the operator and a high investment cost. Our ML model for cell counting (depicted in green box) provides the operator with a cell counting approach of low investment cost that is rapid and accurate, and permits both the direct observation of cell culture and the opportunity to perform cell counts on infected cultures.

Some of the human errors inherent in conventional cell counting approaches can be avoided using automated cell counters (**Figure 2.1**). Many research groups have transitioned to this more reproducible and less time-consuming technique^{19–24}. Unfortunately, at present this technology comes with its own limitations. For example, the majority of the slides used for automated cell counts contain open experimental handling, meaning that they cannot be applied to infected cultures. Moreover, new automated cell counters range in price from €5,000 to €25,000, creating considerable investment cost for R&D labs²⁵. This holds especially true for research groups keen to explore the BEVS as a possibility for specific protein expression but not yet committed to the technology in the longer term. Lastly, the automated cell counters based on BF-microscopy can have a significant error range, particularly, when cells are aggregated or cultures reach high cell densities.

It needs to be noted that the accuracy of manual and automated cell counting techniques based on cell phenotype increases when the sample is derived from cultures exhibiting low levels of cell lysis. These techniques only take into account alive and intact dead cells, and therefore cannot determine the degree of cell lysis. Any extent of cell lysis will necessitate further evaluation, such as through the measurement of lactate dehydrogenase levels²⁶.

Here, we have developed a machine learning (ML) model based on the publicly available YOLOv4 model, together with a user-friendly interface, for the determination of dead and alive insect cells²⁷. Our aim was to maximize the accuracy with an error margin of at most 5%. ML models have significant advantages over other automated cell counting software packages (e.g. ImageJ). Firstly, a good ML model makes manual image (pre-)processing obsolete^{19,21}. Secondly, enabling batch image processing could reduce significantly overall process time in the evaluation of multiple cultures (e.g. during Design of Experiments) (**Figure 2.1**). Such advantages have been deployed in the counting of red blood cells; however, to date an appropriate model for the counting of insect cells remains lacking^{23,28,29}.

2.2 Results & Discussion

To verify that the ML model was accurate for a broad range of Trypan blue-stained cell images, we tested the model on a large data set containing different cell strains, cell densities, and viabilities. The model was tested using a data set of 122 images (66 images from Hi5 cell cultures and 56 images from Sf9 cell cultures) containing 20,046 cells. The majority of the images were captured successively and in a single experimental procedure at 10X magnification, then batch processed by the ML model. The model classified cells as either alive or dead and assigned them blue or red bounding boxes, respectively (**Figure 2.2**). The post-processing thresholds for the confidence interval, intersection over union, and bounding box size (see section Post-

processing) were set to 0.3, 0.3, and 25 px², respectively. These post-processing thresholds, which were optimized by visual inspection, were dependent on cell fitness and density, as well as on microscope settings such as the magnification. Based on visual inspection we could determine that the model was able to identify the presence of the majority of the cells and classify them correctly. Furthermore, the model did not classify as cells any of the cell debris and/or protein aggregation that was visible as small blue dots (**Figure 2.2B**), thus obviating additional manual image processing. Relative to previously reported automated cell counting models, which depended on conventional image processing to eliminate such contaminants, the ML model was fast and reduced the overall process time for cell count determination^{19-21,30}.

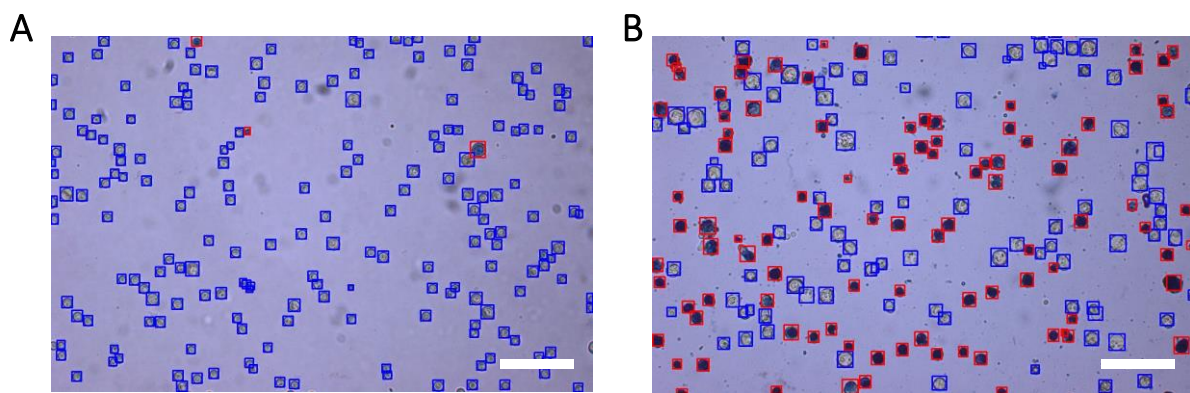


Figure 2.2. ML model classified cells (blue=alive, red=dead) in images originating from test data set.

Images of Hi5 cell cultures taken at 10X magnification with their contents classified by the ML model. Alive cells were indicated by blue bounding boxes and dead cells by red bounding boxes. Scale bar represents 250 μm . (A) Hi5 cell culture grown for 4 d at 28 $^{\circ}\text{C}$ in Sf900iiSFM. (B) Hi5 cell culture 7 days post infection with baculovirus at an MOI of 0.01.

A first qualitative assessment of the ML model's performance in classification was assessed by comparing it to an independent manual inspection of all 122 classified images. The result is summarized in correlation plots (**Figure 2.3A,B**) in which the black dotted diagonals represent the ideal scenario in which the ML-determined and manually determined cell counts are identical. Over the entire range from 5 to >400 cells per FoV, the machine learning model was able to determine the alive cell counts with very high accuracy ($r^2 > 0.99$ from linear fits (red lines) to the data) for both Hi5 (**Figure 2.3A**) and Sf9 cells (**Figure 2.3B**). These correlation coefficients, obtained from the linear fit through the data, are similar or higher than previously obtained using image processing software packages or ImageJ¹⁹⁻²¹. High accuracies were also achieved by the ML model for dead cell counts for Hi5 (**Figure 2.3C**) and Sf9 (**Figure 2.3D**) cells, with a maximum overestimation of $\sim 4.5\%$ for the higher cell counts (>150 cells/FoV), originating from the double counts of aggregated cells. Aggregated cells can result in a significant overestimation of cell counts due to the lack of cell boundary detection, leading to double counts. This is in line with the decreased accuracy observed for

heavily aggregated cultures by manual cell counting methods and the majority of automated cell counters³¹. In general, dead cell detection and classification represents a greater challenge. This is because these cells have less distinct features (e.g. a less pronounced outer boundary and decreased distinction from the blue background relative to white alive cells), and are more susceptible to disintegration as a result of apoptosis. Indeed, the accuracy of (intact) dead cell counts achieved by the ML model exceeded that of previously published work¹⁹⁻²¹. Because the majority of the test images were acquired from cultures with conditions supporting cell growth, the dead cell counts were low relative to the alive cell counts. To assess whether the ML model could accurately determine the number of dead cells even at low cell counts, we magnified this regime (insets **Figure 2.3C,D**). For both cell lines the ML model was able to determine the cell counts with high accuracy. The viability of the cell cultures was determined based on the viable and total cell counts in the individual images and categorized per cell type (**Figure 2.3E,F**). Again, as most of the cell images originated from cultures with conditions supporting cell growth, the higher viabilities are overrepresented in the data set (insets **Figure 2.3E,F**). For both cell lines jointly, on average the difference in viability determined by manual counting and the ML model was $0.99\% \pm 1.55\%$, which is lower than the average operator-to-operator variation in manual viability determination using a counting chamber (2-13%)³² and well within the target (maximum difference of 5%) of this study.

As a second, more quantitative assessment of the performance of our ML model, we constructed a confusion matrix to determine the *F1* score, sensitivity, and recall of all images, both per cell line and for both cell lines jointly (**Figure 2.4**)^{33,34}. The per cell line quantification was performed to reveal any differences in the performance of the model between them. For the alive cell count, this analysis showed that the ML model performed better for Hi5 (*F1*= 0.99) cells than for Sf9 (*F1*= 0.95) cells. This increased performance most likely originated from the larger size of the Hi5 cells, which made them easier to detect³⁵. For both cell lines jointly, the model was able to detect alive cells (**Figure 2.4A**) slightly better than dead cells (**Figure 2.4B**), a consequence of their greater consistency in size and shape and the larger number of alive cells in the training data set. For all investigated conditions (per cell line and jointly; alive and dead cells), the leading performance parameter (*F1* score) exceeded 0.95. These high *F1* scores demonstrate that this ML model is highly suitable for accurate cell density and viability determination of cell cultures.

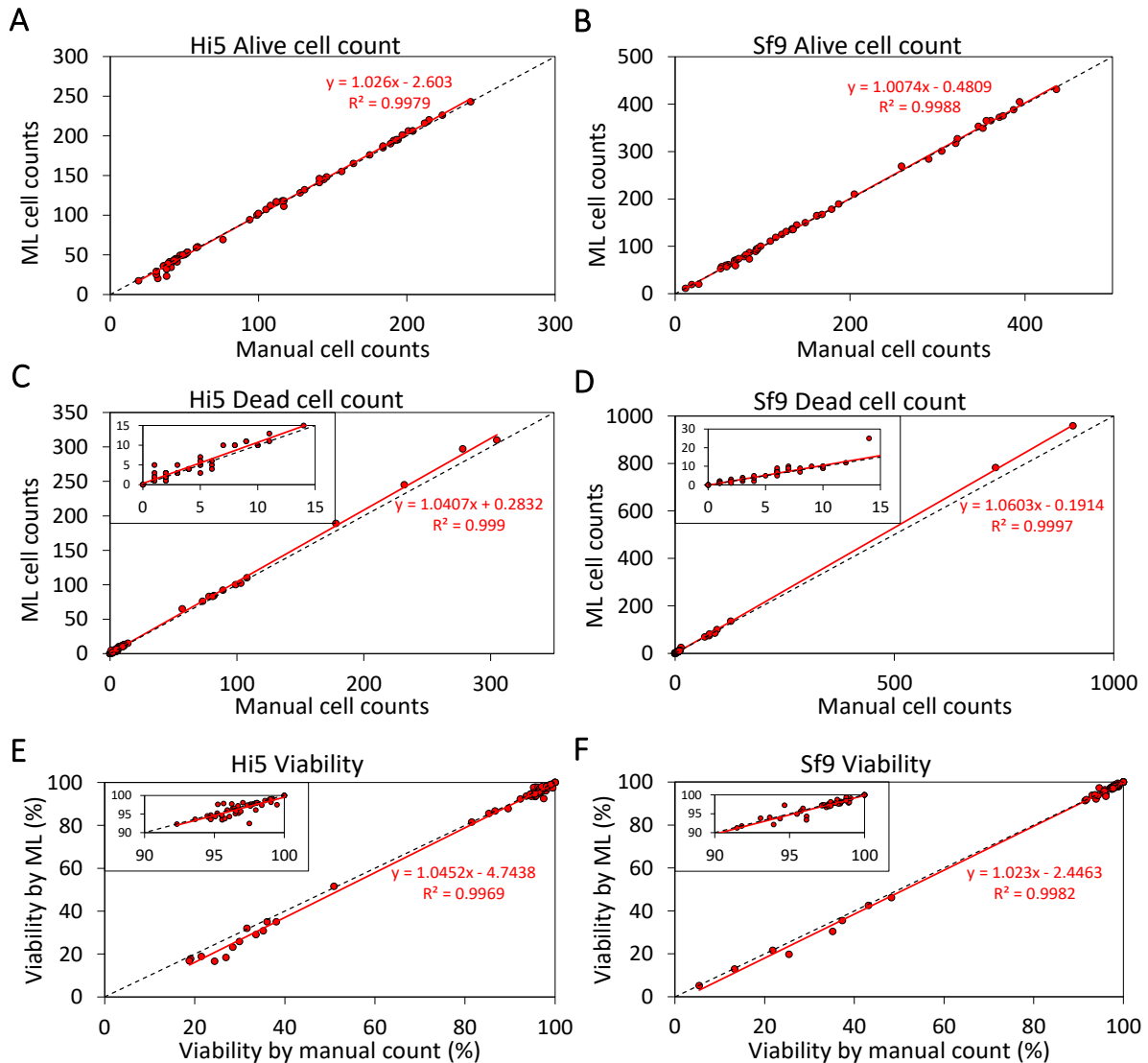


Figure 2.3. Correlation plots between the manual cell count of images and the cell count by the ML model.

(A) Alive cell counts for Hi5 cells ($n = 66$). (B) Alive cell counts for Sf9 cells ($n = 56$). (C) Dead cell counts for Hi5 cells ($n = 66$). Inset: magnification of the region with lower dead cell counts. (D) Dead cell counts for Sf9 cells ($n = 56$). Inset: magnification of the region with lower dead cells counts. (E) Calculated viability of Hi5 cell cultures. Inset: magnification of the region with higher viabilities. (F) Calculated viability of Sf9 cell cultures. Inset: magnification of the region with higher viabilities.

To examine whether there were differences in performance between images with a high and low cell count, we investigated the $F1$ scores across the range of cell densities (Figure 2.5). As we can observe in both panels, we note that the ML model is able to accurately classify both alive and dead cells in images with a very high cell density ($F1 > 0.90$ for cell counts >400 cells/FoV). This allows one to apply the ML model to cell cultures with a high cell density without the need for additional dilution prior to analysis, thus reducing additional experimental error and process time, provided that aggregation is not apparent. If it is, then dilution is required, analogously to other cell detection methods (e.g. manual and automated cell counting). The ML model yields

lower $F1$ scores for both alive (Figure 2.5A) and dead (Figure 2.5B) cell counts at lower cell counts, with this effect being more substantial for the dead cell counts (inset to Figure 2.5B). A decrease of the $F1$ scores with lower cell counts is inherent to their computation: for a low number of cells (TP in Equation (3)), the effect of a single misclassification (either FP or FN in Equation (3)) has a disproportionate influence. This, together with the low total number of dead cells per FoV detailed above, accounts for the more severe decrease in $F1$ scores observed at lower cell counts for dead cells.

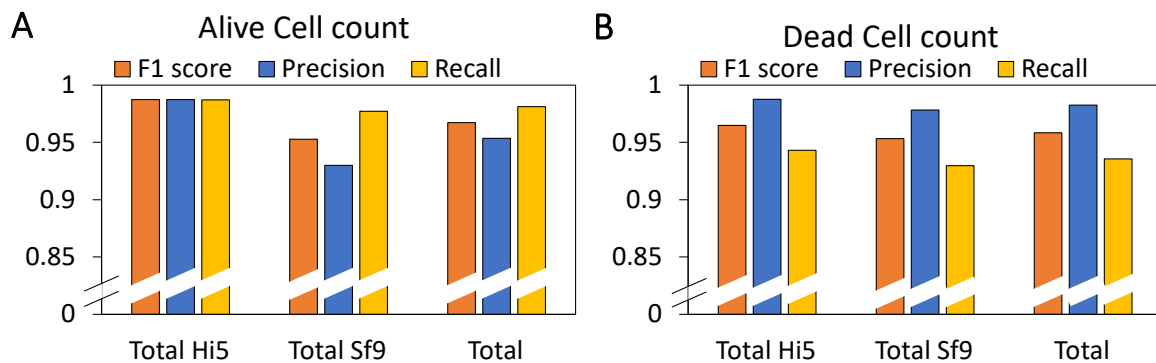


Figure 2.4. Performance of the ML model based on confusion matrix theorem.

The independent performance parameters were calculated using Equations (1)-(3) for Hi5 ($n = 66$ images) and Sf9 ($n = 56$ images) data sets both separately, and jointly (totaling 20,000+ cells in 122 images). False positives, false negatives, and true positives were determined manually. (A) Performance parameters for the alive cell counts both per cell line and jointly. (B) Performance parameters for the dead cell counts both per cell line and jointly.

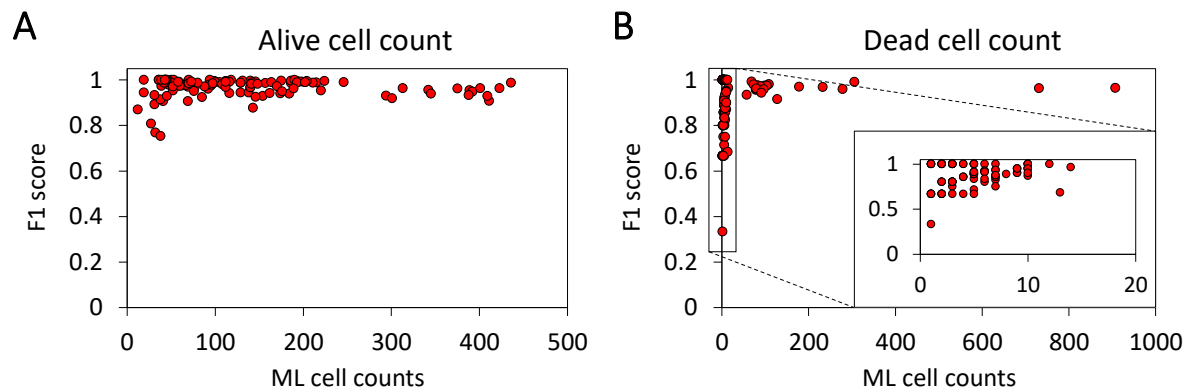


Figure 2.5. Investigation of a drop-off in $F1$ scores at different insect cell counts per image. Sf9 and Hi5 data sets combined.

(A) $F1$ scores for alive cell counts per FoV assigned by the ML model ($n=122$). (B) $F1$ scores for dead cell counts per FoV assigned by the ML model ($n=122$). Inset: magnification of the region with low cell counts.

Given the promising performance of our ML model for insect cells, we next investigated the applicability of the same model to Trypan blue-stained human embryonic kidney (HEK) cells. These cells exhibit a distinctive differentiation pattern similar to that of insect cells, where white and blue markers are used to distinguish

between alive and dead cells, respectively. As before, images were taken of cultures with conditions supporting cell growth, and these were then analyzed using slightly altered post-processing parameters (confidence interval, intersection over union, and bounding box size were set at 0.15, 0.1, and 25 px², respectively) set following visual inspection of the initial classification by the model using default settings. The decrease in the values of the confidence interval and intersection over union parameters followed logically from the smaller size of HEK cells relative to insect cells ([Figure 2.6A](#)).

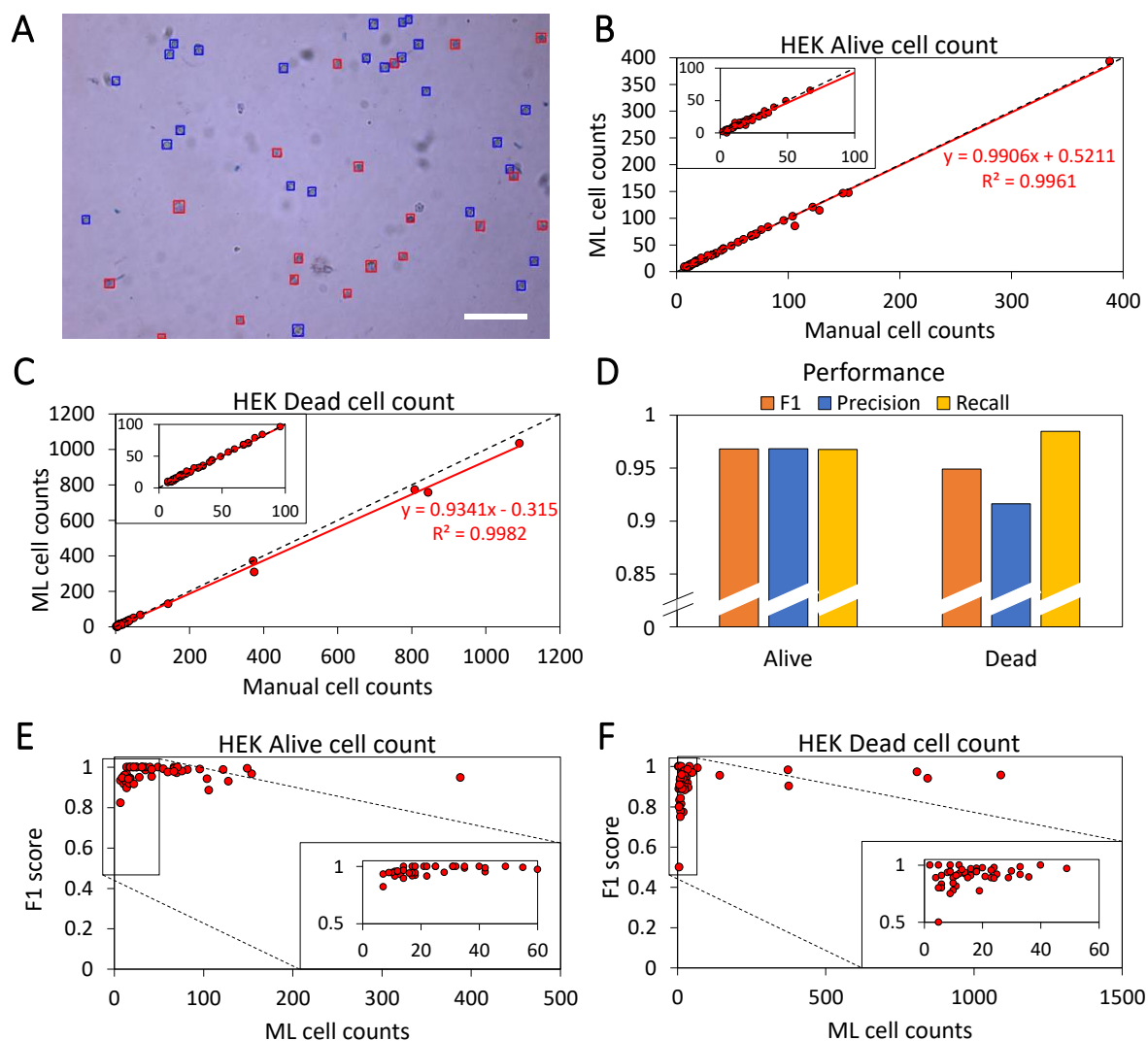


Figure 2.6. Evaluation of the performance of the ML model on HEK cells.

(A) Image of HEK cell culture taken at 10X magnification with contents classified by the ML model. Alive cells are indicated by blue bounding boxes and dead cells by red bounding boxes. Scale bar represents 250 μm . (B) Correlation plot between the alive cell counts determined manually and by the ML model on HEK cells. Inset: magnification of the lower count regimes. (C) Correlation plot between the dead cell counts determined manually and by the ML model on HEK cells. Inset: magnification of the lower count regimes. (D) False positives, false negatives, and true positives were determined manually. The independent performance parameters were calculated over all 6801 HEK cells in all 52 images. (E) $F1$ scores of the alive cell counts assigned by the ML model for HEK cells ($n=52$). Inset: magnification of the low cell count regime. (F) $F1$ scores for dead cell counts assigned by the ML model for HEK cells ($n=52$). Inset: magnification of the low cell count regime.

The correlation plots for HEK cells (**Figure 2.6B,C**) indicated similar performances of the ML model for alive (**Figure 2.6B**) and dead (**Figure 2.6C**) cell counts, with a marginal underestimation for the higher dead cell counts (>200 cells/FoV). Anew, the performance parameters determined that the ML model was able to determine the majority of the cell counts correctly (**Figure 2.6D**; $F1= 0.97$ and 0.95 for alive and dead cell counts, respectively), however, marginally lower than for insect cells. This decreased performance originated from the much smaller size (diameter: 11-15 μm) of HEK cells compared to insect cells (diameter: 17-30 μm), their less pronounced cell boundaries, and most prominently, the lack of training of the ML model on these cells^{12,35}. Similarly to insect cells and especially so for dead cell counts, we observed drop-offs in the $F1$ score for lower cell counts (**Figure 2.6E** and **Figure 2.6F**). The rationale behind this drop-off is analogous to the abovementioned detrimental effects of misclassification at low cell counts on the $F1$ score.

2.3 Conclusions

Here, we have presented an alternative to manual or automated cell counting, for Trypan blue-stained microscopic images of insect cells and HEK cells. Our ML model was able to determine cell counts with very high accuracy, without the need for manual image processing prior to automated cell counting. Our ML model provides a faster and cheaper alternative to manual cell counting and acquisition of a commercially available automated cell counter, respectively. Moreover, the model is able to quickly process a large number of images, allowing the operator the opportunity to rapidly determine the cell counts of multiple cultures. We expect that this ML model will provide a useful tool for operators of cell cultures at all scales, and that it will lower the threshold for scientists requiring protein expression by insect cell production platforms.

2.4 Supplemental information

The supplemental information provides the full ML model as well as a guide on how to install and use it³⁶. Additionally, annotated test and training data sets are supplied in 4TU repository³⁷. Lastly, the complete set of evaluated images ($n = 122$ for insect cells and $n = 52$ for HEK cells) has been added to the same repository.

2.5 Materials & Methods

2.5.1 Cell culturing & preparation for manual cell counting

The two most commonly employed insect cells were used to train and test the ML model: *Trichoplusia ni* (Gibco High Five™; Hi5 cells) and *Spodoptera frugiperda* (Gibco; Sf9). The Hi5 and Sf9 cells were separately cultured in final volumes of 50 ml in 125 ml Erlenmeyer culture flasks using Sf900™ II Serum-free medium (Gibco), and seeded with a cell density of 7.5×10^4 cells/ml and 5.0×10^5 cells/ml, respectively. Samples (~200 μ l) were taken every 24 h for 4 d. The cell culture samples were mixed 1:1 with Trypan blue (Gibco), and 10 μ l of each resulting mixture was transferred to a Countess cell counting chamber slide (Invitrogen). The counting chamber slides were placed under a brightfield microscope, and ~10 fields of view were imaged per counting chamber at a 10X magnification using an Olympus CKX41 microscope (providing a 0.96 mm² field of view per image) and cellSens image acquisition software package (Olympus).

Human embryonic kidney cells (HEK cells) were cultured in 1 l bioreactors using BalanCD HEK293 medium (Irvine Scientific). Images were captured after 2 and 3 d of growth. Sampling, sample preparation, and imaging was performed analogously to that of the insect cells.

2.5.2 Baseline ML model

The cell counter model was based on the You Only Look Once version 4 (YOLOv4) object detection model²⁷. Object detection models take images as input, and output object locations and classes for them. The YOLOv4 model was pre-trained on the MS COCO data set^{38,39}.

2.5.3 Training the model

Data sets were annotated using labImg, a free, open source tool for graphically labelling images⁴⁰. A training set (46 insect cell images containing 5022 alive cells and 938 dead cells) and a validation set (14 insect cell images containing 2345 alive cells and 510 dead cells) were constructed, and the cells were annotated as dead or alive using the aforementioned tool. The training set images contained cell densities ranging from 5 to > 300 cells per field of view (FoV) of 0.96 mm². For the training of the original YOLOv4 model in order to obtain our optimized, insect cell detection ML model, we used an Adam optimizer with an initial learning rate of 2×10^{-4} and a final learning rate of 1×10^{-6} . The number of iterations through the data set (epochs) was set to 100. Our ML model was chosen by picking the model for which the validation set loss was the lowest (“early stopping”), to prevent overfitting. The data sets used and further details of the implementation are provided in the supplemental information³⁷.

2.5.4 Post-processing

The model used three post-processing parameters to produce a final result, namely the confidence score threshold (default = 0.4); the intersection over union threshold (default = 0.3); and the bounding box (bbox) size threshold (default = 200 px²). The

default values were the values used during training/validation. The values of the three post-processing parameters could be adapted to make the model more or less sensitive, with the following consequences. The model will return as a prediction any object with confidence score larger than the confidence score threshold. Decreasing this threshold will lower the threshold for positive object classification, and hence in our context will return more cells at the expense of an increased risk of false positives. The intersection over union threshold dictates how much overlap is allowed between neighboring objects. Lowering this threshold will allow for bounding boxes to be closer together, possibly leading to more detected cells, especially aggregated or slightly deformed ones. However, it also risks false double detections of a single cell. Finally, the bbox size threshold parameter filters out any detections with a small bbox size. Modifying this parameter could be beneficial upon changes in the magnification or cell size; increasing the value of this post-processing parameter will increase the size of the allowed bounding boxes, and vice versa.

2.5.5 Model performance

The model performance was evaluated by the construction of a confusion matrix from a large test data set consisting of 122 images, containing >20,000 alive and dead cells. Images of the test data set were newly acquired and not part of the train and validation data sets. The test set was used in order to understand how well the model functions for different cell strains, cell densities, and viabilities. The numbers of true positives (TP), false positives (FP), and false negatives (FN) on the test set were determined manually^{33,34}. Three metrics were computed to evaluate the model performance. The recall (alternatively referred to as sensitivity or true positive value, *TPV*) measures the extent of error caused by false negatives, and is defined as:

$$TPV = \frac{TP}{TP + FN}. \quad (1)$$

The precision (or positive predictive value, *PPV*) measures the extent of error caused by false positives, and is defined as:

$$PPV = \frac{TP}{TP + FP}. \quad (2)$$

The *F1* score, the leading performance indicator for ML models, is defined the harmonic mean of the precision and the sensitivity:

$$F1 = \left(\frac{PPV^{-1} + TPV^{-1}}{2} \right)^{-1} = \frac{2TP}{2TP + FP + FN}. \quad (3)$$

2.6 References

1. Baghban R, Farajnia S, Rajabibazl M, et al. Yeast Expression Systems: Overview and Recent Advances. *Mol Biotechnol.* 2019;61(5):365-384. doi:10.1007/s12033-019-00164-8
2. Rosano GL, Ceccarelli EA. Recombinant protein expression in Escherichia coli: Advances and challenges. *Front Microbiol.* 2014;5(APR):1-17. doi:10.3389/fmicb.2014.00172
3. Bakhtiar SM, Butt HA, Zeb S, Quddusi DM, Gul S, Dilshad E. *3D Printing Technologies and Their Applications in Biomedical Science.* Vol 1.; 2018. doi:10.1016/B978-0-12-804659-3.00010-5
4. Chen R. Bacterial expression systems for recombinant protein production: E. coli and beyond. *Biotechnol Adv.* 2012;30(5):1102-1107. doi:10.1016/j.biotechadv.2011.09.013
5. Verma R, Boleti E, George AJT. Antibody engineering: Comparison of bacterial, yeast, insect and mammalian expression systems. *J Immunol Methods.* 1998;216(1-2):165-181. doi:10.1016/S0022-1759(98)00077-5
6. Smith GE, Summers MD, Fraser MJ. Production of human beta interferon in insect cells infected with a baculovirus expression vector. 1983. *Biotechnology.* 1992;24(12):434-443. doi:10.1128/mcb.3.12.2156-2165.1983
7. Hu NJ, Rada H, Rahman N, et al. GFP-based expression screening of membrane proteins in insect cells using the baculovirus system. *Methods Mol Biol.* 2015;1261. doi:10.1007/978-1-4939-2230-7_11
8. Felberbaum RS. The baculovirus expression vector system: A commercial manufacturing platform for viral vaccines and gene therapy vectors. *Biotechnol J.* 2015;10(5):702-714. doi:10.1002/biot.201400438
9. van Oers MM. Opportunities and challenges for the baculovirus expression system. *J Invertebr Pathol.* 2011;107(SUPPL.):S3-S15. doi:10.1016/j.jip.2011.05.001
10. Mendonça SA, Lorincz R, Boucher P, Curiel DT. Adenoviral vector vaccine platforms in the SARS-CoV-2 pandemic. *npj Vaccines.* 2021;6(1). doi:10.1038/s41541-021-00356-x
11. Lalonde ME, Durocher Y. Therapeutic glycoprotein production in mammalian cells. *J Biotechnol.* 2017;251(April):128-140. doi:10.1016/j.jbiotec.2017.04.028
12. Thomas P, Smart TG. HEK293 cell line: A vehicle for the expression of recombinant proteins. *J Pharmacol Toxicol Methods.* 2005;51(3 SPEC. ISS.):187-200. doi:10.1016/j.vascn.2004.08.014
13. Tan E, Chin CSH, Lim ZFS, Ng SK. HEK293 Cell Line as a Platform to Produce Recombinant Proteins and Viral Vectors. *Front Bioeng Biotechnol.* 2021;9(December):1-9. doi:10.3389/fbioe.2021.796991
14. Arunkarthick S, Asokan R, Aravintharaj R, Niveditha M, Kumar NKK. A Review of Insect Cell Culture: Establishment, Maintenance and Applications in Entomological Research. *J Entomol Sci.* 2017;52(3):261-273. doi:10.18474/JES17-02PT.1

15. Liu S. *How Cells Grow.*; 2017. doi:10.1016/b978-0-444-63783-3.00011-3
16. Phillips HJ. Dye Exclusion Tests for Cell Viability. In: *Tissue Culture*. Elsevier; 1973:406-408. doi:10.1016/B978-0-12-427150-0.50101-7
17. Stoddart MJ. *Cell Viability Assays: Introduction*. Vol 740.; 2011. doi:10.1007/978-1-61779-108-6_1
18. Zhang M, Gu L, Zheng P, et al. Improvement of cell counting method for Neubauer counting chamber. *J Clin Lab Anal*. 2020;34(1):1-6. doi:10.1002/jcla.23024
19. Aung SM, Kanokwiroon K, Phairatana T, Chatpun S. Automatic counting for live and dead cells from trypan blue-stained images by image analysis based on adaptive k-means clustering. *J Comput Sci*. 2019;15(2):302-312. doi:10.3844/jcssp.2019.302.312
20. O'Brien J, Hayder H, Peng C. Automated quantification and analysis of cell counting procedures using imagej plugins. *J Vis Exp*. 2016;2016(117):1-10. doi:10.3791/54719
21. Aung SM, Kanokwiroon K, Phairatana T, Chatpun S. Live and dead cells counting from microscopic trypan blue staining images using thresholding and morphological operation techniques. *Int J Electr Comput Eng*. 2019;9(4):2460-2468. doi:10.11591/ijece.v9i4.pp2460-2468
22. Al-Khazraji BK, Medeiros PJ, Novielli NM, Jackson DN. An automated cell-counting algorithm for fluorescently-stained cells in migration assays. *Biol Proced Online*. 2011;13(1):9. doi:10.1186/1480-9222-13-9
23. Xu F, Li X, Yang H, Wang Y, Xiang W. TE-YOLOF: Tiny and efficient YOLOF for blood cell detection. *Biomed Signal Process Control*. 2022;73(September 2021):103416. doi:10.1016/j.bspc.2021.103416
24. Kachouie NN, Kang L, Khademhosseini A. Arraycount, an algorithm for automatic cell counting in microwell arrays. *Biotechniques*. 2009;47(3 SUPPL.). doi:10.2144/000113202
25. The Insight Partners. *Automated Cell Counters Market Forecast to 2028 - COVID-19 Impact and Global Analysis By Type and End User.*; 2022. doi:ID: 5646831
26. Kumar P, Nagarajan A, Uchil PD. Analysis of cell viability by the lactate dehydrogenase assay. *Cold Spring Harb Protoc*. 2018;2018(6). doi:10.1101/pdb.prot095497
27. Bochkovskiy A, Wang C-Y, Liao H-YM. YOLOv4: Optimal Speed and Accuracy of Object Detection. Published online 2020. <http://arxiv.org/abs/2004.10934>
28. Zhang D, Zhang P, Wang L. Cell counting algorithm based on YOLOv3 and image density estimation. *2019 IEEE 4th Int Conf Signal Image Process ICSIP 2019*. Published online 2019:920-924. doi:10.1109/SIPROCESS.2019.8868603
29. Alam MM, Islam MT. Machine learning approach of automatic identification and counting of blood cells. *Healthc Technol Lett*. 2019;6(4):103-108. doi:10.1049/htl.2018.5098
30. Drey LL, Graber MC, Bieschke J. Counting unstained, confluent cells by modified bright-field microscopy. *Biotechniques*. 2013;55(1):28-33. doi:10.2144/000114056

31. Jeong EJ, Choi D, Lee DW. U-Net Deep-Learning-Based 3D Cell Counter for the Quality Control of 3D Cell-Based Assays through Seed Cell Measurement. *SLAS Technol.* 2021;26(5):468-476. doi:10.1177/24726303211017532
32. Biggs R, Macmillan RL. The Errors of Some Haematological Methods as They Are Used in a Routine Laboratory. *J Clin Pathol.* 1948;1(5):269-287. doi:10.1136/jcp.1.5.269
33. Fawcett T. An introduction to ROC analysis. *Pattern Recognit Lett.* 2006;27(8):861-874. doi:10.1016/j.patrec.2005.10.010
34. Powers DMW. Evaluation: from precision, recall and F-measure to ROC, informedness, markedness and correlation. 2020;(May). <http://arxiv.org/abs/2010.16061>
35. Janakiraman V, Forrest WF, Chow B, Seshagiri S. A rapid method for estimation of baculovirus titer based on viable cell size. *J Virol Methods.* 2006;132(1-2):48-58. doi:10.1016/j.jviromet.2005.08.021
36. Van Veen E. Cell counter. Published 2023. <https://gitlab.tudelft.nl/nynke-dekker-lab/public/cell-counter>
37. Kuijpers L, Van Veen E, Van der Pol L, Dekker NH. Train, validation, and test data sets underlying publication Automated cell counting for Trypan blue-stained cell cultures using machine learning. Published 2023. <https://doi.org/10.4121/21695819>
38. Lin TY, Maire M, Belongie S, et al. Microsoft COCO: Common objects in context. *Lect Notes Comput Sci (including Subser Lect Notes Artif Intell Lect Notes Bioinformatics)*. 2014;8693 LNCS(PART 5):740-755. doi:10.1007/978-3-319-10602-1_48
39. Bochkovskiy A. YOLOv4 Weights. Accessed March 7, 2023. <https://github.com/AlexeyAB/darknet>
40. Tzutalin. LabelImg. Accessed March 7, 2023. <https://github.com/heartexlabs/labelImg>

3

Optimization of enterovirus-like particle yield during production and purification

Hand, foot, and mouth disease (HFMD) represents an emerging health concern with the risk of causing meningitis, encephalitis, and flaccid paralysis to patients. Enteroviruses, particularly enterovirus A71 (EV71) and coxsackievirus A6 (CVA6), are the main causative agents of HFMD. The lack of a CVA6 vaccine, the inherently costly nature of the EV71 inactivated vaccine, and the rise of other HFMD-causing strains due to the suppression of HFMD-causing viruses, has impelled the field to obtain alternative vaccine technologies. Virus-like particle (VLP) vaccine candidates are one of the solutions proposed to solve these challenges.

Previous studies have demonstrated that the expression of the viral P1 structural proteins and the 3CD protease is sufficient to produce enterovirus-like particles in various organisms, yet optimization based on the interplay between the three most commonly altered infection parameters (multiplicity of infection (MOI), viable cell density at the time of infection (VCD), and the infection period) is lacking. To address this challenge, we performed Design of Experiments (DoE) to optimize the production of both EV71 and CVA6 VLPs. Our results indicated distinctively different preferences for infection parameters between the two types of VLPs, with EV71 VLP production preferring low MOI, low VCD, and long infection period, while CVA6 VLP production preferring for high MOI, high VCD, and long infection period. Additionally, we present a purification process for both VLPs yielding 158 mg/l and 38 ml/l of culture volume for purified EV71 and CVA6 VLPs, respectively. These concentrations translate into thousands to tens of thousands of vaccines, highlighting the economic potential of enterovirus-like particles for vaccine purposes.

This chapter is in preparation for submission for peer review publication as: L. Kuijpers *et al.*, "Optimization of enterovirus-like particle yield during production and purification"

3.1 Introduction

Over the past two decades, hand, foot, and mouth disease (HFMD) has emerged as a growing health concern, particularly in South-East Asia. Multiple outbreaks in Taiwan, Malaysia, China, Vietnam and Cambodia have demonstrated the emergence and spread of HFMD, alarming experienced clinicians¹. The disease is named after the characteristic lesions that develop on the hands, feet, mouth, and buttocks of patients following infection. In some cases, especially with children, the disease can spread to the central nervous system (CNS), leading to severe complications such as aseptic meningitis and encephalitis^{1,2}. Enteroviruses, particularly enterovirus A71 (EV71) and coxsackievirus A6 (CVA6), are the main causative agents of HFMD. For CVA6, the most prevalent strain detected in approximately 50% of HFMD cases, there is no vaccine available to date³⁻⁵. For EV71, on the other hand, substantial progress has been made through the development and employment of an inactivated EV71 vaccine, which effectively suppresses the virus post infection and curbs viral outbreaks⁶. Although this vaccine has multiple advantages compared to attenuated virus vaccines that contain live viruses, it also presents some distinct drawbacks. Firstly, the long virus inactivation procedure required, which can last up to sixty days for some viruses, renders the production process, and ultimately the end product, excessively costly. Large-scale immunization programs demand millions of vaccines doses, and production costs can be a limitation for successful implementation⁷. Secondly, suppressing only one virulent strain provides the opportunity for other virus strains to emerge, considerably reducing the efficiency of the vaccine on the medium term^{4,5}. This continuous cycle can only be broken by multivalent vaccines that target as many viral strains as possible to eradicate the disease.

Various vaccine development approaches have been proposed to obtain multivalent vaccines against HFMD, and a recent strategy involves the utilization of virus-like particles (VLPs). Unlike conventional inactivated or attenuated vaccines, VLPs are macromolecular (self-)assemblies of viral proteins that do not contain genetic material, making them non-infectious and incapable of replication. Their surface structure resembles the immune-inducing patterns of the native virus, thereby enabling recognition by the immune system^{8,9}. This characteristic can be leveraged for vaccine purposes, particularly for viruses that are identified by the immune system based on specific surface pattern (e.g., enteroviruses) as opposed to a single protein (e.g., SARS-CoV-2)^{10,11}. Expression of only a few of the viral proteins should be sufficient to produce enterovirus-like particles.

The genomes of EV71 and CVA6 consist of a ~7.4 kbp positive sense ssRNA which encodes 11 viral proteins (**Figure 3.1**). These proteins are expressed as a 260 kDa polyprotein that is divided into three regions: P1, P2, and P3. The P2 and P3 regions are composed of non-structural proteins, with mixed functionalities, ranging from protease to polymerase activity. The viral capsid is composed of 60 structural

assemblies of proteins originating from the P1 region^{12,13}. During morphogenesis, the P1 is proteolytically cleaved in stepwise fashion into the VP0 (the precursor of VP2 and VP4), VP1, and VP3. Subsequently, VP0 is autocatalytically cleaved into VP2 and VP4 to complete the viral maturation process. It has been hypothesized that this maturation step depends on the presence of RNA in the particles, which may have significant implications for the RNA-depleted VLPs¹⁴⁻¹⁶. VP1 is typically used as a benchmark protein for quantification of enterovirus viral protein and VLP production, and we follow this approach in this work.

Studies focused on investigating enterovirus morphogenesis typically isolate two types of particles: mature virions, which contain RNA, and procapsids, which lack RNA¹². The procapsid, or empty capsid, is hypothesized to be the precursor of the mature virions, suggesting that the RNA enters the capsid at a late stage of the assembly process rather than serving as a scaffold for the viral capsid proteins¹⁷. In addition to mature virions and procapsids, a third particle, the A-particle, is found in the morphogenesis of CVA6; such a third particle could exist for other viruses within the *Enterovirus* genus^{12,18-20}. Unlike mature virions and procapsids, the A-particle is inherently unstable and serves as an uncoating intermediate (i.e., a temporal state of the capsid, induced mostly by cell receptor binding, which triggers conformational changes in the viral capsid and enable the RNA to exit the capsid). The mature virion expands and transforms into the A-particle upon attachment to specific receptors on the host cell surface during the initial stage of infection *in vivo*^{18,19}. Due to the essentially identical atomic structure between the procapsid and the A-particle, and the observation that VLPs closely resemble procapsids (both hypothesized to lack RNA), the A-particle is utilized as an additional benchmark for VLP production¹².

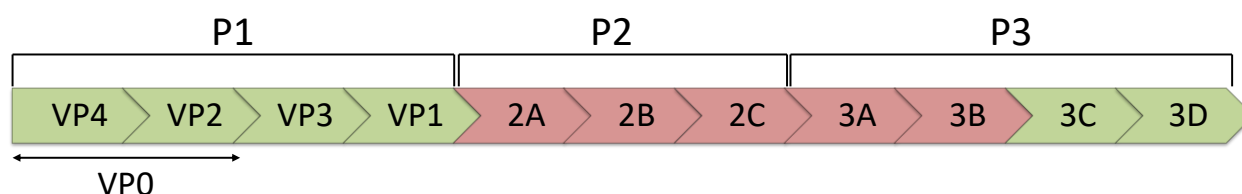


Figure 3.1. Enterovirus polyprotein.

The enterovirus genome is composed of a single-stranded positive sense RNA molecule that encodes a polyprotein of approximately 2,200 amino acids. The polyprotein is subsequently cleaved by viral proteases into 11 mature proteins. Of these proteins, the P1 region encodes the structural proteins of the virion, while the P2 and P3 regions encode non-structural proteins that are involved in viral replication and assembly. Previous studies have shown that expression of only the P1 capsid proteins and the 3CD protease (highlighted in green) is sufficient to produce enterovirus-like particles.

Here, we describe a systematic approach to optimize the virus-like particle (VLP) yield using the baculovirus expression vector system (BEVS). Previous studies have shown that expression of the P1 structural proteins and the 3CD protease is sufficient to produce enterovirus-like particles in various organisms (Figure 3.1)²¹⁻²⁶. While construct optimization has been reported for the production of enterovirus VLPs, optimization based on culturing and infection conditions is mostly limited to

multiplicity of infection (MOI) and infection period (t_{inf})^{23,27–29}. The highest yields obtained for EV71 VLPs using this conventional strategy were 64.3 mg/l of culture volume and 171 mg/l of culture volume for bioreactors and culture flask culture, respectively^{27,28}. The viable cell density at the time of infection (VCD) is usually not considered, and the interplay between these three infection parameters is often ignored. To address this problem, we performed Design of Experiments (DoE) to optimize the production of both EV71 and CVA6 VLPs. A DoE is a systematic, cost-efficient, and effective approach that allows researchers to investigate the relationship between multiple input factors (e.g., MOI, VCD and t_{inf}) and responses (e.g., viral protein yield). It is an iterative process in which critical process parameters are varied, to deduce a more favorable set of input factors (Figure 3.2). The DoE not only provides insight into the optimized conditions but additionally presents a model for the estimation of viral protein yields at conditions (within the boundary conditions of the DoE) that are not experimentally tested. The parallel nature of the approach reduces the process optimization time significantly compared to performing successive experiments³⁰. Additionally, biological variation originating from storage and cell conditions is minimized. There are various models that can be employed for the DoE, but for initial discovery and optimization the full factorial model is the golden standard (Figure 3.2).

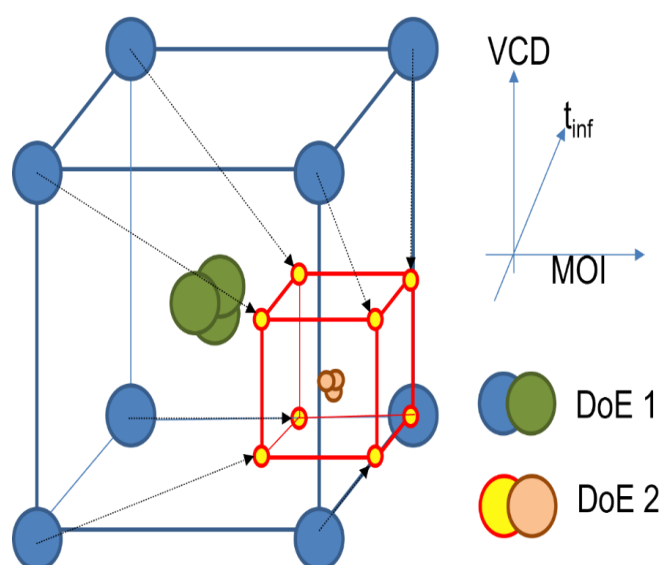


Figure 3.2. Representation of the iterative process of Design of Experiments.

X, Y, and Z-axes represent the input factors for the DoE: multiplicity of infection (MOI), viable cell density at the time of infection (VCD), and infection period (t_{inf}), respectively. These input factors are the culturing conditions subjected to optimization to maximize the output (viral protein production). The blue and green spheres represent the boundary conditions and triplicate experiments of the first iteration of DoE, respectively. Once optimal conditions are determined from the first iteration, the input factors are shifted towards the newly set boundary conditions of the second iteration, represented by the yellow/red and orange spheres. The process continues until the desired optimal conditions are reached.

3.2 Results

3.2.1 Primary iteration of DoE for EV71 and CVA6

Design of experiments (DoE) is a powerful tool for systematically optimizing of desired outputs, called responses (e.g., maximizing viral protein yield, minimizing protein aggregation, minimizing denaturation, or cell death), based on specific chosen process parameter (factors). Here, the chosen (input) factors were multiplicity of infection (MOI), viable cell density at the time of infection (VCD), and infection period (t_{inf}). In the first iteration of experiments, the boundary conditions for each factor were set based on extremes found in literature^{23,27,29,31–36}. In addition, a mock infection, serving as negative control, and three triplicate experiments of the center points of the selected condition were included. These triplicates were designed to assess the level of biological variation between the experiments. The experimental conditions for both EV71 and CVA6 are summarized in **Table 3.1** and **Table 3.2**, respectively.

The DoE was performed to optimize extracellular viral protein (i.e. VLP) production, which yields less complex downstream processing (DSP) than intracellular VLPs. The extracellular viral protein production was read out using western blot (**Figure 3.3A** and **Figure 3.3B** for EV71 and CVA6, respectively). Western blots indicated the presence of VP1 at the anticipated height of 35 kDa for EV71 and 36 kDa for CVA6, as reported in the literature^{31,35}. Although numerous *Picornaviridae* share the same 11 proteins (**Figure 3.1**), slight variations in size for the individual proteins among viruses within a genus are frequently observed. This is exemplified by the differences in VP1 size observed between EV71 and CVA6. Different concentrations of VP1 were measured under different experimental conditions. Notably, no VP1 was observed in the mock infections (negative controls, Δ virus). The other bands visible on the gels were attributed to non-specific interactions with the antibodies and possibly to VP1 precursors that were expressed as the polyprotein P1.

In order to quantitatively determine which of the cultures produced the highest amount of VP1, band intensities were measured using GelAnalyzer software³⁷ and normalized to the highest output (**Figure 3.3C,D**). This allowed for comparison between the different cultures. The triplicates (experiments 9-11) in both experiments indicated highly similar values, suggesting a relatively low level of biological variance. Experiments 2, 6, and the triplicates (experiments 9-11) were the only experiments indicating the significant presence of the VP1 protein for EV71 (**Figure 3.3C**). In contrast, VP1 was present in almost all experiments for CVA6 (**Figure 3.3D**).

Table 3.1. Infection conditions and design matrix first iteration of design of experiments for EV71.

Cultures were infected using the infection parameter presented here. All 12 cultures were derived from the same preculture and diluted accordingly. The design matrix indicates the experiment based on the design space (Figure 3.2), where -1 and 1 represent the lower and upper boundary of the specific infection parameter. Experiments 9-11 are considered triplicates as they have the same infection conditions as the center of the design space (Figure 3.2). Experiment 12 was the negative control (mock infection) that did not receive any virus.

Exp No.	Multiplicity of infection	Infection period (d)	Cell density (cells/ml)	Design Matrix		
				MOI	Infection Period	Cell Density
1	0.001	2	5×10^5	-1	-1	-1
2	0.001	6	5×10^5	-1	1	-1
3	0.001	2	3×10^6	-1	-1	1
4	0.001	6	3×10^6	-1	1	1
5	1	2	5×10^5	1	-1	-1
6	1	6	5×10^5	1	1	-1
7	1	2	3×10^6	1	-1	1
8	1	6	3×10^6	1	1	1
9	0.05	4	1.75×10^6	0	0	0
10	0.05	4	1.75×10^6	0	0	0
11	0.05	4	1.75×10^6	0	0	0
12	n/a	4	1.75×10^6	NC	NC	NC

Table 3.2. Infection conditions and design matrix first iteration of design of experiments for CVA6.

Cultures were infected using the infection parameter presented here. All 12 cultures were derived from the same preculture and diluted accordingly. The design matrix indicates the experiment based on the design space (Figure 3.2), where -1 and 1 represent the lower and upper boundary of the specific infection parameter. Experiments 9-11 are considered triplicates as they have the same infection conditions as the center of the design space (Figure 3.2). Experiment 12 was the negative control (mock infection) that did not receive any virus.

Exp No.	Multiplicity of infection	Infection period (d)	Cell density (cells/ml)	Design Matrix		
				MOI	Infection Period	Cell Density
1	0.01	2	5×10^5	-1	-1	-1
2	5	2	5×10^5	1	-1	-1
3	0.01	7	5×10^5	-1	1	-1
4	5	7	5×10^5	1	1	-1
5	0.01	2	2×10^6	-1	-1	1
6	5	2	2×10^6	1	-1	1
7	0.01	7	2×10^6	-1	1	1
8	5	7	2×10^6	1	1	1
9	2.505	4.5	1.25×10^6	0	0	0
10	2.505	4.5	1.25×10^6	0	0	0
11	2.505	4.5	1.25×10^6	0	0	0
12	n/a	7	1.25×10^6	NC	NC	NC

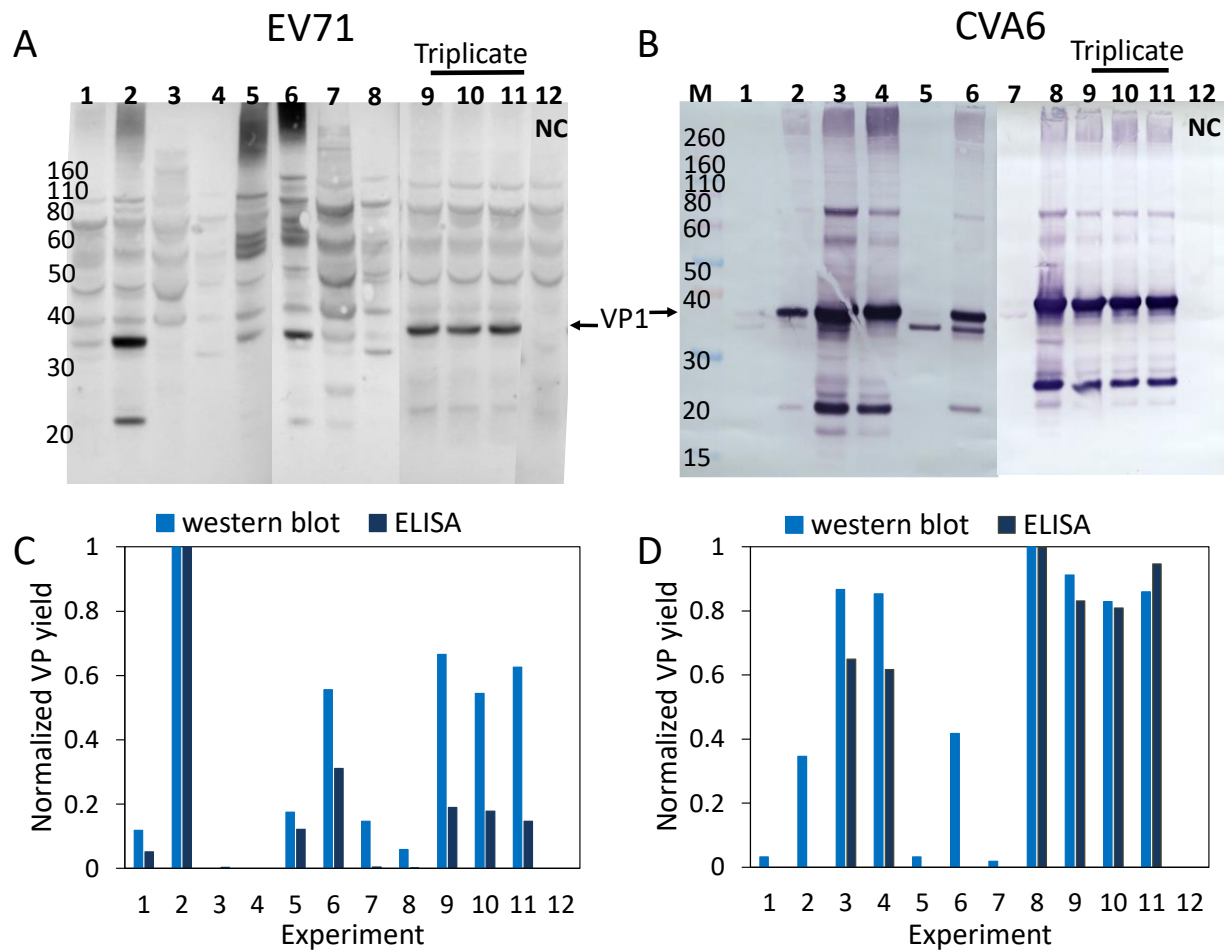


Figure 3.3. Analysis of the first iteration of the DoE for both EV71 and CVA6.

(A) Western blot against EV71 VP1. The most promising experiments were 2, 6, and the triplicates (experiments 9-11). The latter three indicated highly similar band intensities, thus suggesting a low biological variance. (B) Western blot against CVA6 VP1. Anew, the triplicates indicated a low biological variance and the most promising fractions were 3, 4, 6, and 8-11. (C) Quantification and normalization of EV71 western blot band intensities using GelAnalyzer software (light blue)³⁷. Normalized ELISA against EV71 VP1 (dark blue). (D) Quantification and normalization of CVA6 western blot band intensities using GelAnalyzer software (light blue)³⁷. Normalized ELISA against CVA6 A-particle (dark blue).

The experiments with the highest intensity bands were found to be experiment 2 for EV71 and experiment 8 for CVA6. Interestingly, these experiments were on opposite ends of the design space in terms of input factors. For EV71, low MOI, low VCD, and long infection period were preferred, whereas for CVA6, the corresponding input factors were on the high end of the boundary conditions. Furthermore, other infection experiments with long infection periods (exp. 3 and 4, and to a lesser extent the triplicates) also indicated high concentrations of VP1 for CVA6, indicating a preference for extended infection periods independent of MOI or VCD. The only experiment that deviated from this pattern was CVA6 experiment 7, which after visual inspection was suspected to be contaminated and therefore did not produce a large amount of VP1.

To independently verify the western blot results, ELISAs were performed for both EV71 and CVA6 virus origins (**Figure 3.3C** and **Figure 3.3D**, respectively). For EV71 (**Figure 3.3C**) similar conclusions could be drawn from the data: minor signals that were detected in the western blots were not detected by ELISA (**Figure 3.3C**, experiment 7 and 8) most likely due non-specific bands being quantified as VP1. All other experiments indicated similar trends, albeit lower for the western blot in comparison to the ELISA. Overall, the data once again highlighted the importance of extended infection periods for efficient VLP production.

It needs to be noted that the EV71 ELISA probes for the presence of EV71 VP1 protein, whereas the CVA6 A-particle ELISA probes for the presence of assembled particles. Nevertheless, the ELISAs showed similar trends and normalized values as the western blots (**Figure 3.3C,D**). Moreover, this suggests that for CVA6, regardless of the infection conditions, the same ratio existed between total produced VP1 protein and assembled VLPs (**Figure 3.3D**, experiment 3, 4, and 8-11). We note that minor signals detected in the western blots were not detected by ELISA (**Figure 3.3D**, experiment 1, 2, and 5-7); this could be explained by non-specific bands being quantified as VP1. Additionally, the differences in the CVA6 ELISA in comparison to the CVA6 western blot (**Figure 3.3B, D**) were attributed to the target difference of the antibodies (VP1 in **Figure 3.3B** versus A-particle **Figure 3.3D**). Two experiments for CVA6 (**Figure 3.3D**, experiment 2 and 6) were found to deviate from the established pattern, as they show high western blot scores but no corresponding ELISA signal. Apart from the non-specific band quantification described above, these results could be attributed to the high MOI and short infection period used, which may have favored viral protein production but hindered VLP assembly. Either the time for assembly or release of VLPs into the extracellular environment was insufficient.

From the first iteration of DoE, it was concluded that the optimal conditions for EV71 VLP production were low MOI, low VCD, and a long infection period. For CVA6, a second iteration of DoE was conducted to further optimize viral protein expression using the BEVS (see section 3.2.2). In this second iteration, the lower boundaries of the input factors MOI and infection period were increased, whereas the value of the VCD input factor was decreased due to the large amount of contaminating cell debris observed during harvesting. Long infection periods and high MOIs resulted in increased degrees of cell lysis and more cell debris, making it significantly harder to purify the protein of interest. To ease future work, we implemented these change at this step of the process.

3.2.2 Secondary iteration of DoE for CVA6

The second iteration of the viral protein production optimization for CVA6 was performed based on the experimental conditions outlined in **Table 3.3**. Western blot analysis was performed on samples from each extracellular environment, and the results were quantified using GelAnalyzer software, as shown in **Figure 3.4A** and

Figure 3.4B, respectively. In this iteration, all samples except the negative control (experiment 12) indicated VP1 presence (**Figure 3.4A**), strengthening the hypothesis that there were no contaminations in this round of experiments. The highest yields were obtained using high MOI (5), VCD (1×10^6 cells/ml) and infection period (7 d).

Table 3.3. Infection conditions and design matrix second iteration of design of experiments for CVA6.

Cultures were infected using the infection parameter presented here. All 12 cultures were derived from the same preculture and diluted accordingly. The design matrix indicates the experiment based on the design space (**Figure 3.2**), where -1 and 1 represent the lower and upper boundary of the specific infection parameter. Experiments 9-11 are considered triplicates as they have the same infection conditions as the center of the design space (**Figure 3.2**). Experiment 12 was the negative control (mock infection) that did not receive any virus.

Exp No.	Multiplicity of infection	Infection period (d)	Cell density (cells/ml)	Design Matrix		
				MOI	Infection Period	Cell Density
1	0.1	5	1×10^5	-1	-1	-1
2	0.1	5	1×10^6	-1	-1	1
3	0.1	7	1×10^5	-1	1	-1
4	0.1	7	1×10^6	-1	1	1
5	5	5	1×10^5	1	-1	-1
6	5	5	1×10^6	1	-1	1
7	5	7	1×10^5	1	1	-1
8	5	7	1×10^6	1	1	1
9	2.55	6	5.5×10^5	0	0	0
10	2.55	6	5.5×10^5	0	0	0
11	2.55	6	5.5×10^5	0	0	0
12	n/a	7	5.5×10^5	NC	NC	NC

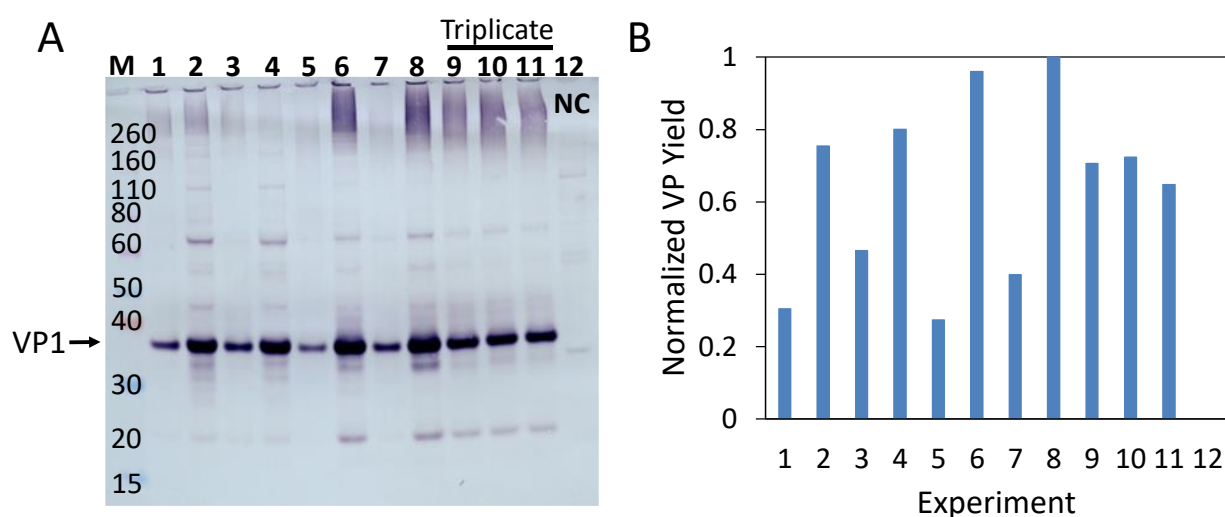


Figure 3.4. Analysis of the second iteration of the DoE for CVA6.

(A) Western blot against CVA6 VP1. Experiment 9-11 are triplicates indicating highly similar bands. (B) Quantification and normalization of EV71 western blot band intensities using GelAnalyzer³⁷.

As stated previously, apart from determining the best infection conditions, the MODDE software also provides a model for the viral protein yield in experiments that were not physically carried out. The performance of this model was assessed based on four key parameters, which were summarized in the summary of fit plot ([Figure 3.5A,B](#)):

- R^2 , a measure of the proportion of the variation in the response that can be explained by the model, overestimates the goodness of fit (i.e., describes how well the statistical model obtained from the software fits the set of experimentally obtained data points). An R^2 value greater than 0.5 is required to indicate statistical significance,
 - This criterion was met for both EV71 and CVA6.
- Q^2 is a cross-validation measure that underestimates the goodness of fit by testing the model's ability to predict new data that was not used in its estimation (i.e., it is a resampling method that uses different portions of the data to test and train a model on different iterations). The Q^2 value tests the model's ability to predict new data that was not used in estimating it, to flag problems like overfitting or selection bias. A Q^2 value greater than 0.1 is required for significance, and greater than 0.5 for a good model. Additionally, the difference between R^2 and Q^2 should not be larger than 0.3 to qualify as a good model.
 - The criteria were satisfied for both EV71 and CVA6.
- Model validity (MV) is a measure of diverse model problems. When the model validity is larger than 0.25, there is no Lack of Fit of the model, which means that the model error is within the same range as the pure error. If this value is less than 0.25 this indicates statistically significant problem(s), such as outliers, an incorrect model, or a transformation problem. It needs to be noted that MV might be low even in very good models (as high as $Q^2 > 0.9$) due to the high sensitivity of the test or highly similar replicates.
 - For EV71, the model validity indicated a Lack of Fit, which was likely due to an absence of response in many experiments (lack of VP1 production), making it hard to fit a statistically significant model. Despite investigating multiple transformations, MV did not increase as desired. The high sensitivity of the assay, the highly similar replicates, and the fact that were many experiments not indicating VP1 protein production could have been attributed to the problems occurred for the EV71 model.
 - In contrast, the CVA6 experiments had a MV of 0.65, indicating no Lack of Fit.
- Reproducibility, which is the variation of the response under the same conditions (in this case center points/triplicates) compared to the total variation of the response, represents the biological variation between different samples.

- High reproducibility values of 0.99 and 0.97 were obtained for EV71 and CVA6, respectively, indicating very low biological variation. Overall, it could be concluded that the model developed for EV71 was unable to accurately predict viral protein production based on the input factors, whereas the model for CVA6 could. An additional iteration of the EV71 DoE is necessary to identify and address the underlying issues with the EV71 model.

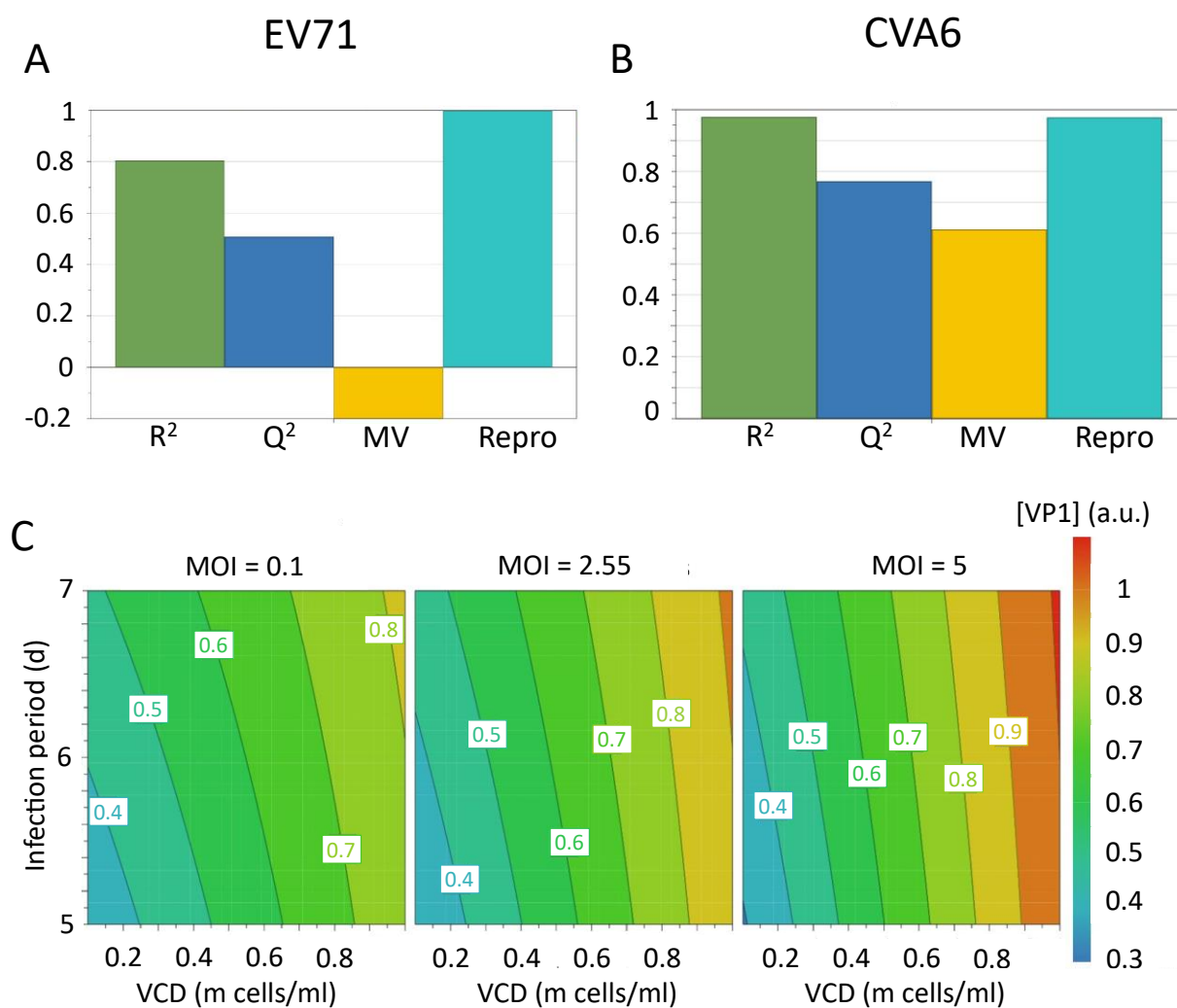


Figure 3.5. Summary of Fit and contour plots.

Summary of fit plot for the first iteration of Design of Experiments for EV71 (A) and the second iteration for CVA6 (B). R² is an indicator for goodness of fit. Q² estimates the prediction power of the model. MV is the model validity and measures the robustness of the model. Repro. is the reproducibility and is a measure of the variability of the replicates in comparison to the overall variability. (A) Performance parameters for the model of EV71: R² (=0.8 > 0.5) indicated significance. Q² (=0.51 > 0.5) determined a good model. MV (=−0.2 < 0.5) indicated a Lack of Fit, outliers, and transformation problems. Repro. (=0.99 > 0.5) indicated marginal biological variance. (B) Performance parameters of the model for CVA6: R² (=0.976 > 0.5) indicated significance. Q² (=0.768 > 0.5) determined a good model. MV (=0.65 > 0.5) indicated an absence in Lack of Fit, outliers, and transformation problems. Repro. (=0.97 > 0.5) indicated marginal biological variance. (C) Contour plots for CVA6 at the three different, measured MOIs

The CVA6 model demonstrated a satisfactory performance, as shown in the model performance indicators (**Figure 3.5B**). Subsequently, the contour plots for viral protein yield at three different measured MOIs were generated for CVA6 (**Figure 3.5C**), which predicted the viral protein production based on the model and allowed for estimation of yields under unmeasured conditions. The plot also confirmed the western blot results and indicated that higher yields could be obtained with longer infection periods and higher VCD. If an additional DoE iteration is conducted, the input factors can be adjusted accordingly to optimize the VLP production further. However, this increase in VCD and longer infection periods may result in more cell debris, which can complicate the purification process.

3.2.3 Optimizing the purification process

Following the successful optimization of viral protein production using the optimized conditions, an optimization study was conducted to improve the purification process. High purity of the VLPs is critical to ensure a high-quality product and enable visualization using electron microscopy (EM). Here, we describe multiple strategies for the downstream processing (DSP) of EV71 and CVA6 VLPs. Initially, the process was optimized for EV71 and later adapted for CVA6. The DSP of VLPs involves multiple steps, including clarification, sucrose cushions/density gradients, and centrifugation. **Figure 3.6** presents the stepwise optimization strategy for obtaining the desired purity for EV71 VLPs (alterations in the process are indicated in red). Previous work suggests that about one-thirds of the total viral protein produced are released into the extracellular environment, while two-thirds remains intracellular²⁸. Whether VLPs are actively transported out of the cells or released due to cell lysis over time remains unknown. Designing a DSP strategy for purification of extracellular VLPs may result in product loss but could significantly reduce purification process time and efforts.

The initial strategy for purifying extracellular VLPs, based on a previous work, reported highly pure material after only a few DSP steps²³. To limit protein aggregation, an additional triton-treatment step was added to the published protocol, yielding strategy A (**Figure 3.6A**). Analysis of the final sucrose density gradient (SDG) fractions indicated a very low protein concentration, which was barely visible on SDS PAGE gel (**Figure 3.7A**). Fortunately, the number of sample contaminating proteins was low. Moreover, on western blot the VP1 band that indicated viral protein expression was clearly visible (**Figure 3.7A**). Direct observation of the most promising fraction (25-30%) by electron microscopy indicated a relatively pure sample with the presence of VLPs (**Figure 3.8A**, red arrow and inset). Notably, while the sample did not contain any baculovirus, there was a background of contaminating protein aggregates, which originated from either the host cell proteins or the viral proteins presented by the SDS PAGE gel.

To exclude these protein aggregates, the triton-treatment was moved up in the process order (strategy B, [Figure 3.6B](#)). Thereby, protein aggregation was prevented prior to the sucrose cushion, thus preventing aggregates from travelling through the 30% sucrose and contaminating the VLP-containing fractions of interest. Both the SDS PAGE gel and the western blot for this strategy looked highly similar to the results obtained when employing strategy A ([Figure 3.7B](#)). However, the EM images have a much clearer background ([Figure 3.8B](#)), and while there were still visible protein aggregates, they were less prevalent. In both strategies (A and B), the particle density was low. To increase the particle density, the production cultures were scaled up from 50 ml to 400 ml, which presented new challenges for the DSP protocol.

After scaled-up viral protein production, strategy C ([Figure 3.6C](#)) yielded poor results. The VP1 protein could be detected in every fraction of the SDG, most likely due to VLP aggregation, binding of VLPs to host cell proteins (HCP), mixing of the SDG layers during harvesting, or reduced efficiency of the SDG due to the small volume ([Figure 3.7C](#)). Although the particle density increased as observed by EM, so did that of the contaminants ([Figure 3.8C](#)). To improve separation, the volume of each sucrose fraction in the SDG was increased from 2 to 6 ml (strategy D, [Figure 3.6D](#)), resulting in a clear distinction between VP1-containing and VP1-absent fractions ([Figure 3.7D](#)). Moreover, the particle density of fraction of interest (25-30%) increased ([Figure 3.8D](#)). However, protein aggregates were still present.

To eliminate these contaminants in the scaled-up viral protein production, a double filtration was introduced prior to SDG (strategy E, [Figure 3.6E](#)). This additional clarification step did not appear to affect the viral protein concentration, as evidenced by the high band intensity similarity between strategies D and E ([Figure 3.7E](#)). Additionally, the number of contaminants were significantly reduced ([Figure 3.8E](#)). To further enhance purity, this step was shifted up in the process (strategy F, [Figure 3.6F](#)). However, the amount of viral protein yield at the end of the process appeared to decrease, as evidenced by the reduced band intensity on western blot ([Figure 3.7F](#)). Contributing to the hypothesis that the total protein concentration was low, the SDS PAGE gel only indicated dim bands ([Figure 3.7F](#)). Surprisingly, EM investigation of the most promising fraction (25-30%) indicated a high particle density and purity ([Figure 3.8F](#)), with only marginal amounts of protein aggregates that could be attributed to VLP disintegration.

The results of strategy F showed the most promising outcomes for EV71 VLP purification, as evident from the low levels of contaminating proteins on SDS PAGE ([Figure 3.7F](#)), clear visualization of VP1 band on western blot ([Figure 3.7F](#)), and presence of VLPs without protein aggregates in the EM image ([Figure 3.8F](#)). The SDG fraction with the highest band intensity in strategy F (25-30%) was subjected to BCA analysis and a total protein concentration of ~15.8 mg/ml (final volume ~4 ml; ~158 mg/l of culture medium) was determined.

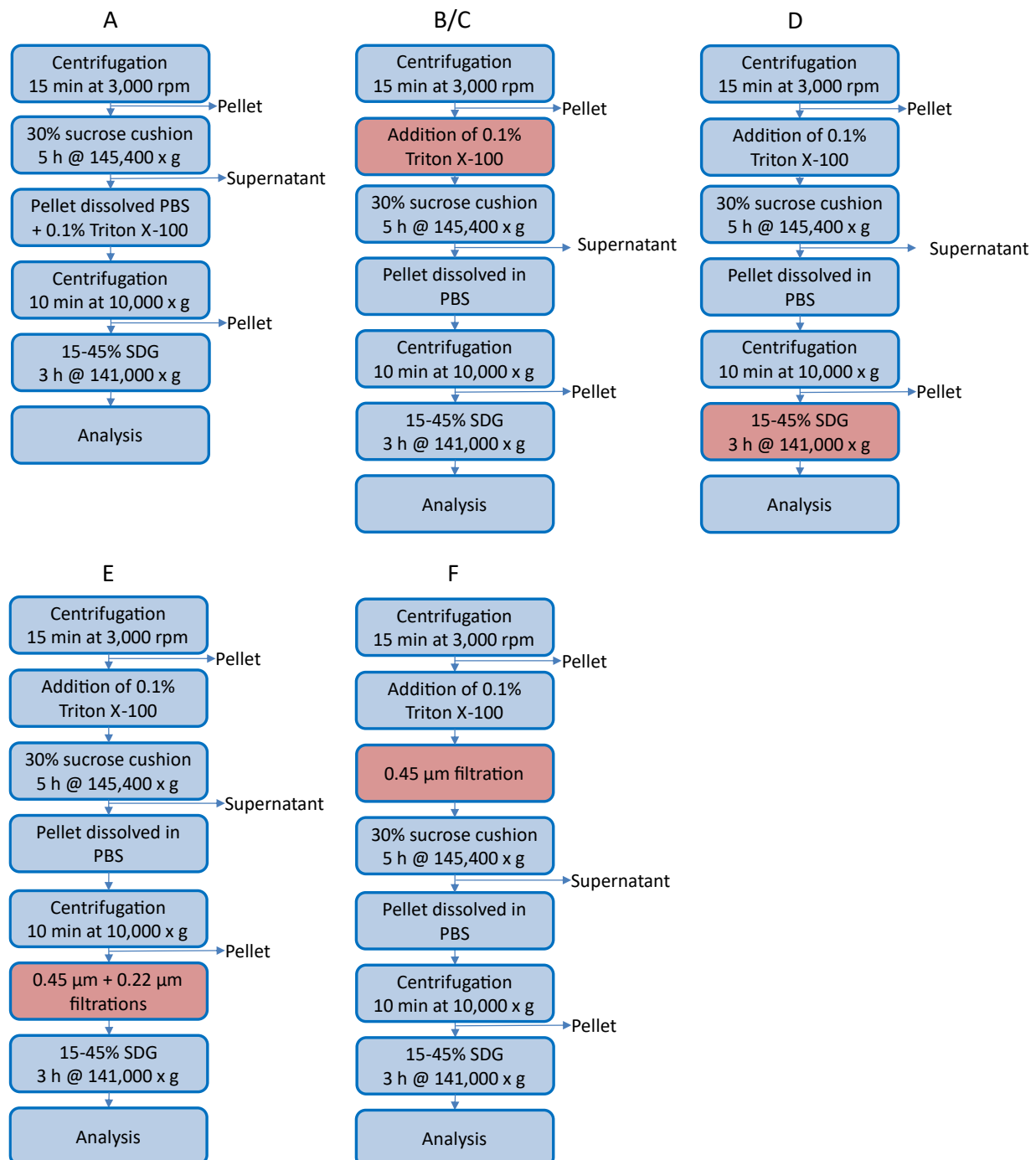


Figure 3.6. Overview investigated EV71 VLP DSP strategies. Strategy A was obtained from literature²³ and the most successful protocol (strategy F) was obtained after stepwise optimization (A through F).

Red boxes indicated changes from the preceding DSP strategy. (A) Strategy for the DSP of EV71 VLPs produced at small scale (50 ml) from the extracellular environment, protocol was adapted from REF²³. (B) As in Strategy A, but with Triton X-100 treatment prior to the sucrose cushion. (C) Identical to strategy B with a scaled-up culture volume (400 ml). (D) As in Strategy C, but with an increased volume of the sucrose density gradient (SDG; 10 \nearrow 30 ml final volume). (E) As in Strategy D, but with additional clarification (filtration) steps prior to SDG. (F) As in strategy E, with additional clarification (filtration) step prior to the sucrose cushion. This was the most successful protocol and maintained the standard for our EV71 VLP purifications.

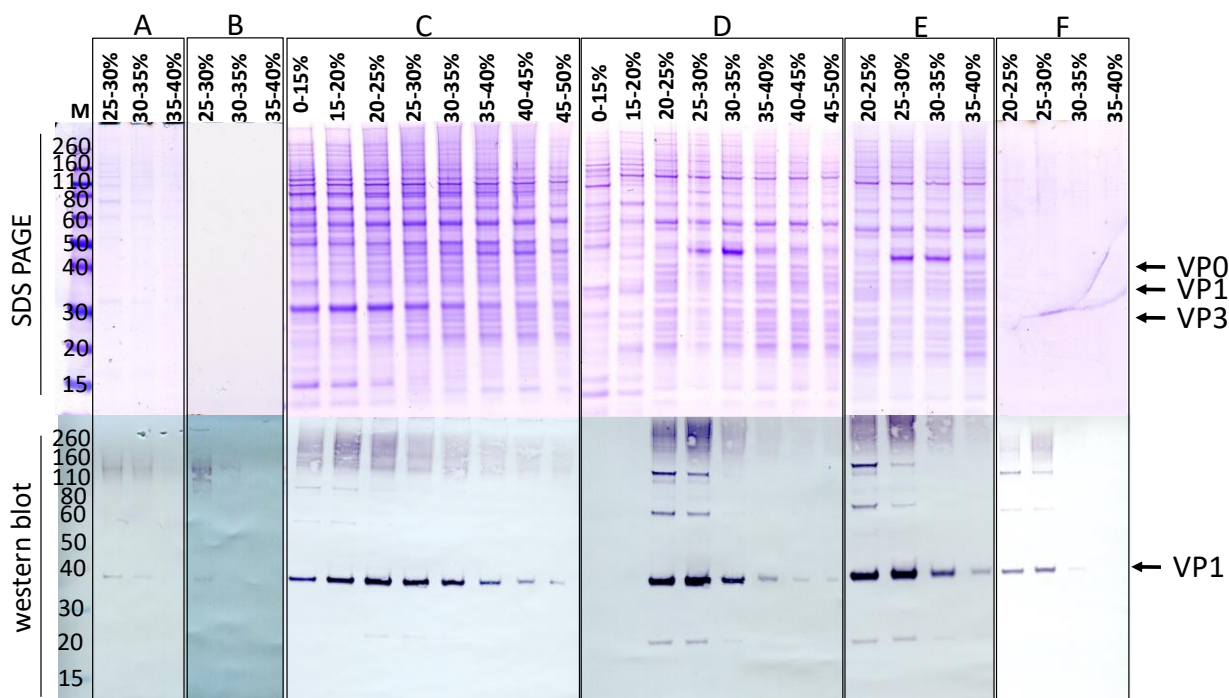


Figure 3.7. independent SDS PAGE gels and western blots for all VP1-indicating samples of the SDGs of each DSP strategy.

All strategies are described in [Figure 3.6](#). Running conditions are described in section 3.4.3. The proteins found on SDS PAGE are hypothesized to be viral proteins VP0 (38 kDa), VP1 (35 kDa), and VP3 (27 kDa).

Since the two VLPs originated from the same *Enterovirus* genus, we expected purification protocols to be universally applicable. To test this hypothesis, DSP strategy F ([Figure 3.6F](#)) was applied to the CVA6 VLP production batches. Unfortunately, the protocol that could successfully purify EV71 VLPs did not yield similar results for CVA6 VLPs, as demonstrated by the widespread distribution of CVA6 VP1 in the majority of the SDG fractions ([Figure 3.9B](#); Strat. F; western blot). Additionally, there are contaminant proteins visible on the SDS PAGE gel ([Figure 3.9B](#); Strat. F; SDS PAGE). The most plausible explanation for these observations is the presence of aggregates resulting from the high MOI, high VCD and prolonged infection period for CVA6 (see section 3.2.2). To ascertain that the previously most promising fraction (25-30%) did not contain VLPs to the extent that the EV71 fractions did, EM images were taken ([Figure 3.9C](#)). The images revealed a clear background with large structures, effectively masking any VLP presence, and supporting the hypothesis of extensive protein aggregation.

To address the issues encountered when applying strategy F to CVA6 VLP purification, we designed strategy G ([Figure 3.9A](#)). Strategy G involved an additional filtration step prior to the sucrose cushion, which resulted in a lower concentration of viral proteins on SDS PAGE gel ([Figure 3.9B](#); Strat. G; SDS PAGE). Furthermore, the gel indicated that the VP1 and VP0 bands were overlapping, VP3 was produced and presented at its correct size (~27 kDa), and analogously to all previous western blots for CVA6, a truncated version of VP1 (VP1*) was apparent^{35,36}. Lastly, at approximately

60 kDa an additional band was visible which could be host cell proteins or an uncleaved VP0-VP3 protein, as previously observed for EV71 and CVA16^{34,36}. The SDS PAGE indicated high purity, as there was only a minimal number of contaminant protein visible, and the western blot showed a clear non-equilibrium distribution of VP1 in multiple fractions, with the 25-30% fractions being the most promising anew (**Figure 3.9B**; Strat. G; western blot). EM images indicated the presence of assembled VLPs in large excess of the observed protein aggregates (**Figure 3.9D**). Overall, we concluded that strategy G yielded highly pure CVA6 VLPs in the most promising SDG fraction (25-30%). The total protein concentration of the purified CVA6 VLPs was determined to be ~3.8 mg/ml (final volume ~4 ml; ~38 mg/l of culture medium).

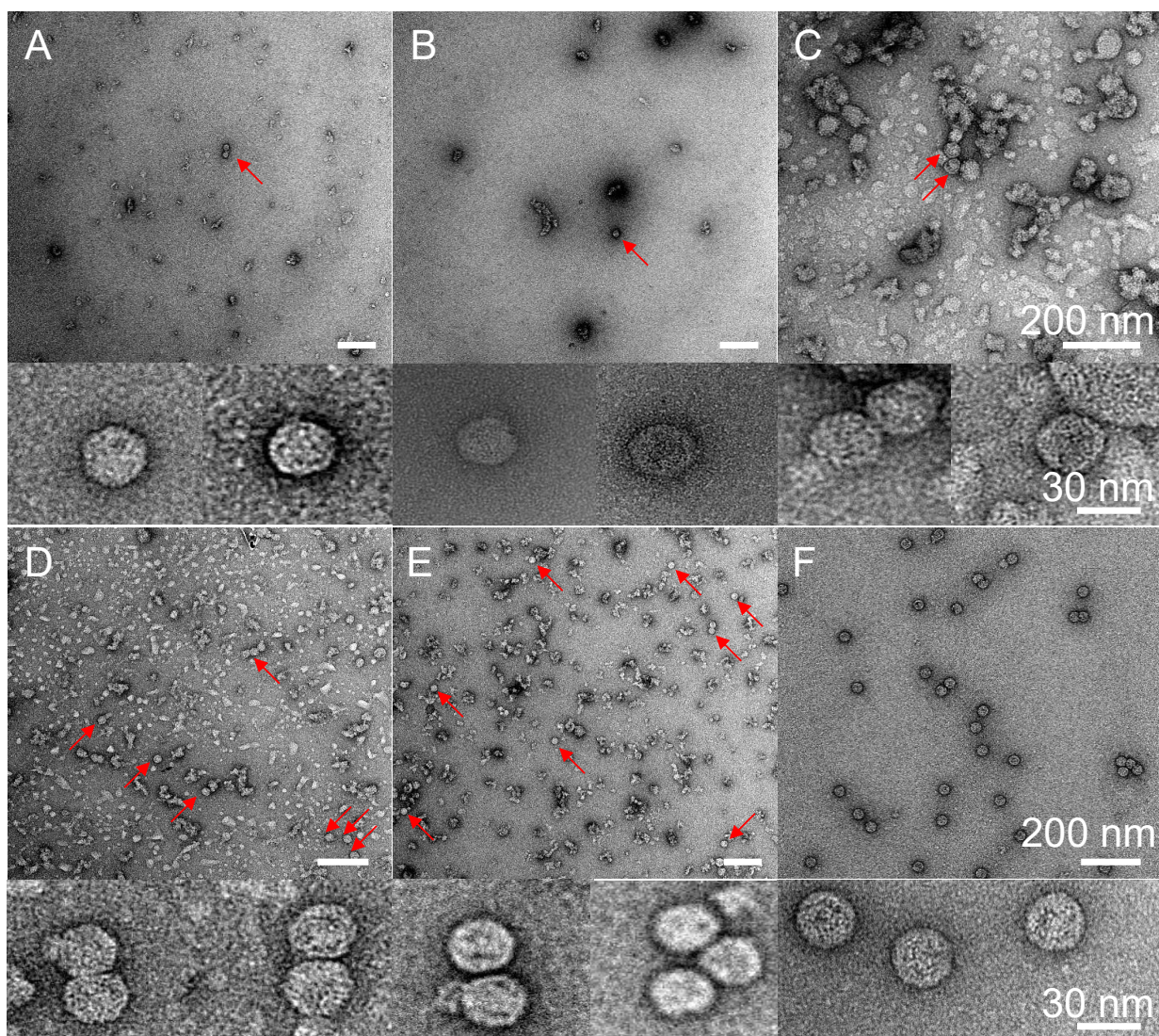


Figure 3.8. Electron microscopy images of most promising fractions of the SDGs of strategies A-F.

All strategies are described in **Figure 3.6**. Experimental conditions are described in section 3.4.6. White scale bars in the labeled images represent 200 nm, whereas in the insets the scale bars represent 30 nm. For each strategy, two examples of VLPs are presented below the images.

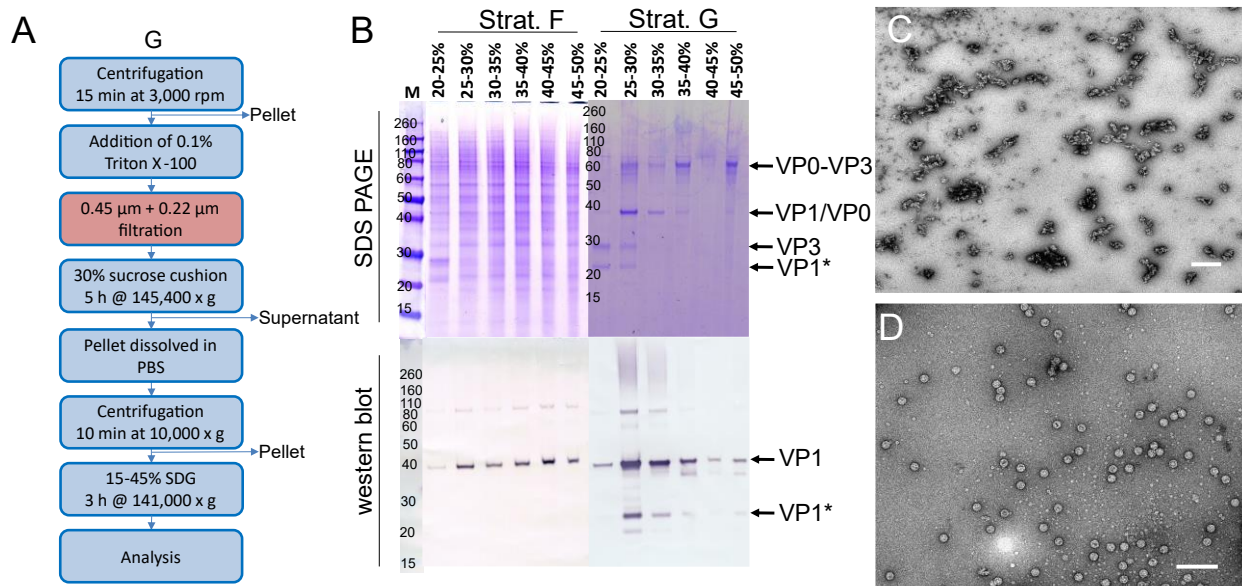


Figure 3.9. CVA6 VLP purification process.

(A) CVA6-specific DSP strategy for the purification of 400 ml cell cultures containing VLPs. (B) SDS PAGE gels and western blots for all VP1-indicating samples of the SDGs of both CVA6 VLP DSP strategies. (C) Electron microscopy image of most promising fraction of the SDG producing by employing strategy F on CVA6 VLPs. Experimental conditions are described in section 3.4.6. The white scale bar indicates 200 nm. (D) Electron microscopy image of most promising fraction of the SDG of strategy G on CVA6 VLPs. Experimental conditions are described in section 3.4.6. The white scale bar indicates 200 nm.

3.3 Discussion

In this study, we have presented a successful optimization of EV71 and CVA6 VLP for potential vaccine purposes. Two optimization studies (production and purification) have been conducted to obtain VLPs with a high production yield and high purity.

Optimization of infection conditions was performed based on western blot band intensity and confirmed using ELISA assays. Thus, for EV71, the optimum infection conditions were determined to be low multiplicity of infection (0.001), a low viable cell density at the time of infection (5.0×10^5 cells/ml), and a long infection period (6 d), but further research is needed to obtain a more accurate model due to Lack of Fit. The EV71 VLP results presented in this study could serve as a basis for future optimization studies aimed at exploring optimal conditions in greater depth, potentially leading to the development of a highly precise model.

For CVA6 VLPs, two iterations of DoE were performed, and the optimum infection parameters were determined to be high MOI (5), high VCD (1.0×10^6 cells/ml), and a long infection period (7 d). The infection period is relatively long in comparison to previous studies, which could be deleterious for its cost-effectiveness^{23,27,29,31-36}. A high MOI was observed in multiple studies, even exceeding the MOI used in this study^{23,27,29,32}.

We note that the model presented in this study exhibited robust performance parameters, indicating a high degree of accuracy and reliability in predicting infection outcomes under non-experimentally measured conditions. Specifically, higher VCD and longer infection periods are recommended as input factors for an additional iteration of DoE to determine an even more favorable set of infection conditions for VLP production. Additionally, a large amount of previous work has described infection with high cell density cultures ($\geq 2,000,000$ cells/ml in comparison to our 1,000,000 cells/ml for CVA6), which could possibly yield higher viral protein yields^{23,24,27,32,35}. However, it is important to consider the potential drawbacks. The trade-off is that higher cell densities over long infection periods can cause cell death and result in an increased amount of cell debris, making VLP purification more challenging. Therefore, a careful balance between these factors must be considered in optimizing the VLP production process further. Additionally, culturing in Erlenmeyer culture flasks limits the operating mode to batch. While medium can be replenished during the infection period, this results in a loss of product and baculovirus. Bioreactors can allow for fed-batch or even continuous feed and harvesting, but will lower the viral protein yield/volume and increase the cost significantly^{27,34}.

Optimization of the purification process for EV71 VLPs generated a final yield of 158 mg/l of culture volume. This yield represented a 2.5-fold increase over the previously reported highest yield obtained in bioreactors of 64.3 mg/l²⁷. Furthermore, a separate process optimization study yielded a final VLP concentration that is ~2- fold lower than the yield presented here³⁴. And lastly, despite using a 100-fold lower MOI (thus lower viral stock consumption) and a 2-fold lower VCD (thus less bioreactor process time), a highly similar yield to the highest reported yield was achieved²⁸. Additionally, given the previously determined potent immunogenicity offered by enterovirus VLPs (EV71) at 1-5 μg , translates to 31,600-158,000 doses per liter of Hi5 culture medium, demonstrating the EV71 VLP vaccine's economical potential^{23,28,35}.

The optimization study of the purification process for CVA6 VLPs resulted in a final yield of 38 mg/l of culture volume, a 4-fold decrease in comparison to the EV71 VLPs due to the additional filtration step. The lack of a previously reported yield for CVA6 VLPs makes it challenging to make comparisons. Still, the previously determined potent immunogenicity offered by enterovirus VLPs (EV71) at 1-5 μg , translates to 7,500-37,500 doses per liter of Hi5 culture medium, confirming the similar economic potential for a CVA6 VLPs to EV71 VLPs^{23,28,35}.

3.4 Materials & Methods

3.4.1 Construction of recombinant baculoviruses

Previously reported construct optimizations for the production of enterovirus A71 (EV71) indicated that the highest viral protein yield was obtained using the P1 and 3CD coding sequences behind the *polh* and *CMV* promoter, respectively²⁸. Two transfer plasmids, containing the aforementioned genes originating from EV71_C4 and CVA6, were amplified using *E. coli* JM109 competent cells (Promega) and isolated using NucleoBond Xtra Midi EF (Macherey-Nagel). The amplified transfer plasmids were checked by double digestion using multiple restriction enzyme pairs. To construct the recombinant baculovirus, the transfer plasmid and *flashBAC* GOLD DNA (Oxford Expression Technologies) were co-transfected into Sf9 cells (Gibco). The two different baculovirus stocks for the EV71 and CVA6 origin viral proteins, respectively, were designated BacV-EV71 and BacV-CVA6. The baculovirus was propagated over the course of 3 passages and titered by end-point-dilution method using Sf9 Easy Titer (Sf9ET) (Kerafast) cells according to the manufacturer's protocol.

3.4.2 Viral protein production & purification

EV71 and CVA6 VLP production was accomplished by infection of High Five™ cells (Gibco). Erlenmeyer culture flasks (125 ml) with 50 ml working volumes of Hi5 cells (cell density dependent on specific experiment) were infected by either BacV-EV71 or BacV-CVA6 (MOI dependent on experiment) in Sf-900IISFM (Gibco). After the infection period (dependent on experiment), the cultures were harvested using centrifugation (Heraeus) at 3,000 rpm for 15 min at 4 °C. The pellet was discarded, and the supernatant was supplemented with Triton X-100 (final concentration 0.1%) to prevent protein aggregation. The viral protein production optimization analysis was performed on this sample. For purification optimization, the most successful protocol started from this point.

The Triton X-100 supplemented supernatant was double filtered using 0.45 µm and 0.22 µm filters (Millex). The filtered supernatant was subjected to sucrose cushion ultracentrifugation (30% W/W sucrose in PBS) for 5 h at 141,000 × g. The pellet was resuspended in 1 ml phosphate-buffered saline (PBS, Gibco) and subjected to another centrifugation (10,000 × g, 10 min), after which the pellet was discarded, and the supernatant was applied onto a discontinuous sucrose density gradient (SDG) (15-45% W/W sucrose in PBS) and ultracentrifuged for 3 h at 141,000 × g (ThermoFisher Scientific). The SDG was harvested by 1 ml sampling from the top. Samples were pooled into 8 concentration ranges based on the percentage of sucrose (0%-15%, 15%-20%, 20%-25%, 25%-30%, 30%-35%, 35%-40%, 40%-45%, and 45%-50%), whereby sucrose density was measured by refractometer (Hanna instruments).

3.4.3 SDS PAGE & Western blot

To confirm the viral protein production of EV71 and CVA6, anti-VP1 (both origins) western blot analysis and SDS PAGE was performed. For this, 40 µl of each culture

was mixed with 10 μ l loading buffer (Intravacc) and heated at 100 °C for 15 min. Then, 15 μ l of each mixture was loaded on NuPAGE™ 10% Bis-Tris gel (Invitrogen) and electrophoresis was performed at 200 V for 45 min. The gel was washed three times for 5 min using purified water. Dependent on the purpose of the gel, it was subjected to staining (SDS PAGE, section 3.4.3.1) or overnight blocking (Western blot, section 3.4.3.2)

3.4.3.1 SDS PAGE

The gel was stained with Imperial™ protein stain (Thermo Fisher Scientific) for 1 h and destained in multiple cycles and overnight using purified water.

3.4.3.2 Western blot

The proteins were blotted onto a nitrocellulose membrane (ThermoFisher Scientific) using a semi-dry blotting machine (Hoefer) run at 60 mA for 60 min. The membrane was washed two times in wash buffer (PBS + 0.1% W/W Tween 20 (Sigma-Aldrich)) and blocked overnight at 4 °C (PBS + 0.1% Tween 20 (Sigma-Aldrich), and 0.5% Protifar (Nutricia)). Next, the membrane was incubated with 1:1,000 of either mouse anti-EV71-VP1 (Abnova, MAB1255-M08) or rabbit anti-CVA6-VP1 (ThermoFisher Scientific, PA5-112001) in block buffer for 90 min on a roller incubator. The membrane was washed five times using wash buffer and incubated with 1:2,000 of either goat anti-mouse IgG Human ads-AP (Southern Biotech, 1030-04) or goat anti-rabbit IgG Human ads-AP (Southern Biotech, 4050-04) in block buffer for 90 min on a roller incubator. The membrane was washed three times using wash buffer and once using purified water. The membrane was colored using AP conjugate substrate kit (BIO-RAD, 1706432). The colorization reaction was terminated by the addition of an excess of purified water.

3.4.4 Enzyme-Linked Immunoassay

EV71 VP1 ELISA was performed using ELISA kit (Abnova, KA1677), according to manufacturer's instructions.

To confirm western blot results for CVA6, an ELISA using anti-CVA6 A-Particle (Creative Biolab) was performed. To this end, 100 μ l of sample was added to a 96-well high-binding ELISA plate (Greiner Bio-One) and 1:1 serial diluted in PBS. The plate was incubated at RT overnight. The plate was subjected to three wash cycles (purified water + 0.05% Tween80 (Sigma-Aldrich)). Plates were blocked using 150 μ l of block buffer (PBS + 0.5% bovine serum albumin (BSA, SERVA)) for 30 min at 37 °C. Each plate was then subjected to three wash cycles using a washer dispenser (BioTek, EL406). The primary antibody (recombinant mouse anti-CVA6 A-particle, Creative Biolabs, PABC-483) was added in a final concentration of 0.1 μ g/mL in 100 μ l/well assay buffer (PBS + 0.05% Tween80) and incubated at 37 °C for 1 h. The plates were washed three times, after which secondary antibody (goat anti-mouse IgG-HRP (Southern Biotech, 1030-05) was diluted 5,000-fold in PBS, and 100 μ l of the result per well was added to the plate and incubated at 37 °C for 1 h. The wells were washed

three times, and 100 μ l of HRP substrate (Ultra TMB-ELISA (Thermo Fisher Scientific)) was added to each well and incubated for 10 min in RT. To quench the reaction, 100 μ l of 0.2 M sulfuric acid was added to each well. The wells' light absorption was measured at 450 nm using a plate reader (BioTek synergy neo2 reader).

3.4.5 Design of Experiments

To investigate the optimized conditions and analyze the output for viral protein production in terms of MOI, VCD, and infection period (the three DoE input factors), a Design of the Experiments was performed using the full-factorial model of model software MODDE12 (Sartorius).

3.4.6 Electron Microscopy

Electron microscopy was employed for the direct visualization of the VLPs. Of each DSP sample, 3 μ L was blotted on EM grids (Quantifoil, carbon-supported, Cu-400) in three consecutive iterations with 60 s of incubation time. Next, grids were subjected to two wash cycles using 10 μ l PBS. Excess liquid was blotted away using filter papers. Staining was performed using 2% uranyl acetate for 1 min. Excess liquid was blotted away using filter paper. Imaging was performed using a Jeol JEM-1400 plus TEM.

3.4.7 Bicinchoninic acid (BCA) total protein assay

Bovine Serum Albumin (BSA), with a stock concentration of 2 mg/ml, was subjected to serial dilution in PBS to generate a standard curve ranging from 0 to 320 μ g/ml. Samples were appropriately diluted in PBS to ensure that their concentrations fell within the linear range of the standard curve. Subsequently, 25 μ l of each sample or standard was added to a 96-well plate, followed by addition of 200 μ l of BCA reagent mixture (a combination of BCA reagent A and B in a 40:1 ratio, sourced from the Pierce™ BCA Protein Assay Kit, Thermo Fisher Scientific) to each well. The plate was then incubated at 37 °C for 30 min, after which the absorbance was measured at 562 nm, and the resulting values were used to calculate the protein concentration using the standard curve.

3.5 References

1. Sabanathan S, Van Tan L, Thwaites L, Wills B, Qui PT, Van Doorn HR. Enterovirus 71 related severe hand, foot and mouth disease outbreaks in South-East Asia: Current situation and ongoing challenges. *Journal of Epidemiology and Community Health*. 2014;68(6):500-502. doi:10.1136/jech-2014-203836
2. Ventarola D, Bordone L, Silverberg N. Update on hand-foot-and-mouth disease. *Clinics in Dermatology*. 2015;33(3):340-346. doi:10.1016/j.clindermatol.2014.12.011
3. Zhang M, Chen X, Wang W, Li Q, Xie Z. Genetic characteristics of Coxsackievirus A6 from children with hand, foot and mouth disease in Beijing, China, 2017–2019. *Infection, Genetics and Evolution*. 2022;106(August):1-9. doi:10.1016/j.meegid.2022.105378
4. Gopalkrishna V, Ganorkar N. Epidemiological and molecular characteristics of circulating CVA16, CVA6 strains and genotype distribution in hand, foot and mouth disease cases in 2017 to 2018 from Western India. *Journal of Medical Virology*. 2021;93(6):3572-3580. doi:10.1002/jmv.26454
5. Zeng H, Lu J, Zheng H, et al. The epidemiological study of Coxsackievirus A6 revealing hand, foot and mouth disease epidemic patterns in Guangdong, China. *Scientific Reports*. 2015;5(May):1-8. doi:10.1038/srep10550
6. Nguyen TT, Chiu CH, Lin CY, et al. Efficacy, safety, and immunogenicity of an inactivated, adjuvanted enterovirus 71 vaccine in infants and children: a multiregion, double-blind, randomised, placebo-controlled, phase 3 trial. *The Lancet*. 2022;399(10336):1708-1717. doi:10.1016/S0140-6736(22)00313-0
7. Elveborg S, Monteil VM, Mirazimi A. Methods of Inactivation of Highly Pathogenic Viruses for Molecular, Serology or Vaccine Development Purposes. *Pathogens*. 2022;11(2):1-25. doi:10.3390/pathogens11020271
8. Qian C, Liu X, Xu Q, et al. Recent progress on the versatility of virus-like particles. *Vaccines*. 2020;8(1):1-14. doi:10.3390/vaccines8010139
9. Tariq H, Batool S, Asif S, Ali M, Abbasi BH. Virus-Like Particles: Revolutionary Platforms for Developing Vaccines Against Emerging Infectious Diseases. *Frontiers in Microbiology*. 2022;12(January). doi:10.3389/fmicb.2021.790121
10. Tan S, Tan X, Sun X, et al. VP2 Dominated CD4+ T Cell Responses against Enterovirus 71 and Cross-Reactivity against Coxsackievirus A16 and Polioviruses in a Healthy Population. *The Journal of Immunology*. 2013;191(4):1637-1647. doi:10.4049/jimmunol.1301439
11. Zhao S, Ke J, Yang B, et al. A protective AAV vaccine for SARS-CoV-2. *Signal Transduction and Targeted Therapy*. 2022;7(1):2-5. doi:10.1038/s41392-022-01158-w
12. Xu L, Zheng Q, Li S, et al. Atomic structures of Coxsackievirus A6 and its complex with a neutralizing antibody. *Nature Communications*. 2017;8(1):1-12. doi:10.1038/s41467-017-00477-9

13. Büttner CR, Spurný R, Füzik T, Plevka P. Cryo-electron microscopy and image classification reveal the existence and structure of the coxsackievirus A6 virion. *Communications Biology*. 2022;5(1). doi:10.1038/s42003-022-03863-2
14. Cao J, Liu H, Qu M, et al. Determination of the cleavage site of enterovirus 71 VP0 and the effect of this cleavage on viral infectivity and assembly. *Microbial Pathogenesis*. 2019;134(June):103568. doi:10.1016/j.micpath.2019.103568
15. Logan G, Newman J, Wright CF, et al. Deep Sequencing of Foot-and-Mouth Disease Virus Reveals RNA Sequences Involved in Genome Packaging. *Journal of Virology*. 2018;92(1). doi:10.1128/jvi.01159-17
16. Arnold E, Luo M, Vriend G, et al. Implications of the picornavirus capsid structure for polyprotein processing. *Proceedings of the National Academy of Sciences of the United States of America*. 1987;84(1). doi:10.1073/pnas.84.1.21
17. Jiang P, Liu Y, Ma HC, Paul A V., Wimmer E. Picornavirus Morphogenesis. *Microbiology and Molecular Biology Reviews*. Published online 2014. doi:10.1128/MMBR.00012-14
18. Lee H, Shingler KL, Organtini LJ, et al. The novel asymmetric entry intermediate of a picornavirus captured with nanodiscs. *Science Advances*. 2016;2(8). doi:10.1126/sciadv.1501929
19. Ren J, Wang X, Hu Z, et al. Picornavirus uncoating intermediate captured in atomic detail. *Nature Communications*. 2013;4. doi:10.1038/ncomms2889
20. Shingler KL, Yoder JL, Carnegie MS, et al. The Enterovirus 71 A-particle Forms a Gateway to Allow Genome Release: A CryoEM Study of Picornavirus Uncoating. *PLoS Pathogens*. 2013;9(3). doi:10.1371/journal.ppat.1003240
21. Zhou Y, Shen C, Zhang C, et al. Yeast-produced recombinant virus-like particles of coxsackievirus A6 elicited protective antibodies in mice. *Antiviral Research*. Published online 2016. doi:10.1016/j.antiviral.2016.06.004
22. Shen C, Ku Z, Zhou Y, et al. Virus-like particle-based vaccine against coxsackievirus A6 protects mice against lethal infections. *Vaccine*. Published online 2016. doi:10.1016/j.vaccine.2016.06.028
23. Kim, HJ Son, HS Lee, SW Yoon, Y Hyeon, JY Gyung, TC Lee JYJ. Efficient expression of enterovirus 71 based on virus-like particles vaccine. *PLoS ONE*. 2019;14(3). doi:10.1371/journal.pone.0210477
24. Lin SY, Sung LY, Yeh CT, Yu CP, Yang JY, Hu YC. Production and purification of virus-like particles of different enterovirus subtypes as vaccines. *Journal of the Taiwan Institute of Chemical Engineers*. 2018;82:1-9. doi:10.1016/j.jtice.2017.10.020
25. Fuenmayor J, Gòdia F, Cervera L. Production of virus-like particles for vaccines. *New Biotechnology*. Published online 2017. doi:10.1016/j.nbt.2017.07.010

26. Dai W, Zhang C, Zhang X, et al. A virus-like particle vaccine confers protection against enterovirus D68 lethal challenge in mice. *Vaccine*. 2018;36(5):653-659. doi:10.1016/j.vaccine.2017.12.057
27. Chung CY, Chen CY, Lin SY, et al. Enterovirus 71 virus-like particle vaccine: Improved production conditions for enhanced yield. *Vaccine*. 2010;28(43):6951-6957. doi:10.1016/j.vaccine.2010.08.052
28. Lin SY, Yeh CT, Li WH, et al. Enhanced enterovirus 71 virus-like particle yield from a new baculovirus design. *Biotechnology and Bioengineering*. 2015;112(10):2005-2015. doi:10.1002/bit.25625
29. Chung Y chi, Huang J huang, Lai C wei, et al. Expression, purification and characterization of enterovirus-71 virus-like particles. 2006;12(6):921-927.
30. Anderson M. Design of experiments. *Industrial Physicist*. 1997;3(2). doi:10.4324/9780203324073_chapter_4
31. Shih-Yeh Lin a , Li-Yu Sung a , Chia-Tsui Yeh b , c , Cheng-Ping Yu b , d , Jyh-Yuan Yang e YCH. Production and purification of virus-like particles of different enterovirus subtypes as vaccines. *Journal of the Taiwan Institute of Chemical Engineers*. 2018;82:1-9.
32. Lin SY, Chung YC, Chiu HY, Chi WK, Chiang BL, Hu YC. Evaluation of the stability of enterovirus 71 virus-like particle. *Journal of Bioscience and Bioengineering*. 2014;117(3):366-371. doi:10.1016/j.jbiosc.2013.08.015
33. Lin YL, Yu CI, Hu YC, et al. Enterovirus type 71 neutralizing antibodies in the serum of macaque monkeys immunized with EV71 virus-like particles. *Vaccine*. 2012;30(7):1305-1312. doi:10.1016/j.vaccine.2011.12.081
34. Lin SY, Chiu HY, Chiang BL, Hu YC. Development of EV71 virus-like particle purification processes. *Vaccine*. 2015;33(44):5966-5973. doi:10.1016/j.vaccine.2015.04.077
35. Zhang W, Dai W, Zhang C, et al. A virus-like particle-based tetravalent vaccine for hand, foot, and mouth disease elicits broad and balanced protective immunity article. *Emerging Microbes and Infections*. 2018;7(1). doi:10.1038/s41426-018-0094-1
36. Gong M, Zhu H, Zhou J, et al. Cryo-Electron Microscopy Study of Insect Cell-Expressed Enterovirus 71 and Coxsackievirus A16 Virus-Like Particles Provides a Structural Basis for Vaccine Development. *Journal of Virology*. 2014;88(11):6444-6452. doi:10.1128/jvi.00200-14
37. Lazar I. GelAnalyzer. GelAnalyzer. Published 2010. <http://www.gelanalyzer.com/>

4

Beyond the RNA: Alternative mechanisms for the stability and maturation of enterovirus-like particles

In the fight to counteract hand, foot, and mouth disease-causing viruses, most prominently enterovirus A71 and coxsackievirus A6, virus-like particles (VLPs) have emerged as a leading contender for the development of a multivalent vaccine. However, compared to inactivated vaccines, VLPs have shown rapid conversion from the highly immunogenic state (N-Ag) to the less immunogenic expanded state (H-Ag) and significantly lower particle integrity lifetimes, rendering the stability of these particles a major issue. This study investigated the reduced capsid stability of VLPs using atomic force microscopy (AFM), cryogenic electron microscopy (cryo-EM), and biochemical assays. Contrary to previous work on enterovirus VLPs, this study demonstrates that nearly one third (31%) of the produced VLPs were able to encapsidate viral RNA. Importantly, this work shows that the RNA presence in the capsids is not the primary factor that determines enterovirus capsid stability, as was previously hypothesized. Furthermore, the viral maturation that results from capsid structural changes and pocket factor binding, may be triggered by additional underlying mechanisms in addition to RNA presence. Because achieving VLP stability comparable to that of virions is of the utmost importance in ensuring the success of VLPs as vaccine candidates, these findings are important for the development of artificial methods of inducing viral maturation or alternative means of capsid stabilization.

4.1 Introduction

Hand, foot, and mouth disease (HFMD) is becoming an increasingly concerning issue in the South-East Asian region¹. Although vaccination campaigns against the conventionally most prevalent strain, enterovirus A71 (EV71), were initially successful, the emergence of other HFMD-causing viruses, most notably coxsackievirus A6 (CVA6), has tempered these successes. To combat the resurfacing of new disease-causing strains, there is a pursuit to develop a multivalent vaccine, which could provide an answer. Virus-like particles (VLPs) have been proposed as a superior alternative to the conventional inactivated vaccines currently available on the market². Due to their non-replicating and non-infectious nature, resulting from the proposed lack of genomic RNA, and their similar surface structure that can trigger immune responses similar or higher than their native virion counterparts, VLP vaccines offer significant advances³. However, stability remains a challenge, despite significant steps being taken with formulation strategies that have extended the particle integrity lifetime multiple fold during storage⁴.

VLPs can be produced using the baculovirus expression vector system (BEVS), in which only the P1 polyprotein and 3CD protein are expressed⁵⁻¹⁰. To date, the enterovirus VLPs has shown to lack RNA in previous reports¹¹⁻¹⁴. Nevertheless, it is possible that host cell proteins or mRNA – including the transcripts of their baculovirus expression vectors - may be encapsidated in VLPs and impact their stability¹⁵.

Several studies have attempted to increase the thermostability of VLPs by subjecting virions to random mutagenesis during cultivation at elevated temperatures and performing reverse engineering to introduce these mutations into VLPs^{16,17}. This methodology has been successfully applied to poliovirus (PV) and enterovirus A71 (EV71) at laboratory scale, and could be adapted for other (enterovirus) VLPs¹⁸⁻²⁰. The stability of the most immunogenic configuration of enteroviruses relies on the presence of a lipid molecule, called the pocket factor, in a region at the base of the canyon within VP1 (hydrophobic pocket)²¹. Moreover, the conversion of their capsids from the highly immunogenic state (D-antigen for PV; N-Ag for other enteroviruses) to the less immunogenic expanded state (C-antigen for PV; H-Ag for other enteroviruses) is linked to dissociation of the pocket factor²²⁻²⁴. Although improved stability in these studies primarily refers to thermostability, which can prevent the conversion from N-Ag to H-Ag, thermostability does not necessarily imply other forms of stability. To date, no studies have investigated the differences in particle stability, specifically with respect to the forces applied to them, between the two candidate particles that are being used and developed for enterovirus vaccine purposes: the immunogenic N-Ag native virions and VLPs.

Apart from the pocket factor, capsid stability depends on the mechanical properties of the protein shell, which may in turn depend on the way it is assembled and/or its

content. As outlined in previous work, there are two major hypotheses describing virion particle assembly^{25,26}. The first hypothesis suggests that the viral capsid is assembled prior to RNA packaging, with viral RNA (vRNA) entering the capsid during the final stage of viral morphogenesis. Evidence supports this hypothesis, as the procapsid is believed to remain in an expanded state to allow vRNA to enter. Moreover, during viral maturation, the VP0 protein is cleaved, leading to significant rearrangements of viral capsid proteins. This cleavage has been hypothesized to be regulated by vRNA presence²⁷⁻²⁹. This maturation process is crucial for enterovirus assembly and affects viral infectivity^{27,30}. The ability of VLPs to assemble in absence of vRNA additionally supports this hypothesis. The second hypothesis posits that the vRNA (or DNA) serves as a scaffold for the viral capsid proteins, or is engaged in recruiting them³¹⁻³⁵. Furthermore, it has been reported that RNA can serve as a stabilizer of enterovirus capsids, and this effect appears to be consistent across this genus³⁶⁻³⁹. We note that, depending on environmental factors such as pH and ionic strength, the scenarios envisaged by these two hypotheses could occur separately or concurrently⁴⁰.

Structurally, virions and VLPs differ in three major ways: First, native virions contain the full RNA construct, whereas VLPs may either be empty or contain vRNA and even host cell RNA. Second, native virions have VP0 cleaved into VP2 and VP4, whereas VLPs have VP0 intact. The mechanism that underlies VP0 cleavage is currently unknown. Third, native virions contain lipid pocket factors in the hydrophobic pockets of the canyons in VP1, whereas for VLPs, these pocket are empty and possibly collapsed^{12,13,23,41,42}. The pocket factor stabilizes the capsid when in transit between cells and unbinding destabilizes it after attachment prior to uncoating^{43,44}.

Viral capsid stability is commonly evaluated using biological techniques such as mutational analysis, ELISA, DLS, and infectious titer^{4,16-20,45}. While these methods provide invaluable information, they do not report directly on the underlying mechanical properties and potential influencers of capsid integrity. For instance, biophysical experiments have indicated that empty capsids produced *in vivo* by enteroviruses are relatively unstable.

In this study, we employed AFM nanoindentation experiments to explore the mechanical properties of VLPs and inactivated virions derived from two virus strains, EV71 and CVA6⁴⁶. Since vRNA has been proposed to be the primary stabilizer of virions, a comparative analysis of native RNA-containing virions and “empty” VLPs at various forces is expected to reveal substantial differences in capsid integrity. In addition, we assessed the ability of enterovirus-like particles to encapsidate vRNA using biochemical assays and interrogated the produced VLPs on this vRNA presence. Furthermore, we utilized electron microscopy (EM) to investigate the structural dissimilarities between VLPs and virions, aiming to shed light on the divergences in capsid stability and discern the essential stabilizing factors of the structure. The

integration of three significant techniques is expected to provide a comprehensive understanding of the biophysical properties and capabilities of enterovirus VLPs. This knowledge can serve as a foundation for the development of future vaccines.

4.2 Results

The production of EV71 and CVA6 VLPs was accomplished using a previously published baculovirus construct (**Figure 4.1A**)⁴⁷. Production and purification protocols were optimized to yield highly pure VLPs. In the final step of purification, sucrose density gradient (SDG) ultracentrifugation was employed to separate the VLPs from contaminants. The fraction with the highest concentration of viral proteins was determined to be 25-30% sucrose based on anti-VP1 western blot analysis (**Figure 4.1B**). Subsequently, the purity of the obtained fraction was evaluated by SDS PAGE analysis, which exhibited a low number of non-enterovirus related bands, indicating high purity of the VLPs (**Figure 4.1C**). Moreover, the viral proteins were identifiable, with significantly lower intensity of the viral protein bands for EV71 VLPs compared to CVA6 VLPs. Notably, evaluation of the CVA6 VLP gel revealed overlapping bands for VP0 and VP1, likely due to their highly similar molecular weights (36 kDa and 35 kDa, respectively)¹². Electron microscopy analysis further confirmed the high purity of the VLPs, exhibiting negligible background signal and absence of protein aggregates for both EV71 and CVA6 (**Figure 4.1D**). The smaller structures visible in the background of the CVA6 VLPs could possibly be VLP precursors, in the form of pentamers, or ferritin molecules, which are produced by many eukaryotic cells and have a size of approximately 8-15 nm^{48,49}.

To evaluate the mechanical stability of capsids derived from different sources, including virions and VLPs from both EV71 and CVA6, we employed atomic force microscopy (AFM)⁴⁶. Nanoindentation force spectroscopy, which has been demonstrated to effectively study structures at both the micro and nanoscale, was used to investigate the mechanical properties of these structures. This technique has been used to evaluate the mechanical properties of a range of structures including lipoproteins, bacteriophages, and protein capsids⁵⁰⁻⁵². We employed the AFM in two ways: in its force spectroscopy mode, the AFM cantilever was used to apply a force to the capsids to investigate their ability to withstand this force or the corresponding mechanical nanoindentation. When the capsids failed (i.e. lost their structural integrity), the corresponding critical force or critical indentation was registered (**Figure 4.2C**); in its imaging mode, the AFM was used to image the capsids before (**Figure 4.2A**) and after (**Figure 4.2B**) such nanoindentations in order to determine their status (intact, buckled, broken, collapsed etc.).

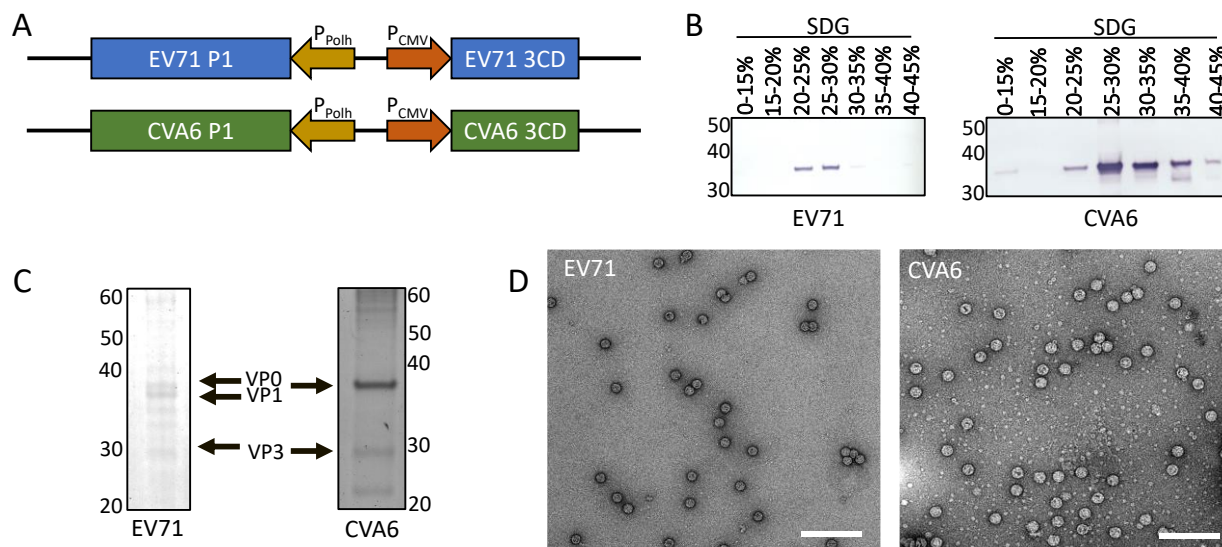


Figure 4.1. Production and evaluation of EV71 and CVA6 VLPs.

(A) Construct design for EV71 and CVA6 VLP production using the baculovirus expression vector system⁴⁷. The P1 region, coding for the structural proteins, and the 3CD protease of the different virus origins were inserted behind the polyhedrin and CMV promoters, respectively. (B) Western blot against the VP1 proteins of EV71 and CVA6. Samples originated from sucrose density gradient (SDG) fractions harvested and pooled based on sucrose percentage. For VLP production from both virus origins, the 25-30% SDG fractions were identified as most promising as they revealed the highest band intensities. (C) SDS PAGE results of the most promising fractions of EV71 and CVA6 SDG. Both VLP types indicated the viral protein bands for VP0, VP1, and VP3, albeit with dimmer bands for EV71. For CVA6, the bands for VP0 and VP1 overlap due to their highly similar molecular weights (36 kDa and 35 kDa, respectively), as can be observed by the increased intensity relative to other bands. (D) Negative stain electron microscopy images of EV71 (left) and CVA6 (right) VLPs. Size bars represent 200 nm.

In the first imaging analysis by AFM, the size of the different capsids was determined independently. It is hypothesized that VLPs are typically up to 5% larger than native virions as they exist in an expanded state^{12,13,23,41,42}. Furthermore, this ~5% difference is linked to the viral maturation which occurs in virions but not in VLPs⁵³. However, the AFM analysis indicated that both VLPs and virions, regardless of their origin, had an average diameter of 29-30 nm (**S.I. Table S.4.1**) and no significant size differences were observed (**Figure 4.2D**). The large spread in the data set could explain the lack of significant differences.

From the nanoindentation experiments, we determined the viral capsid spring constant using a previously established method⁵², in which the slope of the initial linear part of the Force-Displacement (F-Z) curve obtained from AFM nanoindentation was fitted. This fit yielded the total spring constant of the cantilever-particle system, from which the spring constant of the particle could be extracted given independent calibration of the cantilever itself⁵². The capsid spring constant is a key determinant of the mechanical properties of capsids. For EV71, the average spring constants were determined at 0.30 ± 0.18 N/m and 0.25 ± 0.14 N/m for virions (**Figure 4.2E** black; **S.I. Table S.4.1**) and VLPs (**Figure 4.2E** red; **S.I. Table S.4.1**), respectively. Furthermore,

the CVA6 spring constants of 0.38 ± 0.22 N/m and 0.31 ± 0.16 N/m for virions (Figure 4.2E blue; S.I. Table S.4.1) and VLPs (Figure 4.2E violet; S.I. Table S.4.1) also indicated no significant differences, suggesting similar stiffness between VLPs and virions, and from both origins.

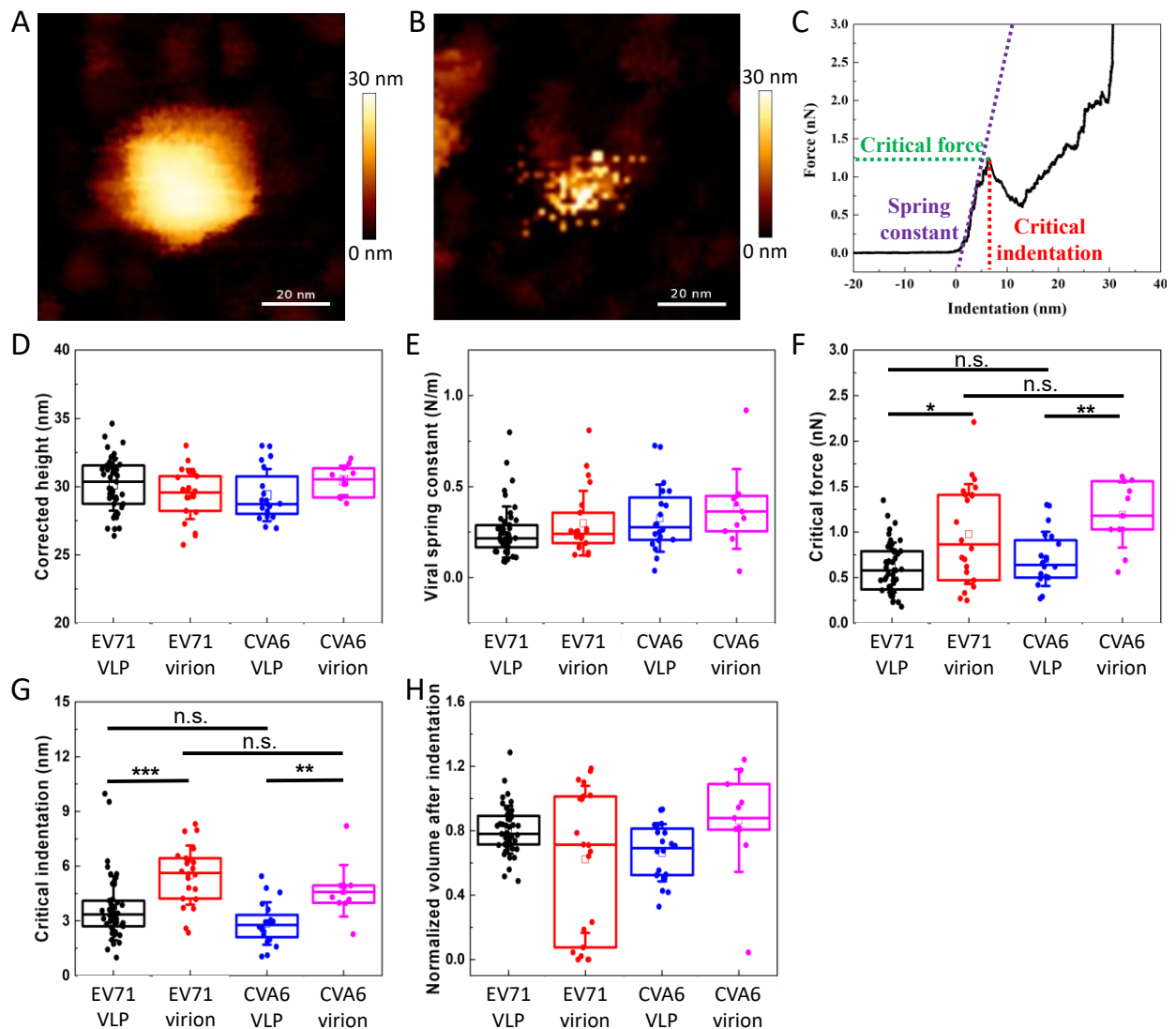


Figure 4.2. AFM results for EV71 VLPs (black), EV71 virions (red), CVA6 VLPs (blue), and CVA6 virions (violet). (A) Example of an EV71 virion prior to nanoindentation. (B) Example of EV71 virion after nanoindentation. (C) Example of a force-indentation curve obtained by AFM, highlighting the critical force (red in nN) and the corresponding critical indentation (green in nm). The spring constant is obtained as described previously⁵² in which the slope of the initial linear part of the force-displacement curve (purple) is fitted yielding the total spring constant of the cantilever-particle system. The spring constant of the cantilever was obtained from the calibration. (D) Corrected height as determined by AFM measurements. (E) Viral spring constant (N/m). (F) Critical force (nN). (G) Critical indentation (nm). (H) Normalized volume after indentation. P values are indicated by asterisks: $p < 0.001$ (***), $p < 0.01$ (**), and $p < 0.05$ (*). N.s.: not significant. (D)-(H) EV71 VLPs (black), EV71 virions (red), CVA6 VLPs (blue), and CVA6 virions (violet).

Building on the viral spring constant and confirming the similarity between the VLPs and virions from both origins, the Young modulus could be extracted (see section 4.4.5.3)⁵² similarly as previously performed for other capsids⁵⁴. The Young's moduli of 0.19 GPa and 0.17 GPa for EV71 and CVA6 virions, respectively, and 0.20 GPa and 0.22 GPa for EV71 and CVA6 VLPs, respectively, are highly similar in comparison to previously reported values for virions and VLPs^{54,55}. Despite having lower viral spring constants and the fact that differences were small the virions presented marginally lower Young's moduli than the VLPs, due to the differences in shell thickness and outer radius (**S.I. Table S.4.2**)⁵⁶.

In contrast to the spring constant, the other AFM-derived mechanical parameters indicated significant differences between virions and VLPs. Virions (**Figure 4.2F**, red and violet for EV71 and CVA6, respectively; **S.I. Table S.4.1**) exhibited a higher critical force than the VLPs (**Figure 4.2F**, black and blue for EV71 and CVA6, respectively; **S.I. Table S.4.1**), indicating their ability to withstand higher forces before failure. No significant differences were found when comparing the virions or VLPs from different origins. This supports the hypothesis that the observed differences between virions and VLPs are either due to structural differences between the two types of particles or due to the presence of specific compounds or nucleic acids in the particles, rather than their virus origins.

Logically following the observations that the spring constants were insignificantly different between virions and VLPs, and the critical force was higher for virions was higher, we observed a higher critical indentation for virions (**Figure 4.2G**, red and violet for EV71 and CVA6, respectively; **S.I. Table S.4.1**) compared to VLPs (**Figure 4.2G**, black and blue for EV71 and CVA6, respectively; **S.I. Table S.4.1**). Thus, indicating that the virions can deform significantly more than the VLPs prior to structural failure.

The differences in critical force and critical indentation suggested a different pathway of deformation and loss of particle integrity between virions and VLPs. This is further supported by the investigation of the state of the particles after indentation (**Figure 4.2H**). The effect is particularly visible for EV71, and to a lesser extent for CVA6. Notably, the VLPs of both origins (**Figure 4.2H**, black and blue) appeared to decrease somewhat in total volume after indentation ($V \sim 0.8$), whereas the virions (**Figure 4.2H**, red and violet) collapsed completely ($V < 0.2$) in multiple instances. These findings suggest that virions are more likely to disassemble completely once initial failure has occurred, indicating another difference in the mechanical properties between the two types of viral particles.

In these experiments, the virions probed had been previously chemically inactivated using formaldehyde, which induces cross-linking of viral capsids and thereby prevents viral genome release^{57,58}. Formaldehyde treatment also confers rigidity to the viral capsids, which inhibits the release of the pocket factor⁴¹. This is thought to

provide an additional contribution to inactivation, as pocket-factor release is believed to be necessary for the initiation of genome release^{41,59}. To investigate whether stabilizing effectors of formaldehyde treatment accounted for the observed differences in the mechanical properties between virions and VLPs, a supplementary batch of CVA6 VLPs underwent the same formaldehyde treatment as the CVA6 virions, after which we again performed nanoindentation force spectroscopy experiments using the AFM. From these experiments, we concluded that there was no significant difference between treated and untreated CVA6 VLPs (**S.I. Figure S.4.1A-C**, green and blue, respectively). We assume the same holds true for EV71. Therefore, it could be concluded that the inactivation process did not have any additional stabilizing effects on the CVA6 virion capsids, and a direct comparison of the two types of capsids, inactivated virions and non-treated VLPs, is justified.

The AFM data revealed significant differences between the virions and VLPs from both virus origins in terms of their mechanical properties. However, this data alone does not explain the underlying differences between the two particle types. AFM is not capable of providing the requisite spatial resolution required to identify viral maturation processes such as VP0 cleaving and pocket factor binding. A previous study utilizing cryo-EM reconstruction of the CVA6 VLP had reported an absence of viral maturation and the complete lack of any internal components, including nucleic acid. To validate these previous findings and conduct our own analysis, we employed cryo-EM to reconstruct the CVA6 VLP. Our attention was primarily focused on the CVA6 VLPs due to their high particle density and purity as compared to the EV71 VLPs, which would minimize any possible interference from any possible contaminants, resulting in higher resolution of the reconstruction.

It is widely accepted that enterovirus VLPs are usually devoid of RNA or any other internal components, and our study confirm this observation, as evidenced by the abundance of empty capsids observed (**Figure 4.3A**). Nonetheless, we also detected a significant proportion, approximately 31%, of the initial 1,128 CVA6 VLPs imaged on carbon-lacking grids exhibited heightened density at the center of their capsids (**Figure 4.3A**), as determined through 2D classification analysis. The absence of the supporting carbon film on the cryo-EM grids allows for an investigation of the electron density at the center of the capsids. The observed increase in electron density within viral capsids is commonly associated with the presence of nucleic acids or large proteins. However, the exact origin of this increased density could not be determined with certainty, owing to the dynamic nature of the structure. In instances where certain parts of the structures are highly dynamic or are oriented differently for individual images, the cryo-EM data processing tends to average out these regions, precluding their resolutions, as in the case of RNA changing orientation or conformation in a particle. Nonetheless, despite the lack of RNA in previous enterovirus VLP reconstructions^{12,13}, the most plausible explanation for this increased density is the presence of vRNA.

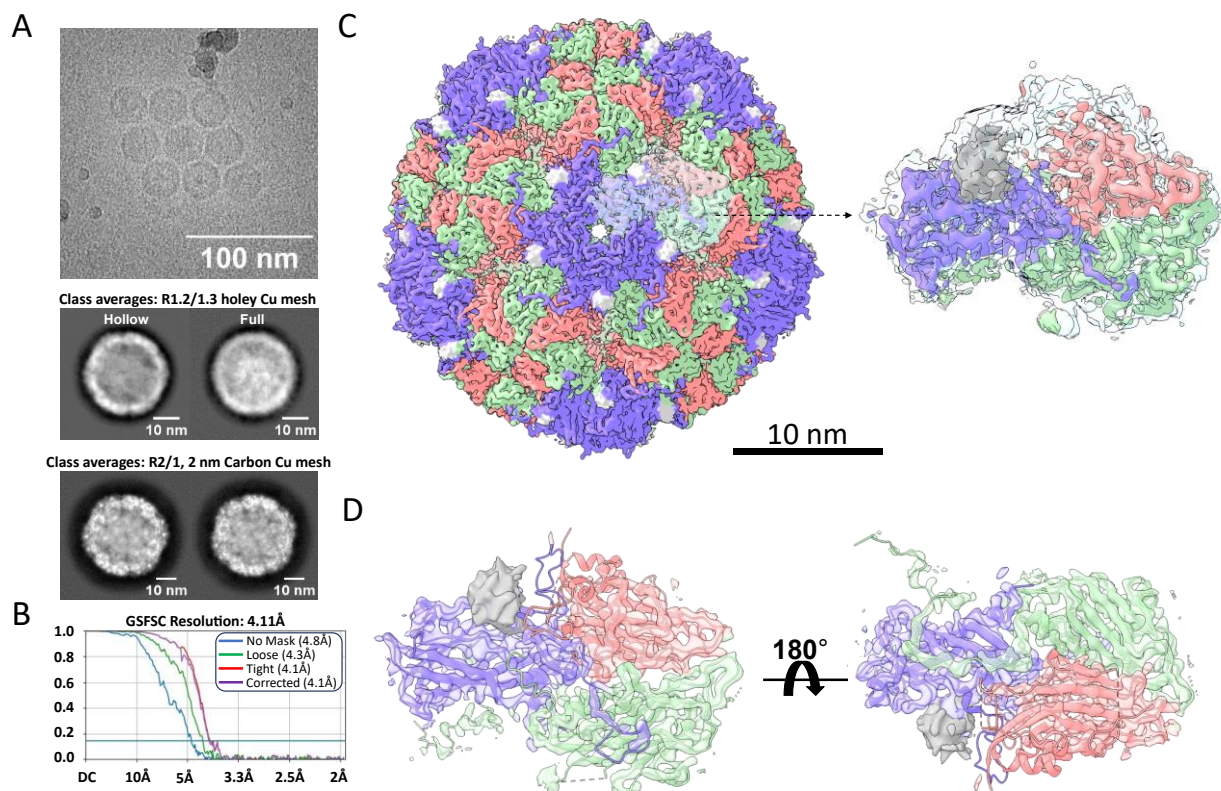


Figure 4.3. Cryogenic electron microscopy analysis of CVA6 virus-like particles.

(A) (top) Raw micrograph, no carbon, 20Kx magnification, cryo-EM, (middle) class averages of particles picked from holey grids, (bottom) class averages of particles picked from carbon-coated grids. (B) Gold-standard Fourier shell correlation coefficient (GSFSC). The method is based on the comparison of two independently reconstructed maps of the same structure (data set is randomly split in two groups), which are Fourier transformed and cross-correlated as a function of spatial frequency. The resulting FSC curve indicates the similarity (y-axis) of the two maps at each resolution (x-axis) and the resolution at which the two maps start to diverge is known as the Fourier shell correlation (FSC) cutoff of the reconstruction (horizontal line)⁶⁰. No mask (blue): no masking applied, both the structure and the solvent are included in this FSC. Loose (green): soft solvent mask applied with loose conditions. Tight (red): similar to Loose, but with tighter constraints of the mask. Corrected (violet): FSC curve calculated using the tight mask with correction by noise substitution as described previously⁶¹. (C) Cryo-EM density of CVA6 VLP full (purple: VP1; green: VP0, and red: VP3) and confidence map at 0.99 confidence (transparent) of the asymmetric unit. Unaccounted-for density is coloured grey. Scale bar represents 10 nm. (D) Fit of ASU of 5yhq to cryo-EM electron density map at 4 Å resolution, coloured by chain (purple: VP1; green: VP0, and red: VP3).

In order to enhance the particle yield for reconstruction, we utilized an alternative grid (R 2/1, 200-mesh holey carbon on copper, coated by a 2 nm carbon layer) that exhibited improved support for the VLPs as compared to the prior grids lacking the carbon layer (Figure 4.3A). However, due to the presence of the carbon layer, we were unable to investigate the increased electron density at the center of the capsids. This was a trade-off that needed to be considered in order to optimize the particle yield. A total of 7,481 particles were used for the structural reconstruction of the CVA6 VLP capsid (Figure 4.3C,D). The effective resolution of the final reconstruction was estimated at 4.1 Å according to the gold-standard Fourier shell correlation coefficient (Figure 4.3B). This method is widely used in the field of cryo-EM to assess the quality of 3D reconstructions of macromolecular structures. The method is based on the comparison

of two independently reconstructed maps of the same structure (data set is randomly split in two groups), which are Fourier transformed and cross-correlated as a function of spatial frequency. The resulting FSC curve indicates the similarity (**Figure 4.3B**, y-axis) of the two maps at each resolution (**Figure 4.3B**, x-axis) and the resolution at which the two maps start to diverge is known as the Fourier shell correlation (FSC) cutoff of the reconstruction (**Figure 4.3B**, horizontal line)^{60,61}. Refinement with optimized parameters resulted in a final EM volume of 4.01 Å resolution (**Figure 4.3C,D**).

The cryo-EM structure of the CVA6 VLP revealed typical surface features associated with enteroviruses such as the conspicuous star-shaped plateau (mesa) at the 5-fold-symmetry axes, a narrow canyon-like depression surrounding the mesa, and an open channel situated at the 2-fold axes (**Figure 4.3C**)¹². Furthermore, the cryo-EM reconstruction revealed that the structural features of the CVA6 VLPs that we produced were highly similar to the previously reported structure (**Figure 4.3D**), thus with VP0 remaining uncleaved and the hydrophobic pocket devoid of the pocket factor¹². This indicated that viral maturation did not occur in the VLPs, including in the 31% of the population that we proposed to contain RNA.

To determine the origin and significance of the increased density inside the CVA6 VLPs observed in the cryo-EM data, we employed a particle stability thermal release assay (PaSTRy)⁶² followed by qRT-PCR on the CVA6 VLPs. The assays are aimed to confirm whether the density was caused by RNA and to identify the source of the RNA. For example, PaSTRy can detect genome release by binding nucleic acids that are released from the capsids with a fluorescent dye (SYBR Green). For these experiments anew, the CVA6 VLPs were chosen for their high particle density and purity in comparison to the EV71 VLPs, which would minimize interference from any contaminants.

As expected, there was a minor fluorescence signal from the start (**Figure 4.4A**, 37-55 °C), indicating the presence of RNA in the environment, most likely due to VLP capsid disintegration. More importantly, a major fluorescence peak at 60°C (**Figure 4.4A**), consistent with the release temperature of viral genomes for enteroviruses was observed⁶³. At this temperature, the viral genomes are released from the capsids, enabling them to bind to the fluorescent dye and present a signal. In this way, we could establish that a portion of the VLPs harbored RNA. As SYBR Green binds RNA indiscriminately, the assay could not, however, discern whether the RNA present in the capsids was viral or originated from the host cell.

To verify the PaSTRy results and investigate the origin of the RNA (host cell/viral), we treated one of the CVA6 VLP samples with RNase (**Figure 4.4B**). This ensured the elimination of all RNA present in the surrounding environment (**Figure 4.4B**). Subsequently, the capsids were disrupted, and any RNA present was isolated and purified. A RT-qPCR was then performed using VP1-specific primers, targeting the P1

region of the CVA6 genome, and resulting in a 176 bp PCR-product (amplicon). Negative control samples did not show any detectable signal (Figure 4.4C, red). Conversely, the positive controls (Figure 4.4C, blue) designed to detect serial diluted plasmid did so perfectly. The obtained curve for the RNase-treated sample (Figure 4.4C, dark green triplo curves) surpassed the cycle threshold at $C_p = 32.2 \pm 0.1$ cycles (S.I. Table S.4.3). This confirmed viral RNA presence in the particles, since all RNA outside of the particles in digested (Figure 4.4B, CVA6 +RNase). Additionally, it confirms that the RNA is viral since the primers are P1 specific.

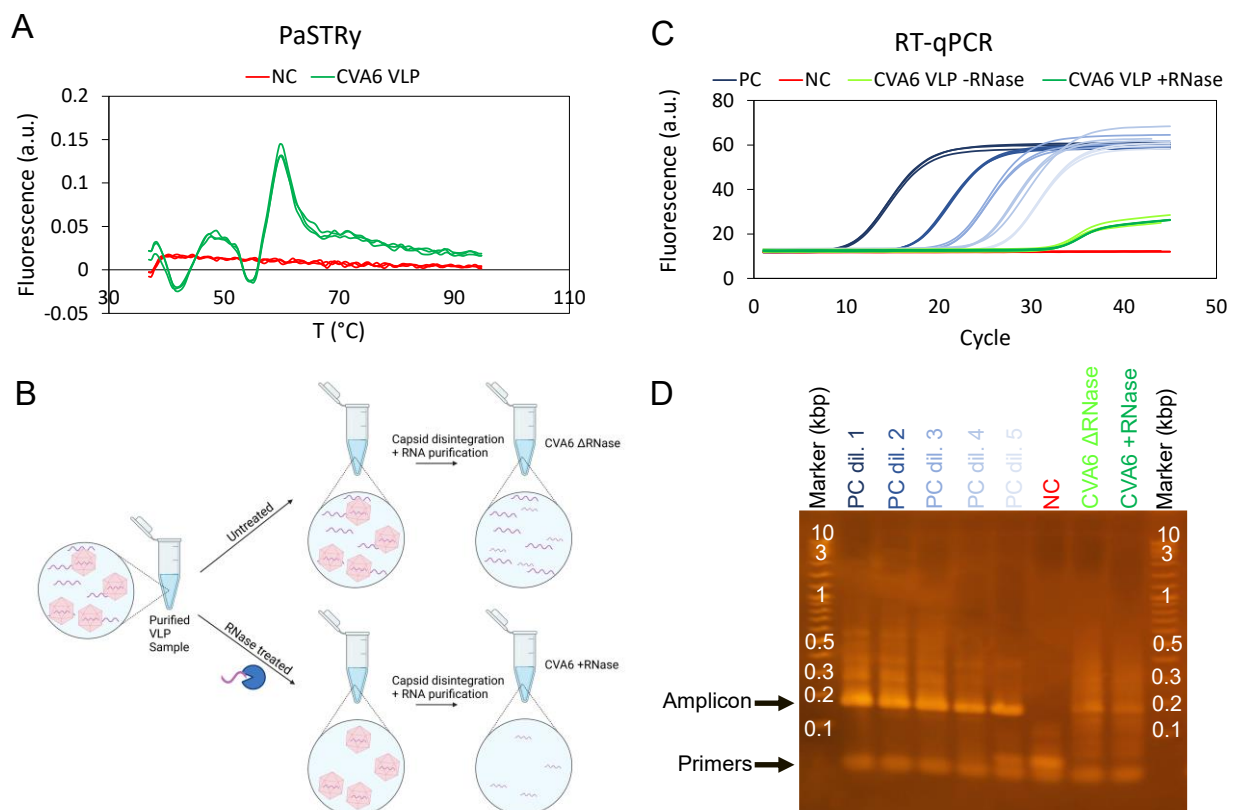


Figure 4.4. RNA presence in CVA6 VLPs.

(A) PaSTRy results for CVA6 VLPs (green lines) indicated a distinct peak at $\sim 60^{\circ}\text{C}$, which correlates with the temperature for enterovirus genome release. Thus, the purified CVA6 VLP samples did contain RNA. Additionally, negative controls (red) indicated no signal for the nucleic acid specific SYBR Green dye. (B) A schematic representation of the RNase assay for investigating the presence of RNA outside the VLP capsids is shown. The purified VLPs were divided into two samples: one sample was treated with RNase, which eliminated any RNA outside of the particles, while the other sample remained untreated. Both samples were then disrupted to extract any RNA present from the capsids, which was purified. If a significant amount of RNA was present outside the capsids, a substantial difference in qRT-PCR would be observed between the RNase-treated and untreated samples. (C) RT-qPCR on untreated (light green) and RNase-treated (dark green) CVA6 VLPs with CVA6 specific primers indicated the presence of CVA6 RNA. Positive control was used in five independent 10-fold dilutions (dark-light blue). Negative control is in red. (D) The product of the qRT-PCR was loaded onto a 1.0% agarose gel. All positive controls (PC dil.1 – PC dil. 5) indicated the 176 bp amplicon (indicated with arrow). The negative control did not indicate this amplicon. And both the RNase-treated (CVA6 +RNase) and untreated (CVA6 ΔRNase) CVA6 VLP samples did show the correct sized amplicon with the same band intensity. All samples indicated the primer pairs at the bottom of the gel (indicated by arrow).

The other CVA6 VLP sample was left untreated (**Figure 4.4B**). If RNA was present outside the capsids, such as due to VLP collapse, the sample should have a higher concentration of total RNA after capsid disruption and RNA purification than the RNase-treated sample. The obtained curve (**Figure 4.4C**, light green triplo curves) surpassed the cycle threshold at $C_p = 31.8 \pm 0.1$ cycles (**S.I. Table S.4.3**), confirming the presence of viral RNA with a marginally lower cycle threshold than the RNase-treated sample. Nonetheless, these differences were statistically significant ($P < 0.05$) (**S.I. Table S.4.3**). This lower cycle threshold of the untreated sample as compared to the RNase-treated sample suggests that some vRNA was released from the capsids into the environment, most likely due to VLP collapse over time. Since the differences observed in the cycle threshold were minor, it could be concluded that the majority of RNA that was detected originated from within the capsids.

Due to the relatively low fluorescence signal obtained from the CVA6 VLP samples in RT-qPCR analysis (**Figure 4.4C**), it is possibly that the signal originated from primer hybridization and amplification rather than detection and amplification of the desired region (amplicon). If apparent, this would result in a short (10-30 bp) amplicon which can be investigated by loading the RT-qPCR product on gel. To exclude this possibility, the resulting PCR product was visualized on a 1.0% agarose gel (**Figure 4.4D**). The gel analysis demonstrated the presence of the 176 bp amplicon in all positive controls (**Figure 4.4D**, PC dil. 1 – PC dil. 5), while it was absent in the negative control (**Figure 4.4D**, NC). Notably, the negative control only showed the presence of the primers at the bottom of the gel, located significantly below the 0.1 kbp marker. Importantly, both the CVA6 VLP samples (with or without RNase treatment), showed the same 176 bp amplicon as the positive controls (**Figure 4.4D**, CVA6 Δ RNase and CVA6 +RNase), again confirming the presence of P1 RNA in both samples. Furthermore, the band intensities for the treated and untreated CVA6 VLP samples were highly comparable. The fact that the RT-qPCR provided a positive signal (**Figure 4.4C**) and the 176 bp amplicon was observed in the RNase-treated sample (**Figure 4.4D**) provided the evidence that the RNA detected must have come from within the capsids.

4.3 Discussion

In order to get a comprehensive understanding of the biophysical properties and capabilities of enterovirus VLPs, we employed cryo-EM for the reconstruction of the CVA6 VLP. The analysis of CVA6 VLPs using cryo-EM revealed the typical surface features associated with enteroviruses such as the conspicuous star-shaped plateau (mesa) at the 5-fold-symmetry axes, a narrow canyon-like depression surrounding the mesa, and an open channel situated at the 2-fold axes. Additionally, we determined that viral maturation did not occur in our VLPs, which left the VP0 intact and the pocket factor unbound, analogous to previously published structure¹². Furthermore, two distinct populations were observed: one with increased density at the center of the

capsids (~31%) and the other without (~69%) (**Figure 4.3A**). The increased density was identified as viral RNA encoding the P1 region of the CVA6 genome by PaSTRy and RT-qPCR (**Figure 4.4A-D**), confirming that enterovirus VLPs can encapsidate RNA. This contrasts with previous reports on other enterovirus VLPs such as cytomegalovirus-like particles, poliovirus VLPs, and previous structure determinations of CVA6 VLPs, which lack both host cell mRNA and vRNA coding for the capsid proteins¹¹⁻¹⁴. It needs to be noted that reconstruction of the particle (**Figure 4.3C**) with this relatively low number of particles (~7,500) and achieving a resolution of 4.01 Å is only feasible if all particles are identical. Therefore, it could be concluded that there was only one type of capsid present and that regardless of the vRNA presence the viral maturation did not occur. However, the capsids' symmetry may have aided in the process of increasing resolution.

Virions and virus-like particles are believed to differ in three major ways: the presence of RNA, the cleaving of VP0 into VP2 and VP4, and the occupation of the hydrophobic pocket with a pocket factor^{12,13,23,41,42}. All three differences are thought to have significant impact on the stability of the capsids and are hypothesized to be involved in the viral maturation process^{24,64-66}. The presence of RNA, for example, is generally regarded to significantly enhance the stability of the viral capsids, most likely due to capsid-RNA interactions, as observed in several *Picornaviridae*^{23,67,68}. Our cryo-EM data, together with the PaSTRy and RT-qPCR results, revealed the presence of viral RNA in the VLPs, effectively ruling out the first hypothesized differences between enterovirus virions and VLPs. As a result, we anticipated similar stabilizing effects of the vRNA on a population of our VLPs.

We investigated these hypotheses regarding stability through atomic force microscopy by performing nanoindentations on virions and VLP capsids from EV71 and CVA6. Nanoindentations were performed to determine the viral spring constants, which was then used to calculate the Young's moduli by using their shell thickness and outer radius^{52,56}. Our results show that the EV71 and CVA6 virions have Young's moduli of 0.19 GPa and 0.17 GPa, respectively, which are comparable to those reported for cowpea chlorotic mottle virus (CCMV)⁵⁴ and hepatitis B virus (HBV)⁵⁵. The Young's moduli of our EV71 and CVA6 VLPs were 0.20 GPa and 0.22 GPa, respectively, which are comparable to those of the empty capsid of CCMV⁵⁴, immature Murine leukemia virus (MLV)⁶⁹, and Norwalk VLPs⁷⁰. It is worth noting that the Young's moduli of both VLPs exhibit a slightly greater magnitude than those of virions, despite having lower spring constants. This apparently paradoxical contrast can be attributed to the VLPs' thinner shell and greater outer radius, which contribute to their slightly enhanced stiffness compared to virions. Nevertheless, it is important to acknowledge that these discrepancies are minor, and the error associated with the spring constant measurements is significant. All calculated moduli were significantly lower than those of bacteriophages λ and Φ29^{51,71}. These substantial discrepancies in mechanical characteristics between bacteriophages and viruses have been previously reported and

are potentially attributed to differences in capsid assembly. Bacteriophages have an active packaging machinery for their DNA, whereas CCMV and MLV self-assemble while integrating the RNA into the capsid. Therefore, it is unlikely that the RNA would exert high pressures onto the viral capsids and the mechanical requirements can be significantly lower for viruses, including EV71 and CVA6. The Young's moduli for both virions and VLPs are similar to those reported for soft plastics, such as low-density polyethylene or Teflon⁷². It needs to be noted that differences in the measuring conditions alter the mechanical properties of the particles significantly, making direct comparison challenging.

The observed differences in critical force (**Figure 4.2F**) and critical indentation (**Figure 4.2G**) indicated that both EV71 and CVA6 virions can withstand more force and deformation prior to structural failure than their VLP counterparts. Upon initial examination, these findings suggested that the RNA presence in virions may provide additional stabilization to the capsids. However, two counterarguments challenge this hypothesis:

Firstly, CVA6 VLPs also contain vRNA as was shown by RT-qPCR (**Figure 4.4C,D**), albeit only certain regions of the genome are available (P1 and 3CD). Furthermore, the AFM data did not reveal distinct populations in the data for VLPs with and without vRNA (**Figure 4.2E-H**). If vRNA was indeed the primary stabilizer, it was expected that part of the VLP population would have exhibited a higher critical force and critical indentation, possibly even comparable to that of the virions. However, within the experimental resolution of our assay, this is not the case. Thus, we conclude that vRNA does not appear to be the primary stabilizing factor for these VLPs.

Secondly, the viral maturation in the form of cleaving of VP0 and binding of the pocket factor may have significantly contributed to the stability of virions. Since binding of the pocket factor stabilizes the capsid when in transit between cells and unbinding destabilizes it after cell attachment prior to uncoating, the reduced stability for the CVA6 VLP (**Figure 4.2E-H**) may have originated from lack of viral maturation^{43,44,73}. As the cryo-EM data on the CVA6 VLPs indicated a homogenous population of capsids in which viral maturation did not occur (**Figure 4.4D**), the increased stability of the virions in comparison the VLPs could be attributed to the maturation.

We could exclude viral inactivation as a stabilizer of the capsids (**Figure S.4.1**). However, it remains unclear whether the main primary factor that attributes stability to virions is due to binding of the pocket factor or to capsid rearrangement resulting from VP0 cleavage. However, as pocket factor binding follows VP0 cleavage in enterovirus morphogenesis, the two processes are likely interconnected. Nonetheless, the reduced stability of VLPs has significant implications for their use as vaccines. To achieve stability comparable to that of virions, artificial methods of inducing viral maturation or alternative means of stabilizing the capsids must be explored. Ultimately, this may be the critical factor in the success of VLP vaccines in the future.

Our finding suggested that VLPs can assemble both with and without vRNA, and that these two capsids are structurally and mechanically indistinguishable, has several important implications. Firstly, RNA cannot be the sole scaffold or driver for viral particle assembly in enterovirus VLPs. Although it is possible that the RNA escaped the capsids after it is used for the particle assembly, this hypothesis is contradicted by the PaSTRy data (**Figure 4.4A**), which indicated that a temperature of 60 °C was required for genome release. Secondly, if the RNA was required for the (completion of) assembly a larger proportion of capsids would contain vRNA than the 31% observed in this study. Additionally, this hypothesis fails to explain the reported excess of empty capsids compared to infective virus *in vivo*⁷⁴. Hence, it is more plausible that these results supports the hypothesis that enterovirus capsids (and thus VLPs) can assemble via two independent pathways (with and without RNA present), as proposed for other enteroviruses^{74–77}.

Thirdly, it is evident that the vRNA, or at least P1, is not solely responsible for the cleavage of VP0 and viral maturation in CVA6. If this were the case, we would observe two distinct populations of VLPs: those containing RNA that undergo viral maturation, and those lacking RNA that do not. This contrasts with other enteroviruses such as hand, foot, and mouth disease virus, where it has been shown that viral maturation is dependent on genomic RNA and occurs only when the capsid proteins are in contact with the RNA^{29,36,37}.

In other enteroviruses many residues playing a crucial role in the viral maturation process are located in the P1 region. In poliovirus, conserved residues 195H (VP2) and 194P (VP2), located near the scissile bond, play a crucial role in executing the maturation cleavage, as demonstrated in previous studies^{22,78,79}. Similarly, residue 107H (VP1) is proposed to regulate VP0 maturation in EV71⁸⁰. In this study, the CVA6 P1 region is available and packaged in the CVA6 VLPs (**Figure 4.4C,D**)⁸¹. The presence of P1 vRNA inside the capsids (**Figure 4.4C**) and the lack of cleavage of VP0 and binding of a pocket factor in VLPs (**Figure 4.3C**) led to the conclusion that the presence of P1 vRNA alone is insufficient to complete the viral maturation process. These findings suggest that vRNA may not be the sole factor responsible for triggering viral maturation, and there may be other underlying mechanisms at play. However, further investigation is needed to fully comprehend the role of vRNA and other factors in the maturation of virus capsids.

4.4 Materials & Methods

4.4.1 Construction of recombinant baculoviruses

Previously reported construct optimizations for the production of enterovirus A71 (EV71) indicated that the highest viral protein yield was obtained using the P1 and 3CD coding sequences behind the polh and CMV promoter, respectively⁴⁷. Two transfer plasmids, containing the aforementioned genes originating from EV71_C4 and CVA6, were amplified using *E. coli* JM109 competent cells (Promega) and isolated using NucleoBond Xtra Midi EF (Macherey-Nagel). The amplified transfer plasmids were checked by double digestion using multiple restriction enzyme pairs. To construct the recombinant baculovirus, the transfer plasmid and *flashBAC* GOLD DNA (Oxford Expression Technologies) were co-transfected into Sf9 cells (Gibco). The two different baculovirus stocks for the EV71 and CVA6 origin viral proteins, respectively, were designated BacV-EV71 and BacV-CVA6. The baculovirus was propagated over the course of 3 passages and titered by end-point-dilution method using Sf9 Easy Titer (Sf9ET) (Kerafast) cells according to the manufacturer's protocol.

4.4.2 VLP production & purification

EV71 and CVA6 VLP production was accomplished by infection of High Five™ cells (Gibco). Erlenmeyer culture flasks (1 l) with 400 ml working volumes of 1.0×10^6 cells/ml Hi5 cells were infected by either BacV-EV71 or BacV-CVA6 (MOI 0.001 and 5, respectively) in Sf-900IISFM (Gibco). Subsequently, the cultures were centrifuged (Heraeus) at 3,000 rpm for 15 min at 4 °C. The pellet was discarded, and the supernatant was supplemented with Triton X-100 (final concentration 0.1%) to prevent protein aggregation. The supernatant was double filtered using 0.45 µm and 0.22 µm filter (Millex). The filtered supernatant was subjected to sucrose cushion ultracentrifugation (30% W/W sucrose in PBS) for 5 h at $141,000 \times g$. The pellet was resuspended in 1 ml phosphate-buffered saline (PBS, Gibco) and subjected to another centrifugation ($10,000 \times g$, 10 min), after which the pellet was discarded, and the supernatant was applied onto a discontinuous sucrose density gradient (SDG) (15-45% W/W sucrose in PBS) and ultracentrifuged for 3 h at $141,000 \times g$ (ThermoFisher Scientific). The SDG was harvested by 1 ml sampling from the top. Samples were pooled into 8 concentration ranges based on the percentage of sucrose (0%-15%, 15%-20%, 20%-25%, 25%-30%, 30%-35%, 35%-40%, 40%-45%, and 45%-50%), whereby sucrose density was measured by refractometer (Hanna instruments).

4.4.3 Virion production and purification

EV71 and CVA6 inactivated virions were provided by Intravacc B.V.

4.4.4 SDS PAGE & Western blot

To confirm the viral protein production of EV71 and CVA6, VP1 (both origins) western blot analysis and SDS PAGE was performed. For this, 40 µl of each culture was mixed with 10 µl loading buffer (Intravacc) and heated at 100 °C for 15 min. Then, 15 µl of each mixture was loaded on NuPAGE™ 10% Bis-Tris gel (Invitrogen) and

electrophoresis was performed at 200 V for 45 min. The gel was washed three times for 5 min using purified water. Dependent on the purpose of the gel, it was subjected to staining (SDS PAGE, section 4.4.4.1) or overnight blocking (western blot, section 4.4.4.2)

4.4.4.1 SDS PAGE

The gel was stained with Imperial™ protein stain (Thermo Fisher Scientific) for 1 h and destained in multiple cycles and overnight using purified water.

4.4.4.2 Western blot

The proteins were blotted onto a nitrocellulose membrane (ThermoFisher Scientific) using a semi-dry blotting machine (Hoefer) run at 60 mA for 60 min. The membrane was washed two times in wash buffer (PBS + 0.1% W/W Tween 20 (Sigma-Aldrich)) and blocked overnight at 4 °C (PBS + 0.1% Tween 20 (Sigma-Aldrich), and 0.5% Protifar (Nutricia)). Next, the membrane was incubated with 1:1,000 of either mouse anti-EV71-VP1 (Abnova, MAB1255-M08) or rabbit anti-CVA6-VP1 (ThermoFisher Scientific, PA5-112001) in block buffer for 90 min on a roller incubator. The membrane was washed five times using wash buffer and incubated with 1:2,000 of either goat anti-mouse IgG Human ads-AP (Southern Biotech, 1030-04) or goat anti-rabbit IgG Human ads-AP (Southern Biotech, 4050-04) in block buffer for 90 min on a roller incubator. The membrane was washed three times using wash buffer and once using purified water. The membrane was colored using AP conjugate substrate kit (BIO-RAD, 1706432). The colorization reaction was terminated by the addition of an excess of purified water.

4.4.5 Atomic force microscopy

4.4.5.1 AFM sample preparation

Prior to AFM measurements, the stock solutions of the viral particles were diluted 8 times using phosphate buffered saline (PBS, Sigma-Aldrich). A hydrophobic glass cover slip was applied as the substrate to immobilize the viral particles during AFM measurements. The hydrophobic coating on the glass cover slip was obtained by applying a hexamethyldisilazane (Sigma-Aldrich) treatment as described previously^{51,52}. A droplet of 20 µl diluted stock solution was deposited on a hydrophobic glass cover slip. After 15 min incubation at room temperature, another 800 µl PBS was added to a liquid receptacle for follow-up AFM imaging and nanoindentation.

4.4.5.2 AFM imaging and nanoindentation

Imaging and nanoindentation experiments of the viral particles were conducted by AFM (NanoWizard, JPK). All experiments were performed in PBS. Before AFM imaging, the cantilever (qp-Bio AC CB2, Nanosensors) with a nominal spring constant of 0.1 N/m was calibrated using the contact-based method. The parameters for imaging both the virions and the VLPs in quantitative imaging (QI) mode were kept constant where the setpoint for imaging was set at 0.07 nN.

After imaging, nanoindentation was performed at the center of a viral particle. The nanoindentation procedure was carried out according to the previous protocol⁵². The settings for nanoindentation were kept constant and set as follows: Z length was 200 nm; setpoint was 3 nN; loading rate was 50 nm/s. Before and after indenting the targeted viral particle, indentations were performed on the glass substrate adjacent to the viral particle to confirm the cleanliness of the tip. Finally, the indented viral particle was imaged again to visualize the structural state of the particle after nanoindentation.

4.4.5.3 Data processing

The viral spring constant of the particles was calculated using the previous method⁵², in which the slope of the initial linear part of the Force-Displacement (F-Z) curve obtained from AFM nanoindentation was fitted yielding the total spring constant of the cantilever-particle system, and the spring constant of the cantilever was obtained from the above described calibration⁵².

To convert the spring constant to the Young's modulus, we utilized a methodology described in previously published literature^{52,54}. This involved assuming that the capsid is a spherical shell undergoing small deformations (i.e., in this idealized scenario, the particle is assumed to be made of a homogenous material with a constant radius and shell thickness⁸²), resulting in the following formula:

$$k_{cap} = \frac{\alpha E h^2}{R}. \quad (1)$$

where h is the shell thickness, R is the outer radius, and α is a proportionality factor dependent on the geometry of the particle. A value of 1 for α provides a reasonable approximation for various capsids^{51,52,54,83}. The outer radius and shell thickness were obtained from the Virus Particle Explorer database⁵⁶.

The F-Z curve can be converted to Force-Indentation (F-D) curve using the previous method⁵² to measure the critical force and critical indentation of the viral particle. The critical force was measured from the ordinate of a discontinuous point on an F-D curve, and the critical indentation was measured from the abscissa of the same discontinuous point.

Due to the convolution of the tip with the sample, the corrected height was used as the size of the measured viral particle. The corrected height was calculated following the prior method⁵² which corrects the imaging force-induced particle deformation.

The volumes of the viral particle before and after indentation were measured using Gwyddion AFM analysis software (gwyddion.net)⁸⁴, and the threshold of the grain for volume calculation was set at 14 nm. By dividing the particle's after-indentation volume by its before-indentation volume, the normalized volume of the particle after

indentation was calculated. For statistical studies, one-way ANOVA method was used. Unless otherwise noted, stated errors are standard deviation (SD).

4.4.6 Electron Microscopy

4.4.6.1 *Negative stain*

Electron microscopy was employed for the direct visualization of the VLPs. Of each DSP sample, 3 μL was blotted on glow discharged EM grids (Quantifoil, carbon-supported, Cu-400) in three consecutive iterations with 60 s of incubation time. Next, grids were subjected to two wash cycles using 10 μl PBS. Excess liquid was blotted away using filter papers. Staining was performed using 2% uranyl acetate for 1 min. Excess liquid was blotted away using filter paper. Imaging was performed using a Jeol JEM-1400 plus TEM.

4.4.6.2 *Cryo-EM*

4.4.6.2.1 Grid preparation

A total of 3.0 μl of CVA6 VLP solution was applied on glow discharged (Quorum GloQube, 18 mA, 90 seconds) Quantifoil grids (R 2/1, 200-mesh holey carbon on copper, coated by a 2 nm carbon layer), on a Leica GP2 vitrification robot at 99% humidity and 20 °C. The sample was incubated for 3 minutes on the surface of the grid before being blotted for 10 seconds from the carbon side of the grid and then immediately flash-cooled in liquid ethane.

4.4.6.2.2 VLP data collection

VLP-containing grids were imaged on a JEM 3200FSC TEM (JEOL), operated at 300 kV. Images were recorded on a K2 Summit direct electron detector (Gatan). A single dataset was collected at a magnification of 40k, corresponding to a pixel size of 0.9751 Å at the specimen level. Image acquisition was performed using the SerialEM software⁸⁵ and micrographs were collected at a defocus range of 0.5-2.5 μm and an electron dose of 58.24 $\text{e}/\text{Å}^2$. A total of 1,828 micrographs were collected from a single grid, with seven shots performed per grid-hole to cover the entire surface of each hole.

4.4.6.2.3 VLP data processing

The CVA6 VLP dataset was processed using the integrated Cryosparc V4.1.1⁸⁶ processing pipeline. Initially, patch motion correction was performed to correct for stage drift and mean induced movement, and then the selected micrographs underwent patch contrast transfer function (CTF) estimation and were manually curated to remove insufficient quality micrographs. Using a manual blob picker with a box size of 512 px, 150 particles were selected and 2D-classified, to be used as input for the template picker tool. A total of 7,481 usable particles were finally selected after multiple iterations of 2D classification and particle picking. The selected particles were extracted and used for ab initio reconstruction of a single model with imposed icosahedral symmetry. This model was further refined using homogeneous refinement to result in an initial cryo-EM map of 4.6 Å resolution. Further homogeneous refinement with optimised parameters of per-particle defocus, per-group CTF

parameters and Ewald sphere correction resulted in a final EM volume of 4.01 Å resolution.

4.4.7 RNA presence determination

4.4.7.1 Particle stability thermal release assay

Purified CVA6 VLPs were mixed 1:4 with SYBR Green II RNA gel stain (500X) in a final volume of 50 µl in a 96 well plate (Lightcycler 480 Multiwell, Roche). PCR was run with 0.03 °C/s increments, 17 measurements/°C, with a temperature ramp from 37 °C to 95 °C. Measurements were taken using FAM green channel (520 nm).

4.4.7.2 Reverse transcription and polymerase chain reaction

The purified CVA6 VLPs were split into two 150 µl samples. One of the samples was treated with 1:100 RNaseI (Thermo Fisher Scientific) to a final concentration of 0.1 U/ml, and incubated for 30 min at 37 °C. Subsequently, both treated and untreated VLP samples underwent viral RNA isolation using the NucleoSpin RNA virus kit (Macherey-Nagel), as per the manufacturer's protocol. The isolated RNA was subject to RT-qPCR using the LightCycler Multiplex RNA Virus master kit (Roche), using a custom running protocol (Table 4.1) and primers (Table 4.2). Of the PCR product 15 µl was mixed with 3 µl 6X loading dye (NEB, Cat#B7024) and the entire 18 µl was loaded onto a 1.0% TAE agarose gel. The gel was run for 1 h at 100 V in TAE buffer, stained for 30 min in ethidium bromide (final concentration 0.25 µg/ml), and destained for 10 min in purified water.

Table 4.1. RT-PCR running protocol.

Step	Temperature (°C)	Time (mm:sec)	Cycle	Ramp (°C/sec)
RT step	50	10:00	1	4.4
Denaturation	95	00:30	1	4.4
Denaturation	95	0:05	45	4.4
Annealing	56	0.10	45	-
Extension	60	0:30	45	2.2
Cooling	37	0:10	1	2.2

Table 4.2. Primers used for RT-PCR for the detection of viral CVA6 RNA.

Primer	Sequence (5' → 3')
CVA6 Probe	[FAM]CGGCGCTGCTGCACGAATCCC[BHQ1]
CVA6 Fw	TACTCTAGGGCTGGTCTGGT
CVA6 Rv	TCGTTCAAGTTGGAGACGAA

4.5 Supplemental information

Table S.4.1. Average parameters for the different capsid structures.

Sample	Number of capsids	Size (nm)	Spring constant (N/m)	Critical force (nN)	Critical indentation (nm)
EV71 VLP	47	30 ± 2	0.25 ± 0.14	0.61 ± 0.27	3.7 ± 1.8
EV71 virion	22	29 ± 2	0.30 ± 0.18	0.98 ± 0.55	5.5 ± 1.6
CVA6 VLP	48	29 ± 2	0.31 ± 0.16	0.66 ± 0.27	2.9 ± 1.3
CVA6 virion	11	30 ± 1	0.38 ± 0.22	1.19 ± 0.36	4.7 ± 1.4
CVA6 inact. VLP	35	-	0.31 ± 0.21	0.70 ± 0.24	3.4 ± 1.4

Table S.4.2. Calculation parameters for Young's moduli.

Sample	Shell thickness (nm)	Capsid outer radius (nm)	Young modulus (M N/m ²)
EV71 VLP	4.5	16.4	202
EV71 virion	5.0	15.9	191
CVA6 VLP	4.9	16.8	216
CVA6 virion	5.9	15.9	173
CVA6 inact. VLP	5.9	15.9	174

Table S.4.3. RT-qPCR analysis of CVA6 VLP samples with and without RNase treatment

Sample	C _p	Conc. (ng/μl)
PC dil. 1	10.9 ± 0.1	2590.0 ± 45.8
PC dil. 2	17.5 ± 0.2	266.33 ± 15.5
PC dil. 3	21.7 ± 0.0	31.57 ± 1.0
PC dil. 4	25.0 ± 0.5	2.41 ± 1.0
PC dil. 5	27.1 ± 0.0	0.23 ± 0.0
NC	0.0 ± 0.0	0.0 ± 0.0
CVA6 VLP ΔRNase	31.8 ± 0.1	0.0005 ± 0.0001
CVA6 VLP +RNase	32.2 ± 0.1	0.0003 ± 0.0001

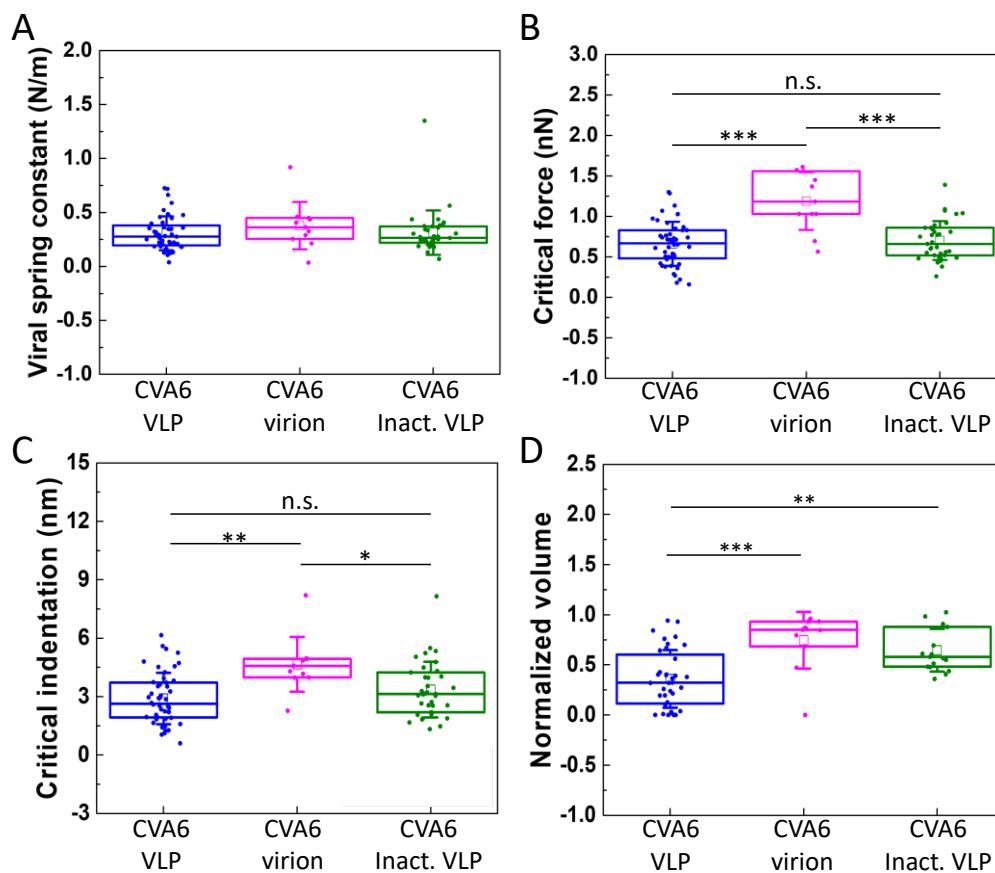


Figure S.4.1. AFM nanoindentation results for the investigation of stabilizing effects of inactivation with formaldehyde on the particle stability.

(A) Viral spring constant (N/m). (B) Critical force (nN). (C) Critical indentation (nm). (D) Normalized volume after indentation. CVA6 VLP (blue), CVA6 inactivated virions (violet), and CVA6 inactivated VLPs (green). P values are indicated by asterisks: $p < 0.001$ (***), $p < 0.01$ (**), and $p < 0.05$ (*). N.s.: not significant

4.6 References

1. Sabanathan S, Van Tan L, Thwaites L, Wills B, Qui PT, Van Doorn HR. Enterovirus 71 related severe hand, foot and mouth disease outbreaks in South-East Asia: Current situation and ongoing challenges. *J Epidemiol Community Health*. 2014;68(6):500-502. doi:10.1136/jech-2014-203836
2. Nguyen TT, Chiu CH, Lin CY, et al. Efficacy, safety, and immunogenicity of an inactivated, adjuvanted enterovirus 71 vaccine in infants and children: a multiregion, double-blind, randomised, placebo-controlled, phase 3 trial. *Lancet*. 2022;399(10336):1708-1717. doi:10.1016/S0140-6736(22)00313-0
3. Schiller J, Lowy D. Explanations for the high potency of HPV prophylactic vaccines. *Vaccine*. 2018.
4. Lin SY, Chung YC, Chiu HY, Chi WK, Chiang BL, Hu YC. Evaluation of the stability of enterovirus 71 virus-like particle. *J Biosci Bioeng*. 2014;117(3):366-371.

- doi:10.1016/j.jbiosc.2013.08.015
5. Zhou Y, Shen C, Zhang C, et al. Yeast-produced recombinant virus-like particles of coxsackievirus A6 elicited protective antibodies in mice. *Antiviral Res.* Published online 2016. doi:10.1016/j.antiviral.2016.06.004
 6. Shen C, Ku Z, Zhou Y, et al. Virus-like particle-based vaccine against coxsackievirus A6 protects mice against lethal infections. *Vaccine.* Published online 2016. doi:10.1016/j.vaccine.2016.06.028
 7. Kim, HJ Son, HS Lee, SW Yoon, Y Hyeon, JY Gyung, TC Lee JYJ. Efficient expression of enterovirus 71 based on virus-like particles vaccine. *PLoS One.* 2019;14(3). doi:10.1371/journal.pone.0210477
 8. Lin SY, Sung LY, Yeh CT, Yu CP, Yang JY, Hu YC. Production and purification of virus-like particles of different enterovirus subtypes as vaccines. *J Taiwan Inst Chem Eng.* 2018;82:1-9. doi:10.1016/j.jtice.2017.10.020
 9. Fuenmayor J, Gòdia F, Cervera L. Production of virus-like particles for vaccines. *N Biotechnol.* Published online 2017. doi:10.1016/j.nbt.2017.07.010
 10. Dai W, Zhang C, Zhang X, et al. A virus-like particle vaccine confers protection against enterovirus D68 lethal challenge in mice. *Vaccine.* 2018;36(5):653-659. doi:10.1016/j.vaccine.2017.12.057
 11. Sainsbury F, Saunders K, Aljabali AAA, Evans DJ, Lomonosoff GP. Peptide-controlled access to the interior surface of empty virus nanoparticles. *ChemBioChem.* 2011;12(16). doi:10.1002/cbic.201100482
 12. Chen, Zhang, Zhou, et al. A 3.0-Angstrom Resolution Cryo-Electron Microscopy Structure and Antigenic Sites of Coxsackievirus A6-Like Particles. *J Virol.* 2018;92(2). doi:10.1128/JVI.01257-17
 13. Wang X, Ku Z, Zhang X, et al. Structure, Immunogenicity, and Protective Mechanism of an Engineered Enterovirus 71-Like Particle Vaccine Mimicking 80S Empty Capsid. *J Virol.* 2018;92(1). doi:10.1128/JVI.01330-17.
 14. Marsian J, Fox H, Bahar MW, et al. Plant-made polio type 3 stabilized VLPs-A candidate synthetic polio vaccine. *Nat Commun.* 2017;8(1). doi:10.1038/s41467-017-00090-w
 15. Routh A, Domitrovic T, Johnson JE. Host RNAs, including transposons, are encapsidated by a eukaryotic single-stranded RNA virus. *Proc Natl Acad Sci U S A.* 2012;109(6). doi:10.1073/pnas.1116168109
 16. Fox H, Knowlson S, Minor PD, Macadam AJ. Genetically Thermo-Stabilised, Immunogenic Poliovirus Empty Capsids; a Strategy for Non-replicating Vaccines. *PLoS Pathog.* Published online 2017. doi:10.1371/journal.ppat.1006117
 17. Bahar MW, Porta C, Fox H, Macadam AJ, Fry EE, Stuart DI. Mammalian expression of virus-like particles as a proof of principle for next generation polio vaccines. *npj Vaccines.* Published online 2021. doi:10.1038/s41541-020-00267-3

18. Xu Y, Ma S, Huang Y, et al. Virus-like particle vaccines for poliovirus types 1, 2, and 3 with enhanced thermostability expressed in insect cells. *Vaccine*. Published online 2019. doi:10.1016/j.vaccine.2019.03.031
19. Kingston NJ, Shegdar M, Snowden JS, et al. Thermal stabilization of enterovirus A 71 and production of antigenically stabilized empty capsids. *J Gen Virol*. 2022;103(8):1-11. doi:10.1099/jgv.0.001771
20. Kingston N, Snowden J, Martyna A, et al. Production of antigenically stable enterovirus A71 virus-like particles in *Pichia pastoris* as vaccine candidate. 2023;57(6):1166-1177. doi:10.15389/agrobiology.2022.6.1166rus
21. Filman DJ, Syed R, Chow M, Macadam AJ, Minor PD, Hogle JM. Structural factors that control conformational transitions and serotype specificity in type 3 poliovirus. *EMBO J*. 1989;8(5). doi:10.1002/j.1460-2075.1989.tb03541.x
22. Plevka P, Perera R, Cardoso J, Kuhn RJ, Rossmann MG. Crystal structure of human enterovirus 71. *Science (80-)*. 2012;336(6086). doi:10.1126/science.1218713
23. Büttner CR, Spurný R, Füzik T, Plevka P. Cryo-electron microscopy and image classification reveal the existence and structure of the coxsackievirus A6 virion. *Commun Biol*. 2022;5(1). doi:10.1038/s42003-022-03863-2
24. Füzik T, Moravcová J, Kalynych S, Plevka P. Structure of Human Enterovirus 70 and Its Inhibition by Capsid-Binding Compounds. *J Virol*. 2022;96(17). doi:10.1128/jvi.00604-22
25. Jiang P, Liu Y, Ma HC, Paul A V., Wimmer E. Picornavirus Morphogenesis. *Microbiol Mol Biol Rev*. Published online 2014. doi:10.1128/MMBR.00012-14
26. Hellen CUT, Wimmer E. Enterovirus Structure and Assembly. In: *Human Enterovirus Infections*. ; 2014. doi:10.1128/9781555818326.ch7
27. Cao J, Liu H, Qu M, et al. Determination of the cleavage site of enterovirus 71 VP0 and the effect of this cleavage on viral infectivity and assembly. *Microb Pathog*. 2019;134(June):103568. doi:10.1016/j.micpath.2019.103568
28. Logan G, Newman J, Wright CF, et al. Deep Sequencing of Foot-and-Mouth Disease Virus Reveals RNA Sequences Involved in Genome Packaging. *J Virol*. 2018;92(1). doi:10.1128/jvi.01159-17
29. Arnold E, Luo M, Vriend G, et al. Implications of the picornavirus capsid structure for polyprotein processing. *Proc Natl Acad Sci U S A*. 1987;84(1). doi:10.1073/pnas.84.1.21
30. Ansardi DC, Morrow CD. Amino acid substitutions in the poliovirus maturation cleavage site affect assembly and result in accumulation of provirions. *J Virol*. 1995;69(3). doi:10.1128/jvi.69.3.1540-1547.1995
31. Bruinsma RF, Wuite GJL, Roos WH. Physics of viral dynamics. *Nat Rev Phys*. 2021;3(2):76-91. doi:10.1038/s42254-020-00267-1
32. Perlmutter JD, Hagan MF. Mechanisms of virus assembly. *Annu Rev Phys Chem*. 2015;66(1):217-239. doi:10.1146/annurev-physchem-040214-121637

33. McPherson A. Micelle formation and crystallization as paradigms for virus assembly. *BioEssays*. 2005;27(4). doi:10.1002/bies.20196
34. Hu T, Shklovskii BI. Kinetics of viral self-assembly: Role of the single-stranded RNA antenna. *Phys Rev E - Stat Nonlinear, Soft Matter Phys*. 2007;75(5). doi:10.1103/PhysRevE.75.051901
35. Rolfsson Ó, Middleton S, Manfield IW, et al. Direct Evidence for Packaging Signal-Mediated Assembly of Bacteriophage MS2. *J Mol Biol*. 2016;428(2):431-448. doi:10.1016/j.jmb.2015.11.014
36. Twarock R, Stockley PG. RNA-Mediated Virus Assembly: Mechanisms and Consequences for Viral Evolution and Therapy. *Annu Rev Biophys*. 2019;48:495-514. doi:10.1146/annurev-biophys-052118-115611
37. Shakeel S, Dykeman EC, White SJ, et al. Genomic RNA folding mediates assembly of human parechovirus. *Nat Commun*. 2017;8(1). doi:10.1038/s41467-016-0011-z
38. Shakeel S, Westerhuis BM, Domanska A, et al. Multiple capsid-stabilizing interactions revealed in a high-resolution structure of an emerging picornavirus causing neonatal sepsis. *Nat Commun*. 2016;7. doi:10.1038/ncomms11387
39. Zhu L, Wang X, Ren J, et al. Structure of Ljungan virus provides insight into genome packaging of this picornavirus. *Nat Commun*. 2015;6. doi:10.1038/ncomms9316
40. Klug A. The tobacco mosaic virus particle: structure and assembly. *Phil Trans R Soc Lond B*. 1999;(354):1-6. [papers2://publication/uuid/85019DC5-FA2B-4D81-A1EE-B07967F4E68E](https://doi.org/10.1098/rstb.1999.0451)
41. Wang X, Peng W, Ren J, et al. A sensor-adaptor mechanism for enterovirus uncoating from structures of EV71. *Nat Struct Mol Biol*. 2012;19(4):424-429. doi:10.1038/nsmb.2255
42. Gong M, Zhu H, Zhou J, et al. Cryo-Electron Microscopy Study of Insect Cell-Expressed Enterovirus 71 and Coxsackievirus A16 Virus-Like Particles Provides a Structural Basis for Vaccine Development. *J Virol*. 2014;88(11):6444-6452. doi:10.1128/jvi.00200-14
43. Grant RA, Hiremath CN, Filman DJ, Syed R, Andries K, Hogle JM. Structures of poliovirus complexes with anti-viral drugs: implications for viral stability and drug design. *Curr Biol*. 1994;4(9). doi:10.1016/S0960-9822(00)00176-7
44. Muckelbauer JK, Kremer M, Minor I, et al. The structure of coxsackievirus B3 at 3.5 Å resolution. *Structure*. 1995;3(7):653-667. doi:10.1016/S0969-2126(01)00201-5
45. Valiente L, López-Argüello S, Rodríguez-Huete A, Valbuena A, Mateua MG. Molecular Determinants of Human Rhinovirus Infection, Assembly, and Conformational Stability at Capsid Protein Interfaces. *J Virol*. 2022;96(23).
46. Roos WH. How to perform a nanoindentation experiment on a virus. *Methods Mol Biol*. 2011;783. doi:10.1007/978-1-61779-282-3_14
47. Lin SY, Yeh CT, Li WH, et al. Enhanced enterovirus 71 virus-like particle yield from a new baculovirus design. *Biotechnol Bioeng*. 2015;112(10):2005-2015. doi:10.1002/bit.25625

48. Theil EC. Ferritin protein nanocages-the story. *Nanotechnol Perceptions*. 2012;8(1). doi:10.4024/N03TH12A.ntp.08.01
49. Zhang S, Zang J, Chen H, Li M, Xu C, Zhao G. The Size Flexibility of Ferritin Nanocage Opens a New Way to Prepare Nanomaterials. *Small*. 2017;13(37). doi:10.1002/smll.201701045
50. Piontek MC, Roos WH. Lipoprotein particles exhibit distinct mechanical properties. *J Extracell Biol*. 2022;1(12). doi:10.1002/jex2.68
51. Ivanovska IL, De Pablo PJ, Ibarra B, et al. Bacteriophage capsids: Tough nanoshells with complex elastic properties. *Proc Natl Acad Sci U S A*. 2004;101(20). doi:10.1073/pnas.0308198101
52. Guo Y, Roos WH. AFM nanoindentation experiments on protein shells: A protocol. In: *Methods in Molecular Biology*. Vol 1886. ; 2019. doi:10.1007/978-1-4939-8894-5_14
53. Tuthill TJ, Groppelli E, Hogle JM, Rowlands DJ. Picornaviruses. *Curr Top Microbiol Immunol*. 2010;343(1). doi:10.1007/82-2010-37
54. Michel JP, Ivanovska IL, Gibbons MM, et al. Nanoindentation studies of full and empty viral capsids and the effects of capsid protein mutations on elasticity and strength. *Proc Natl Acad Sci U S A*. 2006;103(16):6184-6189. doi:10.1073/pnas.0601744103
55. Roos WH, Bruinsma R, Wuite GJL. Physical virology. *Nat Phys*. 2010;6(10):733-743. doi:10.1038/nphys1797
56. Montiel-Garcia D, Santoyo-Rivera N, Ho P, et al. VIPERdb v3.0: A structure-based data analytics platform for viral capsids. *Nucleic Acids Res*. 2021;49(D1). doi:10.1093/nar/gkaa1096
57. Chong P, Hsieh SY, Liu CC, et al. Production of EV71 vaccine candidates. *Hum Vaccines Immunother*. 2012;8(12):1775-1783. doi:10.4161/hv.21739
58. Wilton T, Dunn G, Eastwood D, Minor PD, Martin J. Effect of Formaldehyde Inactivation on Poliovirus. *J Virol*. 2014;88(20):11955-11964. doi:10.1128/jvi.01809-14
59. Smith TJ, Kremer MJ, Luo M, et al. The site of attachment in human rhinovirus 14 for antiviral agents that inhibit uncoating. *Science (80-)*. 1986;233(4770). doi:10.1126/science.3018924
60. Harauz G, van Heel M. Exact filters for general geometry three dimensional reconstruction. *Optik (Stuttg)*. 1986;73.
61. Chen S, McMullan G, Faruqi AR, et al. High-resolution noise substitution to measure overfitting and validate resolution in 3D structure determination by single particle electron cryomicroscopy. *Ultramicroscopy*. 2013;135. doi:10.1016/j.ultramic.2013.06.004
62. Walter TS, Ren J, Tuthill TJ, Rowlands DJ, Stuart DI, Fry EE. A plate-based high-throughput assay for virus stability and vaccine formulation. *J Virol Methods*. 2012;185(1):166-170. doi:10.1016/j.jviromet.2012.06.014

63. Adeyemi OO, Nicol C, Stonehouse NJ, Rowlands DJ. Increasing Type 1 Poliovirus Capsid Stability by Thermal Selection. *J Virol*. Published online 2016. doi:10.1128/jvi.01586-16
64. Flatt JW, Domanska A, Seppälä AL, Butcher SJ. Identification of a conserved virion-stabilizing network inside the interprotomer pocket of enteroviruses. *Commun Biol*. 2021;4(1):1-8. doi:10.1038/s42003-021-01779-x
65. Pevear DC, Tull TM, Seipel ME, Groarke JM. Activity of pleconaril against enteroviruses. *Antimicrob Agents Chemother*. Published online 1999.
66. Lecoq L, Wang S, Dujardin M, et al. A pocket-factor-triggered conformational switch in the hepatitis B virus capsid. *Proc Natl Acad Sci U S A*. 2021;118(17):1-12. doi:10.1073/pnas.2022464118
67. Hadfield AT, Lee WM, Zhao R, et al. The refined structure of human rhinovirus 16 at 2.15 Å resolution: Implications for the viral life cycle. *Structure*. 1997;5(3). doi:10.1016/S0969-2126(97)00199-8
68. Chandler-Bostock R, Mata CP, Bingham RJ, et al. Assembly of infectious enteroviruses depends on multiple, conserved genomic RNA-coat protein contacts. *PLoS Pathog*. 2020;16(12):1-23. doi:10.1371/journal.ppat.1009146
69. Kol N, Gladnikoff M, Barlam D, Shneck RZ, Rein A, Rousso I. Mechanical properties of murine leukemia virus particles: Effect of maturation. *Biophys J*. 2006;91(2). doi:10.1529/biophysj.105.079657
70. Baclayon M, Shoemaker GK, Uetrecht C, et al. Prestress strengthens the shell of norwalk virus nanoparticles. *Nano Lett*. 2011;11(11):4865-4869. doi:10.1021/nl202699r
71. Arkhipov A, Roos WH, Wuite GJL, Schulten K. Elucidating the mechanism behind irreversible deformation of viral capsids. *Biophys J*. 2009;97(7):2061-2069. doi:10.1016/j.bpj.2009.07.039
72. Howard J. Mechanics of motor proteins and the cytoskeleton. *Phys Today*. 2002;55(3). doi:10.1063/1.1472396
73. Hardy JM, Newton ND, Modhiran N, et al. A unified route for flavivirus structures uncovers essential pocket factors conserved across pathogenic viruses. *Nat Commun*. 2021;12(1):1-13. doi:10.1038/s41467-021-22773-1
74. Shingler KL, Cifuentes JO, Ashley RE, Hafenstein S, Makhov AM, Conway JF. The Enterovirus 71 Procapsid Binds Neutralizing Antibodies and Rescues Virus Infection In Vitro. *J Virol*. Published online 2014. doi:10.1128/jvi.03098-14
75. Hesketh EL, Meshcheriakova Y, Dent KC, et al. Mechanisms of assembly and genome packaging in an RNA virus revealed by high-resolution cryo-EM. *Nat Commun*. Published online 2015. doi:10.1038/ncomms10113
76. Kruse I, Peyret H, Saxena P, Lomonosoff GP. Encapsidation of Viral RNA in Picornavirales : Studies on Cowpea Mosaic Virus Demonstrate Dependence on Viral

- Replication . *J Virol.* 2019;93(2). doi:10.1128/jvi.01520-18
77. Peyret H, Lomonossoff GP. Specific Packaging of Custom RNA Molecules into Cowpea Mosaic Virus-like Particles. In: *Recombinant Proteins in Plants. Methods in Molecular Biology.* Humana, New York, NY; 2022:103-111. doi:10.1007/978-1-0716-2241-4_7
 78. Basavappa R, Filman DJ, Syed R, Flore O, Icenogle JP, Hogle JM. Role and mechanism of the maturation cleavage of VP0 in poliovirus assembly: Structure of the empty capsid assembly intermediate at 2.9 Å resolution. *Protein Sci.* 1994;3(10):1651-1669. doi:10.1002/pro.5560031005
 79. Hindiyeh M, Li QH, Basavappa R, Hogle JM, Chow M. Poliovirus mutants at histidine 195 of VP2 do not cleave VP0 into VP2 and VP4. *J Virol.* 1999;73(11):9072-9079.
 80. Zhang YX, Huang YM, Li QJ, et al. A highly conserved amino acid in VP1 regulates maturation of enterovirus 71. *PLoS Pathog.* 2017;13(9):1-23. doi:10.1371/journal.ppat.1006625
 81. Phillips BA, Fennell R. Polypeptide Composition of Poliovirions, Naturally Occurring Empty Capsids, and 14 S Precursor Particles. *J Virol.* 1973;12(2):291-299. doi:10.1128/jvi.12.2.291-299.1973
 82. Marchetti M, Wuite G, Roos W. Atomic force microscopy observation and characterization of single virions and virus-like particles by nano-indentation. *Curr Opin Virol.* 2016;18:82-88. doi:10.1016/j.coviro.2016.05.002
 83. Gibbons MM, Klug WS. Nonlinear finite-element analysis of nanoindentation of viral capsids. *Phys Rev E - Stat Nonlinear, Soft Matter Phys.* 2007;75(3):1-11. doi:10.1103/PhysRevE.75.031901
 84. Nečas D, Klapetek P. Gwyddion: An open-source software for SPM data analysis. *Cent Eur J Phys.* 2012;10(1). doi:10.2478/s11534-011-0096-2
 85. Mastronarde DN. Automated electron microscope tomography using robust prediction of specimen movements. *J Struct Biol.* 2005;152(1). doi:10.1016/j.jsb.2005.07.007
 86. Punjani A, Rubinstein JL, Fleet DJ, Brubaker MA. CryoSPARC: Algorithms for rapid unsupervised cryo-EM structure determination. *Nat Methods.* 2017;14(3). doi:10.1038/nmeth.4169

5

Characterizing single-molecule dynamics of viral RNA-dependent RNA polymerases with multiplexed magnetic tweezers

Multiplexed single-molecule Magnetic Tweezers (MT) have recently been employed to probe the RNA synthesis dynamics of RNA-dependent RNA polymerases (RdRp). Here, we present a protocol for simultaneously probing the RNA synthesis dynamics of hundreds of single polymerases with MT. We describe the preparation of a dsRNA construct for probing single RdRp kinetics. We then detail the measurement of RdRp RNA synthesis kinetics using MT. The protocol is suitable for high-throughput probing of RdRp-targeting antiviral compounds for mechanistic function and efficacy.

This chapter is published as: L. Kuijpers, T. van Laar, R. Janissen, and N. H. Dekker, "Characterizing single-molecule dynamics of viral RNA-dependent RNA polymerases with multiplexed magnetic tweezers," *STAR Protoc.*, vol. 3, no. 3, p. 101606, 2022, doi: 10.1016/j.xpro.2022.101606.

5.1 Introduction

The presented assay allows a quantitative description of the RNA synthesis dynamics of viral RNA-dependent RNA polymerase (RdRp), including the nucleotide incorporation rate, pausing frequency, and pause lifetimes under a variety of conditions¹. The assay further serves as a platform for the systemic screening of RdRp-targeting antivirals and their effects on RNA synthesis, which can be identified by changes in the processivity, pause frequency and pause duration^{1,2}. Due to the high spatiotemporal resolution of the presented technique, the assay can also be used to identify potential sequence motifs acting as copy-back recombination triggers¹.

The protocol is written for researchers with a working understanding of MT experimentation. This protocol, initially designed for the quantitative investigation of bacteriophage $\Phi 6$ RdRp dynamics³, was modified for the RNA viruses enterovirus A71 (EV71) and poliovirus (PV)¹. This protocol describes all steps for constructing the RNA template, setting up the MT experiment to measure RdRp RNA synthesis dynamics, and analysis of the RdRp translocation data. The protocol requires the RdRp of choice to be already purified⁴, and the magnet distance-force relationship to be known^{5,6}.

5.2 Preparation of the RNA construct

Timing: 1 day

The following steps describe the construction of a dsRNA construct containing a short hairpin structure at the 3' overhang of the template strand for RdRp binding and primer extension. The dsRNA construct consists of five fragments initially amplified as DNA, then transcribed to generate RNA fragments that are annealed to obtain the full dsRNA construct (**Figure 5.1**).

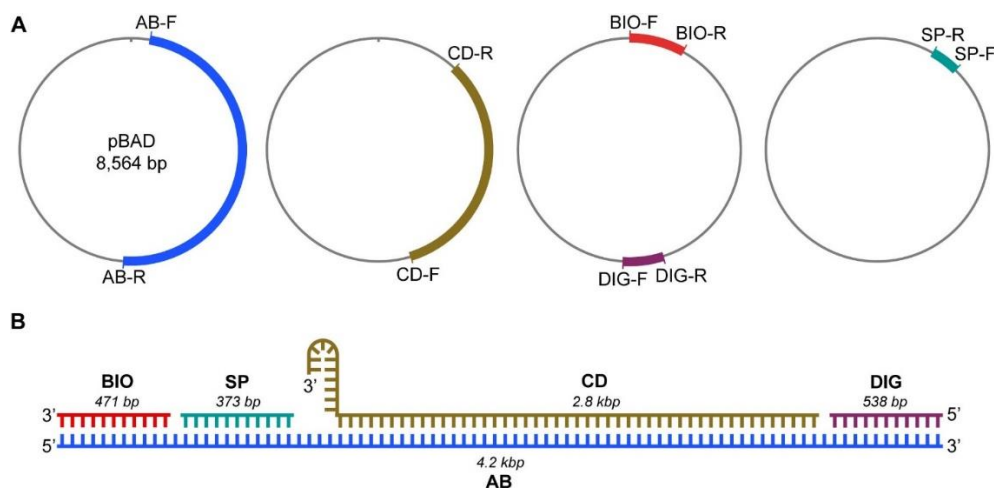


Figure 5.1. dsRNA construct preparation for the RdRp RNA synthesis assay.

(A) Simplified pBAD plasmid maps for PCR amplification of the five DNA fragments. (B) Annealing of the RNA transcripts to generate the dsRNA construct used in MT. The transcripts originate from run-off T7 transcription of the individual DNA fragments. BIO: biotin-enriched handle; DIG: digoxigenin-enriched handle; SP: spacer fragment; CD: RNA synthesis template; AB: construct backbone.

1. The pBAD vector is subjected to gradient PCR with the primer combinations described in the KRT to produce the five DNA fragments ([Figure 5.1](#)). Only one primer in each combination contains a T7 promoter.

PCR reaction pipetting protocol	
Reagent	Volume (μ l)
Template (10 ng/ μ l)	4
Primer F (10 μ M)	4
Primer R (10 μ M)	4
dNTPs (1 mM each)	4
5x HF buffer	32
MilliQ	110.8
Phusion polymerase	1.2

PCR cycle times			
Steps	Temperature ($^{\circ}$ C)	Time	Cycles
Initial Denaturation	98	2'30''	1
Denaturation	94	30''	29
Annealing	58	30''	
Extension	72	45''*	
Final extension	72	8'00''	1
Hold	20	1'00''	1

*For the extension step, use 45 s/kb of the fragment length. Fragment lengths are presented in [Figure 5.1](#).

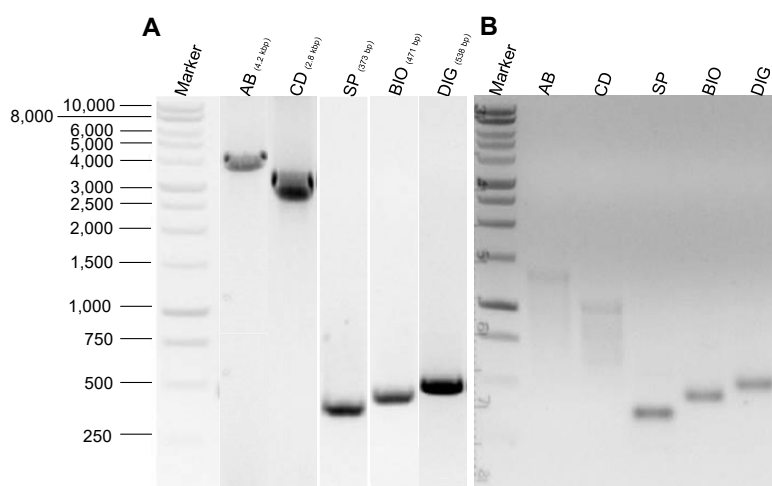


Figure 5.2. Agarose gels for verification of fragment size.

(A) DNA fragments amplified by gradient PCR purified on individual 0.7% agarose gels (here, joined lanes), stained with SYBR safe. (B) Transcribed RNA products running on a 1.0% agarose gel, stained with SYBR Safe. AB: construct backbone; CD: RNA synthesis template; SP: spacer fragment; BIO: biotin-enriched handle; DIG: digoxigenin-enriched handle.

2. Load 20 μl of each DNA fragment into a lane of a 0.7% agarose gel, run for 60 min at 60V, and purify them using gel electrophoresis (**Figure 5.2A**).
3. Stain the gel with SYBR Safe and visualize using blue light.
4. Cut the bands of each DNA fragment out of the gel and purify using the Promega Wizard kit according to the manufacturer's manual.
5. Determine the concentrations of the different DNA eluates with a spectrophotometer and adjust to 10 μM in MilliQ water.

Note: for the conversion of RNA concentration from ng/ μl to molar concentration, the following formula can be used:

$$DNA \text{ (moles)} = \frac{m_{dsDNA} \text{ (g)}}{\left(\left(l_{dsDNA} \text{ (bp)} * \frac{607 \frac{\text{g}}{\text{mol}}}{\text{bp}} \right) + 158 \frac{\text{g}}{\text{mol}} \right)}$$

$$[DNA] \text{ (M)} = \frac{DNA \text{ (moles)}}{V \text{ (l)}}$$

with $m_{dsDNA} \text{ (g)}$ = mass of dsDNA in grams, $l_{dsDNA} \text{ (bp)}$ = length of dsDNA in base pairs, and $V \text{ (l)}$ = volume in liters.

6. For each DNA fragment, prepare the RNA transcription reaction using the Promega T7 transcription kit together with the appropriate pipetting protocol:

Note: since RNases can cleave and degrade the RNA, we recommend the use of RNase free reagents and pipette tips from this point forward.

Transcription of fragments SP, CD and AB	
Transcription mixture	Volume (μl)
PCR product 250 ng	6
Transcription buffer (5X)	10
ATP (100 mM)	1
UTP (100 mM)	1
GTP (100 mM)	1
CTP (100 mM)	1
T7 polymerase	5
MilliQ water	25

Transcription of fragments BIO and DIG	
Transcription mixture	Volume (μ l)
PCR product 250 ng	6
Transcription buffer (5X)	10
ATP (100 mM)	1
UTP (100 mM)	0.5
GTP (100 mM)	1
CTP (100 mM)	1
Bio-UTP/DIG-UTP (10 mM)	5
T7 polymerase	5
MilliQ water	20.5

7. Incubate the transcription reactions for 3 h at 37°C without shaking or rotation.
 8. To each transcription mixture add 0.5 μ l DNaseI and incubate for another 15 min at 37°C.
 9. Purify the synthesized RNA fragments with an RNeasy MinElute cleanup kit, following the [manufacturer's manual](#). Elute the RNA fragments in 1 mM sodium citrate (pH 6.4).
 10. Confirm the RNA fragment size using a 1% agarose gel, run for 60 min at 60 V ([Figure 5.2B](#)).
 11. Determine the concentration of the eluted RNA transcripts with a spectrophotometer.
 12. To anneal the RNA transcripts to the dsRNA construct, mix the SP, CD, and AB RNA transcripts in equimolar ratio and add the DIG and BIO handles in 4x molar excess in SSC buffer (0.5x saline-sodium citrate) in a total reaction volume of 200 μ l.
- Note:** To obtain the force-extension relationship of ssRNA and dsRNA in MT, perform the same annealing reaction as in step 12., but without the CD fragment.
13. Perform the annealing reaction of the dsRNA or ssRNA constructs using the following program in the thermocycler:

Steps	Temperature (°C)	Time (min)	Cycles
Denaturation	65	60	1
Step-wise cooldown for annealing	-1.2	5	51
Hold	5	10	1

5.3 Key resources table

Reagent or Resource	Source	Identifier
Antibodies		
Digoxigenin antibodies	Roche	RRID: AB_514496
Chemicals, peptides and recombinant proteins		
Hellmanex II or III	Sigma-Aldrich	Cat#Z805939
Ethanol	Honeywell	Cat#32221
PBS	Sigma-Aldrich	Cat#P4417
Agarose	Sigma-Aldrich	Cat#A9539
SYBR Safe	FisherScientific	Cat#S33102
MilliQ	Millipore	Cat#ZWMQ22INE E0
SCC buffer (20X)	Promega	Cat#V4261
HEPES	Sigma-Aldrich	Cat#H3784
Pluronic® F127	Sigma-Aldrich	Cat#9003-11-6
BSA	ThermoFisher	Cat#AM2616
NaCl	Sigma-Aldrich	Cat#S9888
MgCl ₂	Sigma-Aldrich	Cat#M8266
DnaseI	ThermoFisher	Cat#EN0525
RdRp	REF ¹	n/a
ApU dinucleotide	IBA Lifescience GmbH	Cat#0-31004
Biotin-16-UTP	Roche	Cat#14470528
Digoxigenin-11-UTP	Roche	Cat#14129222
rNTPs	GE Healthcare	Cat#27-2025-01
T1106 triphosphate	Blake Peterson lab	n/a
Ribavirin triphosphate	Jena Bioscience	Cat#NU-1105L
Superase RNase inhibitor	ThermoFischer	Cat#AM2694
Polystyrene beads 1.50 µm	PolySciences	Cat#17133
Streptavidin-coated Superparamagnetic beads M280	ThermoFischer	Cat#65001
Biological samples		
RNA template	REF ⁷	n/a
pBAD vector	Addgene	RRID:Addgene_37505
Software and algorithms		

Labview 2011	National Instruments	RRID: SCR_014325
Igor Pro 6.37	Wavemetrics	RRID: SCR_000325
Matlab	MathWorks	RRID: SCR_001622
Matlab analysis algorithm	This study	doi.org/10.4121/19145426
Critical commercial assays		
Promega Wizard Genomic DNA purification kit	FisherScientific	Cat#PR-A1120
RNeasy kit	Qiagen	Cat#74004
Promega T7 RiboMAX Express Large Scale RNA Production system	Promega	Cat#P1320
Phusion High-Fidelity PCR Master Mix with HF Buffer	ThermoFisher	Cat#F531S
Experimental models: Cell lines		
RD cell line (one passage P1)	ATCC	RRID: CVCL_1649
Oligonucleotides		
BIO-For	Biolegio	5'- AAGATTAGCGG ATCCTACCTGAC
BIO-REV	Biolegio	5'- TAATACGACTCA CTATAGGAACG GCTTGATATCCA CTTTACG
SP-FOR	Biolegio	5'- TGCCATTCAGGG ACTGCCGATGTC GGTGCAGCCG
SP-REV	Biolegio	5'- TAATACGACTCA CTATAGGAGCG CCGCTTCCATGT CCTGGAACGCT
CD-FOR	Biolegio	5'- ACGCTTTCGCGT ACACCAACAGT TGTATGACGCTG GAAGCGATTCGT G

CD-REV	Biolegio	5'- TAATACGACTCA CTATAGGCCGG ACGTTTCGGATC TTCCGACATGCG C
DIG-FOR	Biolegio	5'- AGCGTAAAATT CAGTTCTTCGTG GCG
DIG-REV	Biolegio	5'- TAATACGACTCA CTATAGGGCTAC CGGTAAACCTCA ACTTCCATTTC
AB-FOR	Biolegio	5'- TAATACGACTCA CTATAGGATCGC CAAGATTAGCG GATCCTACCTGA C
AB-REV	Biolegio	5'- GGTAAACCTCAA CTTCCATTTC
Other		
Coplin Staining Jar	PolySciences	Cat#08415-3
Parafilm	VWR	Cat#291-0057
Flow cell holder	This work	doi.org/10.4121/19145426
Menzel-Gläser coverslips (#1, L x W = 24 x 60 mm)	VWR	Cat#631-1339
Sandblaster	PrepStart 200	Cat#212854
Sonicator	FisherScientific	Cat#13493609
Plasma-PREEN I	Plasmatic Systems Inc.	n/a
Reglo digital pump MS-2/8	Ismatec	Cat#ISM832
Thermo Thermal Cycler	Bio-Rad	Cat#1851148
NanoDrop	FisherScientific	n/a
Hot plate	FisherScientific	Cat#15353518

5.4 Materials & Methods

SCC buffer (pH 7.0)

Reagent	Final concentration	Amount
SCC buffer (20X)	0.5X	2.5 ml
ddH ₂ O	n/a	97.5 ml
Total	n/a	100 ml

Store at 4 °C for up to 3 months, heat to RT prior to use

PBS buffer (pH 7.4)

Reagent	Final concentration	Amount
PBS	0.01M Na ₂ PO ₄ buffer, 0.0027M KCl, 0.137M NaCl	1 tablet
ddH ₂ O	n/a	200 ml
Total	n/a	200 ml

Store at 4 °C for up to 3 months, heat to RT prior to use

Passivation buffer (pH 7.0)

Reagent	Final concentration	Amount
HEPES (1M)	50 mM	5 ml
BSA (50 mg/ml)	1 mg/ml	2 ml
MgCl ₂ (1M)	5 mM	500 µl
ddH ₂ O	n/a	92.5 ml
Total	n/a	100 ml

Store at 4 °C for up to 3 months, heat to RT prior to use

BSA buffer (pH 7.4)

Reagent	Final concentration	Amount
PBS	0.01M Na ₂ PO ₄ buffer, 0.0027M KCl, 0.137M NaCl	1 tablet
BSA (50 mg/ml)	40 µg/ml	1.6 ml
ddH ₂ O	n/a	198.4 ml
Total	n/a	200 ml

Store at 4 °C for up to 3 months, heat to RT prior to use

Preparation buffer (pH 7.4)

Reagent	Final concentration	Amount
HEPES (1M)	50 mM	5 ml
NaCl (1M)	150 mM	15 ml
BSA (50 mg/ml)	20 µg/ml	40 µl
F127 (5%)	0.02%	400 mg
ddH ₂ O	n/a	80 ml
Total	n/a	100 ml

Store at 4 °C for up to 3 months, heat to RT prior to use

Transcription buffer (pH 6.6)

Reagent	Final concentration	Amount
HEPES (1M)	50 mM	5 ml
MgCl ₂ (1M)	5 mM	500 µl
BSA (50 mg/ml)	125 µg/ml	250 µl
F127 (5%)	0.02%	400 µl
DTT (100 mM)	1 mM	1 ml
Suprase (20 U/µl)	0.1 U/µl	500 µl
ddH ₂ O	n/a	92 ml
Total	n/a	100 ml

Store at 4 °C for up to 3 months, heat to RT prior to use

5.5 Step-by-step method details

5.5.1 Preparation of the flow cell

Timing: 2.5 h

1. Use a sandblaster, CNC laser cutter, or diamond drill to drill two holes (~1.0-1.5 mm diameter) into the top cover slip for the inlet and outlet of the flow cell; see [Figure 5.3A](#).
2. Cut a double-layer of parafilm with a scalpel to the desired channel dimensions (here, 5 mm wide and 40 mm long; see also [Figure 5.3A](#)).
3. Clean a (top) coverslip with holes (obtained at step 1) and a (bottom) coverslip without holes by sonicating them for 25 min in 4% (v/v) Hellmanex III in MilliQ water at 40 °C in a coplin staining jar.
4. Wash the coverslips multiple times with MilliQ water.
5. Sonicate the coverslips for 25 min in MilliQ water at 20°C.
6. Sonicate the coverslips for 25 min in Ethanol (e.g., *pro analysis* grade).
7. Dry the coverslips with a nitrogen stream.
8. Apply oxygen plasma to both coverslips (20 seconds, oxygen flow: 2.5 SCFH; 200 W).

9. Assemble the flow cell by melting the double-layer of parafilm between the top and the bottom coverslip on a hot plate (95°C for 30 s; see also [Figure 5.3B](#)).

Note: it is recommended to prepare multiple coverslips for higher throughput or in case of leakage/breaking of flow cells.

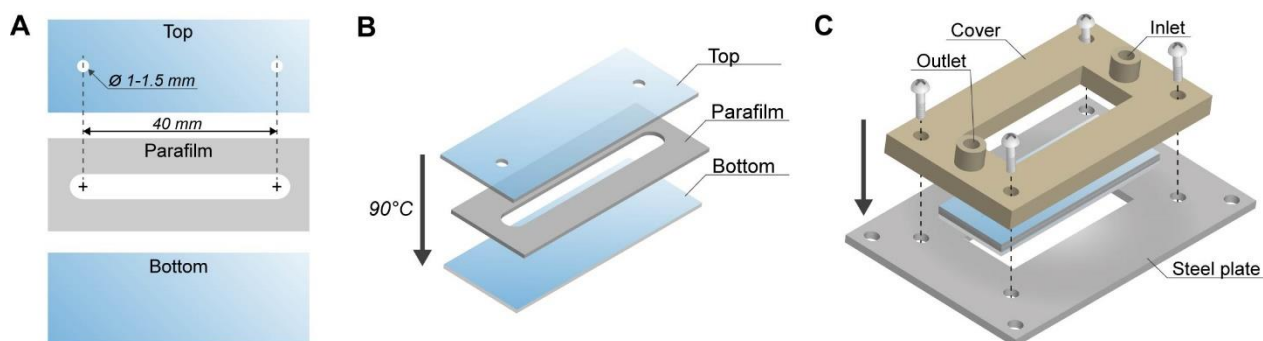


Figure 5.3. Flow cell assembly process.

(A) A flow cell consists of a top coverslip with two holes of 1–1.5 mm diameter, approximately 40 mm from each other, a double layer of parafilm (~200 μm thickness) with cut-out channel in the center, and a bottom coverslip. The total volume of the flow cell channel corresponds to ~70 μL . (B) Representation of flow cell assembly by melting the double-layer of parafilm between the top and bottom coverslips. (C) Assembly of the flow cell in an MT flow cell holder. The technical drawings of the MT flow cell holder parts are available at <https://doi.org/10.4121/19145426>.

5.5.2 Flow cell assembly

Timing: 30 min

The flow cell holder ensures proper attachment to the magnetic tweezers, minimizing potential vibrational influence and mechanical drift to measurement accuracy. Additionally, it adds practical inlet and outlet connections to the flow cell.

10. Assemble the flow cell in a flow cell holder ([Figure 5.3C](#)).

11. Attach the flow cell to the magnetic tweezers instrument and attach the outlet to a tube that is connected to a peristaltic pump ([Figure 5.3C](#)).

Note: any pump type (e.g. peristaltic, syringe) can be used as long as speeds as low as ~200 $\mu\text{L}/\text{min}$ can be achieved.

12. Flow 300 μL PBS buffer through the flow cell by pipetting the solution directly into the inlet ([Figure 5.3C](#)) during pumping and assure full wetting (complete side-to-side covering of the channel with buffer within the flow cell).

Note: throughout the protocol it is important to have all buffers at least at 20°C and use low flow rates (e.g., ~200 $\mu\text{L}/\text{min}$) to minimize the formation of air bubbles in the flow cell. Additionally, prior degassing of the buffers can be beneficial.

13. Perform a leakage test by closing the valve to the pump, filling the inlet with buffer, and observing the reduction in volume at the inlet for ~15 min. A large reduction in volume indicates leakage.

Note: evaporation will also reduce the volume, but only marginally over time. If leakage is apparent, it might be resolved using one of the presented solutions ([Troubleshooting](#); [Problem 1: the flow cell](#)).

5.5.3 Attachment of reference beads to flow cell surface

Timing: 15 min

Reference bead attachment to the surface provides a reference point for displacement of the magnetic beads relative to the surface.

14. Flow 100 μl of polystyrene beads (stock concentration of 1.35×10^{10} beads/ml) diluted 1,500 times in PBS into the flow cell (see [Figure 5.4](#): step 1.).
15. Incubate solution until 5-8 beads per field of view are adhered to the surface.
16. Flush all non-adhered beads out using 1-2 ml PBS buffer.

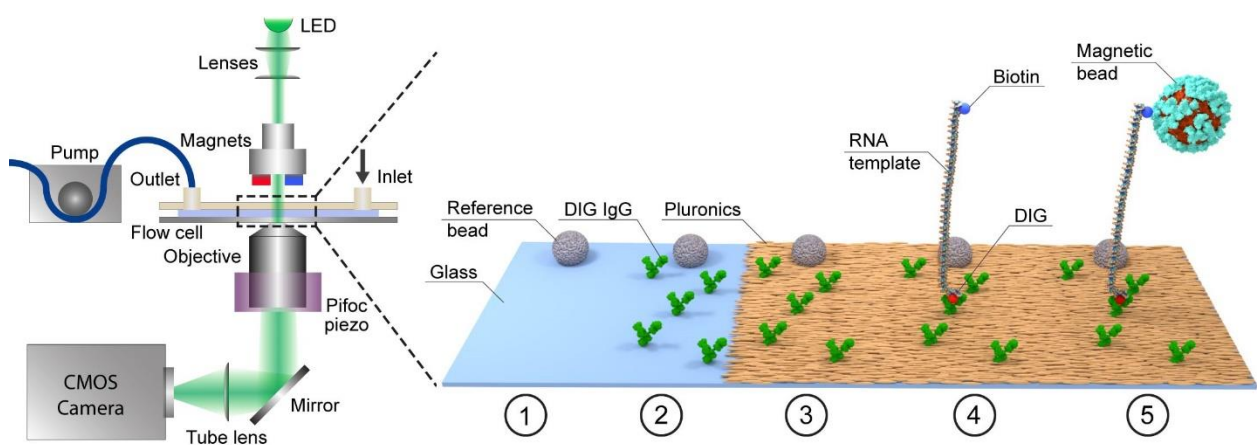


Figure 5.4. Schematic of the MT and step-wise functionalization of the flow cell surface.

(Left) General overview of the MT setup: light originating from an LED travels through the gap between the magnets, illuminates the flow cell, and is captured by the objective. The images are reflected to and recorded by a CMOS camera and analyzed with custom-written software to determine the x, y and z positions of the magnetic beads in real time⁸. The outlet of the flow cell holder is connected to a suction pump. (Right) The steps involved in coating the flow cell surface and tethering the RNA construct: (1) Reference beads are attached to the surface. (2) Anti-DIG antibodies are attached to the surface, serving as an anchor for the RNA construct. (3) Passivation of the glass surface using the poloxamer Pluronic F127 to suppress unspecific adhesion of biomolecules and magnetic beads. The antibodies and reference beads protrude through the surface coating. (4) The RNA construct is anchored to the flow cell via anti-DIG:DIG linkage. (5) A streptavidin-coated magnetic bead is attached to the RNA construct through the strong biotin:streptavidin interaction. Drawings are not to scale.

5.5.4 Attaching digoxigenin antibodies to the flow cell surface

Timing: 70 min

The digoxigenin antibodies provide the RNA construct an anchor point on the surface.

17. Flush 100 μl of 0.1 mg/ml anti-DIG IgG in PBS into the flow cell and incubate for 1 h (see [Figure 5.4](#): step 2.).
18. Flush out non-adhered, residual anti-DIG IgG using 500 μl PBS buffer.

5.5.5 Surface passivation with BSA and F127

Timing: 170 min

Surface passivation ensures that non-specific adhesion of proteins, RNA, or magnetic beads is reduced to a minimum.

19. Flush though the flow cell 500 μl of PBS supplemented with 10 mg/ml BSA (see [Figure 5.4](#): step 3.).
20. Incubate for 2 h.
21. Flush though the flow cell 500 μl BSA buffer.
22. Flush though the flow cell 500 μl of PBS supplemented with 0.5% F127.
23. Incubate for 30 min.
24. Flush though the flow cell 500 μl PBS.

5.5.6 Washing of magnetic beads

Timing: 10 min

Washing the magnetic beads in passivation buffer ensures that non-specific adhesion of magnetic beads to the surface is reduced to a minimum. Furthermore, it allows for a buffer exchange from the manufacturer's storage buffer.

Note: the washing of the magnetic beads can be performed in parallel to the surface passivation. We advise to perform the steps 25.-27. during the incubation of 0.5% F127 in the flow cell (step 23).

25. Add 3.0 μl of M280 magnetic beads to 100 μl of passivation buffer.
26. Mix the solution, then separate the magnetic beads from the liquid using a magnetic stand and discard the supernatant.
27. Repeat previous step 2 more times with fresh passivation buffer. Afterwards, resuspend the magnetic beads in 100 μl preparation buffer.

5.5.7 RNA tethering between surface and magnetic beads

Timing: 35 min

RNA and magnetic bead tethering are crucial for setting up the MT assay.

28. Inject 100 μl of 2 pM RNA construct in preparation buffer into the flow cell (see [Figure 5.4](#): step 4.).

Note: for the conversion of RNA concentration from $\text{ng}/\mu\text{l}$ to M, the following formula can be used:

$$RNA \text{ (moles)} = \frac{m_{dsRNA} \text{ (g)}}{\left(\left(l_{dsRNA} \text{ (bp)} * \frac{641 \frac{\text{g}}{\text{mol}}}{\text{bp}} \right) + 318 \frac{\text{g}}{\text{mol}} \right)}$$

$$[RNA] \text{ (M)} = \frac{RNA \text{ (moles)}}{V \text{ (l)}}$$

with $m_{dsRNA} \text{ (g)}$ = mass of dsRNA in grams, $l_{dsRNA} \text{ (bp)}$ = length of dsRNA in base pairs, and $V \text{ (l)}$ = volume in liters.

29. Incubate for 20 min.

30. Flush 500 μl of preparation buffer through the flow cell to wash away non-tethered RNA constructs.

31. Inject 100 μl of washed magnetic beads and incubate until 200-300 beads are tethered per field of view, typically after ~ 5 min (here, the field-of-view dimensions are $491 \mu\text{m} \times 369 \mu\text{m}$; see [Figure 5.4](#): step 5.).

Note: for this protocol we recommend using M280 beads because they can readily reach forces up to tens of pN, and their hydrophobic surface coating significantly reduces non-specific bead adhesion on the surface compared to hydrophilic M270 beads.

Note: If non-specific bead adhesion to the surface is apparent, it might be resolved using one of the presented solutions ([Troubleshooting; Problem 3: all magnetic beads are adhered to the surface](#))

32. Wash surplus of untethered beads out using 1-2 ml of preparation buffer.

Note: the magnetic beads should be held at a constant force of ≥ 2 pN to exclude potential non-specific bead adhesion on the surface before the initiation of RNA synthesis.

Note: If tether formation is not observed, it might be resolved using one of the presented solutions ([Troubleshooting; Problem 2: absence of tether formation](#)).

5.5.8 Creating a magnetic bead Z-lookup table

Timing: 5 min

Bead Z-position look-up tables are created as a reference to accurately determine the beads' vertical position relative to the focal plane over time. There are different ways to determine the bead Z-position in MT. Here, we create an individual look-up table for each dsRNA-tethered bead and reference bead^{8,9}.

33. Create bead Z-position look-up tables (200 steps, 50 nm step size) at a constant force of 10 pN.

5.5.9 Measuring the force extension curves for dsRNA and ssRNA

Timing: 30 min

This measurement has to be made only once to estimate the extensions of the dsRNA and ssRNA (created by annealing all fragments with the exception of the CD fragment (**Figure 5.1B**) according to Before you Begin, step 12.) constructs as a function of force. This information will be important at later stage to convert the height change of the tethered beads in micrometers to nucleotides synthesized by RdRp.

34. Measure the extension of dsRNA and ssRNA with force ranging from 0.01 to 40 pN.
35. Repeat steps 1.-33. using the ssRNA construct (without CD transcript).
36. Determine the ssRNA $l_{ss}(F)$ and dsRNA $l_{ds}(F)$ extensions. Select the lowest possible force at which the the difference between $l_{ss}(F)$ and $l_{ds}(F)$ is sufficiently large. Larger differences between $l_{ss}(F)$ and $l_{ds}(F)$ will result in a larger bead displacement in I-direction per nucleotide incorporated by the RdRp, and thus an increased spatial resolution. For the RNA constructs used here, 25 pN was chosen; see also **Figure 5.5**.

5.5.10 Ternary complex formation

Timing: 30 min

Ternary complex formation is the construction of the full RNA tether with a stalled RdRp present on the RNA template. Ternary complex formation can significantly increase RdRp re-initiation efficiency when dinucleotide ApC is used.

37. Flush 80 μ l of transcription buffer supplemented with 600 nM RdRp, 0.6 mM ATP, 0.6 mM CTP and 1.2 mM ApC dinucleotide into the flow cell.
38. Incubate for 20 min.
39. Wash out all unbound RdRp with 500 μ l of transcription buffer.

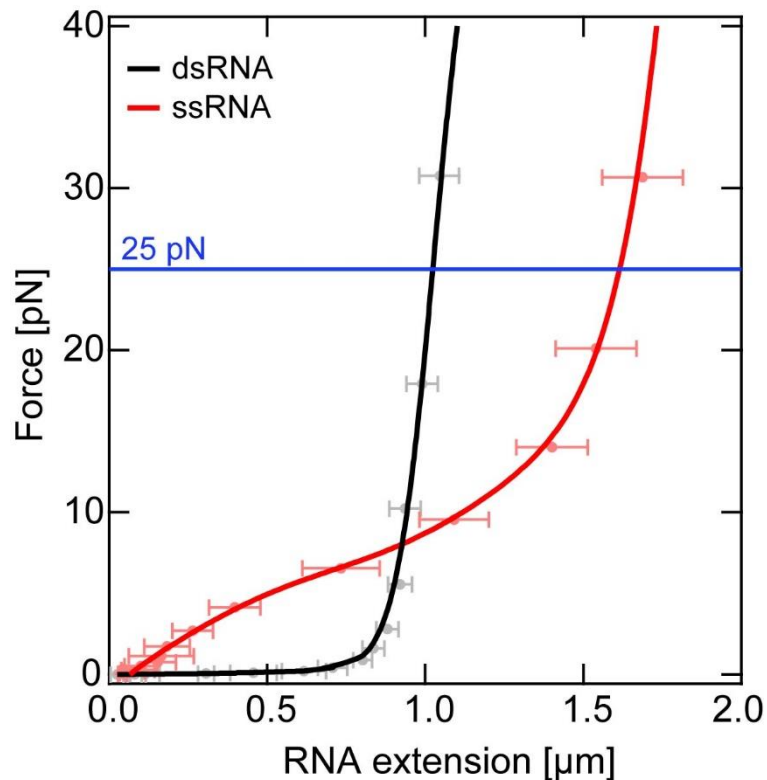


Figure 5.5. Force-extension curves of ssRNA and dsRNA.

Force-extension curve of the dsRNA construct (gray) and the ssRNA construct (red) that lacks the CD fragment. The lines represent a WLC fit to the dsRNA data (black) and a linear interpolation of the ssRNA data (red). During RdRp RNA synthesis, the CD template strand is displaced from the AB strand, gradually increasing the fraction of ssRNA. A constant force of 25 pN (blue) was selected for our experiments due the large difference in extension between dsRNA and ssRNA, which provides high spatial resolution for RdRp RNA synthesis. Error bars represent standard deviation ($N = 8$).

5.5.11 RNA tether characterization

Timing: 15 min

It is important to verify that the dsRNA constructs are singly tethered to a magnetic bead and of correct length. Furthermore, the measured length of each dsRNA tether must be known to convert the reduction in bead height upon RdRp RNA synthesis from micrometers to transcribed RNA nucleotides. The recording of the magnetic bead movement in all three dimensions was conducted with the control software described and published in REF⁸. The measurement parameters were set to: 25 Hz camera frequency, Look Up Table (LUT) range of 10 μm with steps of 50 nm, *quadrant interpolation* as the algorithm used for the bead's Z-position determination, and a Region of Interest (ROI) of 90 px.

40. Start the data acquisition and perform the dsRNA tether characterization by changing the force and magnet rotation over time (see also [Figure 5.6A,B](#)) as follows:

Characterization of dsRNA tether				
Magnet action	Force (pN)	Rotation (turns)	Time (s)	Purpose
Magnet height	0	0	5	Determine z-offset (z_0)
Magnet height	25	0	10	Stretch tether to measurement force
Magnet rotation	25	-30	10	Probe for multiple DNA tethering
Magnet rotation	25	0	10	Return to original rotation state
Magnet rotation	25	2	8	Determine DNA attachment to bead
Magnet rotation	25	-2	16	Return to original rotation state
Magnet height	3	0	5	Relax tether, maintaining low force

Note: the undesired tethering of multiple RNA tethers to one bead is signified by a sharp decrease in the bead Z-position during the rotation of the magnets in the negative direction at high force. Additionally, the rotations provide information instrumental to the determination of the length of the RNA tether, see below.

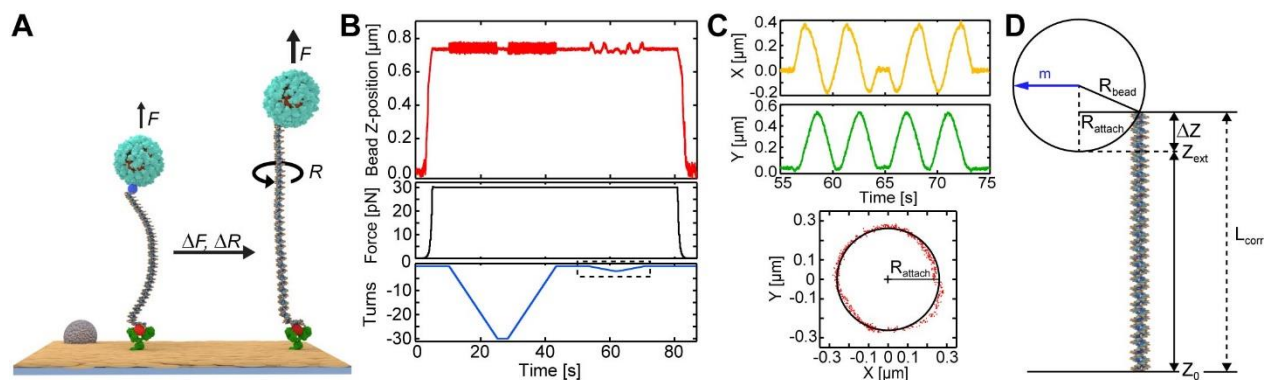


Figure 5.6. dsRNA tether characterization measurement and analysis.

(A) The dsRNA tether is stretched from low to high force (ΔF) as well as rotated (ΔR) with a varying speed and number of turns. (B) Bead Z-position at zero force (top; red) and applied force (middle; black) during the experiment (here, 25 pN), allowing the determination of the apparent end-to-end length (L_{app}) of the dsRNA tether. The magnet is rotated (bottom; blue) to determine whether the dsRNA is singly tethered to the magnetic bead (with -30 turns at the force applied for the RNA synthesis experiment), and to assess the distance R_{attach} between the off-center attachment point of the dsRNA tether and the bead's geometric south pole (as defined when the bead's net magnetic moment (m) aligns with the field, panel D). (C) X- and Y-positions of the magnetic bead during slow rotations (0.25 s/turn; see the dashed box in (B)) allow the determination of R_{attach} using a circular fit. (D) The correct end-to-end dsRNA construct length L_{corr} is the sum of the apparent length Z_{ext} and DZ , where DZ is the height difference between the off-center dsRNA attachment point.

41. From the traces, determine each the magnetic bead's height at zero force (Z_0) and at 25 pN (Z_{ext}); see [Figure 5.6B](#).

42. Determine the radius of the magnetic beads' rotational motion R_{attach} by fitting the plot of X-positions in function of Y-positions with a circle; see [Figure 5.6C](#).

Note: the attachment point of the RNA tether to the magnetic bead is in most instances not perfectly at the bead's geometric south pole ([Figure 5.6D](#))^{10,11}. Therefore, the apparent length of tether (Z_{ext}) can be significantly smaller than the actual tether length (L_{corr}) and needs to be corrected. Slow rotation of the bead will provide crucial information for the correction. While we used Igor Pro (V6.37) as the software platform for the analysis of the bead traces, any other scripting-capable software that is able to import the text file output of the data acquisition software can be used, i.e. commonly used Matlab and Python.

43. Calculate the length difference ΔZ between the RNA attachment point R_{attach} and the bead's south pole using the bead radius R_{bead} and the Pythagorean theorem (see also [Figure 5.6D](#)):

$$\Delta Z = R_{bead} - \sqrt{R_{bead}^2 - R_{attach}^2}$$

44. Add the corrected tether length by adding ΔZ to the apparent end-to-end length Z_{ext} obtained from the calibration measurement (see [Figure 5.6D](#)):

$$L_{corr} = Z_{ext} - Z_0 + \Delta Z$$

45. Calculate the average length of an RNA base by dividing L_{corr} by the number of base pairs in the construct; this value is later used to convert changes in bead Z-position to synthesized RNA products as a function of time.

5.5.12 Measuring RdRp RNA synthesis kinetics

Timing: 2 h

Addition of all nucleotides allows the ternary complexes to re-initiate RdRp RNA synthesis ([Figure 5.7A](#)).

46. Lower the magnet to the appropriate height to apply a constant force of 25 pN (or any other force determined in steps 34.-36.).
47. Re-initiate RNA synthesis by flushing 100 μ l of transcription buffer supplemented with all four rNTPs into the flow cell (the NTP concentration depends on the experiment design; here, 1 mM was chosen).
48. Immediately after, start the measurement and record all magnetic bead Z-positions for 2 h.

Note: complete absence of RdRp trajectories might be resolved using one of the presented solutions ([Troubleshooting](#); [Problem 4: no RdRp activity observed](#)).

5.6 Quantification and statistical analysis

In this section, the protocol describes the analysis of the bead z -displacement (associated with ssRNA displacement during RNA synthesis) obtained in the MT experiment in a step-wise fashion. In the first step, the z -displacement of the magnetic bead is converted into number of nucleotides synthesized, from which the RdRp processivity and the average velocity are calculated. In the last step the protocol guides through the process of constructing the dwell time distributions of the RNA synthesis kinetics, from which the average pause lifetimes and pausing probabilities are extracted. As aforementioned, we used Igor Pro (V6.37) as software platform for the analysis of the RdRp trajectories, however, scripting-capable software that is able to import the delimited text file output from the acquisition software (e.g. Matlab or Python) is equally suited.

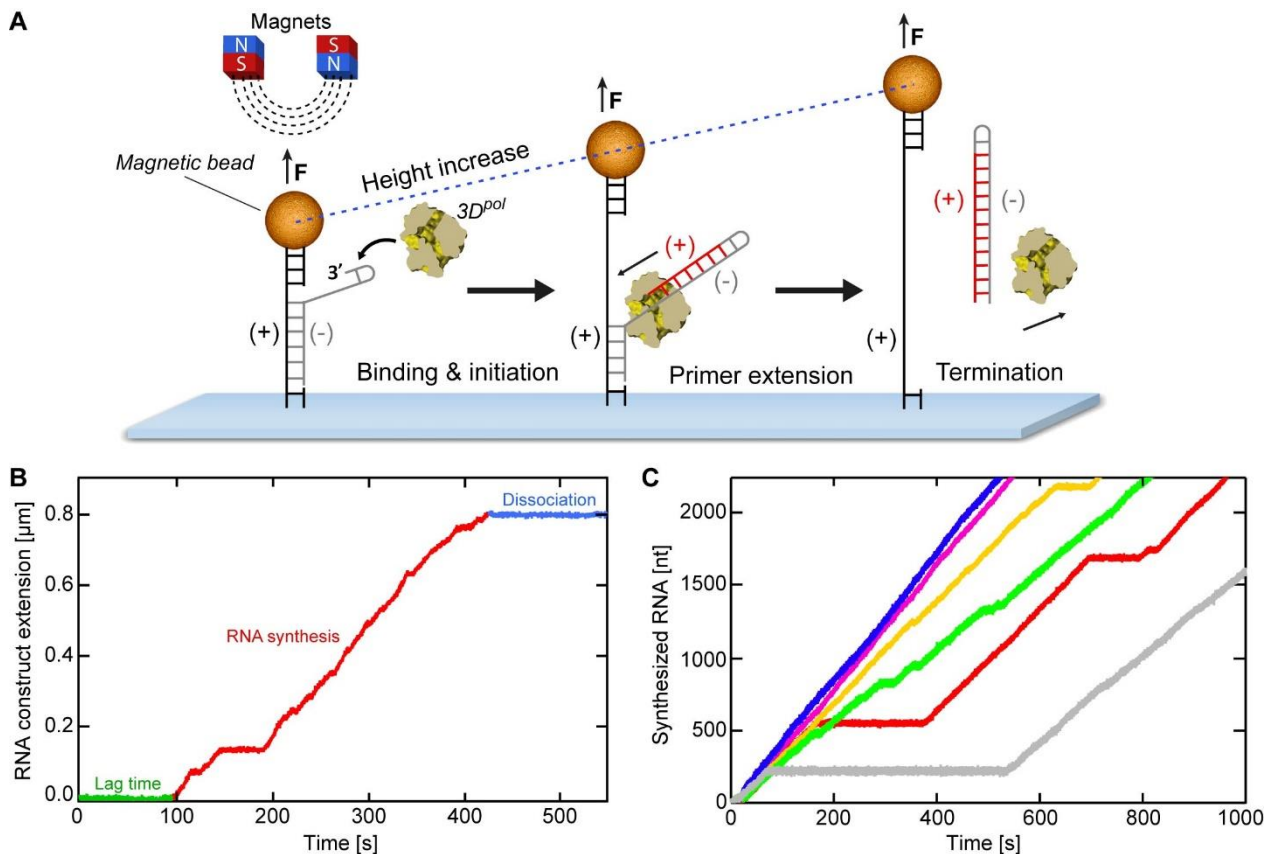


Figure 5.7. Processing of RNA synthesis trajectory data.

(A) Schematic of the single-molecule (+)-strand RNA synthesis assay, showing binding of an RdRp to a hairpin at the 3₀ end of the (-)-strand (gray) of the surface-attached RNA construct. A magnetic bead attached to the RNA construct is subject to a constant force of 25 pN during RNA synthesis. Primer extension (red) from the 3₀ end of hairpin will lead to displacement of the template RNA (gray) from the tethered RNA (black). At 25 pN force, conversion of dsRNA to ssRNA causes a corresponding increase in the distance of the magnetic bead from the surface. (B) Non-processed RdRp RNA synthesis example trajectory, normalized to the initial RNA extension prior NTP-addition. The lag time (green) is the time that the RdRp is inactive before re-initializing RNA synthesis upon NTP-addition and can vastly differ between RdRps. RNA synthesis (red) is intermittent, with stochastic pauses of different lifetimes. Arrest or dissociation of the RdRp causes the RNA extension (or bead z -position) to stop changing (blue). (C) Superimposed, processed example RNA synthesis trajectories that were cut and converted to RNA nucleotides synthesized (data sets from REF¹).

5.6.1 Converting changes in RNA extension to nucleotides synthesized

Timing: 1 h

49. For each individual RdRp trajectory, normalize the RNA extension to the extension before the addition of NTPs. Next, cut out the lag time and final plateaus where there is no RdRp synthesis activity or dissociation has occurred (see [Figure 5.7B,C](#)).
50. Convert the ssRNA extension to the number of RNA nucleotides synthesized, NT_{synth} , using the formula below, where Δl_{meas} represents the measured apparent increase in RNA length, and $l_{\text{ss}}(F) - l_{\text{ds}}(F)$ is the difference in length between the extensions of ssRNA and dsRNA:

$$\alpha = (l_{\text{ss}}(F) - l_{\text{ds}}(F))^{-1},$$

$$NT_{\text{synth}} = \alpha * \Delta l_{\text{meas}}$$

5.6.2 Extracting RdRp processivity and average RNA synthesis velocity

Timing: 1 h

51. Determine the average RdRp processivity from the maximum amount of RNA synthesized in each individual trajectory ($nucleotides_i$; example shown in [Figure 5.8A](#)):
52. Compute the average velocity by dividing individual RdRp processivities (step 51.) by the duration of active RNA synthesis (example shown in [Figure 5.8B](#)):

$$v_{\text{average}} \left(\frac{\text{nt}}{\text{s}} \right) = \frac{\sum_{i=1}^n \frac{nucleotides_i \text{ (nt)}}{time_i \text{ (s)}}}{n}$$

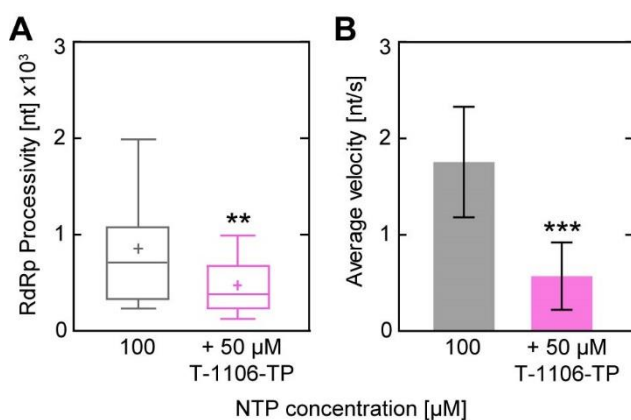


Figure 5.8. RdRp processivity and average RNA synthesis velocity of EV-A71 RdRp.

(A and B) (A) RdRp processivity and (B) average RNA synthesis velocity (meanGSD) derived from example EV-A71 RdRp trajectories in the absence and presence of T-1106 triphosphate (data sets from REF¹). Statistical analyses were performed using unpaired, two-tailed t-tests (significance level: **p < 0.01; ***p < 0.001).

5.6.3 Constructing the dwell time distribution and extracting average pause lifetimes and pausing probability

Timing: 1 h

The construction of the dwell time distribution allows for the calculation of both the average pause probability as well as the average pause lifetime. The dwell times are determined by extracting from all RNA synthesis trajectories the time needed for the RdRp to synthesize a defined number of consecutive nucleotides¹².

53. Filter the individual RNA synthesis trajectories using a 1 Hz sliding mean filter.
54. Construct a dwell time distribution (**Figure 5.9A-C**) of all the RNA synthesis trajectories belonging to the same experimental condition. You may use the MatLab script provided in a repository (<https://doi.org/10.4121/19145426>), which also includes example data.
55. From the dwell time distribution, determine the lifetime where pausing starts. In the example shown in **Figure 5.9B,C**, the lower bound of pausing lifetimes is > 1 s.
56. Calculate the average pause probability P_{pause} by integrating dwell times larger than the pause lifetime lower bound (see example in **Figure 5.9D**):

$$\bar{P}_{\text{pause}} = \frac{\sum_{i=1}^n P_{\text{pause},i}}{n}$$

57. Determine the average pause lifetime by averaging all dwell times larger than the pause lifetime lower bound (see example in **Figure 5.9E**):

$$\bar{\tau}_{\text{pause}} (\text{s}) = \frac{\sum_{i=1}^n \tau_i (\text{s})}{n}$$

5.7 Expected outcomes

The magnetic tweezers protocol presented here enables a quantitative description of RdRp RNA synthesis dynamics, including the nucleotide incorporation rate, pausing frequency, and pause lifetimes, which can be probed under a variety of conditions. The presented data shows the detectable changes in RNA synthesis processivity and pausing dynamics in presence of pyrazine carboxamide nucleotide analog T-1106 (**Figure 5.8** and **Figure 5.9**). The application of this method to variations in conditions, such as NTP concentration, different nucleotide analogs, or even transient roadblocks imposed by RNA-binding proteins, will allow the identification and quantitative characterization of their effect on RdRp translocation and RNA synthesis dynamics. Figures related to the expected outcome of each step of the protocol have been presented.

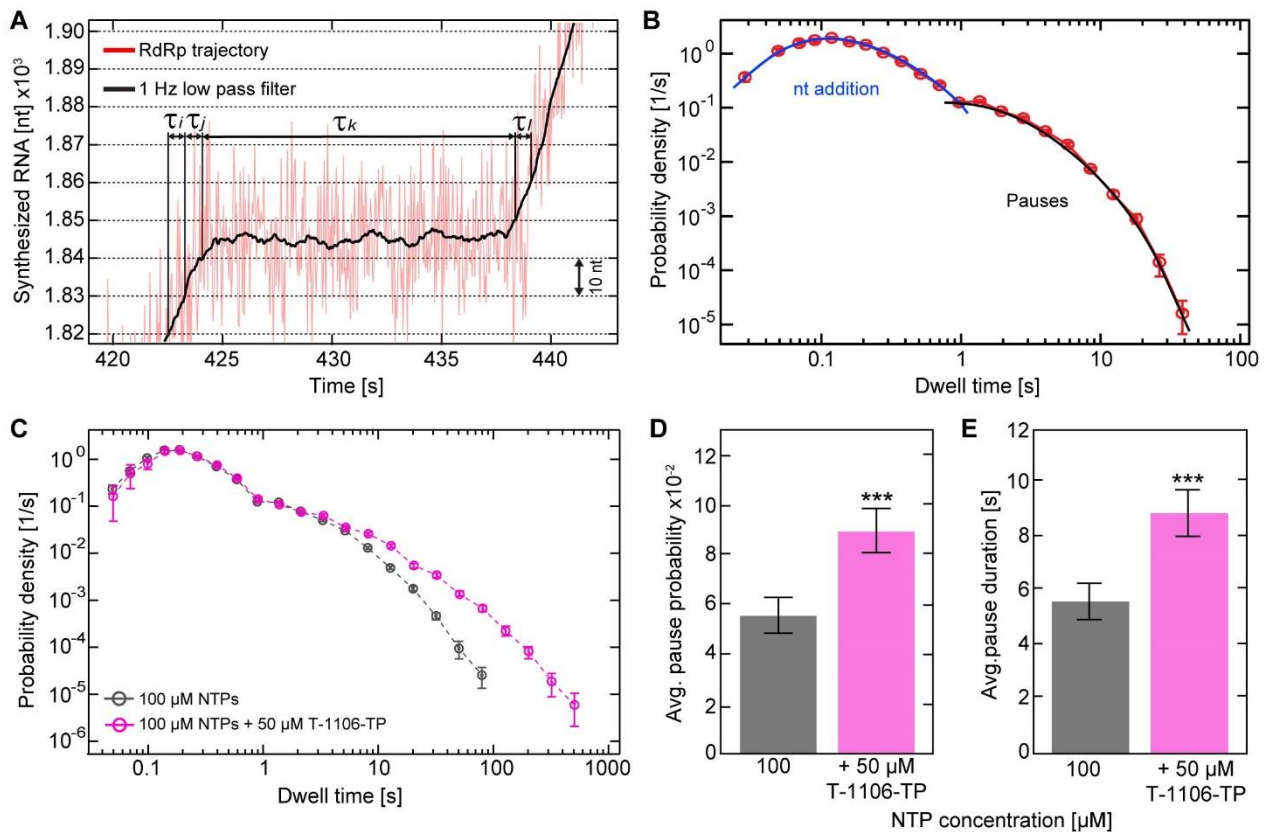


Figure 5.9. Constructing the dwell time distribution and extracting pausing dynamics of EV-A71 RdRp RNA synthesis.

(A) Magnified region of the individual RNA synthesis trajectory shown in Figure 5.7A. The dwell times are determined by extracting the time (t) needed for the RdRp to synthesize a defined number of consecutive nucleotides; the example shows ten-nucleotide dwell time windows as dashed lines. (B) Dwell time probability distribution of 9,981 dwell times extracted from RNA synthesis trajectories using a dwell time window of four nucleotides and binned with six bins per decade. The error bars (AVG GSD) result from bootstrapping with 1,000 iterations. Solid curves show the best fit of a simple model to the data, where the contributions of individual components of the model are separated: the blue curve at short timescales captures the effective pause-free elongation rate, while the black curve corresponds to a single pause state with exponential decay. (C) Superimposed dwell time distributions of EV-A71 RdRp in absence (gray) and presence (magenta) of the nucleotide analog T-1106 triphosphate; data sets from REF¹ (D and E) Quantification of the dwell time distributions in (C): the addition of T-1106 triphosphate (magenta) induces a significant increase in (D) pausing probability (meanGSD) and (E) average pause duration (meanGSEM). Statistical analyses were performed using unpaired, two-tailed t-tests (significance level: *** $p < 0.001$).

5.8 Limitations

A limitation of the presented method is the inability to directly interrogate the RNA products of RdRp activity that are produced in the magnetic tweezers. In addition, the amount of processing power required to determine many tracked bead positions using Z-lookup table cross-correlation can be significant. To avoid crashing or freezing of the software, it is advised to ensure that a PC with sufficient computational power is used for tracking of many magnetic beads.

5.9 Troubleshooting

Problem 1: the flow cell leaks

Potential solutions:

- Reduce the inlet and outlet holes' diameter in the top cover slip (step 1.).
- Tighten carefully the screws of the flow cell (step 10.).
- Check O-rings for graining or damage of the rubber and possibly replace them (step 10.).
- Replace the flow cell in the holder (step 10.).
- Check attachment of inlet and outlet tubing (step 11.).

Problem 2: absence of tether formation

Potential solutions:

- Replace stocks of anti-DIG, RNA construct, RNase inhibitor, and magnetic beads (steps 17., 28., and 31.).
- Use or synthesize a new RNA construct. Contaminations with RNases can cut the dsRNA, thus preventing tether formation (step 28.).
- Increase RNA concentration (step 28.).
- Increase incubation time of magnetic beads (step 31.).

Problem 3: all magnetic beads are adhered to the surface

Potential solutions:

- Increase passivation time of the flow cell (step 20.).
- Use new magnetic bead stock. Make sure magnetic beads are not expired (step 25.).
- Switch hydrophobicity of the beads (from M280 to M270 or vice versa) (step 25.).
- Increase passivation time of the magnetic beads (step 26.).
- Reduce incubation time of the magnetic beads (step 31.).
- Give a short pulse of high force (max. 40 pN) to break non-specific bead adhesion (prior to step 46.).

Problem 4: no RdRp activity observed

Potential solution:

- Use another batch of or purify new RdRp (step 37.).
- Increase ternary complex formation time (step 38.).
- Increase the concentration of rNTPs (step 47.).

Problem 5: output parameters differ significantly between experiments with the same conditions**Potential solution:**

- Exclude outliers (step 49.).
- Ensure that the cropping of the RdRp trajectory is performed correctly: directly after the lag phase and right before reaching the final plateau (step 49.).
- Ensure that all used materials (e.g. RNA, nucleotides, RdRp, buffers, etc.) are from the same batch and within expiration dates (step 28. and 47.).

5.10 References

1. Janissen R, Woodman A, Shengjuler D, et al. Induced intra- and intermolecular template switching as a therapeutic mechanism against RNA viruses. *Mol Cell*. 2021;81(21):4467-4480.e7. doi:10.1016/j.molcel.2021.10.003
2. Seifert M, Bera SC, Van Nies P, et al. Inhibition of sars-cov-2 polymerase by nucleotide analogs from a single-molecule perspective. *Elife*. 2021;10. doi:10.7554/eLife.70968
3. Dulin D, Vilfan ID, Berghuis BA, et al. Elongation-Competent Pauses Govern the Fidelity of a Viral RNA-Dependent RNA Polymerase. *Cell Rep*. 2015;10(6). doi:10.1016/j.celrep.2015.01.031
4. Fields BN, Knipe DM, Howley PM. *Fields Virology*. Philadelphia: Lippincott-Raven Publishers; 1996.
5. Yu Z, Dulin D, Cnossen J, et al. A force calibration standard for magnetic tweezers. *Rev Sci Instrum*. 2014;85(12). doi:10.1063/1.4904148
6. Ostrofet E, Papini FS, Dulin D. Correction-free force calibration for magnetic tweezers experiments. *Sci Rep*. 2018;8(1):2-11. doi:10.1038/s41598-018-34360-4
7. Dulin D, Vilfan ID, Berghuis BA, Poranen MM, Depken M, Dekker NH. Backtracking behavior in viral RNA-dependent RNA polymerase provides the basis for a second initiation site. *Nucleic Acids Res*. 2015;43(21):10421-10429. doi:10.1093/nar/gkv1098
8. Cnossen JP, Dulin D, Dekker NH. An optimized software framework for real-time, high-throughput tracking of spherical beads. *Rev Sci Instrum*. 2014;85(10). doi:10.1063/1.4898178
9. Gosse C, Croquette V. Magnetic tweezers: micromanipulation and force measurement at the molecular level. *Biophys J*. 2002;82(6):3314-3329. doi:10.1016/S0006-3495(02)75672-5
10. Klaue D, Seidel R. Torsional stiffness of single superparamagnetic microspheres in an external magnetic field. *Phys Rev Lett*. 2009;102(2). doi:10.1103/PhysRevLett.102.028302
11. Lipfert J, Hao X, Dekker NH. Quantitative modeling and optimization of magnetic tweezers. *Biophys J*. 2009;96(12):5040-5049. doi:10.1016/j.bpj.2009.03.055
12. Dulin D, Berghuis BA, Depken M, Dekker NH. Untangling reaction pathways through modern approaches to high-throughput single-molecule force-spectroscopy experiments. *Curr Opin Struct Biol*. 2015;34:116-122. doi:10.1016/j.sbi.2015.08.007

6

Induced intra- and intermolecular template switching as therapeutic mechanism against RNA viruses

Viral RNA-dependent RNA polymerases (RdRps) are a target for broad-spectrum antiviral therapeutics. Recently, we demonstrated that incorporation of the T-1106 triphosphate, a pyrazine-carboxamide ribonucleotide, into nascent RNA increases pausing and backtracking by the poliovirus RdRp. Here, by monitoring Enterovirus A-71 RdRp dynamics during RNA synthesis using magnetic tweezers, we identify the “backtracked” state as an intermediate used by the RdRp for both copy-back RNA synthesis and homologous recombination. Cell-based assays and RNAseq experiments further demonstrate that the pyrazine-carboxamide ribonucleotide stimulates these processes during infection. These results suggest that pyrazine-carboxamide ribonucleotides do not induce lethal mutagenesis or chain termination, but function by promoting template switching and formation of defective viral genomes. We conclude that RdRp-catalyzed intra- and intermolecular template switching can be induced by pyrazine-carboxamide ribonucleotides, defining an additional mechanistic class of antiviral ribonucleotides with potential for broad-spectrum activity.

This chapter is published as: R. Janissen, A. Woodman, D. Shengjuler, T. Vallet, K. Lee, L. Kuijpers, I.M. Moustafa, F. Fitzgerald, P. Huang, A.L. Perkins, D.A. Harki, J.J. Arnold, B. Solano, S. Shih, M. Vignuzzi, C. E. Cameron, and N. H. Dekker, “Induced intra- and intermolecular template switching as a therapeutic mechanism against RNA viruses,” *Mol. Cell*, vol. 81, no. 21, pp. 4467-4480.e7, 2021, doi: 10.1016/j.molcel.2021.10.003.

6.1 Introduction

It is still not possible to predict the emergence of viruses capable of founding an epidemic, a fact that has been reconfirmed many times over the past few decades. Since the outbreak of West Nile virus in 1999, one RNA virus after another has emerged, causing significant morbidity and mortality. In 2019, yet another outbreak occurred and rapidly spread globally. While the world is under constant threat of an influenza pandemic¹, the ongoing pandemic was caused by a coronavirus, specifically severe acute respiratory syndrome coronavirus-2 (SARS CoV-2)^{2,3}. An increase of enterovirus D-68 (EV-D68) infections in the US, associated with acute flaccid myelitis in young children, has been registered in the past years, and future outbreaks are anticipated⁴. With recurrent outbreaks of enterovirus A71 in the Asia-Pacific region come hand-foot-and-mouth disease and severe acute flaccid paralysis⁵. This state of affairs demands the availability and rapid development of broad-spectrum antiviral therapeutics to address the next unanticipated and/or unknown viral pathogen.

Viral polymerases have emerged as tractable and highly efficacious antiviral targets⁶. Past and present protocols to treat virus infections have included compounds targeting the viral RNA-dependent RNA polymerase (RdRp). To date, clinically approved antiviral nucleosides have functioned either by terminating nucleic acid synthesis (chain terminators) or by increasing mutational load on the viral genome (lethal mutagenesis)^{7,8}. Resistance to antiviral nucleotides usually comes with a fitness cost, thus increasing the long-term utility of these classes of antiviral agents⁹. The major obstacle to the development of antiviral nucleotides is off-target effects, caused primarily by cellular polymerase utilization of the compounds in question¹⁰. However, the specificity of antiviral nucleotides continues to improve¹¹.

Recently, pyrazine carboxamide nucleoside analogs were approved in Japan to treat influenza virus infection¹². The drug, commercially known as favipiravir, is also known as T-705. It is employed in several countries as a potential antiviral drug against SARS CoV-2 infection based on evidence for its effectiveness in the treatment thereof^{13,14}. Favipiravir is a fluorinated pyrazine carboxamide base analog and requires the cellular nucleotide salvage pathway to convert the base into a nucleoside triphosphate. A version of favipiravir lacking fluorine, known as T-1105, is also active, but its conversion to the triphosphate is less efficient¹⁵. The nucleoside version of T-1105 is referred to as T-1106, and the metabolism of this compound to the triphosphate yields a drug with efficacy superior to favipiravir¹⁵. The results of studies probing the mechanism of action of these compounds have been ambiguous. Some studies were consistent with chain termination¹⁶, while recent results were consistent with lethal mutagenesis¹⁷. Of course, such uncertainty in the mechanism of action complicates worldwide approval beyond Japan.

To gain insights into the underlying mechanism of action of T-1106, we previously used a single-molecule magnetic-tweezers platform to monitor individual poliovirus

(PV) RdRp elongation complexes over thousands of nucleotide-addition cycles and observed the ability of T-1106-TP (superior to that of ribavirin-TP) to cause the RdRp to pause and then backtrack¹⁸. The elongation complex was able to recover from the backtracked state, but recovery required tens to thousands of seconds. As a result, traditional polymerase elongation assays would view these backtracked states as prematurely terminated products¹⁸. This backtracking phenomenon has to date not been observed with either prototypical chain terminators or mutagens. These studies therefore provided very compelling evidence for the existence of a third mechanistic class of antiviral ribonucleoside analogs.

While the structure of the backtracked state of PV is not known, the nascent RNA was likely displaced from template to yield a single-stranded 3' end with lengths greater than tens of nucleotides¹⁸. Such a structure is now known for the SARS CoV-2 RdRp¹⁹. The ability of an RdRp to produce free single-stranded 3' ends was intriguing, because such an end could undergo an intermolecular template switch by annealing to a second template, with resumed synthesis producing a recombinant RNA product.

The goals of the present study were to determine the extent to which the backtracked state represented an intermediate on path for recombination, and to identify the mechanism of action of the pyrazine carboxamide nucleoside analog T-1106. To do so, we introduced the RdRp from EV-A71, a virus prone to recombination in nature²⁰, into our pipeline with the idea that perhaps such backtracked states might also be prevalent with this enzyme. By comparing the EV-A71 and PV RdRps, we provide evidence that the backtracked state is indeed a common intermediate for template switching. Unexpectedly, for EV-A71 RdRp we observed a high frequency of intramolecular template switching, which has been coined “copy-back RNA synthesis” in the literature²¹. Importantly, the capacity for T-1106 to promote recombination was also observed in cells based on RNAseq data from cells infected with EV-A71 in the presence or absence of the drug. Our study therefore makes a clear mechanistic connection between copy-back RNA synthesis and homologous recombination, and provides compelling evidence that an enhancement of the probability of template switching results in an antiviral effect. The experimental paradigm reported here should prove useful in dissecting the contributions and determinants of the RdRp and the template to formation of defective viral genomes, a newly emerging strategy for interfering with virus multiplication and attenuating viral pathogenesis²¹.

6.2 Results

6.2.1 Pausing of EV-A71 RdRp promotes copy-back RNA synthesis

The development of a magnetic-tweezers platform to monitor nucleotide addition by nucleic acid polymerases is unmasking the stochastic behavior of viral polymerases and illuminating states of the polymerase induced by pausing and drugs^{18,22,23}. In this

assay (**Figure 6.1A**), single-stranded RNA is tethered to the surface and a magnetic bead. A template ssRNA, including a 24 nt hairpin structure at its 3' end, is annealed to the tethered ssRNA strand, creating a predominantly double-stranded RNA. Primer-extension from the 3'-end of template RNA will lead to displacement of the template RNA from the tethered RNA. At forces >8 pN, the conversion of dsRNA to ssRNA causes a corresponding increase in the distance of the bead from the surface, thus permitting measurement of nucleotide incorporation with few nucleotide resolution over thousands of cycles of nucleotide addition^{18,22,23}.

In a previous study with PV RdRp, we showed that one consequence of prolonged pausing by the enzyme is backtracking, where the enzyme unwinds the 3'-terminus of nascent RNA¹⁸. It was possible that this state was an intermediate for homologous recombination by an intermolecular template-switching mechanism. Such a template switch would occur by annealing the 3'-terminus of the backtracked, product RNA to a second (acceptor) template. In the magnetic tweezers, there is no acceptor template; therefore, intermolecular template switching cannot occur. In most instances, the nascent RNA reannealed to the original template and RNA synthesis resumed¹⁸.

Here, we evaluate EV-A71 RdRp as it might provide additional insight into the backtracked state. As illustrated in **Figure 6.1B**, pauses of differing duration interrupted processive nucleotide addition by EV-A71 RdRp (quantified in **Figure S.6.1C**). For PV RdRp, we previously observed an inverse correlation between nucleotide concentration and pause probability¹⁸. In this context, EV-A71 behaved similarly (**Figure 6.1C**, **Figure S.6.1A,B**). Pausing is thought to occur in response to misincorporation and happens more often at low nucleotide concentration¹⁸. Such a response might facilitate correction by pyrophosphorolysis^{18,24}.

At some frequency for PV RdRp, however, the paused state undergoes backtracking¹⁸. Surprisingly, under the same conditions, EV-A71 RdRp undergoes reverse translocation (referred to as "reversals"), based on the decrease in position of the bead relative to the surface (**Figure 6.1D**). Pauses induced by low nucleotide concentrations, found to be drivers of backtracking by PV RdRp¹⁸, are also drivers of reversals by EV-A71 RdRp (**Figure 6.1E,F**). While it was not possible to identify sequence motifs at locations where reversals occurred, GC-rich regions favored reversals (**Figure S.6.2**). Given the assay design, the only ways for the bead to approach the surface would be for the EV-A71 RdRp to dissociate and initiate primer extension via the accessible 3' ssRNA end of the bead handle, or to reanneal the displaced template ssRNA to the tethered ssRNA. Our control experiments excluded the former possibility, as in absence of the template ssRNA strand the RdRp was not able to perform primer-extension (**Figure S.6.1E,F**). For the latter scenario to occur, nascent ssRNA would have to be displaced from the template ssRNA. We hypothesized that this could occur as a result of pausing by EV-A71 RdRp followed by backtracking, which produces a single-stranded 3'-end that can be used by EV-A71 RdRp as a primer for copy-back RNA

synthesis (Figure 6.1G). This hypothesis was tested in the following experiments. That a single polymerase could carry out both the initial round of RNA synthesis and copy-back RNA synthesis is supported by the good agreement of the kinetic behavior of the polymerases during both processes (Figure S.6.1D).

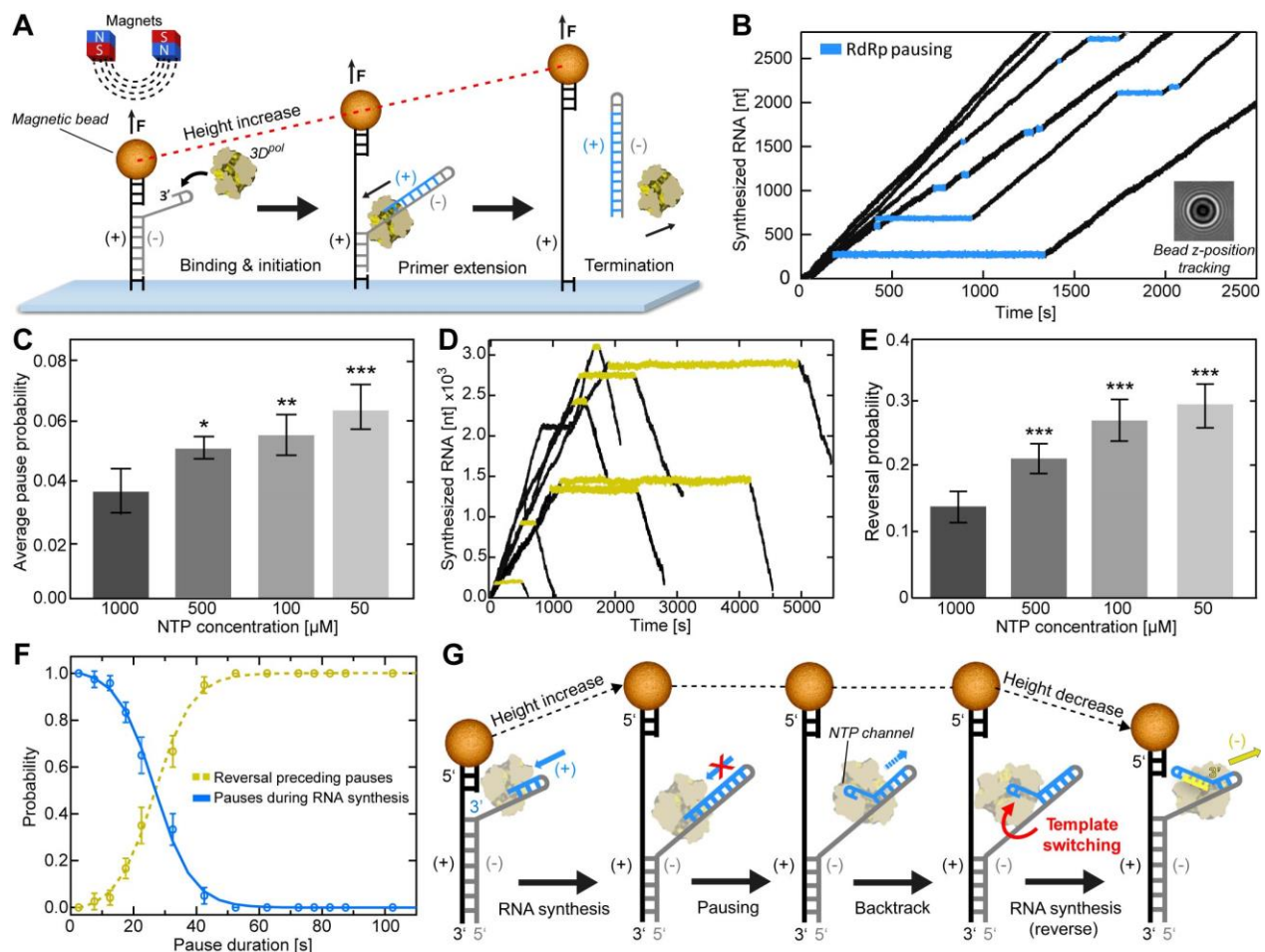


Figure 6.1. Magnetic tweezers assay of EV-A71 RdRp reveals pause-dependent copy-back RNA synthesis.

(A) Schematic of the single-molecule (+)-strand RNA synthesis assay, showing the binding of an RdRp to a hairpin at the 3'-end of the (-)-strand (grey) of the surface-attached RNA construct. A magnetic bead attached to the RNA construct is subject to a constant force of 25 pN during RNA synthesis (blue). (B) Sample EV-A71 RdRp trajectories showing stochastic pausing behavior over time, inferred via the change of the diffraction pattern of the attached magnetic bead (inset) at a rate of 50 Hz. Within individual trajectories, the data in blue highlight single pauses of different duration and template position during processive RNA synthesis. (C) Comparison of the average pause frequency (\pm SD) at different rNTP concentrations extracted from dwell-time distributions (Figure S.6.1A). Dataset statistics and experimental parameters for each condition are provided in Table S.6.1. (D) Sample individual RdRp elongation trajectories showing the occurrence of reversal events following extended pausing (yellow). (E) The average occurrence probability (\pm SD) of reversals per RdRp for all measured conditions. (F) The probability of observing pauses of specified pause durations during RNA synthesis (blue) co-plotted with the probability of reversals (yellow); the crossover point is found at \sim 26 s. (G) Proposed model underlying the reversal events, in which pause-induced elongation complex is followed by copy-back RNA synthesis of the newly synthesized (+)-strand RNA (blue). Synthesis of a new (-)-strand (yellow) results in reannealing of the original (+)-strand template (grey) to the complementary ssRNA tether (black), leading to an overall decrease in RNA tether extension. Statistical analyses were performed using ANOVA with comparative Tukey post-hoc test (significance levels p: *** = 0.001; ** = 0.01; * = 0.05). See also Figure S.6.1 and Figure S.6.2.

6.2.2 A recombination-deficient EV-A71 RdRp variant attenuates virus population

The availability of a recombination-defective EV-A71 RdRp derivative would prove very useful in making the strongest case for a relationship between the observation of backtracking or reversals and recombination. In PV RdRp, Y275H was identified as a substitution that impaired recombination substantially, although the molecular basis for the reduced recombination efficiency is yet not known^{25,26}. We engineered the orthologous Y276H substitution into RdRp-coding sequence of EV-A71. In the context of a subgenomic replicon, Y276H EV-A71 had no growth defect when compared to WT (**Figure 6.2A**), in agreement with previous observations²⁷. By plaque assay and RT-qPCR, Y276H and WT EV-A71 were indistinguishable (**Figure 6.2B,C**). To assess the recombination efficiency, we transfected the subgenomic replicon RNA described above (donor template) and an EV-A71 genomic RNA deleted for 3D^{pol}-coding sequence (acceptor template) into cells; recombination between these RNAs produced viable virus (**Figure 6.2D**). The yield of recombinant virus was reduced by nearly 100-fold (**Figure 6.2E**).

Previous studies have indicated that the ability of PV RdRp to catalyze recombination is required for PV to cause disease in a mouse model, even though growth of recombination-defective PV mutants in cell culture appears equivalent to or better than WT. We evaluated the virulence of Y276H EV-A71 in a mouse model that supports infection by oral inoculation. These mice express human SCARB2 protein, which is a receptor for EV-A71²⁸. The population of viruses carrying the Y276H EV-A71 was highly attenuated in this model relative to WT (**Figure 6.2F**), in agreement with a recently published study²⁷.

6.2.3 Recombination deficiency of Y275(6)H RdRps originates from enhanced binding to nascent RNA and diminished backtracking

Based on the data gathered in the past for PV RdRp and those described above for EV-A71 RdRp, our mechanism for template switching begins with RdRp pausing, followed by backtracking, and ending with either resolution of the backtrack (PV) or reversals (EV-A71). The availability of a recombination-defective EV-A71 RdRp, Y276H RdRp, should facilitate establishment of a correlation between reversal events observed using the magnetic tweezers and the requirements of the template-switching process.

The kinetics of correct nucleotide addition were unchanged for Y276H RdRp relative to WT (note the overlap of probability density in the dwell-time distributions up to 3 s in **Figure 6.3A**). In contrast, the rate of processive nucleotide addition for the recombination-defective derivative appeared compromised by a 2-fold increase in pausing frequency (**Figure 6.3B**) and a 4-fold increase in the duration of the pause (**Figure 6.3C**). The overall processivity of this derivative was also reduced by 4-fold (**Figure 6.3D**). The reversals observed with Y276H RdRp derived from a pause-dependent mechanism as observed for WT (**Figure 6.3E**). Interestingly, because the

typical duration of pauses beyond which reversals were observed increased by five-fold (~ 123 s vs. ~ 26 s, compare [Figure 6.1F](#), [Figure 6.3E](#)), more than the typical duration of pauses themselves, we predicted that the incidence of reversals would decrease for Y276H RdRp relative to WT. Such a decreased occurrence of reversals (by 4-fold, [Figure 6.3F](#)) was indeed observed experimentally. With pausing elevated and reversals diminished, the backtrack intermediate should accumulate. This was not observed, suggesting that an inability to backtrack is the functional defect associated with the Y276H RdRp derivative that interferes with recombination.

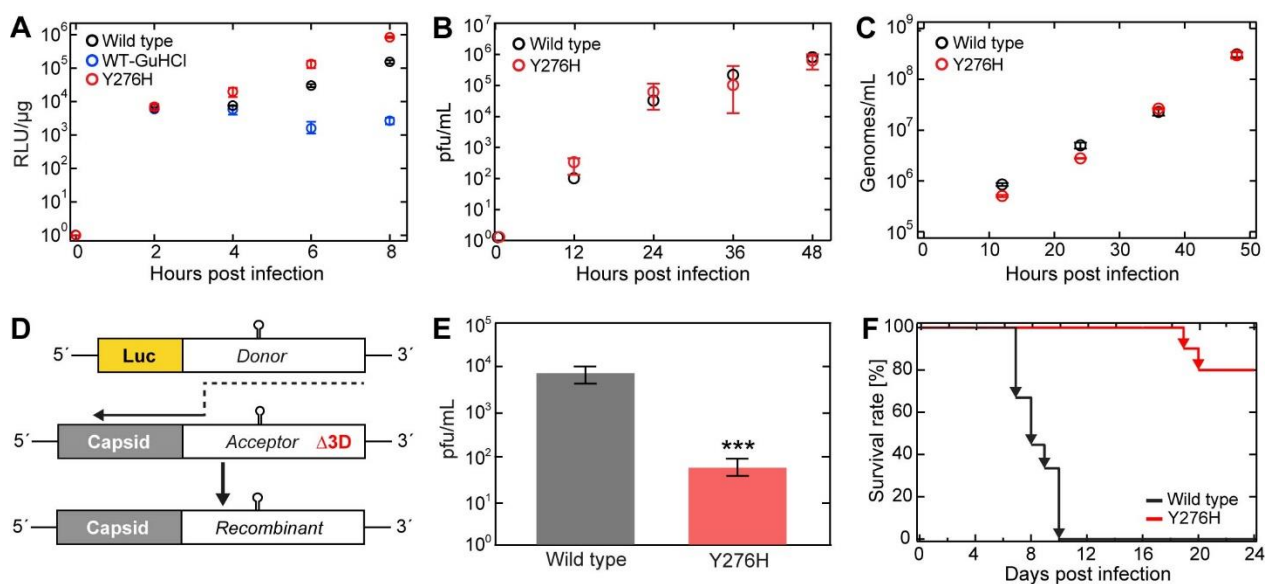


Figure 6.2. EV-A71 Y276H RdRp variant exhibits significance decrease in recombination efficiency and virulence.

(A) Replication efficiency of the EV-A71 wild type (WT) and Y276H variant subgenomic replicons in RD cells as a function of time post transfection. GuHCl refers to the presence of guanidine hydrochloride, a potent inhibitor of replication. Luciferase activity is reported in relative light units (RLU; $\text{AVG} \pm \text{SD}$) per microgram of total protein ($n = 3$ replicates per time point). (B) EV-A71 WT (black) and Y276H variant (red) single-step growth curves ($\pm \text{SD}$; $n = 3$) confirm similar plaque formation. (C) EV-A71 WT (black) and Y276H variant (red) single-step growth curves ($\text{AVG} \pm \text{SD}$; $n = 3$ for each time point). RD cells were infected with virus equivalent to 200 genomes/cell. Samples were taken at the indicated times and the genome amount of virus titer was quantified via RT-qPCR. (D) Cell-based recombination assay. EV-A71 C2-strain firefly luciferase-encoding sub-genomic replicon (donor) and full-length EV-A71 C2-MP4 strain genome (acceptor) carrying a lethal deletion of the $3D^{\text{pol}}$ region are co-transfected in RD cells. Only upon co-transfection can replication-competent virus be generated by RdRp-mediated template switch from donor to acceptor (indicated by dashed black arrow). (E) The Y276H mutation in the EV-A71 replicon inhibits recombinant yield. Resulting recombinant virus were quantified by pfu/ml ($\text{AVG} \pm \text{SD}$; $n = 3$). (F) EV-A71 C2-MP4 WT and Y276H virulence in hSCARB2 mice. 21-day old mice were orally inoculated with either WT or Y276H virus ($n = 10$ per virus) at a dose equivalent to 2×10^7 genomes and scored for survival post-infection. Effect of Y276H variant is severely attenuated relative to WT. Statistical analysis consisted of an unpaired, two-tailed t-test (significance level p : *** ≤ 0.001)

We next questioned the reason for the inability of Y276H RdRp to form a backtrack intermediate. For backtracking to occur, the paused polymerase needs to release the 3'-end from the active site. The stability of the RdRp at the 3'-end can be inferred from the steady-state rate constant for single-nucleotide incorporation²⁹. A reduction in the

value of this rate constant implies increased affinity for the terminus. Indeed, the Y276H RdRp elongation complex was 3-fold more stable than that formed by WT RdRp on the synthetic template developed to monitor elongation by enteroviral RdRps (**Figure 6.3G**)^{29,30}. It is therefore likely that the increase in pausing frequency and pause duration originate from the enhanced affinity of the Y276H RdRp for the 3'-end of nascent RNA, which ultimately leads to the observed inability of the Y276H RdRp to backtrack.

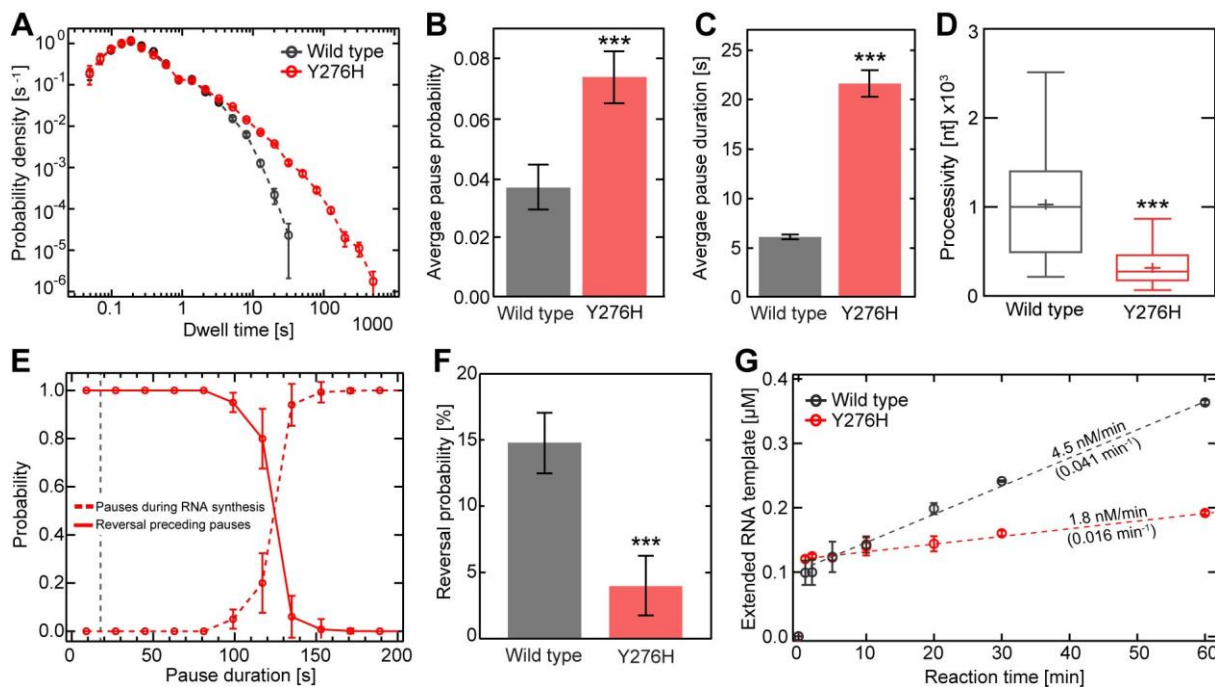


Figure 6.3. EV-A71 Y276H RdRp variant is impaired for copy-back RNA synthesis.

(A) Superimposed dwell-time distributions for EV-A71 Y276H RdRp (red) and WT (black) RdRp. The dwell times used for the construction of the distributions are the time needed for the RdRps to synthesize four consecutive nucleotides. The Y276H variant exhibits a broad increase in the probability and duration of long pauses compared to WT. The error bars (AVG±SD) result from bootstrapping with 1,000 iterations. (B-D) Quantification of the data in panel (A). In comparison to WT RdRp, the Y276H variant shows a significant increase in (B) average pausing probability (±SD) and (C) average apparent pause duration (±SEM). The processivity (D) is significantly decreased for the Y276H RdRp variant compared to WT. (E) The probability of observing pauses of specified durations during RNA synthesis (red line) co-plotted with the probability of observing reversals (red dashed line); the crossover point amounts to ~123 s. (F) The Y276H RdRp (red) variant causes significantly fewer reversal events (AVG±SD) than WT RdRp (grey). (G) In vitro bulk RNA synthesis assay results (AVG±SD; n = 3 repetitions) showing the amount of extended Sym/SubU template for EV-A71 WT and Y276H RdRp over time. Dashed lines represent linear regressions fitted to the data, revealing significantly lower approximated rates of RNA extension (values above the dashed lines) and turnover (values below the dashed lines; unit: RNA min⁻¹ RdRp⁻¹) for the Y276H RdRp variant compared to WT. Statistical analyses were performed using unpaired, two-tailed t-tests (significance level p: *** ≤ 0.001).

The availability of the orthologous derivative in PV, Y275H RdRp, provided the opportunity to determine if the mechanism causing the recombination defect is conserved for both viral polymerases. As shown in **Figure 6.4A-D**, Y275H RdRp and Y276H RdRp behaved similarly relative to their respective WT RdRp (based on features of the dwell-time distribution, including pause probability and average pause duration, as well as processivity). In contrast to EV-A71 RdRp, backtracking of PV

RdRp is readily detectable (Figure 6.4F, inset) due to the fact that the backtracked intermediate is its end point and not followed by a reversal. Similar to the trigger of reversals in EV-A71 RdRp (Figure 6.4F), backtracking of PV RdRp derived from a pause-dependent mechanism (Figure 6.4E). Therefore, for Y275H RdRp, a decrease in the incidence of backtracking should be discernible, providing empirical validation of our hypothesis that recombination defects in both polymerases may originate from a conserved backtracked intermediate. Indeed, the probability of backtracking was reduced for Y275H RdRp relative to WT RdRp (Figure 6.4F). The significant reduction in backtracking probability for Y275H RdRp may reduce the incidence of template-switching-proficient backtracks. Similar to the recombination-defective EV-A71 polymerase, Y275H RdRp exhibits a substantially more stable elongation complex than WT (Figure 6.4G).

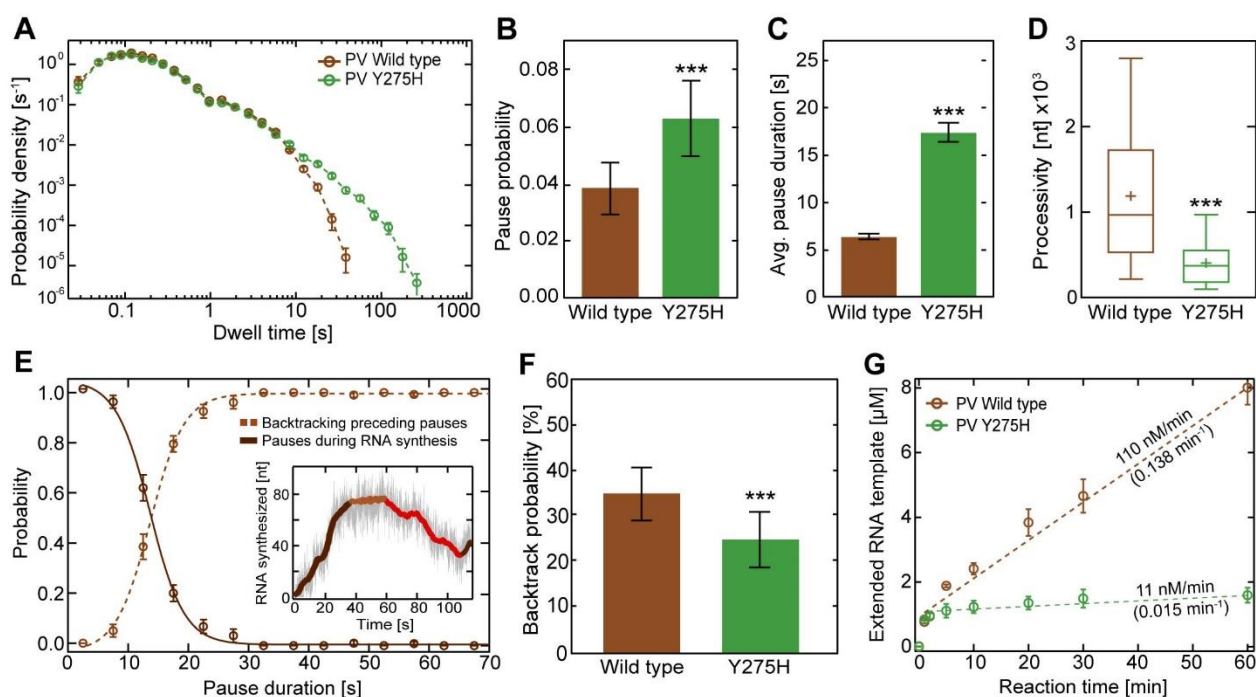


Figure 6.4. PV Y275H RdRp is impaired for backtracking.

(A) Superimposed dwell-time distributions of poliovirus Y275H RdRp variant (green) and WT (brown) RdRp. The 275H variant exhibits a broad increase in the probability and duration of long pauses compared to WT. The dwell-time window was set to 4 nt, and the error bars (AVG \pm SD) result from bootstrapping with 1,000 iterations. (B-D) Quantification of the data in panel (A). In comparison to WT RdRp, the Y275H variant shows a significant increase in (B) average pausing probability (\pm SD) and (C) average apparent pause duration (\pm SEM) during RNA synthesis. The processivity (D) is significantly decreased for the Y275H RdRp variant compared to WT. (E) The probability of observing pauses of specified durations during PV WT RNA synthesis (dark brown) co-plotted with the probability of observing backtracking (light brown dashed line); the crossover point is found at \sim 14 s. (F) The Y275H variant (green) shows a significantly decreased backtracking probability (AVG \pm SD) than WT RdRp (brown). (G) In vitro bulk RNA synthesis assay results (AVG \pm SD; $n = 3$ repetitions) showing the amount of extended Sym/SubU template for PV WT and Y275H RdRp over time. Dashed lines represent linear regressions fitted to the data, revealing significantly lower approximated rates of RNA extension (values above the dashed lines) and turnover (values below the dashed lines; unit: RNA min^{-1} RdRp $^{-1}$) for the Y275H RdRp variant compared to WT. Statistical analyses were performed using unpaired, two-tailed t-tests (significance level p : *** ≤ 0.001).

6.2.4 Conformational dynamics of the RNA-binding channel as a determinant of the type and efficiency of RdRp-catalyzed template switching

It has become increasingly clear that the biochemical properties of enzymes are governed as much by their conformational dynamics as by their three-dimensional structure^{19,31,32}. The conformational dynamics of PV RdRp is an important contributor to the specificity and efficiency of its polymerase function³³. The availability of structures of the RdRp from PV and EV-A71^{34,35}, and models of the PV Y275H and EV-A71 Y276H RdRps produced for this study, permitted us to determine whether structure and/or dynamics explain the differences observed in the propensity for a RdRp to catalyze copy-back RNA synthesis or the impact of the Y275(6)H substitution on backtracking or intramolecular template switching. Structural differences provided little, if any, insight (**Figure 6.5A-C**); therefore, we turned to dynamics.

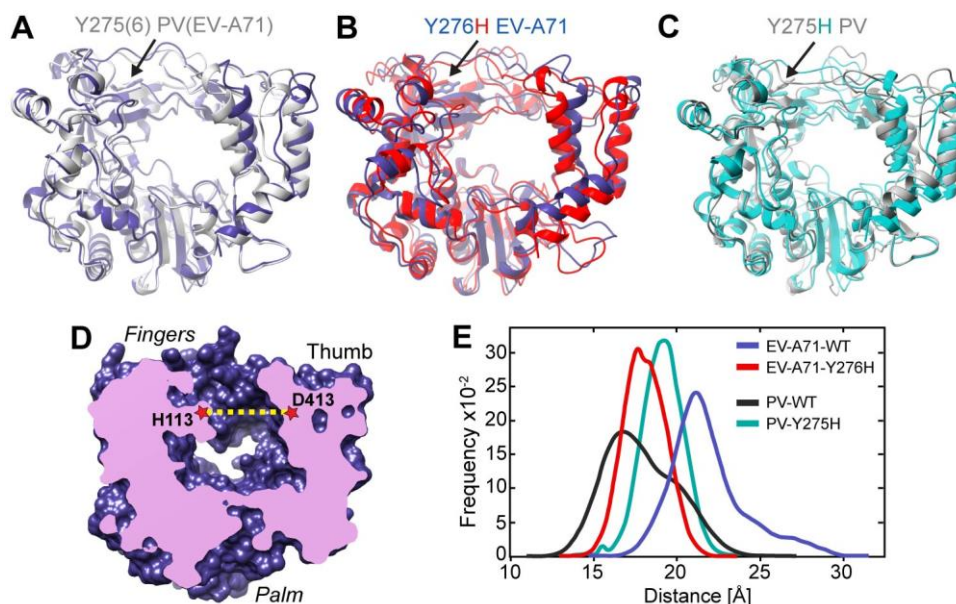


Figure 6.5. RNA-duplex channel dimensions and conformational dynamics of EV-A71 and PV RdRps.

(A) Superimposed crystal structures of EV-A71 WT (blue) and PV WT (grey) shown as cartoons. (B) Superimposed crystal structures of EV-A71 WT (blue) and major conformation of its Y276H mutant (red). (C) Superimposed crystal structures of PV WT (grey) and major conformation of its Y275H mutant (cyan). The major conformation of the Y275(6)H mutants resulted from MD simulations. (D) Cut-through volume rendering of EV-A71 WT crystal structure (PDB 3N6L), where the RNA duplex channel can be observed in the center of the structure. The channel width was assessed by measuring the distance between His-113 at the fingers and Asp-413 at the thumb domains in EV-A71, or their equivalent residues Ser-112 and Asp-412 in the PV WT crystal structure (PDB 1RA6). (E) RNA duplex channel widths measured for EV-A71 WT (blue) and PV WT (black) from their crystal structures, and from MD simulations for the EV-A71 Y276H variant (red).

We have previously established a pipeline for evaluating the conformational dynamics of picornaviral polymerases by using molecular dynamics simulations (MD)^{32,36}. This pipeline evaluates correlated motions of the conserved structural motifs and in reports on the dynamics of the open and occluded states of the catalytic site that drive specificity of nucleotide selection³⁶. The pipeline also evaluates dynamics of the RNA-

binding channel. Here, we have monitored the time-dependent changes in the distance of two residues lining opposite sides of the RNA-binding channel: H113 and D413 in case of EV-A71 (**Figure 6.5D**), and S112 and D412 in case of PV. The average size of the RNA-binding channel of PV WT RdRp was smaller (by ~ 4 Å) than that of EV-A71 WT RdRp (**Figure 6.5E**).

Interestingly, introduction of the EV-A71 Y7276H substitution decreased the average size of the RNA-binding channel by ~ 3 Å over the duration of time sampled (**Figure 6.5E**) to a similar size observed for PV WT RdRp. In contrast, PV Y275H exhibited a ~ 2 Å increase, rendering the channel size similar for both Y275(6)H RdRp variants.

The observed differences in the conformational dynamics of the RNA duplex channel strongly suggest that this parameter could influence the ability and degree of copy-back RNA synthesis. In particular, copy-back RNA synthesis of the nascent RNA strand by EV-A71 WT RdRp may be facilitated by increased spatial dynamics in the active center that allow the newly synthesized RNA strand to form a new primer by “snap-back” priming after backtracking.

6.2.5 RdRp backtracking in response to incorporation of the pyrazine carboxamide, T-1106, promotes intra- and intermolecular template switching *in vitro* and in cells.

Our study thus far makes a very compelling case for the ssRNA 3'-end produced by RdRp backtracking serving as an intermediate for both intra- and intermolecular template switching. Our interest in backtracking, however, was motivated by our previous observation that incorporation of T-1106 ribonucleoside triphosphate (T-1106-TP) into nascent RNA induced backtracking in PV¹⁸. In the context of our current findings, we would expect T-1106 ribonucleotide to promote copy-back RNA synthesis and/or homologous recombination in EV-A71. If this is the case, then T-1106 may actually represent an antiviral ribonucleoside whose antiviral activity could be attributed to a post-incorporation event unrelated to termination or mispairing, in this case template switching.

We compared EV-A71 RdRp elongation dynamics in the magnetic tweezers in the absence and presence of T-1106-TP. Incorporation of T-1106 ribonucleotide induced elevated levels of pausing (**Figure 6.6A-C**), diminished processivity (**Figure 6.6D**), and led to an increased incidence of reversals (**Figure 6.6E**) whose dynamics (**Figure 6.6A**) were, as in the absence of drug, comparable to those of forward translocation. Together, these behaviors reflect increased intramolecular template switching (copy-back RNA synthesis) in the presence of T-1106-TP. We also verified that the outcome of T-1106-TP utilization by PV RdRp was as expected based on our previous study (**Figure S.6.3**)¹⁸. Indeed, T-1106-TP induced detectable backtracking by PV RdRp (**Figure S.6.3D**), consistent with a greater likelihood for intermolecular template switching (homologous RNA recombination).

T-1106 inhibits EV-A71 multiplication in cells (**Figure S.6.4A**). However, in the presence of T-1106 concentrations between 200 μ M and 600 μ M, a clear increase in recombination was observed (**Figure 6.6F**). Notably, the resulting IC₅₀ value of 340 \pm 140 μ M for EV-A71 is comparable with those previously found (T-1106: 510 \pm 30 μ M; clinically used ribavirin: 550 \pm 30 μ M) for PV RdRp¹⁸. Using a subgenomic replicon expressing luciferase (**Figure 6.6G**), we showed that T-1106 did not affect reporter expression in the presence of the replication inhibitor guanidine hydrochloride (GuHCl), consistent with the drug having no effect on translation of the viral polyprotein. Replication-dependent, reporter expression was inhibited (**Figure 6.6H**). Antiviral ribonucleosides that function by lethal mutagenesis do not significantly reduce replication-dependent, reporter expression³⁷. It is therefore possible that the observed inhibition reflects a reduction in the amount of replication-competent replicon RNA resulting from enhanced copy-back RNA synthesis in the presence of T-1106-TP, and concomitant production of truncated (defective) replicons.

Our results are so far consistent with the idea of ribonucleotide analogs promoting copy-back RNA synthesis and homologous RNA recombination. We performed the same experiments with the recombination-defective variant, Y276H EV-A71. With this variant, T-1106 failed to increase recombination (**Figure S.6.4C**), consistent with the RdRp serving as the mediator of the effect of T-1106. Using the Y276H-encoding subgenomic replicon, we showed that translation was not impacted by the presence of T-1106, as observed for WT EV-A71 (**Figure S.6.4D**). Replication-dependent reporter expression was not impaired by the presence of T-1106 as observed for WT EV-A71 (**Figure S.6.4E**). This observation confirms that the reduction in replication-dependent reporter expression for WT EV-A71 (**Figure 6.6H**) was indeed caused by a backtracking-induced phenomenon like the production of defective viral genomes²¹.

Given that the impact of the drug on template switching-dependent mechanisms underlying copy-back and homologous recombination is alleviated for the recombination-defective variant Y276H, does this mean that a facile route to the development of resistance to this mechanistic class of antiviral ribonucleotides exists? To address this possibility, we evaluated the sensitivity of Y276H EV-A71 to T-1106. There was no more than a 2-fold change in the observed sensitivity of this derivative to T-1106 relative to WT (compare panels A, B in **Figure S.6.4**). Therefore, elimination of the template-switching dependent activity is insufficient for resistance to T-1106 and perhaps all members of the pyrazine-carboxamide class of antiviral ribonucleosides.

To directly assess the impact of T-1106 on the sequence of the viral genomes produced by WT EV-A71, we performed next-generation RNA sequencing on RD cells infected with EV-A71 WT in the absence and presence of T-1106. RNA sequencing revealed that T-1106 drug dosages between 400-600 μ M increased the frequency of genomes with sequences consistent with copy-back RNA synthesis (**Figure 6.6I**) and homologous recombination (**Figure 6.6J**). We did not observe any evidence for triggers

of template switching being related to sequence motifs in the absence or presence of T-1106 (**Figure S.6.5**), in agreement with our magnetic tweezers results and our previous observations made in EV-A71 cell-based assays²⁰. Interestingly, copy-back RNA synthesis occurred with higher probability in guanine- and cytosine-rich regions of the genome (**Figure S.6.5D**), consistent with our *in vitro* single-molecule observations (**Figure S.6.2**).

Collectively, these studies make an unambiguous mechanistic link between intra- and intermolecular template-switching processes by showing that they share the same backtracked intermediate produced by the same triggers. Notably, with respect to the potential mechanism of action of pyrazine carboxamide ribonucleoside analogs, the RNA sequencing results did not exhibit any change in the mutational load (**Figure 6.6K**) or termination of RNA synthesis. Instead, the mechanism of action of this class of antiviral ribonucleotides appears attributable to the induction of intra- and intermolecular template-switching leading to production of defective viral genomes.

6.3 Discussion

Among the last frontiers in RdRp enzymology is a mechanistic description of RNA recombination. In most RNA viruses, recombination is primarily an RdRp-mediated process. In PV, which is one of the best studied RNA virus models, it has been shown that recombination involves an RdRp-mediated template-switching mechanism in cells³⁸ and that RdRp is sufficient to catalyze the template-switching reaction *in vitro*³⁹. Recently, a renaissance in the study of RNA recombination has begun, as evidenced by the development of cell-based assays to probe the incidence of recombination^{20,40–42}.

In our earlier work that monitored PV RdRp elongation dynamics at the single-molecule level *in vitro*, we observed extensive RdRp pausing followed by backtracking in response to incorporation of diverse ribonucleotide analogs. This phenomenon was especially pronounced in the presence of the pyrazine carboxamide, T-1106¹⁸, which is known now to also induce pauses and backtracking in SARS CoV-2 RdRp²³. In a typical single-molecule experiment, we observed the extrusion of tens of nucleotides of ssRNA by PV RdRp in response to backtracking, the probability of which increased in response to T-1106-TP utilization¹⁸ (**Figure S.6.5E**). Given sufficient time, the drug-induced ssRNA reannealed, the RdRp rebound to the primer-template junction, and elongation resumed.

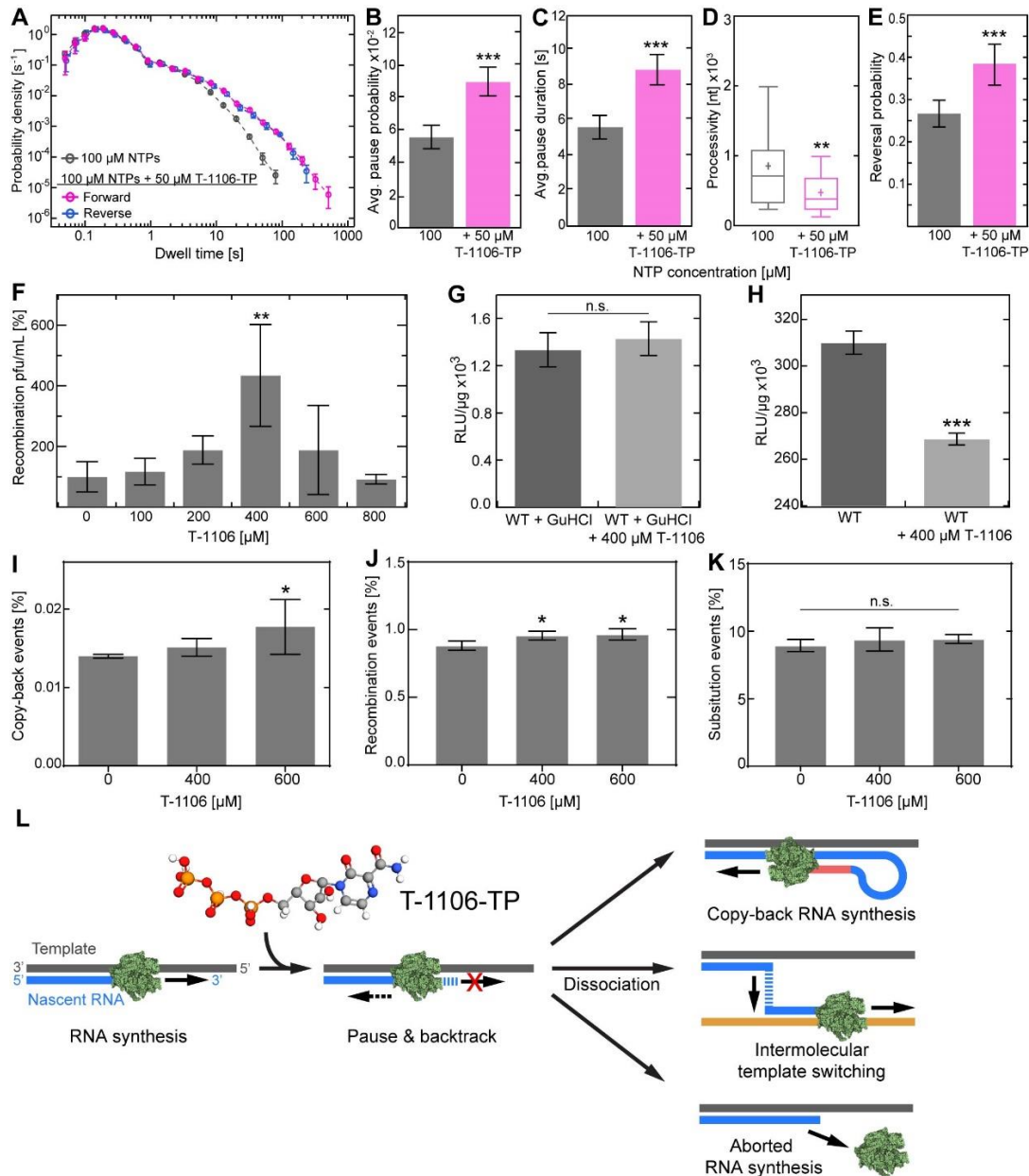


Figure 6.6. Pyrazine carboxamide T-1106 induces an increase in intra- and intermolecular template switching in vitro and in cell.

(A) Superimposed dwell-time distributions of EV-A71 RdRp forward RNA synthesis activity in the presence (magenta) or absence (grey) of the nucleotide analogue T-1106-TP. The reverse RNA synthesis dwell-time distribution in absence of T-1106-TP (blue) is superimposed. The dwell-time window was set to 4 nt, and the error bars (\pm SD) result from bootstrapping with 1,000 iterations. (B-E) The addition of T-1106-TP changed significantly the pausing behavior of WT RdRp, exhibiting significantly increased (B) pausing probability (\pm SD) and (C) average pause duration (\pm SEM), which led to a (D) significantly decreased in RNA synthesis processivity, and (E) vastly increased copy-back RNA synthesis probability. (F) Cell-based recombination assays conducted in presence of different concentrations of T-1106. Relative viable WT recombinant yield, normalized as a percentage of a carrier (DMSO) treated control (AVG \pm SD; N = 3 replicates for each condition). Calculated IC₅₀ amounts to 340 \pm 140 μ M T-1106; the HeLa cell toxicity (CC₅₀) of T-1106 was found to be >2 mM¹⁸. (G, H) EV-A71 donor translation (G) and replication (H) efficiency (AVG \pm SD) for WT RdRp. (I-K) The frequency of identified (I) copy-back RNA synthesis and (J) homologous recombination events, extracted from RNAseq, were significantly increased upon T-1106 addition, while (K) no change in mutation occurrence within the EV-A71 genome was observed. (L) Model mechanism of pyrazine carboxamide nucleotide analogue causing stall in RNA synthesis leading to copy-back RNA synthesis, intermolecular template switching, or abortive genome synthesis by RdRp dissociation. Statistical

analyses were performed using ANOVA with comparative Tukey post-hoc test (significance levels α : *** = 0.001; ** = 0.01; * = 0.05; n.s. = non-significant), and unpaired, two-tailed t-tests (significance level p : *** \leq 0.001). See also [Figure S.6.3](#) and [Figure S.6.4](#).

Observation of such spatiotemporal dynamics of the nascent RNA-template-RdRp complex was unprecedented and motivated further study. Intriguingly, cell-based recombination studies in PV and other RNA viruses have shown that favipiravir and its derivate T-1106 increase recombination frequency ([Figure 6.6E](#))^{43–47}. Since PV RdRp backtracking propensity represented the sole change in RNA synthesis dynamics in response to T-1106 treatment, it could represent a recombination intermediate. With that possibility in mind, this study added the EV-A71 RdRp, because EV-A71 has been suggested to undergo high rates of recombination in nature²⁰. EV-A71 recombination is a major cause of the recurring outbreaks in Asia^{5,48}.

The first major conclusion of this study is that the viral RdRp has evolved to sense and to respond to incorporation of an incorrect nucleotide or nucleotide analogue by pausing and backtracking, thereby producing a recombinogenic 3'-end. Nucleotide misincorporation will be increased at lower nucleotide concentrations and in the presence of skewed nucleotide pools¹⁸. Under these conditions, both EV-A71 and PV RdRps exhibit an increase in the probability and duration of pausing ([Figure 6.1C](#), [Figure S.6.1B](#), respectively)¹⁸. Similarly, utilization of T-1106-TP increases the pause probability and duration for both polymerases (EV-A71: [Figure 6.6B,C](#); PV: [Figure S.6.3B,C](#)). The average pause duration is measured in the tens of seconds for both enzymes (EV-A71: [Figure S.6.2B](#); PV: [Figure S.6.3C](#)), not milliseconds as typically observed for nucleotide addition⁴⁹. We suggest that the consequence of a misincorporation- or ribonucleotide analogue-induced pause is backtracking in both systems. In the case of PV RdRp, there is no debate because the backtracked state was observed to accumulate during the course of an experiment ([Figure 6.4F](#)) and does so more frequently upon utilization of T-1106 triphosphate ([Figure S.6.5E](#))¹⁸. In contrast, several known chain terminators did not induce backtracking of PV RdRp¹⁸. With EV-A71 RdRp, the backtracked state does not accumulate. Instead, the probability of reversals increases ([Figure 6.1](#), [Figure 6.6D](#)), which reflects the use of the 3'-end of nascent RNA as a new primer for copy-back RNA synthesis ([Figure 6.1G](#)). Backtracking would thus be the simplest mechanism for liberating the 3'-end for use as a primer.

While it has been speculated that RNA recombination and copy-back RNA synthesis are mechanistically related based on observations that circumstances which elevate RNA recombination also elevate copy-back RNA synthesis²¹, how these processes were connected was unknown. Our study is consistent with two fates for the ssRNA produced by backtracking. The first is intermolecular template switching, which is homologous RNA recombination. The second is intramolecular template switching, which is copy-back RNA synthesis. This conclusion is supported by RNAseq analysis of EV-A71 genomes produced during replication in cells in the absence or presence of

T-1106 (**Figure 6.6I,J**). Therefore, this study makes an unequivocal mechanistic link between these two template-switching processes by demonstrating that they share the same backtracked intermediate and triggers.

Why are there two different outcomes for the backtracked state? This state accumulates with the PV RdRp, but does not accumulate with the EV-A71 RdRp. For copy-back RNA synthesis to occur, the nucleic-acid-binding site needs to be sufficiently large to accommodate a three-stranded intermediate at the time of initiation (**Figure 6.1G**). Analysis of the dynamics of the nucleic-acid-binding site of EV-A71 RdRp demonstrated a clear ability of this enzyme to accommodate such an intermediate with an approximate diameter of $\sim 24\text{\AA}$. (**Figure 6.5D**). The corresponding site in PV RdRp is on average 4\AA smaller (**Figure 6.5D**). Presumably, the dimensions of PV RdRp are too small to accommodate such an intermediate. If so, then the dimensions of the RNA-binding site sampled by an RdRp may predict the capacity of a virus polymerase to catalyze copy-back RNA synthesis.

The product of copy-back RNA synthesis will lead to a truncated dsRNA that is defective in its coding capacity and/or a potent activator of innate immune responses²¹. Whether or not production of copy-back RNA is deliberate is unclear but may be for some viruses because the copy-back RNA can dampen the intensity of the infection²¹. During replication in the cell when the backtracked state arises, templates complementary to the single-stranded 3'-end would be present. Under these conditions, perhaps intermolecular template switching would perhaps be favored for both enzymes.

Over the past few years, a connection has been made between RdRp fidelity and recombination^{20,40,48,50-52}. With more incorporation errors and/or consumption of nucleotide analogs by the RdRp comes an increase in the frequency of recombination both in cells and in test tubes⁴⁸. The reason for this has not been clear. Our studies provide a mechanism. Recombination is thought to provide a means to suppress the impact of deleterious mutations^{42,49,53}. Our data would suggest that a balance between mutation and recombination must exist, because increasing the frequency of recombination exhibits antiviral activity in cells (**Figure 6.6F,I**, **Figure S.6.4C**) attributable to production of defective genomes (**Figure 6.6G**). Consistent with too much recombination being inhibitory to virus genome replication, not every event that could trigger recombination (**Figure 6.1C**, **Figure 6.6B**, and **Figure S.6.3B**) actually does so; only a fraction of paused polymerases actually undergo copy-back synthesis (**Figure 6.1E**, **Figure 6.6D**) or accumulate in the backtracked state (**Figure S.6.3E**). Our previous study of PV RdRp suggested that only a subset of elongation complexes were competent for misincorporation or incorporation of certain nucleotide analogs¹⁸. If this is the case, then these misincorporation-competent elongation complexes may be the only complexes competent for backtracking and template switching.

For an event to trigger template switching, that event must first trigger backtracking. Our studies have focused on the perception of nucleotide addition as correct or incorrect as a mechanism to induce backtracking and consequentially template switching. However, other mechanisms to induce backtracking may exist. One intriguing possibility is that certain template sequences may direct the RdRp to pause and/or backtrack. Sequence- and factor-dependent pausing is well represented in the DNA-dependent RNA polymerase literature⁵⁴. In the case of the respiratory syncytial virus (RSV), it is known that guanine- and cytosine-rich regions promote copy-back RNA synthesis⁵⁵. In this system, these sequences alter polymerase elongation capacity. It is intriguing to speculate that these sequences promote backtracking. While our single-molecule and RNAseq experiments did not correlate backtracking to specific sequences, the incidence of copy-back RNA synthesis increased in guanine- and cytosine-rich regions of template (**Figure S.6.3**, **Figure S.6.5**).

Our interpretation that the backtracked state and copy-back synthesis contributing to recombination are of biological relevance is supported by mechanistic evaluation of RdRp derivatives known to be defective for recombination in cells (**Figure 6.2**)²⁵. PV Y275H RdRp exhibits one of the strongest recombination-defective phenotypes described²⁵, but the molecular basis for the defect is not known for this mutant or the others reported in the PV system or other viral systems^{26,42,53}. Here, we show that EV-A71 Y276H RdRp exhibits an equally strong recombination defect in cells (**Figure 6.2**). Both the PV and EV-A71 recombination-defective derivatives retain the ability to sense and respond to errors based on their ability to pause even more frequently (and with longer duration) than WT (**Figure 6.3B,C**, **Figure 6.4B,C**). The increased pausing did not translate to an equal increase in backtracks or copy-back synthesis (**Figure 6.3F**, **Figure 6.4F**). The inability to produce the 3' ssRNA intermediate following backtracking appeared to be caused by an increase in the stability of these enzymes with the 3'-end of nascent RNA-template duplex (**Figure 6.3G**, **Figure 6.4G**). We conclude that release of the nascent RNA-template duplex by the RdRp is an obligatory step in converting the paused RdRp elongation complex into a backtracked state with a recombinogenic, single-stranded 3'-end. This level of detail for the mechanism of RdRp-mediated RNA recombination is unprecedented. Several recombination-defective/impaired RdRp variants are known^{42,53,56}, and it is possible that the mechanistic basis for the defects will be different²⁶. Therefore, evaluation of these derivatives may enable a genetic dissection of the mechanism of template switching and illumination of steps and/or intermediates masked by analyzing WT RdRp.

Given the details on the mechanism of template switching elucidated by this study, it is now clear that the conformational dynamics of the RdRp required to support template switching are substantial. For intramolecular template switching (copy-back synthesis) to occur, the enzyme has to flip to move in the opposite direction and expand the RNA-binding channel to accommodate an additional strand of RNA. For

intermolecular template switching (homologous recombination) to occur, the enzyme would have to relocate from the site of backtracking to the new primed-template junction without dissociating into solution. Such polymerase acrobatics are well documented for HIV RT⁵⁷⁻⁵⁹. Interestingly, nucleotide analogs also promote substantial changes in the conformational dynamics of HIV RT, as observed here for the EV-A71 RdRp⁵⁸.

The pyrazine carboxamide ribonucleoside analog T-1106 does not appear to induce chain termination (**Figure 6.6E**, **Figure S.6.3D**) or lethal mutagenesis (**Figure 6.6K**), in contrast to previous accounts^{16,17,60}. For structurally similar analogs like ribavirin, which contains a triazole carboxamide pseudo base, lethal mutagenesis represents the main underlying mechanism of action^{18,61}. While both analogs induce backtracking intermediates (EV-A71: **Figure 6.6D**; PV: **Figure S.6.3E**), the antiviral mechanism of action of T-1106 appears to be limited to induced template-switching¹⁸. Perhaps the ability of the T-1106 pseudo base to form a transient basepair within nascent RNA enables priming of copy-back synthesis, a point to further examine in future studies.

Both past observations and recent investigations suggest that the identified recombination mechanism and its susceptibility to drugs may be conserved across RNA viruses. Historical findings described defective virus genomes (DVG) that likely originated from copy-back RNA synthesis for vesicular stomatitis virus⁶², Sendai virus⁶³, measles, and parainfluenza⁶⁴⁻⁶⁶. Recent findings have confirmed this hypothesis for several viruses²¹, and searched for underlying mechanism and trigger(s): in RSV, G:C-rich genome regions (rather than genome motifs) were found to promote copy-back RNA synthesis⁵⁵, a similar trigger to the one we identify here for EV-A71, and in SARS CoV-2 a sequence motif-independent RdRp pause/backtracking intermediate susceptible to T-1106 was identified^{19,23}.

In conclusion, our studies reveal the power of magnetic tweezers for the mechanistic characterization of RdRp-catalyzed RNA recombination. The ability to detect an important recombinogenic intermediate and follow the fate of that intermediate provides the first direct mechanistic connection between RNA recombination and copy-back RNA synthesis. We have further elaborated the mechanism of action of the pyrazine carboxamide class of compounds and discovered that T-1106 functions by promoting formation of the recombinogenic intermediate. This leads us to suggest that this class of compounds may be particularly efficacious against those viruses either known to produce defective viral genomes by copy-back RNA synthesis or associated with high rates of recombination. An important aspect of this class of antiviral compounds is that the barrier to resistance for the virus may be insurmountable. Mutants that were resistant to T-1106-induced template switching remain highly sensitive to the drug, presumably due to an inability to combat the deleterious effects of accumulated mutations^{42,49,53}. Altogether, our results define inducible intra-and

intermolecular template switching (Figure 6.6K) as a tractable mechanistic target with broad-spectrum appeal.

6.4 Materials & methods

6.4.1 Key resources table

REAGENT or RESOURCE	SOURCE	IDENTIFIER
Antibodies		
Digoxigenin antibodies	Roche	RRID: AB_514496
Bacterial and virus strains		
SURE Competent Cells	Agilent technologies	Cat#200238
Chemicals, peptides, and recombinant proteins		
ApU dinucleotide	IBA Lifesciences GmbH	Cat#0-31004
Biotin-16-dUTP	Roche	Cat#11093711103
Digoxigenin-11-dUTP	Roche	Cat#11093681103
rNTPs	GE Healthcare	Cat#27-2025-01
Streptavidin-coated superparamagnetic beads	Thermo Fischer	Cat#65001
T-1106 triphosphate	Blake Petersen Lab	
Ribavirin triphosphate	Jena Bioscience	Cat#NU-1105L
Dulbecco's Modified Eagle's Medium	Thermo Fischer	Cat#31966021
Streptomycin	Thermo Fischer	Cat#15140122
Superase RNase inhibitor	ThermoFischer	Cat#AM2694
Critical commercial assays		
Ribomax large scale RNA production kit	Promega	Cat#P1300
T7 mMESSAGE mMACHINE kit	Thermo Fischer	Cat#AM1344
Qubit RNA Broad Range assay kit	Thermo Fischer	Cat#Q10211
TransIT-mRNA transfection kit	MirusBio	Cat#MIR2250
Direct-zol-96 RNA purification kit	Zymo Research	Cat#R2056
Quant-iT RNA assay kit	Thermo Fischer	Cat#Q33140
Next rRNA Depletion Kit	New England Biolabs	Cat#E6310L
NEBNext Ultra II RNA Library preparation kit	New England Biolabs	Cat#E7775
NextSeq500/550 Mid Output kit v2.5	Illumina	Cat#20024907
Mycoplasma Detection Kit	Lonza	Cat#LT07-318
RNeasy MinElute cleanup kit	Quiagen	Cat#74204
Deposited data		
Single-Molecule Magnetic Tweezers data	This study	DOI: 10.4121/c.5608934
Raw and processed RNAseq data	This study	NIH GEO: GSE183959
Experimental models: Cell lines		
RD cell line	ATCC	RRID: CVCL_1649
Experimental models: Organisms/strains		
Transgenic human hSCARB2-expressing mice	REF ⁶⁷	
Oligonucleotides		
5'-aacuguugguguacgcgaaagcgu	GE Healthcare Dharmacon	
5'-taatacgactcactataggatcgccaagattagcggatcctacctgac	Biolegio	AB-For

5'-ggttaacctcaacttcatttcc	Biolegio	AB-Rev
5'-cccctcgaggggaaaaaaaaaacggtatgacgctggaag	Biolegio	CD-For
5'-taatagactcactatagggcgactttcggatctccgacatgcgc	Biolegio	CD-Rev
5'-aagattagcggatcctactgac	Biolegio	Bio-For
5'-bio-taatagactcactataggaacggcttgatccactttacg	Biolegio	Bio-Rev
5'-agcgtaaaattcagttcttcgtggcg	Biolegio	Dig-For
5'-dig-aatacactcactatagggctaccggttaacctcaacttcatttcc	Biolegio	Dig-Rev
5'-tgccattcaggactgccgatgtcgggtcagccg	Biolegio	SP-For
5'-taatagactcactataggagcgcgcttccatgtcctggaacgct	Biolegio	SP-Rev
5'-acgttctcagtgccgactgtag	IDT	MP4-3156-Fwd
5'-ccttggaagagcttc	IDT	C2/4-5057-Rev
5'-gaagctctttccaagg	IDT	C2/4-5057-Fwd
5'-ctggtataacaaatttacc	IDT	C2/4-7384-Rev
5'-atcaatcacaccatcatgtgcatgcaataaaaacttattg	IDT	Y276H-Fwd
5'-caataagttttattgcatgacatgatgggtgtgattgat	IDT	Y276H-Rev
5'-acgtagcccagcgcgtggccg	IDT	Eag-I-Rev
5'-agcagtctgactagtaaagacc	IDT	SpeI-Fwd
5'-cggcagcccagaagaact	IDT	qPCR-Fwd
5'-gccaccctatcctcctgga	IDT	qPCR-Rev
5'-FAM-tcacatgaagttgtgtaaggatgcta-BHQ	Biosearch Technologies	qPCR-Probe
Recombinant DNA		
Plasmid pBB10	REF ⁶⁸	pBB10
pSumoEV-A71-3D	This study	
pSumoEV-A71-3D-Y276H	This study	
pSumoPV-3D	REF ²⁹	
pSumoPV-3D-Y275H	REF ²⁵	
pEV-A71-MP4	REF ⁶⁹	
pEV-A71-Y276H	This study	
pEV-A71-C2-replicon	REF ²⁰	
pEV-A71-MP4-Δ3D	REF ²⁰	
Software and algorithms		
MatLab R13	MathWorks Inc.	RRID: SCR_001622
Igor Pro 6.37	Wavemetrics	RRID: SCR_000325
LabView 2011	National Instruments	RRID: SCR_014325
ImageQuant	GE Healthcare Life Sciences	RRID: SCR_014246
ImageLab	BioRad	www.bio-rad.com/en-ch/product/image-lab-software
VODKA	REF ⁵⁵	
Bowtie2	REF ⁷⁰	RRID: SCR_016368
BBTools	Joint Genome Institute	RRID: SCR_016968
bcl2fastq v2.2	Illumina	RRID: SCR_015058

6.4.2 Human embryonic rhabdomyosarcoma cell culture

Human embryonic rhabdomyosarcoma RD cells (ATCC CAT#CCL-136, RRID: CVCL_1649) were grown in Dulbecco's Modified Eagle Medium (DMEM; ThermoFischer). Media was supplemented with 100 U/ml penicillin (ThermoFischer), 100 µg/ml streptomycin (ThermoFischer), and 10% Heat Inactivated (HI)-FBS (ThermoFischer). All cells were passaged in the presence of trypsin-EDTA. Cell were maintained at 37°C/5% CO₂. Prior to the experiments, RD cells were tested for mycoplasma using the MycoAlert Mycoplasma Detection Kit (Lonza) and were negative: B/A ratio < 1; no mycoplasma reads were detected.

6.4.3 Generation of transgenic human hSCARB2-expressing mice

Transgenic mice expressing hSCARB2 were generated as described previously⁶⁷, and kindly provided by Dr. Satoshi Koiki (Tokyo Metropolitan Institute of Medical Science, Japan). The mice were housed and fed at the National Laboratory Animal Center (NLAC), NARLabs, Taiwan. Experiments were carried out in accordance with the 'Guide for the care and use of laboratory animals', the recommendations of the Institute for Laboratory Animal Research and Association for Assessment and Accreditation of Laboratory Animal Care International standards. The animal experiment protocol was approved by the Institutional Animal Care and Use Committee in the Chang Gung University (CGU 106-117), Taiwan. The hSCARB2-expressing mice were housed at room temperature ranging between 20 and 23 °C with a relative humidity between 55 and 60%, and kept under a 12/12 h light/dark cycle. For the experiments, three-week-old female and male pathogen-free hSCARB2 mice were randomly distributed in the experimental groups of animals.

6.4.4 Plasmids

The mouse adapted EV-A71 C2-MP4 infectious clone was kindly provided by Dr. Jen-Reng Wang (Cheng Kung University, Taiwan) and modified by insertion of a ribozyme sequence between the T7 promoter and viral genome sequence in a pBR-derived plasmid^{68,71}. The EV-A71 C2 replicon was modified from a previously described EV-A71 C2-2231 replicon by addition of a T7-ribozyme and polyA sequence inserted at the 5' and 3' end of the replicon sequence in a pBR-derived plasmid⁷². The EV71Δ3D template was constructed from the full-length EV-A71 C2-MP4 infectious clone by removal ~800 nt between the blunt cutting restriction sites (*ScaI* and *NruI*) within the 3D^{pol} coding region. The Y276H mutant replicon and infectious clone were constructed by using site-directed mutagenesis. The sequences of the primers (Integrated DNA Technologies, Inc.; IDT) used for the plasmid construction are described in the [Key Resources Table](#).

6.4.5 Purification, 5'-³²P Labeling, and Annealing of sym/sub

RNA oligonucleotides were purified, labeled, and annealed as described previously³¹. Poliovirus RNA-dependent RNA polymerase (3D^{pol}): Assembly of stable,

elongation-competent complexes by using a symmetrical primer-template substrate (sym/sub).

6.4.6 Expression and purification of Enterovirus A-71 RdRp

Mutation of the Y276 codon was performed by standard PCR mutagenesis. Expression and purification of WT and mutant 3D^{pol} enzymes followed previous procedures with some minor modifications^{39,73,74}. 3D^{pol} is expressed as a fusion protein to SUMO and an N-terminal polyhistidine tag that increases protein production, eases purification and allows for production of 3D^{pol} with the naturally occurring Gly1^{73,74}.

Protein purification: buffer B (100 mM potassium phosphate, 500 mM NaCl, 5 mM imidazole, 5 mM β -mercaptoethanol, 60 μ M ZnCl₂, 20% w/v glycerol, pH 8.0) and buffer C (100 mM potassium phosphate, 500 mM NaCl, 60 μ M ZnCl₂, 5 mM β -mercaptoethanol, 20% w/v glycerol, pH 8.0) were prepared. Cell pellets were resuspended in 50 ml lysis buffer (50 ml buffer B, 1.4 μ g/ml pepstatin A, 1 μ g/ml leupeptin, 1 mM PMSF, 0.1% N-P40) and subjected to sonication. Cell lysates were centrifuged at 30,000 g and 4°C for 30 min. Supernatant was applied to Ni-NTA (Invitrogen) columns pre-equilibrated with buffer C1 (buffer C, 5 mM imidazole and 0.1% N-P40). The resin was washed with three bed volumes each of buffer C1 and buffer C2 (buffer C, 5 mM imidazole), and protein was eluted using high imidazole buffers C3 (buffer C, 50 mM imidazole) and C4 (buffer C, 500 mM imidazole). The polyhistidine tag and SUMO protein domain were cleaved from 3D^{pol} using the protease Ulp1. Protein solutions were dialyzed against 80 mM Tris-HCl, 500 mM NaCl, 20% w/v glycerol, 10 mM β -mercaptoethanol, 60 μ M ZnCl₂, pH 8.0 overnight (optimal buffer for protease cleavage), and then dialyzed against 100 mM potassium phosphate, 20% w/v glycerol, 10 mM β -mercaptoethanol, 60 μ M ZnCl₂, pH 8.0 for 2-3 h. A second Ni-NTA column was used to separate the purified 3D^{pol} from the cleaved polyhistidine tag/SUMO domain, using procedures identical to the first Ni-NTA column. For WT and Tyr276His 3D^{pol}, additional phosphocellulose and Q-sepharose columns were used to ensure protein solutions were free of trace contaminants of nuclease and phosphatase activities^{73,74}. Proteins were >95% homogeneous as estimated by coomassie-blue staining of SDS PAGE gels. Protein is stable at 4°C for 3-4 months under high salt conditions (80 mM Tris-HCl, 500 mM NaCl, 20% w/v glycerol, 10 mM β -mercaptoethanol, 60 μ M ZnCl₂, pH 8.0).

6.4.7 *In vitro* RNA synthesis, cell transfection, and recombinant virus quantification

The EV-A71 C2 replicon and C2- Δ IRES-replicon were linearized with *Sal*I. The EV-A71-MP4, EV71 Δ 3D cDNA were linearized with *Eag*I. All linearized cDNA was transcribed *in vitro* using T7 RNA Polymerase treated with 2U DNase Turbo (ThermoFisher) to remove residual DNA template. The RNA transcripts were purified using RNeasy Mini Kit (Qiagen) before spectrophotometric quantification. Purified RNA (amounts as specified elsewhere) in RNase-free H₂O were transfected into cell lines using TransMessenger (Qiagen). The mixture was incubated according to the

manufacturer's instructions and added to RD cell monolayers in 12-well tissue culture plates. Virus amount was quantified by plaque assay. Briefly, media supernatant and cells were harvested at time-points post transfection (specified in the main text), subjected to three freeze-thaw cycles and clarified. Supernatant was then used on fresh RD cells in 12-well plates, virus infection was allowed to continue for 30 min. Media was then removed, and cells were subjected to 2x PBS (pH 7.4) washes before a 1% (w/v) agarose-media overlay was added. Cells were incubated for 3-4 days and then fixed and stained with crystal violet for virus quantification.

6.4.8 Single-step growth curve for EV-A71 WT and Y276H full-length virus

RD cells in 12-well plates were infected by each virus at a MOI of 0.1 in triplicate in serum-free media. After 1 h, cells were extensively washed by PBS and refreshed in 10% serum-containing media. Virus was harvested at different time-points post infection and the virus yield was quantified by plaque assay.

6.4.9 Real time qPCR analysis

Viral RNA was isolated with QiaAmp viral RNA purification kit (Qiagen), as recommended by the manufacturer. The real time qPCR analysis was performed by the Genomics Core Facility of The Pennsylvania State University. DNase-treated RNA was reverse-transcribed using the High Capacity cDNA reverse transcription kit (Applied Biosystems) and the protocol provided with the kit. Quantification by real time qPCR was done by adding 10 or 20 ng of cDNA in a reaction with 2x TaqMan Universal PCR Master Mix (Applied Biosystems, Foster City CA) in a volume of 20 μ l, with primers 5'-CGGCAGCCCAGAAG AACT-3' (forward) and 5'-GCCACCCTATCTCCCTGGAT-3' (reverse) and probe 5'-[6-Fam]-TCACCATGAAG TTGTGTAAGGATGCTA-3' in a 7300 real time qPCR machine (Foster City). A standard curve was generated using *in vitro* transcribed RNA.

6.4.10 Luciferase assays

Supernatant was removed from transfected cell monolayers, and cells were briefly washed with PBS and lysed using 100 μ l 1x Glo Lysis Buffer (Promega®) per well in a 12-well plate. The oxidation reaction was catalyzed by the addition of 10 μ l cell lysate to 10 μ l room temperature *Bright-Glo* Luciferase Assay System (Promega®) substrate. Luciferase activity was measured using a luminometer with values normalized to protein content of the extract using a protocol as previously described⁷³.

6.4.11 Infection of transgenic human hSCARB2-expressing mice

For infection of mice expressing hSCARB2, 2×10^7 genome copies of WT and Y276H mutant EV-A71 C2-MP4 viruses were intragastrically inoculated into 21-day old mice using metallic gastric tubes. The inoculated mice were monitored daily for clinical disease symptoms, reflected by the disease scores defined as: 1. jerky movement; 2. paralysis of one hind leg; 3. paralysis of both hind legs; 4. death.

6.4.12 *In vitro* transcription of EV-A71 genomes for RNAseq

Mouse-adapted EV-A71 C2-MP4 cDNA was linearized with *EagI*. The linearized cDNA was *in vitro* transcribed using the T7 mMESSAGE mMACHINE kit (ThermoFisher) following manufacturer's instructions. Reactions were treated with TURBO DNase (2U/reaction) to remove the DNA template. The RNA transcript was purified using the RNeasy MinElute Cleanup Kit (Qiagen). Purified RNA was quantified *via* Qubit 4 fluorometer using the Qubit RNA Broad Range assay kit (ThermoFisher). The quality of the transcripts was confirmed by agarose gel electrophoresis.

6.4.13 Virus infection with EV-A71 and rescue

In vitro transcribed RNA was transfected into RD cells *via* TransIT-mRNA transfection kit (Mirus Bio) following the manufacturer's instructions. Briefly, RD cells were seeded in 6-well tissue culture plates at 8.0×10^5 cells/well (DMEM-GlutaMAX, 10% FBS, 1% P/S) and incubated overnight at 37°C/5% CO₂. The day of the transfection, media was replaced with 2% FBS-containing media and then the transfection mixture containing 2.5 µg of EV-A71 C2-MP4 RNA was added dropwise. 48 h post-transfection, at nearly full CPE, the cells were freeze-thawed three times and then spun at 20,000 g for 10 min at 4°C to remove cellular debris. Viral titers were determined by plaque assay. This viral supernatant (P₀) was passaged once to scale up and generate P₁ virus, which was used for the subsequent RNAseq experiments.

6.4.14 Drug treatment of EV-A71-infected RD cells

RD cells were seeded in a 96-well tissue culture plate at 3.0×10^4 cells/well and incubated overnight at 37°C/5% CO₂. Afterwards, cells were treated with T-1106 for 3 h before infection (doses are specified in [Figure 6.6K](#)). T-1106-treated cells were then infected at an MOI of 10 with EV-A71-C2-MP4 in triplicate. After infection, the cells were washed extensively with PBS, and the medium was replaced with T-1106. Infection proceeded until cytopathic effect was observed (48 h.p.i.).

6.4.15 Next-generation RNAseq

Total RNA was isolated with Direct-zol-96 RNA purification kit (Zymo Research) following manufacturer's instructions. The recommended in-column DNase I treatment was also conducted to remove genomic DNA. Purified RNA was quantified with a microplate reader (Tecan M200 Infinite Pro) using the Quant-iT RNA assay kit (ThermoFisher). Ribosomal RNA was removed using the NEBNext rRNA Depletion Kit (Human/Mouse/Rat) (New England Biolabs). Sequencing libraries were prepared using the NEBNext Ultra II RNA Library preparation kit for Illumina (New England Biolabs) and the pooled library was loaded in a NextSeq500/550 Mid Output kit v2.5 (Illumina) for sequencing in a NextSeq500 (151 cycles, 8 nucleotides of index).

6.4.16 Bulk RdRp turnover experiments

1 µM WT and YH variants of poliovirus or EV-A71 C2-MP4 RdRp were incubated with ³²P-labelled 20 µM RNA primer-template duplex (sym/subU) and 500 µM rNTPs. At

various time points (described in text) the reaction was quenched by the addition of 500 mM EDTA and 35% formamide. Quenched reactions were mixed with an equal volume of loading buffer (75% formamide, 0.025% bromophenol blue and 0.25% xylene cyanol) and heated to 70°C prior to loading on a denaturing PAGE gel. Products were resolved from substrates by denaturing polyacrylamide gel electrophoresis (18.5% acrylamide, 1.5% bisacrylamide, 1x TBE buffer, 7 M Urea). Electrophoresis was performed in 1x TBE at 90 W. Gels were visualized using a PhosphorImager and quantified using ImageQuant software (GE Healthcare, RRID: SCR_014246).

6.4.17 RNA constructs for single-molecule RNA synthesis experiments

The RNA template used in our single-molecule assay is analogous to the sequences used in previous studies of PV and $\Phi 6$ RdRp RNA synthesis kinetics^{18,75}. The RNA tether construct consists predominantly of a dsRNA, assembled by hybridization of a 2.8 kb template ssRNA to a 4.1 kb complementary strand, and two ~500 bases ssRNA strands containing either biotin or digoxigenin for the tethering between magnetic beads and the surface, as previously described in detail¹⁸. In contrast to the previously used hairpin for Poliovirus RdRp RNA synthesis initiation, terminating the 3' end of the template, we used for the hairpin structure 24 bases with the following sequence: 5'-AACUGUUGGUGUACGCGAAAGCGU-3'. Essentially, the hairpin mimics a primer and promotes primer-dependent RNA synthesis initiation²⁹.

The RNA constructs were assembled by first subjecting Plasmid pBB10 to PCR amplification using primers AB-For, AB-Rev, CD-For, CD-Rev, Bio-For, Bio-Rev, Dig-For, Dig-Rev, SP-For, and SP-Rev, listed in the Key Resource Listing. Single-stranded RNA sequences were produced from these amplicons *via in vitro* run-off transcription using T7 RNA polymerase from the Ribomax large-scale RNA production system (Promega). Transcription reactions for the AB, CD and SP ssRNA fragments contained 500 ng DNA amplicon, 10 μ l T7 buffer, 5 μ l T7 polymerase, 1 μ l 100 mM CTP, and 1 μ l of 100 mM for all other NTPs (ATP, UTP, GTP) in a reaction volume of 50 μ l. For the synthesis of BIO ssRNA, the UTP amount was reduced to half and the reaction mix was supplemented with 4.7 μ l of 10 mM biotin-16-UTP (Roche), while for DIG ssRNA the UTP amount was reduced only to 0.63 μ l with supplement of 3.7 μ l or 10 mM digoxigenin-11-UTP (Roche, RRID: AB_514496). The synthesized ssRNA fragments were purified using a RNeasy MinElute cleanup kit (Qiagen) and eluted in 1 mM sodium citrate buffer (pH 6.4).

These different ssRNA fragments were then assembled into a dsRNA construct for the single-molecule studies conducted on Poliovirus and Enterovirus A-71 RdRp *via* hybridization. The ssRNA fragments were first mixed in equimolar ratio in 200 μ l 0.5x SSC buffer, with the exception of the biotin (BIO) and digoxigenin (DIG)-enriched handles, which were added in four times molar excess in respect of the AB strand (1 μ g AB, 1.4 μ g CD, 360 ng SP, 450 ng BIO, and 516 ng DIG). Afterwards, the RNA mix was heated for 1 h to 65°C, cooled with a rate of 0.24°C/min down to 25°C. The final

dsRNA construct was purified with RNeasy MinElute cleanup kit and eluted in 1 mM sodium citrate. All RNA concentrations were photometrically determined (Nanodrop).

6.4.18 Magnetic tweezers experimental configuration

The magnetic tweezers implementation used in this study has been described previously^{18,76}. Briefly, light transmitted through the sample was collected by a 50x oil-immersion objective (CFI 50XH, Plan Achromat, 50x, NA = 0.9, Nikon) and projected onto a 12-megapixel CMOS camera (#FA-80-12M1H, Falcon2, Teledyne Dalsa) with a sampling frequency of 50 Hz. The applied magnetic field was generated by a pair of vertically aligned permanent neodymium-iron-boron magnets (Webcraft) separated by a distance of 1 mm, suspended on a motorized stage (#M-126.PD2, Physik Instrumente) above the flow cell. Image processing of the collected light allows tracking the real-time position of both surface attached reference beads and superparamagnetic beads coupled to the dsRNA constructs in three dimensions over time. The bead x , y , z position tracking was achieved using a cross-correlation algorithm realized with custom-written software in LabView (2011, National Instruments Corporation, RRID: SCR_014325). In this software, bead positions were determined with spectral corrections to correct for camera blur and aliasing⁷⁷.

6.4.19 Single-molecule RdRp RNA synthesis assay

The flow cell preparation used in this study has been described in detail elsewhere^{18,76}. In brief, polystyrene reference beads (#17133, Polysciences GmbH) of 1.5 μm in diameter were diluted 1:1500 in PBS buffer (pH 7.4; Sigma Aldrich) and then adhered to the nitrocellulose-coated (Invitrogen) surface of the flow cell. Afterwards, digoxigenin antibodies (Roche, RRID: AB_514496) at a concentration of 0.1 mg/ml were incubated for 1 h within the flow cell, following a 2 h incubation of 10 mg/ml BSA (New England Biolabs) diluted in PBS (pH 7.4) buffer. After washing with PBS buffer, 100 μl of streptavidin-coated superparamagnetic beads (DynaBeads, LifeTechnologies; prior diluted 1:400 from stock) with a diameter of 1.5 μm were added resulting in the attachment of the beads to the surface-tethered dsRNA constructs. Afterwards, unbound beads were washed out with PBS buffer.

The preparation of RdRp:RNA ternary complexes was also performed as described previously^{18,75}. Briefly, 1 μM RdRp in 100 μl EV buffer (50 mM HEPES, 5 mM MgCl_2 , 125 $\mu\text{g/ml}$ BSA, 1 mM DTT, 1 U Superase RNase inhibitor, pH 6.6), supplemented with 600 μM ATP, 600 μM CTP, and 1.2 mM ApC, was flushed into the flow cells containing the dsRNA constructs. Stalled RdRp complexes were formed during 20 min of incubation at room temperature. Afterwards, the flow cell was washed with EV buffer and the RNA chain elongation was re-initiated by adding all four rNTP in an equimolar concentration of 1 mM, unless stated otherwise, and in presence or absence of nucleotide analogs. The single-molecule measurements were conducted for 2 h at constant pulling forces of 25 pN at 24°C with a camera acquisition rate of 50 Hz.

6.4.20 Molecular Dynamics simulations (MD)

The starting coordinates for the all-atom MD simulations systems prepared by the accessory program “tleap” of AMBER18 suite⁷⁸. The crystal structure 3N6L of EV71 RdRp was used to prepare the starting coordinates for MD simulations of the WT system⁷⁹. The Y276H mutant system prepared by *in silico* replacement of Tyr at position-276 by a His; the steric clashes generated in the mutant system removed by subsequent energy minimization and equilibration. The WT PV RdRp was investigated previously by all-atom MD simulations (150 ns), using the 1RA6 structure as starting coordinates for the MD simulations^{36,39}. The Y275H mutant of PV RdRp was prepared by replacing Tyr-275 of 1RA6 structure by histidine; energy minimization and equilibration of the system removed any steric clashes in the mutant system.

For the performed MD simulations, the protein parameters of Amber14SB force field was used during calculations⁸⁰. All MD simulations were performed in explicit water (TIP3P model), imposing a minimal distance of 12 Å between the edge of the solvent box and any protein atom⁸¹. Calculations of the non-bonded interactions used a cutoff radius of 9 Å with periodic boundary conditions applied; particle mesh Ewald method was used to treat electrostatic interactions⁸². The SHAKE algorithm was employed to constrain hydrogens bonded to heavy atoms⁸³. The simulations were performed by first relaxing the systems in two cycles of energy minimization using SANDER program. Subsequently, the systems were slowly heated to 300 K using the parallel version PMEMD under NVT conditions (constant volume and temperature); Langevin dynamics with collision frequency ($\gamma = 2$) was used to regulate temperatures⁸⁴. The heated systems were then subjected to equilibration by running 100 ps of MD simulations under NPT conditions (constant pressure and temperature) with 1 fs integration time steps. MD trajectories were collected over 200 ns at 1 ps interval and 2 fs integration time steps. Analyses of the trajectories from MD simulations were performed using CPPTRAJ program⁸⁵. MD simulations were carried out on a multi-GPU workstation with 32-core processor (AMD Ryzen Threadripper 2990WX) and four Nvidia GTX 1080 Ti graphics cards.

6.5 Quantification and statistical analysis

6.5.1 Next-generation RNAseq analysis

Reads were first demultiplexed using the bcl2fastq v2.2 conversion software (Illumina, RRID: SCR_015058). The reads were adapter- and quality-trimmed using BBDuk and the optical duplicates removed using Clumpify, all part of the BBTools suite (RRID: SCR_016968). Reads were aligned to EV-A71 WT reference genomes using bowtie2⁷⁰. To identify deletions, the unaligned reads were processed *via* BMAP (a splice-aware aligner). To identify copybacks, reads were processed *via* VODKA, where the entire viral genome length was used as a template to generate the copyback index⁵⁵. In both cases, the output data was analyzed using an in-house R script.

6.5.2 Single-molecule data processing

RNA synthesis trajectories were processed using custom-written Igor v6.37 (RRID: SCR_000325) and MatLab R2013b (RRID: SCR_001622)-based custom-written scripts. The measured z-positions of magnetic beads during the RNA synthesis process were converted to synthesized RNA products as a function of time, using the empirically determined force-extension relationships for dsRNA and ssRNA molecules under the employed buffer conditions^{18,75}. Briefly, for the conversion from bead z-position to synthesized nucleotides, we used the formula:

$$N_T(F) = N \frac{L(F) - L_{ds}(F)}{L_{ss}(F) - L_{ds}(F)},$$

where for the applied force F , N represents the number of nucleotides of the template (2,820 nt), $L(F)$ is the measured extension of the tether, $L_{ds}(F)$ is the full dsRNA length, and $L_{ss}(F)$ is the full length of a ssRNA tether. To reduce the effect of Brownian noise in the applied statistical analyses, all measured elongation trajectories were filtered to 1 Hz using a sliding mean average filter.

6.5.3 Statistical dwell time analysis of single RdRp elongation trajectories

The stochastic RNA synthesis dynamics of EV-A71 and PV RdRp were quantitatively assessed by a statistical analysis of elongation and pausing using a recently described bias-free dwell-time analysis^{18,75,76}. Using this approach, the times needed for RdRp to elongate through consecutive dwell time windows of four nucleotides - defined as *dwell times* - were determined for all measured RdRp trajectories under the same conditions to construct dwell time probability distributions (e.g. **Figure S.6.1A**). The dwell times were bootstrapped 1,000 times to estimate the standard deviation and confidence intervals of the distributions^{18,76}. All dwell-time distributions qualitatively exhibit the same features, such as a peak at short time scales (~200 ms) and a tail of gradually decreasing probability in time scales ranging between 1 and 1,000 s. While the peak reflects fast kinetic processes consisting of nucleotide addition, NTP hydrolysis, PPi release, and translocation, the tail originates from off-pathway pauses, consistent with the previous observations for the PV RdRp¹⁸.

The quantitative description of the duration and probability of pauses during RNA synthesis derive from these dwell time distributions. To calculate the average pause probabilities (\pm SD), the dwell time distributions were integrated starting from a chosen threshold of 3 s, where single pauses are detectable within a dwell time window of 4 nt, similar to the value obtained in our previous single-molecule study of PV RdRp dynamics¹⁸. The apparent lifetime of these pauses is determined by averaging all dwell times (\pm SEM) exceeding this threshold of 3 s.

The probabilities of EV-A71 copy-back RNA synthesis (also referred as *reversals*) and PV backtracking were determined by dividing their occurrence by the total amount of RNA synthesis trajectories per pooled data set.

The enzyme processivities reflect the measured length of synthesized RNA chains (in nucleotides) for each measured RdRp defining their termination event, and the average velocity (\pm SD) resulted from dividing individual RdRp processivities by their active RNA synthesis duration.

6.5.4 Sequence analysis of copy-back locations from single-molecule and RNAseq assays

The sequence analysis was performed similar to the analysis used in the previously published study of EV-A71 recombinants yielding from transfected cell-based assays²⁰.

From the *in vitro* single-molecule experiments, the sequences at which template switching occurred were extracted for analysis. The locations of template switching on the template RNA strand were determined by measuring the distance of the bead (in nucleotides) where reversals occur relative to the bead position before RNA synthesis was induced with NTPs. We used a sequence window of 31 nucleotides (-15 to +15 nucleotides around the detected locations) for extracting the sequences that were subjected to sequence analysis. This window size was determined based on two parameters. First, in a recently reported EV-A71 cell-based recombination assay, 'copy-choice' recombination occurred in regions with a sequence homology of between 5-11 nucleotides between the two parental template strands²⁰. Second, the accuracy of the used assay is limited by the stiffness of the ssRNA construct and the corresponding degree of Brownian noise which accounts for a resolution of ± 10 nucleotides. The window size of 31 nucleotides therefore guarantees to comprise any possible sequence motif that could be encountered in cells.

The analysis of the RNA sequencing data obtained from infected cells provided the exact copy-back RNA synthesis locations. We used a sequence window of 25 nucleotides (-12 to +12 nucleotides around the detected locations) to guarantee capturing potential sequence motifs with a length between 5 - 11 nucleotides²⁰ up- and downstream the encountered copy-back locations.

From all extracted sequences of copy-back locations, we calculated the G:C and A:U densities, as well as the amount of successive G|C or A|U nucleotides. *De novo* sequence motif search for these location sequences were performed using the MEME suite (Version 5.0.1)⁸⁶ with 1st-order background modelling and variable sequence motif width between 4-11 nt.

6.6 Supplemental figures

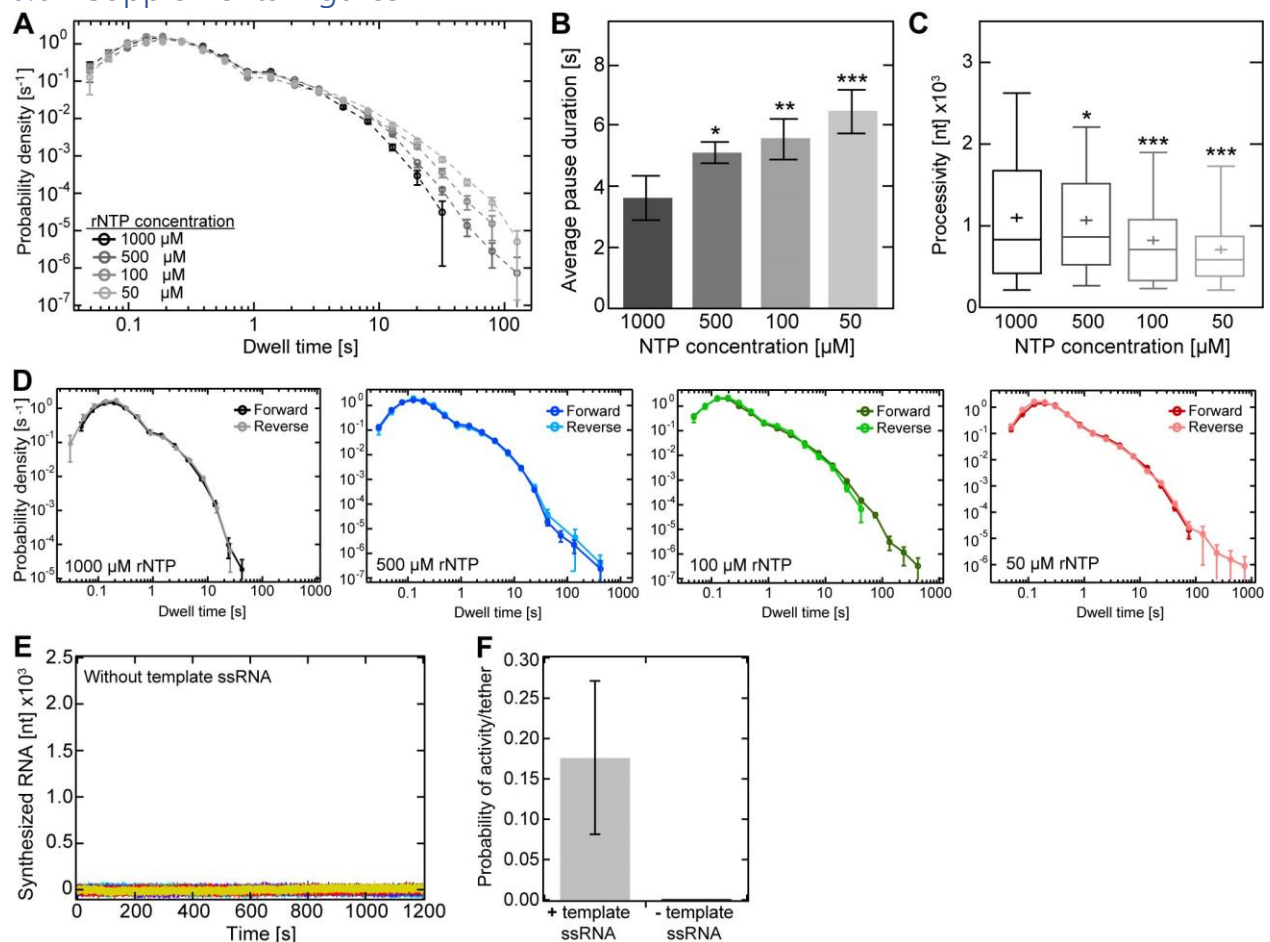


Figure S.6.1. EV-A71 RdRp exhibits increased pausing upon nucleotides deficiency, but similar forward and reverse RNA synthesis dynamics.

(A) Dwell time distributions of EV-A71 wild type RdRp RNA synthesis dynamics at different nucleotide concentrations (50 μM - 1 mM). Dwell time window was set to 4 nt and the error bars ($\pm SD$) result from bootstrapping with 1,000 iterations. (B, C) Comparison of extracted quantitative pause values during RNA synthesis upon nucleotide deficiency shown in Fig. 1, such as (B) average ($\pm SEM$) pause duration, and (C) RNA synthesis processivity. (D) Superimposed dwell time distributions of forward (dark colors) and reverse RNA chain elongation (light colors) at different rNTP concentrations (50 μM - 1 mM). (E) EV-A71 RdRp trajectories in absence of the template ssRNA strand exhibited no RNA synthesis activity. (F) Average probability ($\pm SD$) of RNA synthesis activity encountered in presence and absence of the template ssRNA strand ($n = 100$ tethers each). Statistical analyses were performed using one-way analysis of variance (ANOVA) with comparative Tukey post-hoc test (significance levels α : *** = 0.001; ** = 0.01; * = 0.05). Related to [Figure 6.1](#).

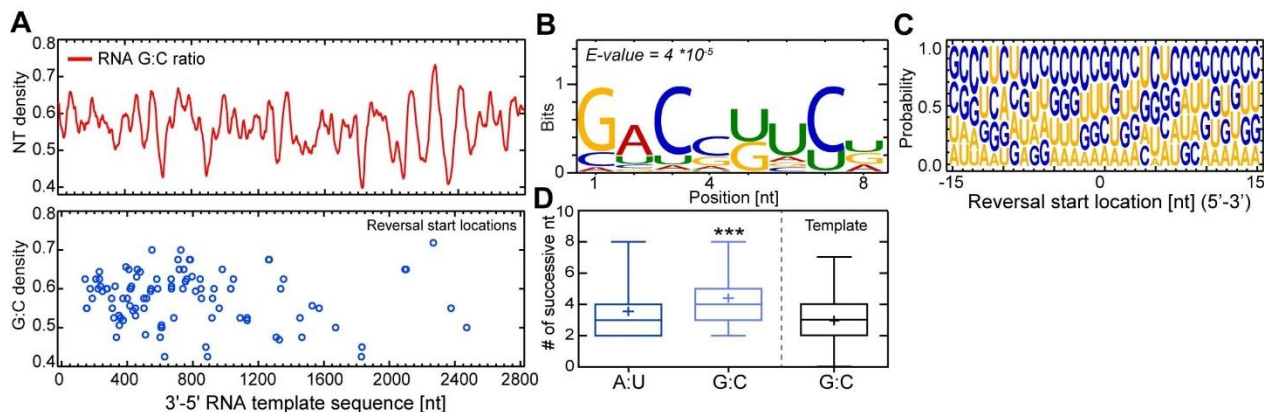


Figure S.6.2. EV-A71 copy-back RNA synthesis occurs sequence-independent in vitro.

(A) Analysis of sequences where copy-back RNA synthesis predominantly occurred (31 nt window) did not exhibit any hotspots with respect to the RNA template sequence (upper panel, red line). The G:C density at those copyback RNA synthesis locations (lower panel, blue circles) did also not reflect any apparent correlation. (B) With the absence of apparent copy-back RNA synthesis hotspots, the sequences where copy-back RNA synthesis predominantly occurred were subject to de novo sequence motif search using MEME, a multiple sequence alignment algorithm that searches for conserved sequence motifs. The computed sequence conservation at locations of reversal events showed a bit score <1 and a probability (E-value) strongly below the 95% confidence interval threshold. Both results reveal no evidence of a predominant sequence motif as trigger. (C) Sequence logo of position-dependent nucleotide abundance within the sequences where copy-back RNA synthesis predominantly occurred showed that guanosines and cytosines were most abundant, which can hamper effective melting of the RNA duplex during RNA synthesis, resulting in an increase of RdRp to pause and arrest. In agreement, (D) a higher abundance of successive G:C (light blue) nucleotides within those sequences were found compared to both the average amount encountered in the ssRNA template (black) and successive A:U (light blue). Statistical analysis was performed using one-way analysis of variance (ANOVA) with comparative Tukey post-hoc test (significance level $\alpha: *** = 0.001$). Related to [Figure 6.1](#).

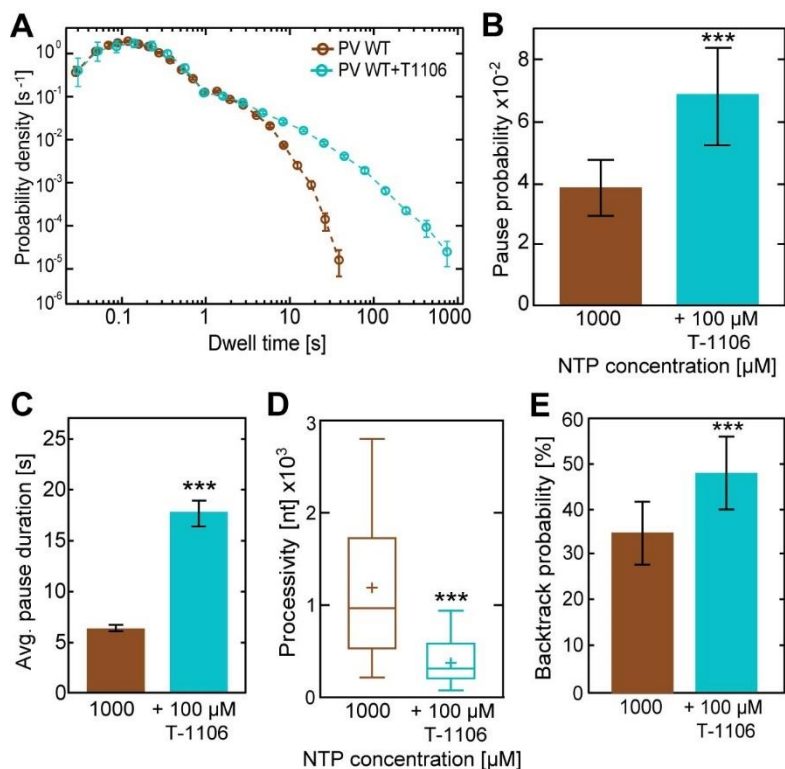


Figure S.6.3. T-1106 increases PV RdRp pausing and backtracking.

(A) Superimposed dwell time distributions of PV WT RdRp (brown) exhibit increased pausing probability and duration in presence of T-1160-TP (cyan). Dwell times are associated with polymerases advancing 4 nt. The error bars represent the estimate of the standard deviations via bootstrapping with 1,000 iterations. (B-E) In presence of T-1106-TP, wild type poliovirus RdRp exhibits significantly higher (B) average ($\pm\text{SD}$) pausing probability of (C) extended apparent duration (AVG $\pm\text{SEM}$) during RNA synthesis, leading to a decreased (D) processivity but higher (E) backtracking probability. Statistical analysis consisted of unpaired, two-tailed t-tests (significance level $p: *** \leq 0.001$; $* \leq 0.05$). Related to [Figure 6.6](#).

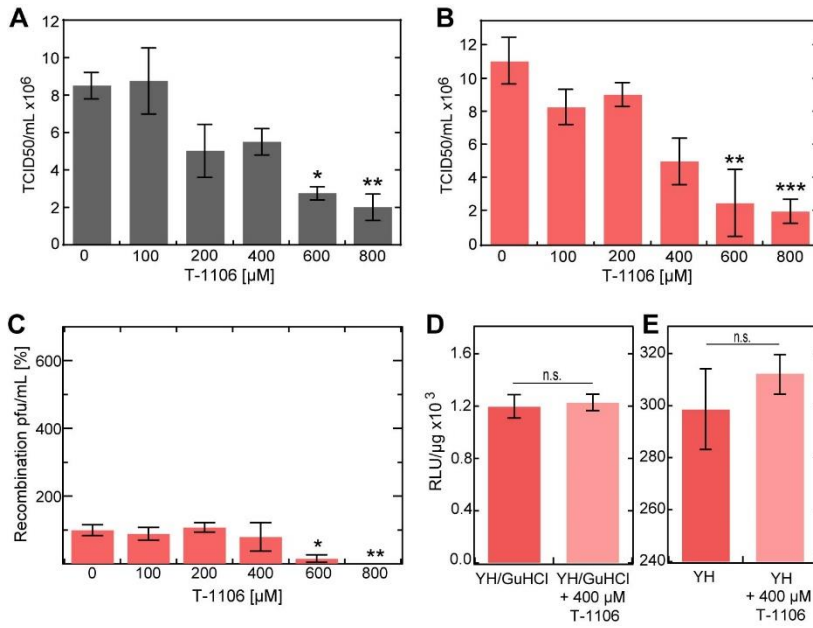


Figure S.6.4. T-1106 dose response of EV-A71 WT and Y276H variant full-length viruses.

RD cells infected with (A) EV-A71 wild type and (B) Y276H donor genomes at MOI 1 in the presence of increasing concentration of T-1106. Following total cytopathic effect (CPE), cell culture supernatants were used to quantify virus by TCID50. (C) Relative Y276H viable recombinant yield normalized as a percentage of a carrier (DMSO)-treated control (AVG \pm SD; $n = 3$ for each condition). Calculated IC₅₀ amounts to 280 \pm 90 μ M T-1106 (D,E) EV-A71 donor translation (D) and replication (E) efficiency (AVG \pm SD) for Y276H RdRp variant. All statistical

analyses were performed using one-way analyses of variance (ANOVA) with comparative Tukey post-hoc test (significance levels α : *** = 0.001; ** = 0.01; * = 0.05; n.s. = non-significant). Related to [Figure 6.6](#).

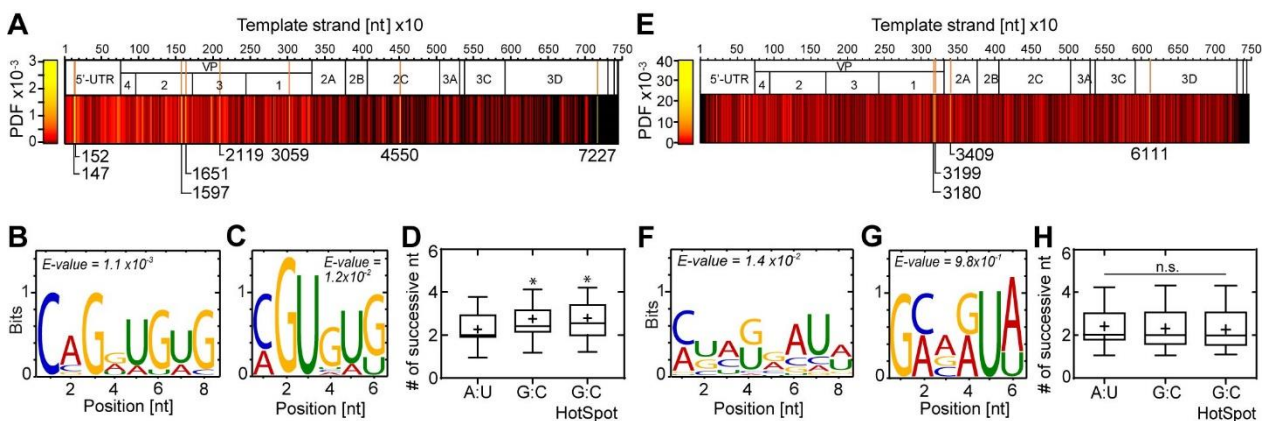


Figure S.6.5. EV-A71 copy-back RNA synthesis and intermolecular template switching occur sequence independent in cell culture.

(A) Probability density plot of identified copy-back locations relative to the EV-A71 WT genome sequence. While the majority of copy-back RNA synthesis locations are randomly distributed across the genome sequence, 8 hot spots were identified at the 5' -UTR, VP2, VP3, VP1, 2C and 3D coding regions. (B, C) Sequences (25-nt window) where copy-back RNA synthesis occurred were subject to de novo sequence motif search using MEME. The computed sequence conservations for (B) all copy-back locations and at (C) copy-back hot spots reveal no evidence of a predominant or conserved sequence motif as trigger. (D) A higher abundance of successive G:C base pairs within the copy-back sequences were found compared to the amount of successive A:U. (E) Probability density plot of identified intermolecular recombination locations relative to the EV-A71 WT genome sequence. Recombination locations are randomly distributed across the genome sequence, and 4 hot spots were identified at the VP1, 2A and 3D coding regions. (F, G) Sequences (25-nt window) where template switching occurred were subject to de novo sequence motif search. The computed sequence conservations for (F) all recombination events and at (G) recombination hot spots showed also no evidence of a predominant or conserved sequence motif as trigger. (H) No differences in the amount of successive G:C and A:U base pairs at recombination locations and hot spots were observable. Statistical analyses were performed using one-way analysis of variance (ANOVA) with comparative Tukey post-hoc test (significance level p : * = 0.05; n.s. = nonsignificant). Related to [Figure 6.6](#).

6.6.1 Supplementary tables

Table S.6.1. Single molecule experimental parameters and measurement statistics.

Table of experimental parameters, such as NTP and T-1106 concentrations, as well as dwell times as statistical measure for all experiments performed in this study. The number of nucleotides is an alternative statistical measure that reflects the total length of synthesized RNA monitored from pooled trajectories. The applied force was hold constant at 25 pN for all experiments. Related to [Figure 6.1](#), [Figure 6.3](#), [Figure 6.4](#), and [Figure 6.6](#).

RdRp	EV-A71 C2-MP4				
[NTP]	1 mM	500 μ M	100 μ M	50 μ M	100 μ M
[NA]	-	-	-	-	50 μ M T-1106
Dwell times	9981	16356	13430	10042	6570
Nucleotides	39.9 kb	65.4 kb	53.7 kb	40.1 kb	26.3 kb
RdRp	EV-A71 Y276H	PV WT	PV WT	PV Y275H	
[NTP]	1 mM	1 mM	1 mM	1 mM	
[NA]	-	-	100 μ M T1106	-	
Dwell times	4881	5715	4839	3836	
Nucleotides	19.5 kb	22.9 kb	19.4 kb	15.3 kb	

6.7 References

1. Carrasco-Hernandez R, Jácome R, Vidal YL, de León SP. Are RNA viruses candidate agents for the next global pandemic? A review. *ILAR J.* 2017;58(3). doi:10.1093/ilar/ilx026
2. Ghanbari R, Teimoori A, Sadeghi A, et al. Existing antiviral options against SARS-CoV-2 replication in COVID-19 patients. *Future Microbiol.* 2020;15(18). doi:10.2217/fmb-2020-0120
3. Zhu N, Zhang D, Wang W, et al. A Novel Coronavirus from Patients with Pneumonia in China, 2019. *N Engl J Med.* 2020;382(8). doi:10.1056/nejmoa2001017
4. Park SW, Pons-Salort M, Messacar K, et al. Epidemiological dynamics of enterovirus D68 in the United States and implications for acute flaccid myelitis. *Sci Transl Med.* 2021;13(584). doi:10.1126/scitranslmed.abd2400
5. Puenpa J, Wanlapakorn N, Vongpunsawad S, Poovorawan Y. The History of Enterovirus A71 Outbreaks and Molecular Epidemiology in the Asia-Pacific Region. *J Biomed Sci.* 2019;26(1). doi:10.1186/s12929-019-0573-2
6. Tsai C-H, Lee P-Y, Stollar V, Li M-L. Antiviral Therapy Targeting Viral Polymerase. *Curr Pharm Des.* 2006;12(11). doi:10.2174/138161206776361156
7. Seley-Radtke KL, Yates MK. The evolution of nucleoside analogue antivirals: A review for chemists and non-chemists. Part 1: Early structural modifications to the nucleoside scaffold. *Antiviral Res.* 2018;154. doi:10.1016/j.antiviral.2018.04.004
8. Yates MK, Seley-Radtke KL. The evolution of antiviral nucleoside analogues: A review for chemists and non-chemists. Part II: Complex modifications to the nucleoside scaffold. *Antiviral Res.* 2019;162. doi:10.1016/j.antiviral.2018.11.016
9. Irwin KK, Renzette N, Kowalik TF, Jensen JD. Antiviral drug resistance as an adaptive process. *Virus Evol.* 2016;2(1). doi:10.1093/ve/vew014
10. Arnold JJ, Sharma SD, Feng JY, et al. Sensitivity of Mitochondrial Transcription and Resistance of RNA Polymerase II Dependent Nuclear Transcription to Antiviral Ribonucleosides. *PLoS Pathog.* 2012;8(11). doi:10.1371/journal.ppat.1003030
11. Coats SJ, Garnier-Amblard EC, Amblard F, et al. Chutes and ladders in hepatitis C nucleoside drug development. *Antiviral Res.* 2014;102. doi:10.1016/j.antiviral.2013.11.008
12. Mifsud EJ, Hayden FG, Hurt AC. Antivirals targeting the polymerase complex of influenza viruses. *Antiviral Res.* 2019;169. doi:10.1016/j.antiviral.2019.104545
13. Joshi S, Parkar J, Ansari A, et al. Role of favipiravir in the treatment of COVID-19. *Int J Infect Dis.* 2021;102. doi:10.1016/j.ijid.2020.10.069
14. Shannon A, Selisko B, Le N, et al. Favipiravir strikes the SARS-CoV-2 at its Achilles heel, the RNA polymerase. *bioRxiv Prepr Serv Biol.* Published online 2020. doi:10.1101/2020.05.15.098731
15. Furuta Y, Takahashi K, Shiraki K, et al. T-705 (favipiravir) and related compounds:

- Novel broad-spectrum inhibitors of RNA viral infections. *Antiviral Res.* 2009;82(3). doi:10.1016/j.antiviral.2009.02.198
16. Sangawa H, Komeno T, Nishikawa H, et al. Mechanism of action of T-705 ribosyl triphosphate against influenza virus RNA polymerase. *Antimicrob Agents Chemother.* 2013;57(11). doi:10.1128/AAC.00649-13
 17. de Avila AI, Moreno E, Perales C, Domingo E. Favipiravir can evoke lethal mutagenesis and extinction of foot-and-mouth disease virus. *Virus Res.* 2017;233. doi:10.1016/j.virusres.2017.03.014
 18. Dulin D, Arnold JJ, van Laar T, et al. Signatures of Nucleotide Analog Incorporation by an RNA-Dependent RNA Polymerase Revealed Using High-Throughput Magnetic Tweezers. *Cell Rep.* 2017;21(4). doi:10.1016/j.celrep.2017.10.005
 19. Malone B, Chen J, Wang Q, et al. Structural basis for backtracking by the SARS-CoV-2 replication-transcription complex. *bioRxiv.* Published online January 2021:2021.03.13.435256. doi:10.1101/2021.03.13.435256
 20. Woodman A, Lee K-M, Janissen R, et al. Predicting Intraserotypic Recombination in Enterovirus 71. *J Virol.* Published online November 2018:JVI.02057-18. doi:10.1128/JVI.02057-18
 21. Vignuzzi M, López CB. Defective viral genomes are key drivers of the virus-host interaction. *Nat Microbiol.* 2019;4(7). doi:10.1038/s41564-019-0465-y
 22. Dulin D, Vilfan ID, Berghuis BA, et al. Elongation-Competent Pauses Govern the Fidelity of a Viral RNA-Dependent RNA Polymerase. *Cell Rep.* 2015;10(6). doi:10.1016/j.celrep.2015.01.031
 23. Seifert M, Bera SC, van Nies P, et al. Inhibition of SARS-CoV-2 polymerase by nucleotide analogs: a single molecule perspective. *bioRxiv.* Published online January 2021:2020.08.06.240325. doi:10.1101/2020.08.06.240325
 24. Jin Z, Leveque V, Ma H, Johnson KA, Klumpp K. NTP-mediated nucleotide excision activity of hepatitis C virus RNA-dependent RNA polymerase. *Proc Natl Acad Sci U S A.* 2013;110(5). doi:10.1073/pnas.1214924110
 25. Acevedo A, Woodman A, Arnold JJ, et al. Genetic recombination of poliovirus facilitates subversion of host barriers to infection. *bioRxiv.* Published online January 2018:273060. doi:10.1101/273060
 26. Kempf BJ, Watkins CL, Peersen OB, Barton DJ. An Extended Primer Grip of Picornavirus Polymerase Facilitates Sexual RNA Replication Mechanisms. Pfeiffer JK, ed. *J Virol.* 2020;94(16). doi:10.1128/JVI.00835-20
 27. Tee HK, Tan CW, Yogarajah T, et al. Electrostatic interactions at the five-fold axis alter heparin-binding phenotype and drive enterovirus A71 virulence in mice. *PLoS Pathog.* 2019;15(11). doi:10.1371/journal.ppat.1007863
 28. Yamayoshi S, Yamashita Y, Li J, et al. Scavenger receptor B2 is a cellular receptor for

- enterovirus 71. *Nat Med.* 2009;15(7):798-801. doi:10.1038/nm.1992
29. Arnold JJ, Cameron CE. Poliovirus RNA-dependent RNA polymerase (3D(pol)). Assembly of stable, elongation-competent complexes by using a symmetrical primer-template substrate (sym/sub). *J Biol Chem.* 2000;275(8):5329-5336. doi:10.1074/jbc.275.8.5329
 30. Shi W, Ye H-Q, Deng C-L, Li R, Zhang B, Gong P. A nucleobase-binding pocket in a viral RNA-dependent RNA polymerase contributes to elongation complex stability. *Nucleic Acids Res.* 2020;48(3):1392-1405. doi:10.1093/nar/gkz1170
 31. Cameron CE, Moustafa IM, Arnold JJ. Dynamics: the missing link between structure and function of the viral RNA-dependent RNA polymerase? *Curr Opin Struct Biol.* 2009;19(6). doi:10.1016/j.sbi.2009.10.012
 32. Moustafa IM, Shen H, Morton B, Colina CM, Cameron CE. Molecular dynamics simulations of viral RNA polymerases link conserved and correlated motions of functional elements to fidelity. *J Mol Biol.* 2011;410(1). doi:10.1016/j.jmb.2011.04.078
 33. Cameron CE, Moustafa IM, Arnold JJ. Fidelity of Nucleotide Incorporation by the RNA-Dependent RNA Polymerase from Poliovirus. In: *Enzymes.* Vol 39. ; 2016. doi:10.1016/bs.enz.2016.02.002
 34. Shu B, Gong P. Structural basis of viral RNA-dependent RNA polymerase catalysis and translocation. *Proc Natl Acad Sci U S A.* 2016;113(28). doi:10.1073/pnas.1602591113
 35. Gong P, Peersen OB. Structural basis for active site closure by the poliovirus RNA-dependent RNA polymerase. *Proc Natl Acad Sci U S A.* 2010;107(52):22505-22510. doi:10.1073/pnas.1007626107
 36. Moustafa IM, Korboukh VK, Arnold JJ, et al. Structural dynamics as a contributor to error-prone replication by an RNA-dependent RNA polymerase. *J Biol Chem.* 2014;289(52). doi:10.1074/jbc.M114.616193
 37. Crotty S, Maag D, Arnold JJ, et al. The broad-spectrum antiviral ribonucleoside ribavirin is an RNA virus mutagen. *Nat Med.* 2000;6(12). doi:10.1038/82191
 38. Kirkegaard K, Baltimore D. The mechanism of RNA recombination in poliovirus. *Cell.* 1986;47(3):433-443. doi:10.1016/0092-8674(86)90600-8
 39. Arnold JJ, Cameron CE. Poliovirus RNA-dependent RNA Polymerase (3D pol) Is Sufficient for Template Switching in Vitro. *J Biol Chem.* 1999;274(5):2706-2716. doi:10.1074/jbc.274.5.2706
 40. Lowry K, Woodman A, Cook J, Evans DJ. Recombination in Enteroviruses Is a Biphasic Replicative Process Involving the Generation of Greater-than Genome Length "Imprecise" Intermediates. *PLoS Pathog.* 2014;10(6). doi:10.1371/journal.ppat.1004191
 41. Woodman A, Arnold JJ, Cameron CE, Evans DJ. Biochemical and genetic analysis of the role of the viral polymerase in enterovirus recombination. *Nucleic Acids Res.* 2016;44(14). doi:10.1093/nar/gkw567

42. Kempf BJ, Watkins CL, Peersen OB, Barton DJ. Picornavirus RNA Recombination Counteracts Error Catastrophe. *J Virol.* 2019;93(14). doi:10.1128/JVI.00652-19
43. Abdelnabi R, Morais ATS de, Leyssen P, et al. Understanding the Mechanism of the Broad-Spectrum Antiviral Activity of Favipiravir (T-705): Key Role of the F1 Motif of the Viral Polymerase. *J Virol.* 2017;91(12). doi:10.1128/jvi.00487-17
44. Gowen BB, Wong MH, Jung KH, Smee DF, Morrey JD, Furuta Y. Efficacy of favipiravir (T-705) and T-1106 pyrazine derivatives in phlebovirus disease models. *Antiviral Res.* 2010;86(2). doi:10.1016/j.antiviral.2009.10.015
45. Arnold JJ, Cameron CE. Poliovirus RNA-dependent RNA polymerase (3Dpol): pre-steady-state kinetic analysis of ribonucleotide incorporation in the presence of Mg²⁺. *Biochemistry.* 2004;43(18):5126-5137. doi:10.1021/bi035212y
46. Julander JG, Furuta Y, Shafer K, Sidwell RW. Activity of T-1106 in a hamster model of yellow fever virus infection. *Antimicrob Agents Chemother.* 2007;51(6). doi:10.1128/AAC.01494-06
47. Eyer L, Nencka R, de Clercq E, Seley-Radtke K, Ružek D. Nucleoside analogs as a rich source of antiviral agents active against arthropod-borne flaviviruses. *Antivir Chem Chemother.* 2018;26. doi:10.1177/2040206618761299
48. Lee K-M, Gong Y-N, Hsieh T-H, et al. Discovery of Enterovirus A71-like nonstructural genomes in recent circulating viruses of the Enterovirus A species. *Emerg Microbes Infect.* 2018;7(1):111. doi:10.1038/s41426-018-0107-0
49. Dolan PT, Whitfield ZJ, Andino R. Mechanisms and concepts in RNA virus population dynamics and evolution. *Annu Rev Virol.* 2018;5. doi:10.1146/annurev-virology-101416-041718
50. Li C, Wang H, Shi J, et al. Senecavirus-Specific Recombination Assays Reveal the Intimate Link between Polymerase Fidelity and RNA Recombination. Pfeiffer JK, ed. *J Virol.* 2019;93(13). doi:10.1128/JVI.00576-19
51. Korboukh VK, Lee CA, Acevedo A, et al. RNA virus population diversity, an optimum for maximal fitness and virulence. *J Biol Chem.* 2014;289(43). doi:10.1074/jbc.M114.592303
52. Poirier EZ, Mounce BC, Rozen-Gagnon K, et al. Low-Fidelity Polymerases of Alphaviruses Recombine at Higher Rates To Overproduce Defective Interfering Particles. Dermody TS, ed. *J Virol.* 2016;90(5):2446-2454. doi:10.1128/JVI.02921-15
53. Xiao Y, Rouzine IM, Bianco S, et al. RNA Recombination Enhances Adaptability and Is Required for Virus Spread and Virulence. *Cell Host Microbe.* 2016;19(4). doi:10.1016/j.chom.2016.03.009
54. Kang JY, Mishanina T V., Landick R, Darst SA. Mechanisms of Transcriptional Pausing in Bacteria. *J Mol Biol.* 2019;431(20). doi:10.1016/j.jmb.2019.07.017
55. Sun Y, Kim EJ, Felt SA, et al. A specific sequence in the genome of respiratory syncytial

- virus regulates the generation of copy-back defective viral genomes. *PLoS Pathog.* 2019;15(4):e1007707. doi:10.1371/journal.ppat.1007707
56. Kim H, Ellis VD, Woodman A, Zhao Y, Arnold JJ, Cameron CE. RNA-dependent RNA polymerase speed and fidelity are not the only determinants of the mechanism or efficiency of recombination. *Genes (Basel)*. 2019;10(12). doi:10.3390/genes10120968
 57. Liu S, Abbondanzieri EA, Rausch JW, Grice SFJL, Zhuang X. Slide into Action: Dynamic Shuttling of HIV Reverse Transcriptase on Nucleic Acid Substrates. *Science (80-)*. 2008;322(5904):1092-1097. doi:10.1126/science.1163108
 58. Liu S, Harada BT, Miller JT, Le Grice SFJ, Zhuang X. Initiation complex dynamics direct the transitions between distinct phases of early HIV reverse transcription. *Nat Struct Mol Biol.* 2010;17(12). doi:10.1038/nsmb.1937
 59. Abbondanzieri EA, Bokinsky G, Rausch JW, Zhang JX, Le Grice SFJ, Zhuang X. Dynamic binding orientations direct activity of HIV reverse transcriptase. *Nature*. 2008;453(7192). doi:10.1038/nature06941
 60. Jin Z, Smith LK, Rajwanshi VK, Kim B, Deval J. The Ambiguous Base-Pairing and High Substrate Efficiency of T-705 (Favipiravir) Ribofuranosyl 5'-Triphosphate towards Influenza A Virus Polymerase. *PLoS One*. 2013;8(7). doi:10.1371/journal.pone.0068347
 61. Vignuzzi M, Stone JK, Andino R. Ribavirin and lethal mutagenesis of poliovirus: Molecular mechanisms, resistance and biological implications. *Virus Res.* 2005;107(2):173-181. doi:10.1016/j.virusres.2004.11.007
 62. Lazzarini RA, Keene JD, Schubert M. The origins of defective interfering particles of the negative-strand RNA viruses. *Cell*. 1981;26(2 PART 2). doi:10.1016/0092-8674(81)90298-1
 63. Re GG, Gupta KC, Kingsbury DW. Genomic and copy-back 3' termini in Sendai virus defective interfering RNA species. *J Virol.* 1983;45(2). doi:10.1128/jvi.45.2.659-664.1983
 64. Whistler T, Bellini WJ, Rota PA. Generation of defective interfering particles by two vaccine strains of measles virus. *Virology*. 1996;220(2). doi:10.1006/viro.1996.0335
 65. Yount JS, Kraus TA, Horvath CM, Moran TM, López CB. A Novel Role for Viral-Defective Interfering Particles in Enhancing Dendritic Cell Maturation. *J Immunol.* 2006;177(7). doi:10.4049/jimmunol.177.7.4503
 66. Calain P, Curran J, Kolakofsky D, Roux L. Molecular cloning of natural paramyxovirus copy-back defective interfering RNAs and their expression from DNA. *Virology*. 1992;191(1). doi:10.1016/0042-6822(92)90166-M
 67. Fujii K, Nagata N, Sato Y, et al. Transgenic mouse model for the study of enterovirus 71 neuropathogenesis. *Proc Natl Acad Sci U S A*. 2013;110(36). doi:10.1073/pnas.1217563110
 68. Petrushenko ZM, Lai CH, Rai R, Rybenkov V V. DNA reshaping by MukB: Right-handed knotting, left-handed supercoiling. *J Biol Chem.* 2006;281(8). doi:10.1074/jbc.M504754200

69. Wang Y-F, Chou C-T, Lei H-Y, et al. A Mouse-Adapted Enterovirus 71 Strain Causes Neurological Disease in Mice after Oral Infection. *J Virol.* 2004;78(15):7916-7924. doi:10.1128/JVI.78.15.7916-7924.2004
70. Langmead B, Salzberg SL. Fast gapped-read alignment with Bowtie 2. *Nat Methods.* 2012;9(4). doi:10.1038/nmeth.1923
71. Kung Y-H, Huang S-W, Kuo P-H, et al. Introduction of a strong temperature-sensitive phenotype into enterovirus 71 by altering an amino acid of virus 3D polymerase. *Virology.* 2010;396(1):1-9. doi:10.1016/j.virol.2009.10.017
72. Tang W-F, Huang R-T, Chien K-Y, et al. Host MicroRNA miR-197 Plays a Negative Regulatory Role in the Enterovirus 71 Infectious Cycle by Targeting the RAN Protein. López S, ed. *J Virol.* 2016;90(3):1424-1438. doi:10.1128/JVI.02143-15
73. Arnold JJ, Bernal A, Uche U, et al. Small ubiquitin-like modifying protein isopeptidase assay based on poliovirus RNA polymerase activity. *Anal Biochem.* 2006;350(2). doi:10.1016/j.ab.2005.11.001
74. Gohara DW, Ha CS, Kumar S, et al. Production of “Authentic” Poliovirus RNA-Dependent RNA Polymerase (3Dpol) by Ubiquitin-Protease-Mediated Cleavage in *Escherichia coli*. *Protein Expr Purif.* 1999;17(1):128-138. doi:10.1006/prev.1999.1100
75. Dulin D, Vilfan ID, Berghuis BA, et al. Elongation-Competent Pauses Govern the Fidelity of a Viral RNA-Dependent RNA Polymerase. *Cell Rep.* 2015;10(6):983-992. doi:10.1016/j.celrep.2015.01.031
76. Janissen R, Arens MMA, Vtyurina NN, et al. Global DNA Compaction in Stationary-Phase Bacteria Does Not Affect Transcription. *Cell.* 2018;174(5). doi:10.1016/j.cell.2018.06.049
77. Cnossen JP, Dulin D, Dekker NH. An optimized software framework for real-time, high-throughput tracking of spherical beads. *Rev Sci Instrum.* 2014;85(10). doi:10.1063/1.4898178
78. Case D, Ben-Shalom I, Brozell S, et al. *AMBER 2018*. University of California, San Francisco; 2018.
79. Wu Y, Lou Z, Miao Y, et al. Structures of EV71 RNA-dependent RNA polymerase in complex with substrate and analogue provide a drug target against the hand-foot-and-mouth disease pandemic in China. *Protein Cell.* 2010;1(5):491-500. doi:10.1007/s13238-010-0061-7
80. Maier JA, Martinez C, Kasavajhala K, Wickstrom L, Hauser KE, Simmerling C. ff14SB: Improving the Accuracy of Protein Side Chain and Backbone Parameters from ff99SB. *J Chem Theory Comput.* 2015;11(8). doi:10.1021/acs.jctc.5b00255
81. Jorgensen WL, Chandrasekhar J, Madura JD, Impey RW, Klein ML. Comparison of simple potential functions for simulating liquid water. *J Chem Phys.* 1983;79(2). doi:10.1063/1.445869

82. Darden T, York D, Pedersen L. Particle mesh Ewald: An $N \cdot \log(N)$ method for Ewald sums in large systems. *J Chem Phys.* 1993;98(12):10089-10092. doi:10.1063/1.464397
83. Ryckaert JP, Ciccotti G, Berendsen HJC. Numerical integration of the cartesian equations of motion of a system with constraints: molecular dynamics of n-alkanes. *J Comput Phys.* 1977;23(3). doi:10.1016/0021-9991(77)90098-5
84. Feller SE, Zhang Y, Pastor RW, Brooks BR. Constant pressure molecular dynamics simulation: The Langevin piston method. *J Chem Phys.* 1995;103(11). doi:10.1063/1.470648
85. Roe DR, Cheatham TE. PTRAJ and CPPTRAJ: Software for processing and analysis of molecular dynamics trajectory data. *J Chem Theory Comput.* 2013;9(7). doi:10.1021/ct400341p
86. Bailey TL, Boden M, Buske FA, et al. MEME SUITE: tools for motif discovery and searching. *Nucleic Acids Res.* 2009;37(Web Server):W202-W208. doi:10.1093/nar/gkp335

7

Concluding remarks

As stated by numerous PhD candidates regarding their respective concluding dissertations, I too can affirm that the work presented in this dissertation does not fully capture the extensive effort invested in the project, nor does it encompass the entirety of the planned experiments. In line with typical research endeavors, the most productive experiments often arise in the project's final year. Consequently, this work serves as a basis for future investigations, not only from a biophysical perspective but also from a biochemical standpoint. This chapter aims to illuminate potential avenues for subsequent studies.

7.1 Translating the protocol for multivalent vaccine purposes

The natural progression of this work involves applying the protocol to other viruses in the *Enterovirus* genus and subsequently other genera. However, as elucidated in **Chapter 3**, VLPs from diverse virus origins thrive under distinct production and purification conditions. Despite having highly similar genomes and viral proteins, viruses within the same genus can vary significantly, as demonstrated by the differences in cell receptor recognition and virus-associated diseases¹. This variability is further evidenced by the significant efforts to produce poliovirus VLPs using the BEVS, not only in this project but also by other research groups. The main challenge arose from the lack of an immunogenic D-antigen particle configuration, which is crucial for vaccine applications. Many research efforts have shifted from the BEVS to other production platforms, such as yeast², plants³, and mammalian cells⁴. All three systems have inherent limitations, including a lack of scalability and persistent risk associated with using mammalian cells in the production process. In this work, we were able to produce D-ag poliovirus-like particles on multiple occasions but were unable to reproduce those results consistently. Future endeavors should explore this opportunity further, and possible distinctions between successful and unsuccessful experiments may be identified.

The produced VLPs need to be evaluated for their ability to elicit an immune response and its extent. While animal studies are increasingly controversial, they remain necessary until animal-free testing becomes reliable and accepted by regulatory authorities. Efforts have been made to reduce the use of animal models in research, dating back to the 1950s and continuing to this day, known as the 3Rs (replace, reduce, and refine)^{5,6}. Substantial progress has been made to produce *in vitro* and *ex vivo* models that resemble human tissue and organs^{7,8}. Organ-on-chip models, which mimic human organs and tissues using microfluidic devices, are a relatively new but highly promising technology⁹⁻¹¹. Moreover, the body-on-chip methods, which combines multiple functional units of human organs, has also been proposed¹². Nevertheless, many of these technologies are still in the early stages of development, and it will take a considerable amount of time before they become applicable in clinical trials.

7.2 Cell culture maintenance

In **Chapter 2** of this dissertation, a novel approach to cell counting was presented using machine learning (ML) models. This methodology offers several advantages, as described in the chapter in detail, but still has limitations. The first major limitation of the presented method is that it still relies on the use of a dye to discriminate between alive and dead cells, which can be toxic to the cells. This raises the possibility of inaccurate determination of cell culture status over time. To address these concerns, various techniques are in development for the determination of cell fitness based on cell morphology¹³⁻¹⁵. Additionally, some techniques have been commercialized in the

form of software or annotated data sets for label-free cell segmentation^{16,17}. For insect cells, differentiation can be made between alive and dead cells based on for instance size and membrane integrity (granular cell edges). While morphology-based cell detection technologies have been developed for certain human cell lines such as HEK cells and cancerous cells, a dye-free detection method for insect cells is currently unavailable.

The second major limitation of the ML model, along with conventional and automated cell counters, is that sampling is still required, which is time-consuming and can potentially introduce contaminations. The determination of a cell culture's state by means of sampling and analysis is referred to as at-line (in a lab in proximity of the bioreactor) or off-line (analysis in a different laboratory, possibly a third party) sensing (Figure 7.1). In recent years, non-destructive techniques have been developed for real-time monitoring of cell concentration and viability in bioreactors using in-line (during the process) or on-line (at a branch in the process) sensing^{18–20} (Figure 7.1). ML implementation in conjunction with on-line measurements has been demonstrated using double differential digital holographic microscopy (D3HM), which measures the cell density, diameter, and circularity, but has yet to be commercialized^{21,22}. This methodology still exhibits errors of up to 25% in some measurements compared to off-line cell density determinations, requiring further optimization to ensure that on-line techniques can compete with off-line ones. However, once fully optimized, it is anticipated that in-line and on-line measurements will outcompete off-line measurements due to reduced process time, lower risk of contamination, lack of requirement for an operator, and overall cost reduction.

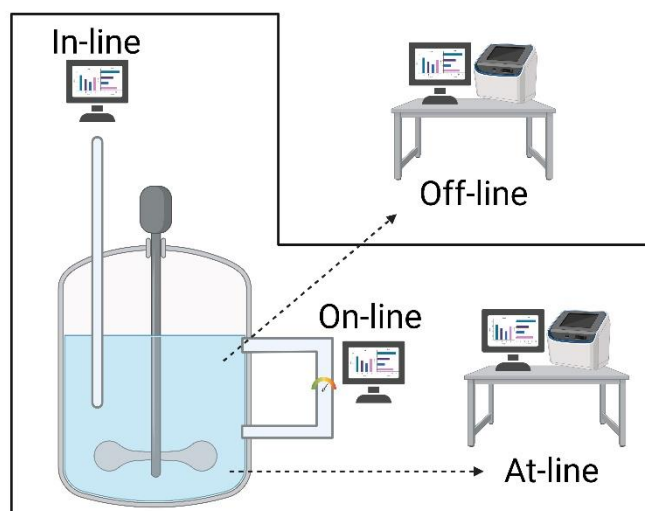


Figure 7.1. Schematic presentation of the different forms of cell culture monitoring.

In-line: measurement is directly taken in the process. On-line: measurement is taken at a branch of the process or through a bypass. At-line: sampling is required, and analysis is performed in a laboratory in proximity of the bioreactor (in-house). Off-line: sampling is required, and analysis is performed in a different laboratory (possibly with a third party).

7.3 Virus detection

The detection of viruses presents a significant challenge in virology research, primarily due to the limited availability of antibodies required for accurate quantification. Currently, the most common method for quantification, enzyme-linked immunosorbent assay (ELISA), requires costly, purified antibodies, mostly sourced from mice and rabbits. In addition, accurate quantification of viral proteins or capsid structures using ELISAs requires individual optimization studies of the assay, which is time-consuming and costly, and often not performed unless necessary. Commercially available antibodies are limited and mostly targeted at well-studied viruses, leaving many viruses understudied.

Enteroviruses are an example of viruses that have only limited commercially available antibodies. Until recently, only poliovirus antibodies were available. Antibodies for EV71 viruses and CVA viruses were added to the inventory subsequently. Moreover, as discussed in **Chapter 4**, viruses can assemble in various types of particles, including native virions, empty particles, procapsids, and uncoating intermediates, each of which could bind antibodies in different ways and with different affinities. Thus, the specificity and target of the antibodies must be considered in experimental design. Misuse of antibodies can lead to erroneous results, highlighting the need for optimization of antibodies for each type of particle^{23–25}.

Structural characterization of virions and VLPs is required to understand the binding of specific epitopes, structural regions, or antigens in general by antibodies to the cell. The interaction between cells and viruses can differ significantly between viruses in the same genus. Therefore, additional research towards cheaper and more accessible production of antibodies is required to advance virus research. One potential solution is the bioengineering of antibodies, where immunogenicity, binding affinity, specificity, and function of antibodies can be modified^{26,27}. While the engineering of antibodies for therapeutic applications is already advanced, with over a hundred FDA-approved engineered antibodies, this approach is still lacking for the detection of viral proteins in research²⁸.

A major challenge faced during the production and purification process, as described in **Chapter 3**, is the lack of a real-time readout of VLP production. While intermediate samples can be taken from the infected culture for analysis, a method for continuous monitoring of VLP production is lacking. Direct fluorescent antibodies (DFA) are a promising approach for this purpose, as they provide a direct observation for the presence of an antigen, unlike western blot and ELISA techniques²⁹. Developing a DFA-based method for monitoring VLP production could greatly improve the efficiency of VLP production and purification, by allowing for real-time adjustment to the process parameters. This would also reduce the need for costly and time-consuming optimization studies that are currently required for accurate quantification of viral protein production.

7.4 Stabilization studies

The AFM experiments described in **Chapter 4** are a prime example of how the technique can be employed to investigate viral particle stability and show discrepancies between particle origins. The stability of the most immunogenic configuration of enteroviruses is reliant on the presence of the pocket factor, a lipid molecule, in a region at the base of the canyon within VP1 (hydrophobic pocket)³⁰. Additionally, the conversion from the highly immunogenic state (D-antigen for PV; N-Ag for other enteroviruses) to the less immunogenic expanded state (C-antigen for PV; H-Ag for other enteroviruses) of these particles is linked with the dissociation of the pocket factor³¹⁻³³. If the hydrophobic pocket remains intact in VLPs, a variety of compounds (e.g., pleconaril) can be explored as potential stabilizers of the VLPs³⁴.

Additionally, **Chapter 4** demonstrated that the presence of P1 viral RNA (vRNA) alone is insufficient to stabilize the VLPs, as evidenced by the absence of two populations in the AFM experiments. To further investigate the stabilizing effects of RNA presence and the triggering mechanism of viral maturation, it could be attempted to insert the full genome into the VLPs. However, it should be noted that these experiments would only be useful for research purposes and may not be suitable for vaccine applications, as the absence of infective and replicative capsids in VLPs might be compromised by the presence of vRNA. Furthermore, it was shown that the full genome could potentially trigger viral maturation, which was not observed in our experimental set-up using only P1 vRNA. These findings highlight the importance of investigating the role of vRNA in stabilizing and maturing VLPs and its potential impact on VLP-based vaccines.

Other groups have demonstrated that the stability of VLPs can be improved by subjecting virions to random mutagenesis during cultivation at elevated temperatures, and reverse engineer these mutations in VLPs^{4,35-37}. This methodology has been successfully applied to poliovirus (PV) and enterovirus A71 (EV71) and could be adapted for other (enterovirus) VLPs. Although the improved stability is primarily thermostability, which can prevent the conversion from the N-ag to H-ag, it does not necessarily imply general enhanced stability. To date, no studies have investigated the differences in stability between the two immunogenic states. Although conducting such experiments will be challenging due to the difficulty of separating the two types of particles and the continuous conversion of N-Ag to H-Ag, it poses an additional research question that needs to be addressed.

7.5 Biophysics developments

The AFM experiments described in **Chapter 4** represent an important step towards understanding viral particle stability and differences between particle origins. However, this work could be extended by investigating different buffer and storage

conditions, supplementation with adjuvants for enhanced stability, and possibly introducing stabilizing mutations^{4,35,36}. Buffer conditions can significantly impact the stability of virus capsids, thus formulation conditions for the VLPs may play a critical role in determining the ultimate success of the vaccine. In this study, AFM experiments were performed in phosphate-buffered saline (PBS) to mimic physiological conditions as closely as possible. Since highly pure and concentrated samples of both EV71 and CVA6 were produced using the protocols presented in **Chapter 3**, formulation conditions could be tested relatively easily.

Moreover, it would be interesting to investigate the possibility of combining AFM with fluorescence measurements. During this dissertation work, it was discovered that the so-called “empty” VLPs are not actually empty and instead contain vRNA. EM analysis revealed that VP0 was not cleaved in the VLPs that contained RNA. Given that the only vRNA present in the experimental set-up was P1, this finding suggests that the presence of P1 alone may not be sufficient to initiate viral maturation. It is possible that additional genomic material is needed, which could encode specific viral proteins or contain a maturation-triggering signal. Alternatively, it is possible that P1 (and potentially the vRNA in general) may not be responsible for the viral maturation process at all, as this has not been definitively proven. By combining AFM and fluorescence measurements, it may be possible to assess whether the full genome is required for viral maturation, or whether shorter oligos or even just the presence of coding sequences for specific proteins would suffice. Additionally, direct observation of the vRNA during nanoindentation experiments could provide insight into the different types of particle disintegration and ultimately lead to a better understanding of the (bio)mechanical properties of the different particles.

Another potential avenue for AFM investigations is the study of VLP release from cells into the extracellular environment. The present study was unable to determine whether the VLPs were actively transported out of cells or simply released into the environment through cell lysis. High-speed AFM studies have demonstrated that virus release can be measured over time, and combining this technique with fluorescence microscopy could add more clarity³⁸. Investigating VLP release in this way could also provide information on the mechanisms involved, such as membrane-mediated exocytosis.

In the field of electron microscopy (EM), particularly cryogenic EM, there is ongoing rapid development. While cryo-EM data (pre-)processing can be performed in real-time, and recent advancements have improved the resolution of highly dynamic regions of the structure, such as the ability to generate trajectories to visualize molecular motions using deep learning, it remains a non-real-time technique^{39,40}. As a result, it is not possible to follow, for example, viral capsid assembly in real-time. Despite efforts to address these challenges, they may be inherent limitations to the technique. The cryo-EM research presented in this dissertation can be complemented

by investigations of vRNA packaging in both virions and VLPs. Characterizing specific intermediates may be challenging due to the similarities between particles and the rapid conversion of one state to the next. However, mutations and kinetic trapping can be employed to preserve specific assembly intermediates⁴¹⁻⁴³.

The approach detailed in **Chapter 5** provides a protocol for simultaneously probing the RNA synthesis dynamics of hundreds of single polymerases with MT. However, like all assays, this approach comes with its particular limitations, such as the inability to directly interrogate the RNA products of the RNA-dependent RNA polymerase (RdRp) produced in the magnetic tweezers (MT). To supplement the approach, sequencing data originating from the MT could be considered in follow-up experiments, which would provide more compelling evidence compared to using sequence data from separate experiments. It is important to acknowledge that matching the RNA product obtained from the MT to the sequenced product for the MT can be challenging. This is since there may be thousands of RNA products present in the outflow. Furthermore, fluorescence could be added to the MT to allow for direct observation of the RdRp on the RNA. This add-on could be employed for the direct observation of the RdRp template-switching and discrimination between RdRp-containing and RdRp-lacking RNA constructs, enabling a more accurate determination of the assay's efficiency. Based on the highly similar dwell time distributions between the forward traces and the reversals, which originated from the transcription of the newly synthesized RNA strand through means of copy-back synthesis, we have concluded that the observed activity was derived from a single polymerase working in both directions (see **Chapter 6**). However, other work suggests an alternative explanation, in which a second polymerase grabs the 3' end of the newly synthesized RNA, extruding from the RdRp after a backtracking event, and initiates transcription⁴⁴. The use of combined MT and fluorescence could provide direct observation of the number of polymerases present while replicating and, in turn, a definitive answer as to which mechanism is apparent. This combination of techniques has already been employed in highly diverse fields of research⁴⁵⁻⁴⁷.

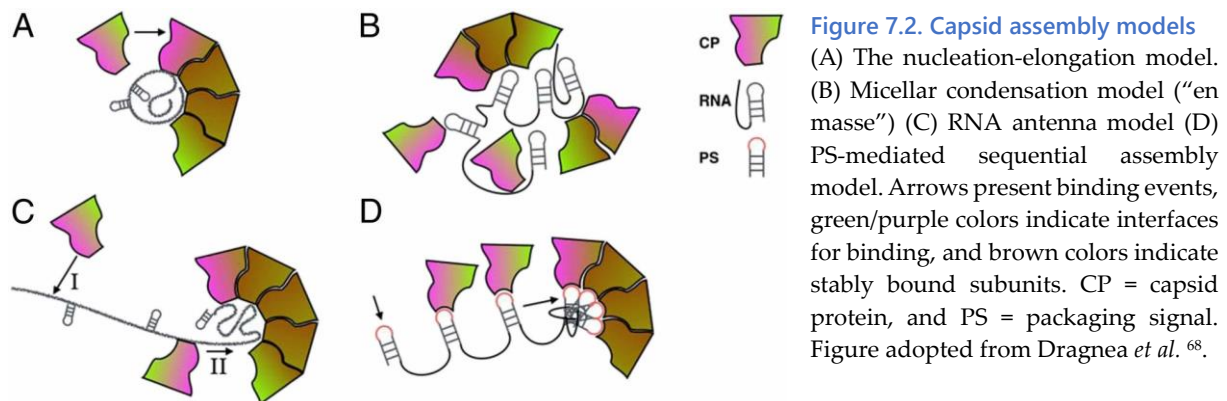
Chapter 6 revealed that the stochastic pausing of the RdRp triggers copy-back synthesis and recombination events. Since the pausing behavior is unique and differentiates significantly between the different polymerases, copy-back synthesis and recombination probabilities can be investigated for polymerases of other viruses. This would be especially interesting with polymerases having a significantly higher or lower pausing probabilities than the enterovirus RdRp to identify correlations. In opposition to previous reported work, our data suggests that the instability of the RdRp on RNA, rather than the RNA sequence, enables template switching. To this further, these specific copy-back sequences could be introduced into the RNA constructs⁴⁸. Also, constructs containing G-C rich sequences, which should make it harder for the RdRp to melt, could contribute to increased pausing, instability and therefore template switching. Additionally, other triggers for recombination, such as

secondary structures or mismatched base pairing could be investigated⁴⁹. Lastly, temperature sensitivity could be explored as recent studies suggest that the elongation and pause dynamics of the PV RdRp change at elevated temperature, although viruses from different origins were differently affected⁵⁰.

Outside of the scope of this project, there is a current and widely discussed topic in the field of (entero)virology regarding the dynamics of capsid assembly. As outlined in previously published work and partly discussed in **Chapter 4**, there are two major hypotheses for the describing viral particle assembly^{51,52}. The first hypothesis suggests that the viral capsid is assembled first, with the RNA entering the capsid at one of the final stages of viral morphogenesis. This hypothesis is supported by evidence showing that the procapsid remains in an expanded state, possibly providing enough room for the RNA to enter the capsid, although for some enteroviruses this opening was determined to be too small. Those viruses expel capsid pentamers to provide an opening large enough for enough release, which possibly indicates a reverse process for assembly⁵³. Additionally, in the process of viral maturation, the VP0 protein gets cleaved in the last stage of viral maturation, rearranging the viral capsid proteins significantly and hypothesized to be regulated by RNA presence⁵⁴⁻⁵⁶. Viral maturation is a critical process in the assembly of enterovirus assembly and has significant effects on the infectivity of the virus^{54,57}. Furthermore, the ability of VLPs to assemble in absence of RNA supports this argument. The second hypothesis suggests that the RNA/DNA serves as a scaffold for the viral capsid proteins, or even more critically, is involved in recruiting them^{43,58-61} (**Figure 7.2**). It is also possible that both scenarios occur simultaneously and represent two distinct pathways of viral assembly, depending on environmental factors such as pH and ionic strength⁶². An example of this duality is the experimental work with VLPs, which indicated that viral capsid proteins can, in addition to forming empty particles in the absence of DNA, condense DNA in optical traps⁶³. Due to the absence of comparable experimental data on enteroviruses and only the initial identification of RNA-capsid interaction regions, it would be advantageous to perform analogous experiments using capsid precursors in the form of protomers or pentamers^{32,33,64}. It would be interesting to investigate different parts of the enterovirus genome, to possibly identify a compaction-triggering sequence, similar to what has been observed in HIV⁶⁵. Furthermore, the observation in **Chapter 4** of both RNA-filled and empty capsids contributes to the hypothesis that the capsid is assembled first, and the RNA comes in at a later stage. Alternatively, it could also be that the P1 region is insufficient to function as a scaffold and RNA assembly requires longer oligos for one of the mechanisms proposed below or there are indeed two distinct pathways for assembly that occur simultaneously.

There are many proposed mechanisms for capsid assembly around the genome. The nucleation-elongation model (**Figure 7.2A**) describes a scenario in which the genome is condensed prior to recruiting capsid proteins. The assembly is driven by the interaction between the negatively charged genome and the positively charged capsid

protein. A second possibility is the “en masse” model, whereby low ionic strength and weak subunit-subunit interactions lead to assembly through disordered intermediates, or through the nucleation-and-growth model, in which a particle is formed through sequential addition of subunits on a polymer⁵⁸ (Figure 7.2B). The antenna model (Figure 7.2C), in which the RNA acts as a searcher and recruiter of viral proteins^{66,67}. In the PS-mediated model, capsid proteins are added one by one, and with the capsid proteins have specific affinity for packaging sequences in the viral genome⁶⁰ (Figure 7.2D). Anew, fluorescence experiments in combination with MT could provide answers on which model is preferred for each virus. However, experiments involving nucleic acids bound on both ends, such as MT, acoustic force and optical trap experiments, may limit the investigation of this proposed mechanism. Instead, flow stretch experiments with a singular tethered end of the nucleic acid combined with fluorescence microscopy may provide a solution.



7.6 Final remarks

Looking back at the original goals of the project and the final product in the form of this dissertation, it can be concluded that many of the goals were achieved. Although the research shifted towards different viruses than originally foreseen, we succeeded in producing, purifying, and biophysically characterizing enterovirus-like particles from various virus origins. Along the way, we established protocols for these three stages and published two of them, which can serve as a foundation for future research, either at Intravacc or in other laboratories interested in expanding on our work. The renewed interest in vaccine research following the COVID-19 pandemic, has contributed greatly to the advancement of vaccinology research fields. Despite the frequent emergence of new infectious agents, we are often unprepared for their impact. Therefore, we should continue to invest in vaccine research to not only prevent future pandemics, disease, death, and suffering, but also acquire a fundamental understanding of these continuously evolving biological threats and protect against the danger they pose to human survival.

7.7 References

1. Xu L, Zheng Q, Li S, et al. Atomic structures of Coxsackievirus A6 and its complex with a neutralizing antibody. *Nat Commun.* 2017;8(1):1-12. doi:10.1038/s41467-017-00477-9
2. Sherry L, Grehan K, Snowden JS, et al. Comparative Molecular Biology Approaches for the Production of Poliovirus Virus-Like Particles Using *Pichia pastoris*. *mSphere.* 2020;5(2). doi:10.1128/msphere.00838-19
3. Marsian J, Fox H, Bahar MW, et al. Plant-made polio type 3 stabilized VLPs-A candidate synthetic polio vaccine. *Nat Commun.* 2017;8(1). doi:10.1038/s41467-017-00090-w
4. Bahar MW, Porta C, Fox H, Macadam AJ, Fry EE, Stuart DI. Mammalian expression of virus-like particles as a proof of principle for next generation polio vaccines. *npj Vaccines.* Published online 2021. doi:10.1038/s41541-020-00267-3
5. The Principles of Humane Experimental Technique. *Med J Aust.* 1960;1(13). doi:10.5694/j.1326-5377.1960.tb73127.x
6. Kirk RGW. Recovering The Principles of Humane Experimental Technique. *Sci Technol Hum Values.* 2018;43(4). doi:10.1177/0162243917726579
7. Wagar LE, Salahudeen A, Constantz CM, et al. Modeling human adaptive immune responses with tonsil organoids. *Nat Med.* 2021;27(1). doi:10.1038/s41591-020-01145-0
8. Marrazzo P, Maccari S, Taddei A, et al. 3D reconstruction of the human airway mucosa in vitro as an experimental model to study NTHi infections. *PLoS One.* 2016;11(4). doi:10.1371/journal.pone.0153985
9. Shanti A, Hallfors N, Petroianu GA, Planelles L, Stefanini C. Lymph Nodes-On-Chip: Promising Immune Platforms for Pharmacological and Toxicological Applications. *Front Pharmacol.* 2021;12. doi:10.3389/fphar.2021.711307
10. Kiener M, Roldan N, Machahua C, et al. Human-Based Advanced in vitro Approaches to Investigate Lung Fibrosis and Pulmonary Effects of COVID-19. *Front Med.* 2021;8. doi:10.3389/fmed.2021.644678
11. Tang H, Abouleila Y, Si L, et al. Human Organs-on-Chips for Virology. *Trends Microbiol.* 2020;28(11). doi:10.1016/j.tim.2020.06.005
12. Wu Q, Liu J, Wang X, et al. Organ-on-a-chip: Recent breakthroughs and future prospects. *Biomed Eng Online.* 2020;19(1). doi:10.1186/s12938-020-0752-0
13. Yu WH, Li CH, Wang RC, Yeh CY, Chuang SS. Machine learning based on morphological features enables classification of primary intestinal t-cell lymphomas. *Cancers (Basel).* 2021;13(21). doi:10.3390/cancers13215463
14. Lan Y, Huang N, Fu Y, et al. Morphology-Based Deep Learning Approach for Predicting Osteogenic Differentiation. *Front Bioeng Biotechnol.* 2022;9(January):1-13. doi:10.3389/fbioe.2021.802794
15. Yao K, Rochman ND, Sun SX. Cell Type Classification and Unsupervised Morphological Phenotyping From Low-Resolution Images Using Deep Learning. *Sci Rep.* 2019;9(1):1-

13. doi:10.1038/s41598-019-50010-9
16. Lovell GF, Porto DA, Jackson TR, et al. Abstract 1305: Classification of cell morphology using machine learning and label-free live-cell imaging. *Cancer Res.* 2021;81(13_Supplement):1305-1305. doi:10.1158/1538-7445.am2021-1305
17. Edlund C, Jackson TR, Khalid N, et al. LIVECell—A large-scale dataset for label-free live cell segmentation. *Nat Methods.* 2021;18(9):1038-1045. doi:10.1038/s41592-021-01249-6
18. Lourenço ND, Lopes JA, Almeida CF, Sarraguça MC, Pinheiro HM. Bioreactor monitoring with spectroscopy and chemometrics: A review. *Anal Bioanal Chem.* 2012;404(4). doi:10.1007/s00216-012-6073-9
19. Akbari S, Anderson P, Zang H, et al. Non-invasive real-time monitoring of cell concentration and viability using Doppler ultrasound. *SLAS Technol.* 2022;27(6):368-375. doi:10.1016/j.slant.2022.09.003
20. Rösner LS, Walter F, Ude C, John GT, Beutel S. Sensors and Techniques for On-Line Determination of Cell Viability in Bioprocess Monitoring. *Bioengineering.* 2022;9(12):1-25. doi:10.3390/bioengineering9120762
21. Pais DAM, Galvão PRS, Kryzhanska A, Barbau J, Isidro IA, Alves PM. Holographic imaging of insect cell cultures: Online non-invasive monitoring of adeno-associated virus production and cell concentration. *Processes.* 2020;8(4). doi:10.3390/PR8040487
22. Altenburg JJ, Klaverdijk M, Cabosart D, et al. Real-time online monitoring of insect cell proliferation and baculovirus infection using digital differential holographic microscopy and machine learning. *Biotechnol Prog.* 2022;(December):1-10. doi:10.1002/btpr.3318
23. ten Have R, Thomassen YE, Hamzink MRJ, et al. Development of a fast ELISA for quantifying polio D-antigen in in-process samples. *Biologicals.* Published online 2012. doi:10.1016/j.biologicals.2011.11.004
24. Kingston NJ, Grehan K, Snowden JS, et al. Development of an Enzyme-Linked Immunosorbent Assay for Detection of the Native Conformation of Enterovirus A71. *mSphere.* 2022;7(3). doi:10.1128/msphere.00088-22
25. Lim PY, Cardoso MJ. Development of a sandwich ELISA to detect virus-like-particles in enterovirus A71 vaccines. *J Virol Methods.* 2019;270(April 2018):113-119. doi:10.1016/j.jviromet.2019.05.005
26. Lo KM, Leger O, Hock B. Antibody engineering. *Antibodies Infect Dis.* Published online 2015:319-343. doi:10.1128/9781555817411.ch19
27. Jain M, Kamal N, Batra SK. Engineering antibodies for clinical applications. *Trends Biotechnol.* 2007;25(7):307-316. doi:10.1016/j.tibtech.2007.05.001
28. Mullard A. FDA approves 100th monoclonal antibody product. *Nat Rev Drug Discov.* 2021;20(7). doi:10.1038/d41573-021-00079-7

29. Abbas AK, Lichtman AH, Pillai S, Baker DL. *Chapter 5: Antibodies and Antigens*. Vol 1.; 2010.
30. Filman DJ, Syed R, Chow M, Macadam AJ, Minor PD, Hogle JM. Structural factors that control conformational transitions and serotype specificity in type 3 poliovirus. *EMBO J*. 1989;8(5). doi:10.1002/j.1460-2075.1989.tb03541.x
31. Plevka P, Perera R, Cardoso J, Kuhn RJ, Rossmann MG. Crystal structure of human enterovirus 71. *Science (80-)*. 2012;336(6086). doi:10.1126/science.1218713
32. Büttner CR, Spurný R, Füzik T, Plevka P. Cryo-electron microscopy and image classification reveal the existence and structure of the coxsackievirus A6 virion. *Commun Biol*. 2022;5(1). doi:10.1038/s42003-022-03863-2
33. Füzik T, Moravcová J, Kalynych S, Plevka P. Structure of Human Enterovirus 70 and Its Inhibition by Capsid-Binding Compounds. *J Virol*. 2022;96(17). doi:10.1128/jvi.00604-22
34. Pevear DC, Tull TM, Seipel ME, Groarke JM. Activity of pleconaril against enteroviruses. *Antimicrob Agents Chemother*. Published online 1999.
35. Fox H, Knowlson S, Minor PD, Macadam AJ. Genetically Thermo-Stabilised, Immunogenic Poliovirus Empty Capsids; a Strategy for Non-replicating Vaccines. *PLoS Pathog*. Published online 2017. doi:10.1371/journal.ppat.1006117
36. Kingston N, Snowden J, Martyna A, et al. Production of antigenically stable enterovirus A71 virus-like particles in *Pichia pastoris* as vaccine candidate. 2023;57(6):1166-1177. doi:10.15389/agrobiology.2022.6.1166rus
37. Kingston NJ, Shegdar M, Snowden JS, et al. Thermal stabilization of enterovirus A 71 and production of antigenically stabilized empty capsids. *J Gen Virol*. 2022;103(8):1-11. doi:10.1099/jgv.0.001771
38. Harel S, Altaras Y, Nachmias D, et al. Analysis of individual HIV-1 budding event using fast AFM reveals a multiplexed role for VPS4. *Biophys J*. 2022;121(21):4229-4238. doi:10.1016/j.bpj.2022.08.035
39. Tegunov D, Cramer P. Real-time cryo-electron microscopy data preprocessing with Warp. *Nat Methods*. 2019;16(11). doi:10.1038/s41592-019-0580-y
40. Zhong ED, Bepler T, Berger B, Davis JH. CryoDRGN: reconstruction of heterogeneous cryo-EM structures using neural networks. *Nat Methods*. 2021;18(2). doi:10.1038/s41592-020-01049-4
41. Nakamichi Y, Miyazaki N, Tsutsumi K, et al. An Assembly Intermediate Structure of Rice Dwarf Virus Reveals a Hierarchical Outer Capsid Shell Assembly Mechanism. *Structure*. 2019;27(3). doi:10.1016/j.str.2018.10.029
42. Katen SP, Chirapu SR, Finn MG, Zlotnick A. Trapping of Hepatitis B Virus Capsid Assembly Intermediates by Phenylpropenamide Assembly Accelerators. *ACS Chem Biol*. 2010;5(12). doi:10.1021/cb100275b
43. Bruinsma RF, Wuite GJL, Roos WH. Physics of viral dynamics. *Nat Rev Phys*.

- 2021;3(2):76-91. doi:10.1038/s42254-020-00267-1
44. Dulin D, Vilfan ID, Berghuis BA, Poranen MM, Depken M, Dekker NH. Backtracking behavior in viral RNA-dependent RNA polymerase provides the basis for a second initiation site. *Nucleic Acids Res.* 2015;43(21):10421-10429. doi:10.1093/nar/gkv1098
 45. Guo Q, He Y, Lu HP. Interrogating the activities of conformational deformed enzyme by single-molecule fluorescence magnetic tweezers microscopy. *Proc Natl Acad Sci U S A.* 2015;112(45):13904-13909. doi:10.1073/pnas.1506405112
 46. Sarkar R, Rybenkov V V. A guide to magnetic tweezers and their applications. *Front Phys.* 2016;4(DEC). doi:10.3389/fphy.2016.00048
 47. Long X, Parks JW, Bagshaw CR, Stone MD. Mechanical unfolding of human telomere G-quadruplex DNA probed by integrated fluorescence and magnetic tweezers spectroscopy. *Nucleic Acids Res.* 2013;41(4):2746-2755. doi:10.1093/nar/gks1341
 48. Sun Y, Kim EJ, Felt SA, et al. A specific sequence in the genome of respiratory syncytial virus regulates the generation of copy-back defective viral genomes. *PLoS Pathog.* 2019;15(10):1-20. doi:10.1371/journal.ppat.1008099
 49. Bera SC, Seifert M, Kirchdoerfer RN, et al. The nucleotide addition cycle of the SARS-CoV-2 polymerase. *Cell Rep.* 2021;36(9). doi:10.1016/j.celrep.2021.109650
 50. Seifert M, Nies P Van, Papini S, et al. Temperature controlled high-throughput magnetic tweezers show striking difference in activation energies of replicating viral RNA-dependent RNA polymerases. 2020;48(10):5591-5602. doi:10.1093/nar/gkaa233
 51. Jiang P, Liu Y, Ma H-C, Paul A V., Wimmer E. Picornavirus Morphogenesis. *Microbiol Mol Biol Rev.* Published online 2014. doi:10.1128/MMBR.00012-14
 52. Hellen CUT, Wimmer E. Enterovirus Structure and Assembly. In: *Human Enterovirus Infections.* ; 2014. doi:10.1128/9781555818326.ch7
 53. Buchta D, Füzik T, Hrebík D, et al. Enterovirus particles expel capsid pentamers to enable genome release. *Nat Commun.* 2019;10(1). doi:10.1038/s41467-019-09132-x
 54. Cao J, Liu H, Qu M, et al. Determination of the cleavage site of enterovirus 71 VP0 and the effect of this cleavage on viral infectivity and assembly. *Microb Pathog.* 2019;134(June):103568. doi:10.1016/j.micpath.2019.103568
 55. Logan G, Newman J, Wright CF, et al. Deep Sequencing of Foot-and-Mouth Disease Virus Reveals RNA Sequences Involved in Genome Packaging. *J Virol.* 2018;92(1). doi:10.1128/jvi.01159-17
 56. Arnold E, Luo M, Vriend G, et al. Implications of the picornavirus capsid structure for polyprotein processing. *Proc Natl Acad Sci U S A.* 1987;84(1). doi:10.1073/pnas.84.1.21
 57. Ansardi DC, Morrow CD. Amino acid substitutions in the poliovirus maturation cleavage site affect assembly and result in accumulation of provirions. *J Virol.* 1995;69(3). doi:10.1128/jvi.69.3.1540-1547.1995

58. Perlmutter JD, Hagan MF. Mechanisms of virus assembly. *Annu Rev Phys Chem.* 2015;66(1):217-239. doi:10.1146/annurev-physchem-040214-121637
59. McPherson A. Micelle formation and crystallization as paradigms for virus assembly. *BioEssays.* 2005;27(4). doi:10.1002/bies.20196
60. Rolfsson Ó, Middleton S, Manfield IW, et al. Direct Evidence for Packaging Signal-Mediated Assembly of Bacteriophage MS2. *J Mol Biol.* 2016;428(2):431-448. doi:10.1016/j.jmb.2015.11.014
61. Hu T, Shklovskii BI. Kinetics of viral self-assembly: Role of the single-stranded RNA antenna. *Phys Rev E - Stat Nonlinear, Soft Matter Phys.* 2007;75(5). doi:10.1103/PhysRevE.75.051901
62. Klug A. The tobacco mosaic virus particle: structure and assembly. *Phil Trans R Soc Lond B.* 1999;(354):1-6. papers2://publication/uuid/85019DC5-FA2B-4D81-A1EE-B07967F4E68E
63. Marchetti M, Kamsma D, Cazares Vargas E, et al. Real-Time Assembly of Viruslike Nucleocapsids Elucidated at the Single-Particle Level. *Nano Lett.* Published online 2019. doi:10.1021/acs.nanolett.9b02376
64. Chandler-Bostock R, Mata CP, Bingham RJ, et al. Assembly of infectious enteroviruses depends on multiple, conserved genomic RNA-coat protein contacts. *PLoS Pathog.* 2020;16(12):1-23. doi:10.1371/journal.ppat.1009146
65. Ding P, Kharytonchyk S, Waller A, et al. Identification of the initial nucleocapsid recognition element in the HIV-1 RNA packaging signal. *Proc Natl Acad Sci U S A.* 2020;117(30). doi:10.1073/pnas.2008519117
66. Van Rosmalen MGM, Kamsma D, Biebricher AS, et al. Revealing in real-time a multistep assembly mechanism for SV40 virus-like particles. *Sci Adv.* 2020;6(16). doi:10.1126/sciadv.aaz1639
67. Garmann RF, Goldfain AM, Manoharan VN. Measurements of the self-assembly kinetics of individual viral capsids around their RNA genome. *Proc Natl Acad Sci U S A.* 2019;116(45). doi:10.1073/pnas.1909223116
68. Dragnea B. Watching a virus grow. *Proc Natl Acad Sci U S A.* 2019;116(45):22420-22422. doi:10.1073/pnas.1915986116

Summary

Vaccination is the most effective strategy in humanity's fight against viruses. The concept of vaccination was first proposed by Dr. Edward Jenner in the 18th Century, and its efficacy has been proven over time, providing unparalleled protection against viral infections. Large-scale vaccination campaigns have been successful in eradicating diseases such as smallpox in 1980. In recent times, the coronavirus pandemic has brought vaccines to the forefront of public, academic, and industry interest.

Apart from conventional live vaccines, which were originally designed and employed by Jenner, there has been a significant expansion in vaccine types, including mRNA, viral vector, attenuated, and inactivated vaccines, each with their own advantages and limitations. Furthermore, virus-like particles (VLPs), a novel class of vaccines, have emerged as a promising alternative to traditional vaccine design strategies, potentially offering improved efficacy and safety. VLPs are multimeric nanoparticles derived from one or more viral structures. They are typically empty or devoid of genetic material, rendering them non-replicative and non-infectious. Despite the proposed absence of genetic material, VLPs possess immune-inducing surface patterns resembling those of the native virus, making them recognizable to the immune system. This unique feature can be exploited for vaccine purposes. VLP-based vaccines offer a safer alternative to traditional vaccines and present an opportunity to create vaccines against viruses that recognize specific viral surface structures instead of a single protein. Large-scale production of VLPs can potentially mitigate many of the drawbacks of current vaccines, such as extreme storage conditions (mRNA), vector immunity (vector), reversion (attenuated), and high production costs (inactivated). Therefore, VLP-based vaccines hold great promise in the fight against viral infection, by providing a safer and superior product.

The safety and efficacy of VLP-based vaccines have been established through extensive research. At present, the market has numerous VLP vaccines available, with HPV VLP vaccines being the most prominent. Its success has set the standard and paved the way for the development of other VLP-based vaccines.

In this work, we demonstrated the feasibility of producing and purifying virus-like particles that closely resemble enterovirus A71 (EV71) and coxsackievirus A6 (CVA6). Both viruses have a positive sense RNA genome of ~7.4 kilobase pairs (kbp), which encodes a 260 kDa polyprotein that is stepwise cleaved into eleven viral proteins. Enteroviruses, and most prominently EV71 and CVA6, are the main causative agents of hand, foot, and mouth disease (HFMD). HFMD is named after the characteristic

lesions that develop on the hands, feet, mouth, and buttocks of infected individuals. In severe cases, especially among children, the disease can spread to the central nervous system (CNS), resulting in complications such as aseptic meningitis and encephalitis. By employing VLPs, a multivalent vaccine can be developed to target multiple viral strains simultaneously, providing an opportunity for the prevention and control of HFMD.

We utilized the baculovirus expression vector system (BEVS) to produce the enterovirus-like particles. For the insect cell lines employed in the BEVS, cell counting is crucial for the maintenance and manipulation of cell cultures. It is a vital aspect of assessing cell viability and determining proliferation rates, which are critical to maintaining the health and functionality of the culture. In **Chapter 2**, we introduce a machine learning (ML) model based on YOLOv4, capable of performing cell counts with high accuracy (>95%) for Trypan blue-stained insect cells. The model was trained, validated, and tested using images of two distinctly different insect cell lines, *Trichoplusia ni* (High Five™; Hi5 cells) and *Spodoptera frugiperda* (Sf9). The model achieved *F1* scores of 0.97 and 0.96 for alive and dead cells respectively, demonstrating substantially improved performance over other cell counters. Furthermore, the ML model is versatile, as an *F1* score of 0.96 was also obtained on images of Trypan blue-stained human embryonic kidney (HEK) cells that the model had not been trained on. Our implementation of the ML model comes with a straightforward user interface and can image in batches, which makes it highly suitable for the evaluation of multiple parallel cultures (e.g., in Design of Experiments). Overall, this approach for accurate classification of cells provides a fast, bias-free alternative to manual counting.

Previous studies have shown that the expression of the viral P1 structural proteins and the 3CD protease is sufficient to produce enterovirus-like particles in various organisms. However, there has been a lack of optimization based on the interplay between the three most commonly altered infection parameters, namely multiplicity of infection (MOI), viable cell density at the time of infection (VCD), and the infection period (t_{inf}). In **Chapter 3** we addressed this point by using Design of Experiments (DoE) to optimize the production of both EV71 and CVA6 VLPs. Our results indicated distinctively different preferences for infection parameters between the two types of VLPs, with EV71 VLP production preferring low MOI, low VCD, and long infection period, while CVA6 VLP production preferring for high MOI, high VCD and long infection period. Additionally, we developed a purification process for both VLPs, resulting in yields of 158 mg/l and 38 ml/l of culture volume for purified EV71 and CVA6 VLPs, respectively. These concentrations translate into thousands to tens of thousands of vaccines, highlighting the economic potential of enterovirus-like particles for vaccine purposes.

Virus-like particles have been identified as a promising approach for the development of a multivalent vaccine. However, their stability is a major issue due to the

significantly lower particle integrity lifetimes compared to inactivated vaccines. In **Chapter 4**, the VLPs produced using the optimized protocols described in **Chapter 3** were subjected to biophysical characterization. We employed multiple biophysical techniques such as transmission electron microscopy and atomic force microscopy, to elucidate the origins of the reduced VLP stability (on average 1.5-2-fold lower) in comparison to native virions. Contrary to previous work on enterovirus VLPs, this study demonstrates that a substantial portion (31%) of the produced VLPs were able to encapsidate viral RNA (vRNA). Additionally, this work shows that the presence of vRNA in the capsids may not be the primary factor in enterovirus capsid stability. Furthermore, vRNA may not be the sole factor responsible for triggering the stabilizing viral maturation, and other underlying mechanisms may be at play. To achieve stability comparable to that of virions, artificial methods of inducing viral maturation or alternative means of stabilizing the capsids are of the utmost important to ensure success of VLPs as vaccine candidates.

In **Chapter 5**, we present a protocol for the simultaneous investigation of RNA synthesis dynamics of hundreds of single polymerases with magnetic tweezers (MT). The protocol encompasses the entire process, starting from RNA construct preparation to quantitative and statistical analysis of the MT measurements of RNA synthesis kinetics. The protocol enables the measurement of hundreds of RNA tethers simultaneously, resulting in the characterization of single-molecule dynamics, which is presented in the subsequent chapter.

Chapter 6 of this dissertation showcases the potential of magnetic tweezers (MT) for the detailed mechanistic characterization of the viral RNA-dependent RNA polymerase (RdRp). By examining the pause dynamics and probabilities of each viral polymerase, we were able to decipher their individual mechanistic properties. In particular, we investigated the effects of the T-1106 triphosphate, a pyrazine-carboxamide ribonucleotide with antiviral properties, on the enterovirus A71 RdRp. Our result indicated that T-1106 incorporation into nascent RNA led to increased pauses and backtracking by the RdRp. Additionally, we identified the backtracked state as an intermediate used by the RdRp for copy-back RNA synthesis and homologous recombination, suggesting that pyrazine-carboxamide ribonucleotides function by promoting template switching and formation of defective genomes. Finally, we demonstrated that MT can scan promising antiviral candidates and indicate the most propitious ones for further development. The detailed mechanistic characterization of viral RdRp dynamics afforded by MT is a promising avenue for identifying and optimizing antiviral therapeutics.

Chapter 7 of this dissertation provides concluding remarks and aims to illuminate potential avenues for subsequent studies. This work can serve as a basis for future investigations, not only from a biophysical perspective but also from a biochemical standpoint.

Samenvatting

Tot op heden is vaccinatie de meest effectieve strategie in de strijd van de mensheid tegen virussen. Het concept van vaccinatie werd voor het eerst voorgesteld door dr. Edward Jenner in de 18^e eeuw en de werkzaamheid ervan is in de loop der tijd bewezen, waarbij ongeëvenaarde bescherming tegen virale infecties wordt geboden. Grootschalige vaccinatiedcampagnes hebben met succes pokken uitgeroeid in 1980. Recenter heeft de coronaviruspandemie vaccins op de voorgrond van de publieke, academische, en industriële aandacht gebracht.

Naast conventionele vaccins met volledig functionerend levend virus, zoals oorspronkelijk bedacht en toegepast door Jenner, is er een significante uitbreiding van vaccintypen geweest, waaronder mRNA, virale vector, verzwakte, en geïnactiveerde vaccins, elk met hun eigen voordelen en beperkingen. Daaropvolgend zijn “virus-like partikels” (VLPs), een nieuwe klasse van vaccins, naar voren gekomen als een veelbelovend alternatief voor traditionele vaccinontwerpen. Ze bieden mogelijk een verbeterde werkzaamheid en veiligheid. VLPs zijn nanopartikels opgebouwd uit herhalingen van één of meerdere virale eiwitten. De aanname is dat ze leeg zijn of ten minste geen genetisch materiaal bevatten, waardoor ze niet kunnen repliceren, noch infectieus zijn. Ondanks de afwezigheid van genetisch materiaal hebben VLPs immuunrespons-inducerende oppervlaktepatronen die lijken op die van het oorspronkelijke virus, waardoor ze herkend kunnen worden door het immuunsysteem. Deze unieke eigenschap kan worden geëxploiteerd voor vaccindoeleinden, dit geldt vooral voor vaccins tegen virussen waarvan de virale oppervlaktegeometrie en structuur wordt herkend door het immuunsysteem in plaats van een enkel eiwit. Grootschalige productie van VLP vaccines kan mogelijk veel van de nadelen van huidige vaccins wegnemen of significant verminderen, zoals extreme opslagcondities (mRNA), vectorimmunitet (virale vector), terug muteren naar actief infectieus virus (verzwakt) en hoge productiekosten (geïnactiveerd). Derhalve bieden VLP vaccins een veelbelovend perspectief in de strijd tegen virale infecties, en zijn het mogelijk veiligere en superieure vaccins.

De veiligheid en werkzaamheid van VLP vaccins zijn vastgesteld door uitgebreid onderzoek. Momenteel zijn er talloze VLP vaccins op de markt, waarbij HPV VLP vaccins het meest prominent zijn. Het succes van deze vaccins heeft de standaard gezet en de weg geëffend voor de ontwikkeling van toekomstige VLP vaccins.

In dit proefschrift hebben we de haalbaarheid getest van de productie en zuivering van VLPs die zijn afgeleid van twee virussen: enterovirus A71 (EV71) en coxsackievirus

A6 (CVA6). Beide virussen hebben een RNA-genoom van ongeveer 7.4 kilobasenparen (kp), dat codeert voor een 260 kDa polyproteïne dat sequentieel wordt geknipt in elf virale eiwitten. Enterovirussen, en met name EV71 en CVA6, zijn de belangrijkste aanstichters van hand-voet-mondziekte (HVMZ). HVMZ is vernoemd naar de karakteristieke laesies die zich ontwikkelen op de handen, voeten, mond en billen van geïnfecteerde personen. In ernstige gevallen, vooral bij kinderen, kan de ziekte zich verspreiden naar het centrale zenuwstelsel (CZS), resulterend in complicaties zoals aseptische meningitis en encefalitis. Door gebruik te maken van VLPs kan een multivalent vaccin worden ontwikkeld dat zich op meerdere virale stammen tegelijk richt, waardoor er mogelijkheden ontstaan voor de preventie en controle van HVMZ.

Om de “enterovirus-like partikels” te ontwikkelen hebben we gebruik gemaakt van het baculovirus expressie vector systeem (BEVS). Voor het onderhoud en de manipulatie van insectenculturen, die worden gebruikt in de BEVS, is celtelling essentieel. Het is een cruciaal aspect bij het beoordelen van cel vitaliteit en het bepalen van proliferatiesnelheden, die kritisch zijn voor het behoud van de gezondheid en functionaliteit van de cultuur. In **Hoofdstuk 2** introduceren we een “machine learning” (ML) model gebaseerd op YOLOv4, dat in staat is om celtellingen uit te voeren met hoge nauwkeurigheid (>95%) voor Trypan blauw-gekleurde insectencellen. Het model is getraind, gevalideerd en getest met behulp van afbeeldingen van verschillende insect celtypen: *Trichoplusia ni* (High Five™; Hi5) and *Spodoptera frugiperda* (Sf9). Het model behaalde *F1* scores 0.97 en 0.96 voor respectievelijk levende en dode cellen, wat aanzienlijk betere prestaties zijn dan andere celtelmethodes. Bovendien is het ML-model veelzijdig, zoals geïllustreerd werd door een *F1* score van 0.96 voor Trypan blauw-gekleurde humane embryonale nier (HEK) cellen waarop het model niet was getraind. Naast het ML-model is een gebruiksvriendelijke applicatie ontworpen, die afbeeldingen in grote partijen kan analyseren, wat het model zeer geschikt maakt voor evaluatie van meerdere parallelle culturen (bijvoorbeeld gedurende “Design of Experiments”). Deze methode biedt een nauwkeurige classificatie van cellen en een sneller en onbevooroordeeld alternatief voor handmatige celtellingen.

Eerdere studies hebben aangetoond dat de expressie van de virale P1-structurele eiwitten en de 3CD protease voldoende is om “enterovirus-like partikels” te produceren in verschillende organismen. Echter is er een gebrek aan optimalisatie op basis van de wisselwerking tussen de drie meest aangepaste infectieparameters: veelheid van infectie (MOI), levende celdichtheid op het moment van infectie (VCD), en de infectieperiode (t_{inf}). In **Hoofdstuk 3** hebben we dit punt aangepakt door gebruikt te maken van “Design of Experiments” (DoE) om de productie van zowel EV71 als CVA6 VLPs te optimaliseren. Onze resultaten indiceerde onderscheidende voorkeuren voor infectieparameters tussen de twee soorten VLPs, waarbij EV71 VLP-productie de voorkeur gaf aan een lage MOI, lage VCD en lange infectieperiode, terwijl CVA6 VLP-productie de voorkeur gaf aan een hoge MOI, hoge VCD en lange infectieperiode. Daarnaast hebben we een zuiveringsproces ontwikkeld voor beide VLPs, wat

resulteerde in opbrengsten van respectievelijk 158 mg/l en 38 mg/l van het cultuurvolume voor de gezuiverde EV71 en CVA6 VLPs. Deze concentraties vertalen zich in duizenden tot tienduizenden vaccins, wat het economische potentieel van “enterovirus-like partikels” voor vaccinatie benadrukt.

Virus-like partikels zijn geïdentificeerd als een veelbelovende benadering voor de ontwikkeling van een multivalent vaccin. Echter is hun stabiliteit een belangrijk probleem gezien de lagere mate van deeltjesintegriteit over het verloop van tijd in vergelijking met geïnactiveerde vaccins. In **Hoofdstuk 4** wordt uitgebreid over hoe de VLPs, geproduceerd met behulp van de geoptimaliseerde protocollen beschreven in **Hoofdstuk 3**, zijn onderworpen aan biofysische karakterisering. We hebben meerdere biofysische technieken toegepast, waaronder transmissie-elektronenmicroscopie en atoomkrachtmicroscopie, om de oorzaken van de verminderde VLP-stabiliteit (gemiddeld 1.5-2 keer lager) in vergelijking met het oorspronkelijke virus te achterhalen. In tegenstelling tot eerder onderzoek naar enterovirus-VLPs, toont deze studie aan dat een considerabel deel (31%) van de geproduceerde VLPs in staat was om viraal RNA (vRNA) in te kapselen. Bovendien toont dit werk aan dat de aanwezigheid van vRNA in de capsiden mogelijk niet de dicterende factor is voor de stabiliteit van enterovirus-capsiden. Alsook kan vRNA niet de enige factor zijn die verantwoordelijk is voor het activeren van de stabiliserende virale “rijping”, en is het hoogstwaarschijnlijk dat andere onderliggende mechanismen een rol spelen. Als VLPs de stabiliteit willen bereiken die vergelijkbaar is met die van virussen, zijn methoden nodig om virale rijping kunstmatig op te wekken. Als alternatief kunnen ook (chemische) aanvullingen op de vaccinformulering worden ingezet om de capsiden te stabiliseren, wat van groot belang kan zijn om het succes van VLPs als vaccin te waarborgen.

In **Hoofdstuk 5** presenteren wij een protocol voor het gelijktijdig onderzoeken van honderden polymerases met respect tot hun RNA-synthese dynamica met behulp van magnetische pincetten (MT). Het protocol omvat het gehele proces, beginnend bij het samenstellen van het RNA-construct tot de kwantitatieve en statistische analyse van de MT-metingen. Het protocol maakt het mogelijk om honderden RNA-ketens gelijktijdig te analyseren, wat resulteert in de karakterisering van de “single-molecule” dynamica, die worden gepresenteerd in het hiernavolgende hoofdstuk.

Hoofdstuk 6 van dit proefschrift toont het potentieel van magnetische pincetten (MT) voor de gedetailleerde mechanische karakterisering van het virale RNA-afhankelijke RNA-polymerase (RdRp). Door de pausedynamica en -kansen van deze polymerases te onderzoeken, konden we hun individuele mechanische eigenschappen ontcijferen. In het bijzonder onderzochten we de effecten van T-1106 trifosfaat, een pyrazine-carboxamide ribonucleotide met antivirale eigenschappen, op de enterovirus A71 RdRp. Onze resultaten toonden aan dat T-1106-incorporatie in het RNA leidde tot meer en langer pauzeren en het “backtracken” van de RdRp. Bovendien

identificeerden we de “backtrack” staat as een intermediair die werd gebruikt door de RdRp voor “copy-back” RNA synthese en homologe recombinitie, wat suggereert dat pyrazine-carboxamide ribonucleotiden werken door het bevorderen van “template switching” en de vorming van defecte genomen. Ten slotte hebben we aangetoond dat MT veelbelovende antivirale kandidaten kan scannen en de meest veelbelovende kandidaten kan aanduiden voor verdere ontwikkeling. Hierdoor, is de gedetailleerde mechanische karakterisering van virale RdRp-dynamica die door MT wordt geboden, een veelbelovend pad voor de identificatie en optimalisatie van antivirale therapieën.

Hoofdstuk 7 van dit proefschrift bevat conclusies en beoogde potentiële aanknooppunten voor toekomstig onderzoek. Dit werk kan dienen als basis voor verder onderzoek, vanuit zowel een biofysisch als een biochemisch oogpunt.

Acknowledgements

This dissertation is an exemplification that the whole is greater than the sum of its parts. The interplay between industry and academia, Delft and Groningen, PhDs, technicians, and postdocs, colleagues and friends, hard work and leisure time, contributed to a final product, unobtainable by me alone. It goes without saying that there are many people that need to be thanked, and moreover, that I will forget someone in this acknowledgement. If so, you will have to forgive me, and I do thank you for all your help and efforts during my PhD. It is not for lack of appreciation, merely the lack of sleep while writing this dissertation, that you are not mentioned here.

First, I would like to extend my gratitude to **Nynke** and **Leo**, who allowed me to join this project on their Delft Global grant and have advocated for the continuation of the work into a PhD. Their open way of communicating, providing me with feedback, advice, and suggestions, as part of the scientific supervision was vital to the successful completion of my PhD. To Nynke, I wish to extend my gratitude for her consistent support. I consider myself fortunate to have been under her mentorship. Her insightful feedback and encouragement have consistently motivated me to pursue excellence and to explore the frontiers of knowledge. I am deeply appreciative of the commitment and effort she has dedicated to shaping me into an independent researcher. To Leo, I wish to convey my appreciation for his insights and extensive expertise in the relevant subject matter. Your mentorship has not only broadened my comprehension of the topic but has also provided me with a profound understanding of its intricate nuances and complexities. To the both of you, I express my sincerest appreciation.

Secondly, I extend my gratitude to the other committee members, dr. **Arjen Jakobi**, prof. dr. ir. **Stan Brouns**, prof. dr. ir. **John van Noort**, prof. dr. **Monique van Oers**, dr. **Dimphna Meijer**, and prof. dr. **Chirlmin Joo**, who have taken the time and effort to read and assess my dissertation and challenge its content and scientific soundness during my defense. Specifically, I would like to thank Arjen, not only for being part of my committee, but also for being part of a great collaboration. The time and effort he put in ranging from hands-on training, all the way to reading, assessing, and providing feedback on the yearly progress reports, presentations, and dissertation were instrumental to this work.

For the organization, especially during the contract negotiations for the PhD, I must acknowledge **Belen**, who has spent endless hours (even during her holidays) making sure the details in the contract were hammered out. Most likely, it is due to these

significant efforts that it took 8 months and not 2 years. Also during the final stages of the trajectory, she always pushed me with words of advice to ensure a successful completion in a timely manner.

From Delft's side the amount of support has been immense. I would like to thank **BN**, the **ND lab**, and its former members for their words of encouragement, advice, and helpful suggestions along the way. Lab excursions, (scientific) discussions, countless lab meeting meetings, and journal clubs have broadened my horizon. Furthermore, conferences were turned quickly into great adventures. In relation to the research presented in this dissertation, I extend a special acknowledgment to **Theo** and **Edo**. Their substantial contributions have been pivotal to the development of the two methods papers featured in this body of work. I am deeply appreciative of their collaborative efforts and the positive impact they have had on the scientific contributions presented here. Additionally, I wish to express my gratitude to **Wiel** for his contributions to my electron microscopy training, subsequent troubleshooting efforts, and help with the cryo-EM data acquisition.

Next, I want to thank **Intravacc B.V.** for providing the funding for my PhD. Even though we changed direction from the original proposal, I hope the created knowledge remains in the company and can be beneficial for future endeavors. Furthermore, I wish to express my gratitude to the (former) technicians, scientists, and other support staff who have provided assistance throughout this journey by means of training, expert opinions, and assistance with assays or company-related challenges. I would like to extend specific thanks to **Astrid**, **Olaf**, **Tom**, **Gerco** and **Bèr** for their contribution to USP, **Sven**, **Aart** and **Martijn** for their involvement with the DSP and DoE. I also want to acknowledge the assistance provided by **Arnoud**, **Justin**, **Larissa**, **Geert-Jan**, **Jeroen**, **Zaskia**, **Robert**, **Wichard**, and **Bas van Brienen** across various assays. Gratitude is due to **Ramon** and **Hugo** for their contributions to mass spectrometry, **Jolande** for her biosafety training and advice, and **Peter Soema**, **Matthijn**, **Wilfried**, **Yvonne** and **Dinja** for their guidance and acting as a sounding board. A special thanks goes out to **Wouter van den Braak**, not only for designing the most successful constructs, but also for his assistance in addressing day-to-day challenges and offering solutions.

To all aforementioned stakeholders, I need to extend my gratitude for having the patience and the confidence in me to yield the desired outcomes. Hitting a major roadblock in the early stages of the project was frustrating to all, but fortunately we managed to adapt, overcome, and continue. I hope you all agree that in the end, we managed to complete this project to everyone's liking.

I want to thank my paranymphs **Daniel** and **Nikola** who will be standing by my side through the defense. Daniel, the countless jokes, scientific monologues, and conversations have enriched my time in Delft. Looking back, I can't help but feel that your support and encouragement played a crucial role in helping me navigate the

challenging final phase of my PhD. Your uplifting presence made a significant difference, and I'm truly grateful for it. I have no doubt that you will excel in academia, and I can't wait to follow your journey, albeit from a distance. Nikola, our friendship that deepened during our master's studies means a lot to me. The fact that we've maintained our connection over time brings me great joy. Despite our infrequent meetings, when we do catch up, it's as if time hasn't passed, which truly exemplifies genuine camaraderie. I want to express my heartfelt gratitude for your constant and cherished friendship.

For all problems, small or big, personal, work related, or scientific, I have had exceptional support from you, **Richard**. You took me under your wing during the master's project and haven't stopped coaching me since. A major part of this dissertation is thanks to your endless efforts and time. Despite not steering my research anymore, your door remained always open for a scientific discussion or just a friendly talk. For all the additional work I have bestowed upon you, I would like to extend my deepest gratitude. I hope we maintain our (scientific) connection in the future.

To my collaborative partners, **Natasha, Yuzhen** and prof. dr. **Wouter Roos**, thank you for the patience and time to explain and introduce me to your expertise in biophysics. Your steadfast commitment and remarkable knowledge have notably elevated the quality and the scope of the conducted research. I hold deep appreciation for the privilege of working in partnership with each of you and for the constructive influence you've had on the results of both my PhD project and our collaborative endeavors. Your contributions have been instrumental in ensuring that this dissertation transcends mere biological experiments, embodying the essential biophysical analyses we aimed to achieve.

To my students, **Jelle, Georgiana**, and **Abbas**, I want to express my gratitude for the hard work and teaching me how to become a more structured, patient, and overall better supervisor. All three of you should be proud of the accomplishments during your internships which contributed greatly to this final product.

Whoever is under the misconception that this dissertation is a product of the scientific accomplishments of the abovementioned institutions and researchers alone, is sorely mistaken. I would not have been able to complete this work without some very important people in my life. My family, starting off with my **father** and **mother**. I want to thank you for how you raised me and helped me become the person I am today. At times, I am sure, you were wondering whether I would reach this point, which has been a tremendous motivator. No words will suffice to express my gratitude for the selfless sacrifices you have made in your life to enrich mine. To my **brother**, who has never stopped believing we would end up here, I owe nothing but praise. The reinforcement, encouragement, and advice you have provided me with over the years

have been a guideline throughout my life. You are the person I want to make most proud of me.

Additionally, the unconditional love and support from my (extended) family, **Els, Charlotte, Maria, Peter, Dagmar, Bastiaan, Marieke, Tim, Denise, and Michiel**, has been overwhelming, for which I am forever indebted. The Sinterklaas evenings are still one of the highlights of my year and now that our family is growing, it is great to see the younger generation tag along.

To my in-laws, **Telma, Adrian, and Gaspar**, thank you for welcoming me with open arms. The love and willingness to bind two families into one, exemplified by your presence during the most important events of my life, has been heartwarming. I hope to break the language barrier soon, to fully integrate into the Argentinian side of the family.

To my oldest friends, **Jeffrey, Arvin, Vincent, Oscar, and Joshua**, thank you for cheering me up when the cards were down and celebrating the successes whenever they came along in our lives. Having dinner or drinks with you guys has been among the fondest memories of the past 10 years. I can honestly say that our friendship has truly stood the test of time.

To my chosen family, **Kees, Joost, Thijs, Bas**, and by extension **Karen**, who have seen both highs and lows of my time as a PhD candidate. Thank you for all dinners, game nights, lazy football weekend afternoons, hockey games, and nights out, but above all listening ears, shoulders to cry on, heartfelt advice, and words of wisdom. On many occasions your perspective has changed my thought process, decision making, and in general my life. Sharing with you my professional and personal successes and failures, as you did with me, has been an absolute privilege. Thank you for being part of my life.

Lastly, to **Magdalena**. Thank you for all the dinners, support, words of encouragement, showing me the right direction, and in general love and care during the last four years. You have enriched my life in more ways than I thought possible. Your unwavering support, encouragement, and understanding have been my anchor throughout this journey. Your presence has illuminated even the toughest moments, and your believe in me has been my driving force. Thank you for being my constant source of strength and inspiration. I look forward to a wonderful future with you. Whatever obstacle comes our way, I know we can face it together. I love you.

Louis Kuijpers, August 2023

Curriculum Vitae

Louis Christiaan Kuijpers

08-JUN-1990	Born in Voorburg, The Netherlands
2002-2008	Secondary school College Het Loo, Voorburg, The Netherlands
2008-2015	B.Sc. Life Science & Technology Delft University of Technology, Delft, The Netherlands Leiden University, Leiden, The Netherlands
2015	Student Research Assistant Delft University of Technology, Delft, The Netherlands
2015-2017	M.Sc. Life Science & Technology Specialization tracks: Cell Factory & Biocatalysis Delft University of Technology, Delft, The Netherlands
2015-2017	M.Sc. Honours Programme Delft University of Technology, Delft, The Netherlands
2017-2018	Process Engineering Internship Xendo B.V., Leiden, The Netherlands
2018-2019	Research Associate Delft University of Technology, Delft, The Netherlands Intravacc B.V., Bilthoven, The Netherlands
2019-2023	Ph.D. Bionanoscience Delft University of Technology, Delft, The Netherlands Intravacc B.V., Bilthoven, The Netherlands Promoter: prof. dr. Nynke H. Dekker Co-promoter: dr. Arjen Jakobi

List of publications

6. **L. Kuijpers** *et al.*, “Beyond the RNA: Alternative mechanism for the stability and maturation of enterovirus-like particles” *Manuscript in preparation*
5. **L. Kuijpers** *et al.*, “Optimization of enterovirus-like particle yield during production and purification” *Manuscript in preparation*
4. **L. Kuijpers**, E. van Veen, L. van der Pol, and N.H. Dekker, “Automated cell counting for Trypan blue-stained cell cultures using machine learning.” *Manuscript in revision for PLOS One*
3. **L. Kuijpers**, T. van Laar, R. Janissen, and N. H. Dekker, “Characterizing single-molecule dynamics of viral RNA-dependent RNA polymerases with multiplexed magnetic tweezers,” *STAR Protoc.*, vol. 3, no. 3, p. 101606, 2022, doi: 10.1016/j.xpro.2022.101606.
2. R. Janissen, A. Woodman, D. Shengjuler, T. Vallet, K. Lee, **L. Kuijpers**, I.M. Moustafa, F. Fitzgerald, P. Huang, A.L. Perkins, D.A. Harki, J.J. Arnold, B. Solano, S. Shih, M. Vignuzzi, C. E. Cameron, N. H. Dekker, “Induced intra- and intermolecular template switching as a therapeutic mechanism against RNA viruses,” *Mol. Cell*, vol. 81, no. 21, pp. 4467-4480.e7, 2021, doi: 10.1016/j.molcel.2021.10.003.
1. F. Wu, P. Swain, **L. Kuijpers**, X. Zheng, K. Felter, M. Guurink, J. Solari, S. Jun, T. Shimizu, D. Chaudhuri, B. Mulder, and C. Dekker. “Cell Boundary Confinement Sets the Size and Position of the *E. coli* Chromosome,” *Curr. Biol.*, 2019, doi: 10.1016/j.cub.2019.05.015.

